MIT/WHOI

Massachusetts Institute of Technology
Woods Hole Oceanographic Institution

Joint Program
in Oceanography/
Applied Ocean Science
and Engineering

DOCTORAL DISSERTATION

U-Th Dating of Lacustrine Carbonates

by

Christine Y. Chen

February 2020

U-Th Dating of Lacustrine Carbonates

by

Christine Y. Chen

A.B., Princeton University, 2013

Submitted in partial fulfillment of the requirements for the degree of

Doctor of Philosophy

at the

MASSACHUSETTS INSTITUTE OF TECHNOLOGY

and the

WOODS HOLE OCEANOGRAPHIC INSTITUTION

February 2020

Author . . . .
Joint Program in Oceanography/Applied Ocean Science and Engineering
Massachusetts Institute of Technology
and Woods Hole Oceanographic Institution
January 10, 2020

Certified by . . . .
David McGee
Thesis Supervisor
Massachusetts Institute of Technology

Accepted by . . . .
Oliver Jagoutz
Chair, Joint Committee for Marine Geology and Geophysics
Massachusetts Institute of Technology/
Woods Hole Oceanographic Institution

U-Th Dating of Lacustrine Carbonates

by

Christine Y. Chen

Submitted to the Joint Program in Oceanography/Applied Ocean Science and
Engineering
Massachusetts Institute of Technology
and Woods Hole Oceanographic Institution
on January 10, 2020, in partial fulfillment of the
requirements for the degree of
Doctor of Philosophy

Abstract

Carbonates are prevalent in many modern and ancient lacustrine settings, but reconstructions of past lake levels or environments from such materials have been hindered by poor chronology. Uranium-thorium (U-Th) dating has the potential to fill a gap in current geochronological tools for such archives, but past attempts have been confounded by poor understanding of the complex makeup of lacustrine carbonates, leading to misguided conclusions on both the utility of certain geochronological tools as well as the age of these deposits. This thesis showcases strategies for the successful application of U-Th geochronology to two types of lacustrine carbonates: lake bottom sediments and tufa deposits. Chapter 2 presents a systematic approach to U-Th dating carbonate-rich lake sediments using the ICDP sediment core from Lake Junín, Peru. Chapters 3–5 seek to demonstrate the descriptive power of combining precise U-Th dates on tufas and other carbonates with geologic observations of their depositional context at all scales—from the outcrop to the microscale. Here, the tufas originate from a transect of closed-basin lakes in the central Andes of northern Chile. With improved sample selection and leveraging of the incontrovertible constraints of stratigraphy and coevality, we are able to test the validity of U-Th data. Combining quality-controlled geochronological constraints with careful characterization of different carbonate facies can yield new insight on the character of lake level changes. These case studies offer frameworks for interpreting scattered geochronologic data of any size or system. By embracing the noise in our data, we now have a richer understanding of the controls on uranium in these deposits. Of all the lessons learned, we hold the following as most important: for the determination of the age of lacustrine carbonates, geologic context—in the form of sedimentological observations, additional geochemical data, and paleoecological descriptions—is of equal importance to the numerical accuracy and precision of geochronological measurements.

Thesis Supervisor: David McGee
Title: Associate Professor

Biography

Christine Yifeng Chen (陈一枫) is the only child of Dr. Xinghao Chen (陈星浩) and Lanying Tian (田兰英). Her parents immigrated to the United States to continue their education after rules restricting the age of university students prevented them from doing so in their home country. Her father first arrived in the United States at the age of 27 by way of New York City on January 20, 1985; he remembers the date well because it was the day of President Ronald Reagan's second inauguration. Using most of the money he had on him, he bought a bus ticket to Newark, New Jersey, to make his way towards Rutgers University, where he had been accepted for the doctoral program in Electrical Engineering and Computer Science. Her mother joined him two years later after getting accepted to the same program. After completing a masters degree in 1990, her mother gave birth to Christine on March 12, 1991. With the help of grandparents from both sides of the family, her parents raised Christine while her father completed his dissertation in 1993. Wanting to give Christine the best childhood possible, both of her parents made the decision to remain in America, despite being far away from family in China.

In 1994, the family moved to the Greater Binghamton Area as both parents started jobs at IBM in Endicott, NY. There, they lived in a home with a backyard where Christine spent the majority of her childhood, exploring the nearby woods and creeks with her best friends down the street. Together, they wrote stories and made drawings about their adventures together. Second to spending time outside, going to school was her next favorite activity. She was always stymied by the question, "What is your favorite subject?" because all of them were fun and interesting to her in different ways. Christine attended grade school until graduating from Union Endicott High School in the spring of 2009. That fall, she enrolled at Princeton University on a full-tuition financial aid scholarship. She stepped onto campus with the intention to major in Geosciences, not only because of her interest in soil and agriculture, but also because the course catalog indicated that it was the only major to offer free field trips. Her first geology trip in October 2009 to southern California marked a major turning point in her life: scrambling down steep slopes of volcanic craters, crawling through narrow spaces of water-carved canyons, and ascending the majestic star dunes in Death Valley, she was the happiest she had ever been. The most lasting impression of the trip was made by Mono Lake and its oddly sculptured spires and knobs of tufa, exposed due to the lowering of lake levels from human demands on water. The fact that she devoted her dissertation in part to the study of tufas, many years later, may be more than a happy coincidence.

Acknowledgments

Like all scientists, I stand on the shoulders of giants. This work would not have been feasible without the efforts of countless others before me. I have added my piece to the edifice of human knowledge, and I hope others will find it sound, sound enough to build, modify, or improve on. Likewise, the fact that I am graduating with a PhD from MIT and Woods Hole was an improbability only made possible by the collective effort of all those who have invested in me at different points in my life.

Where do I begin? I suppose from the start. My mother and father both came to America on student visas in the 1980s to continue their education after some delays in doing so in their home country. I am grateful to the United States of America for providing them and other immigrants the opportunity to pursue their dreams of self-betterment and a better life. As they completed their degrees at Rutgers University, they were also able to experience a slice of the American way, and they noticed that kids here seemed to have a lot of fun: they played sports, like soccer or basketball; some had hobbies playing musical instruments or making art; and kids hung out with other kids, often terrorizing the neighborhood. In short, kids seemed happy. And so, despite being in a foreign place thousands of miles away from all other family, they decided to stay in America to raise me, so that I might have a happy childhood. And I did. I am grateful to my parents for making that sacrifice.

Growing up, I was lucky to live on a street with two other girls of essentially the same age as me: Debbie Miller and Laura Jurewicz. I cannot think of any two more perfect people to have grown up with. Somehow, we found each other. These are my strongest memories: crash courses on red wagons and black sleds; expeditions up the creek that felt like our secret; climbing Zarathustra and getting pine needles and sap in our hair; scavenger hunts and board games created from our imagination; riding our bikes recklessly up and down and around the steep curve of our street; and lighting things on fire that we probably shouldn't. There are other memories, less clear, but all warm. When I think about the kind of person I want to be, it is the person who we would have dreamt of being back then. I am grateful to them for making me feel like I could be myself and still belong.

I had several teachers in grade school who supported my diverse interests and long after-school stays. Sadly, some of their names now escape me. But I can remember Mrs. Simon, Mr. and Mrs. Stanko, Mr. Materese, Mrs. Golden, Ms. Henry, Mr. Friend, Ms. Trupp, Mr. Johnson, Mr. Hubert, Mr. Rinde, and my 6th grade teacher whose birthday is on June 4 and whose favorite music artist is Pink. I am grateful to them for making me feel at home.

In college, I spent the majority of my time ensconced in the incomparable Guyot Hall, a timeless building with gargoyles of fossils and even a geologic feature named after it (yes, not the other way around). There, in Guyot 16, a dusty and old wood-trimmed room with models of mineral lattices cluttering the ceiling, is where I first met Adam Maloof, to whom I owe everything. His sincere interest and commitment to my academic development over my four years of undergrad profoundly changed the way I saw the world, and my role in it. He saw potential in me that I did not know I had. I am forever grateful to him for believing in me, so that I could believe in myself.

On the second floor of Guyot, I met my second family: Jon Husson, Blake Dyer, Catherine Rose, Brenhin Keller, Kyle Samperton, Clara Blättler, and Liz Lundstrom. They are the closest people I will ever have to siblings, and I am forever grateful to them for taking me under their wings. Everyone has now left that nest, but I am so, so proud of them and all that they have achieved. I also share many wonderful and unforgettable memories with Frederik Simons and Blair Schoene, who I thank for being models of kind professors who genuinely care for their students, remembering each one of us as people first. I think back on these days with warm fondness, as if a sunbeam were shining on my heart.

My graduate school experience can only be described as a fulfillment of dreams that I did not realize I had. I have had the incredible privilege of traveling to far-flung and remote places where few have ever been, as a true explorer and observer of the unknown and mysterious. Watching NOVA on PBS every week, my eight-year-old self would hardly dare to believe that I could one day be such a scientist, let alone ever be granted a title like "National Geographic Young Explorer." It is an impossible dream made real in this version of the universe. I am grateful to my advisor, David McGee, for enabling these opportunities, and I appreciate his patience and trust in granting me the broad autonomy to chart this path for myself. Jay Quade, Kristin Bergmann, Tim Lowenstein, Andrew Ashton, and Roger Summons have been generous with their time and supportive as my thesis committee members, mentors, and collaborators, and with luck, I hope those connections continue.

An acknowledgment of all those who have helped me get here would not be complete without mentioning the many other students, post-docs, researchers, and people who I am grateful to have known and learned from. To nama a few: Elena Steponaitis, Christopher Kinsley, Gabi Serrato Marks, Michaela Fendrock, Irit Tal, Adam Jost, Ben Hardt, Chris Hayes, Rick Kayser, Charlotte Skonieczny, Francois Tissot, Nick Scroxton, Josh Murray, Yan Zhang, Zixuan 'Crystal' Rao, Jade Fischer, AJ Iversen, Almanzo Seguin, and Ruth Tweedy as fellow lab mates and friends; Kim Huppert, Justin Stroup, Roger Fu, Maya Stokes, Sebastian Jimenez Rodriguez, Francisco González Pinilla, Héctor Orellana, Matías Frugone Alvarez, and Kristian Olson as the best field partners one could ask for; Jade Zimmerman, Blas Valero-Garcés, and Claudio Latorre as invaluable facilitators of my research; Arielle Woods, Sophie Lehmann, Liseth Pérez, Antje Schwalb, Rob Hatfield, Joe Stoner, Don Rodbell, Pedro Tapia, and Mark Abbott as collaborators on the Junín project; and Melody Abedinejad, Erin Wedding, Ronni Schwarz, Brian Smith, Michael Richard, Kris Kipp, Meg Tivey, Megan Jordan, Brandon Milardo, Lauren Hinkell, Jen Fentress, Vicki McKenna, Julia Westwater, and Lea Fraser for making sure that the sun rises everyday.

There are also a great many friends and colleagues with whom I have made wonderful memories: Kai Sheng Tai, Julia Yan, Kevin Zhang, Greg Ely, Sharon Newman, David Wang, Danielle Gruen, Rohini Shivamoggi, Julia Wilcots, Mara Freilich, Marianna Linz,

Catherine Wilka, Luis Lena, Erik Lindgren, Eva Golos, Michael McClellan, Jimmy Bramante, Jeehyun Yang, Marjorie Cantine, Brian Green, Xinqian Cui, Gareth Izon, Athena Eyster, Sam Goldberg, Mukund Gupta, Ainara Sistiaga, Jorsua Herrera, Fatima Husain, Mike Eddy, Annie Bauer, Ken Ferrier, Alex Andrews, Dan Amrhein, Ben Mandler, Bryan Kaiser, Paul Richardson, Dino Bellugi, Mike Sori, Jaap Nienhaus, Seulgi Moon, Jean-Arthur Olive, Niya Groveza, Ben Klein, Jeemin Rhim, Noah Anderson, Tyler Tamasi, Martin Wolf, Patrick Beaudry, Stephanie Brown, Ellen Lalk, Tyler Mackey, Rose Palermo, Lizzy Wallace, Billy Shinevar, Varun Madiath, and so many more.

Graduate school also marked another deep awakening, this time about how the world really works. I made many mistakes, but in the process, I see more clearly the barriers to transformational progress in our field and discipline. I have also come to a better understanding of myself. The burden of seeing is a constant weight on my mind, but it is better than inadvertently becoming part of the problem. For inspiring me and for lessons learned, I thank countless people on Twitter for opening my mind to ideas from outside of my bubble. Attitudes change, but only because brave people jump into the fire and make it happen: I will continue to challenge the status quo and to pay my good fortune forward whenever I can.

Funding sources: National Science Foundation, Massachusetts Institute of Technology, Geological Society of America, MIT MISTI, Comer Foundation, American Philosophical Society, National Geographic Society, Explorers Club.

Contents

List of Figures

List of Tables

Chapter 1

Introduction

Geology, at its core, is a discipline of science concerned with the reconstruction of events and processes throughout the history of time. As such, geochronology is of unparalleled importance to the field, providing constraints on past rates of change of fundamental processes on Earth (e.g., evolution, tectonics, climate change) and testing hypotheses of causal relationships of critical events in Earth history (e.g., mass extinctions). Before the discovery of radioactivity (Becquerel, 1896), geologists told time the old fashioned way: by making careful qualitative observations of rocks. It began with the principles of superposition and cross-cutting relationships (Avicenna, 1027; Steno, 1669), followed by the principle of faunal successions (Smith, 1816), which enabled early geologists to correlate strata from around the world to formulate a geologic timescale of Earth history. This relative timescale was then put in absolute terms starting with the first application of uranium decay series in the measurement of geologic age by Arthur Holmes in his paper, “The Association of Lead with Uranium in Rock-Minerals and Its Application to the Measurement of Geological Time” (Holmes, 1911).

Since then, our understanding of isotopes and our ability to measure them have improved, and over the past few decades, the increased sophistication of mass spectrometric techniques has led to the proliferation of geochronological measurements of increasing precision. However, in the excitement of generating and advancing such quantitative measurements, the application of the aforementioned principles of stratigraphy to form relative constraints on sequences was relegated and at times considered lesser than the numerical information generated from isotopic analyses. Research efforts were mainly focused on decreasing analytical uncertainties and increasing numerical accuracy on measurements.

Today, mass spectrometry for uranium series isotopes is at a level of technological advancement such that the amount of material needed for an analysis is of a scale on par with the sub-centimeter cross cutting and stratigraphic relationships commonly observed in lacustrine sediments and shorezone deposits. These incontrovertible constraints can now be leveraged as equally powerful information to assess the accuracy of geochronological data. Furthermore, the precision of individual analyses is now high enough such that the scatter of dates itself can represent geologically meaningful information rather than problems related to the analytical measurement ("dispersion" or "geologic scatter").

This thesis aims to recombine the age-old axioms underpinning the field of geology with modern day uranium-thorium (U-Th) dating techniques for the determination of the age of lacustrine carbonates. These materials are historically considered to be non-ideal for this geochronological tool and thus often not worth the investment of time, resources, and personnel. We apply U-Th dating to two types of lacustrine carbonate deposits: lake sediments and tufas.

Chapter 2 presents a systematic approach to U-Th dating carbonate-rich sediments from the ~100-m-long drill core from Lake Junín, Peru. Deep sediment cores from long-lived lake basins are fundamental records of paleoenvironmental history, but the power of these reconstructions has often been limited by poor age control. U-Th dating has the potential to fill a gap in current geochronological tools available for such sediment archives. The U-Th dating results from the sediment core form the foundation of an age-depth model spanning ~700 kyrs. High uranium concentrations (0.3–4 ppm) of these sediments allow us to date smaller quantities of material, giving us the opportunity to improve sample selection by avoiding detrital contamination, the greatest limiting factor to the success of previous U-Th dating efforts in other lake basins. The dates from 174 analyses on 55 bulk carbonate samples revealed significant scatter that could not be resolved with traditional isochrons, suggesting that at least some of the sediments have not remained closed systems. To understand the source of noise in the geochronological data, we first apply threshold criteria that screen samples by their U/Th ratio, reproducibility, and $\delta^{234}\mathrm{U}_{\mathrm{initial}}$ value. We then compare these results with facies types, trace element concentrations, carbonate and total organic carbon content, color reflectance, mineralogy, and ostracode shell color to investigate the causes of open system behavior.

We find that the greatest impediment to U-Th dating of these sediments is not detrital contamination, but rather post-depositional remobilization of uranium. After examining U-Th data in these contexts, we identify samples that have likely experienced the least amount of alteration, and use dates from those samples as constraints for the age-depth model. Our work has several lessons for future attempts to U-Th date lake sediments, namely that geologic context is equally important as the accuracy and precision of analytical measurements when determining the age of sample materials. In addition, we caution that significant geologic scatter may remain undetected if not for labor intensive tests of reproducibility achieved through replication. As a result of this work, the deep sediment core from Lake Junín is the only continuous record in the tropical Andes spanning multiple glacial cycles that is constrained entirely by independent radiometric dates. As such, this record is uniquely poised to offer new insights on past climate and environmental changes in the tropical Andes, complementing and testing the long but tuned sediment records from Sabana de Bogotá to the north (~5°S; Groot et al., 2011) and Lake Titicaca to the south (~16°S; Fritz et al., 2004, 2007).

Chapters 3–5 focus on U-Th dating of tufas and other lacustrine shorezone deposits. In arid regions worldwide, extensive build-ups of porous carbonate rock called "tufa" are unmistakable evidence for past landscape occupation by pluvial lakes. These tufas frequently exhibit a rich diversity of architectural structure, morphology, composition, and texture, but leveraging these characteristics to reconstruct the conditions and processes responsible for this diversity is often limited by uncertainties in the timing and rate of tufa formation. Conversely, past attempts at dating tufas have been confounded by poor understanding of the complex makeup of these deposits, leading to misguided conclusions on both the utility of certain geochronological tools for tufas as well as their age.

Chapters 3–5 present data from late Pleistocene lake basins in the central Andes for insight. We demonstrate the descriptive power of combining (1) precise U-Th dates on tufas and other lake carbonates with (2) geologic observations of their depositional context at all scales—from the outcrop to the microscale. These analyses inform one another: taking advantage of our ability to U-Th date small (<10 mg) amounts of powder, we use petrography to improve sample selection, and then test data for internal consistency by applying physical stratigraphic and coevality constraints. From this, we observe that U-Th dates on dense (non-porous) or crystalline materials more often yield data that pass these tests. We also document open system behavior in deposits that would nominally pass traditional geochemical criteria for valid U-Th dates. Pairing quality-controlled U-Th dates with outcrop and petrographic observations, we present more nuanced insights on the timing and variability of past lake levels associated with tufa formation. Dates calculated from measurements are only as good as the interpretation of the geologic materials utilized—only then should geochronological data be used to infer the timing or duration of a specific process or event. By combining the geologic context of lacustrine sediments and tufas with U-Th geochronological constraints, our interpretations are more closely aligned with that which is the truth.

Chapter 2

U-Th dating of lake sediments: Lessons from the 700 kyr sediment record of Lake Junín, Peru

2.1 Introduction

Since the founding of the International Continental Scientific Drilling Program (ICDP) in 1996 (Colman, 1996), scientific teams have recovered dozens of deep lake sediment cores from nearly every continent in the world. Due to their continuity, resolution, and wide geographic distribution, these sediment records have provided important long-term perspectives on Earth's terrestrial environmental history. As the spatial and temporal coverage of such records expand, the next step is to combine these records with complementary studies from marine and ice cores to address longstanding questions about the linkages and causal relationships among terrestrial, marine, and atmospheric phenomena. Here, the challenge lies in comparing the timing, rate, and duration of past land surface and ecosystem changes to those of past events identified elsewhere in the oceans, atmosphere, and other continental regions. Thus, the extent to which tests for leads and lags in the climate system are useful is limited not by the quality of environmental proxy interpretation, but rather by the quality of the temporal constraints.

While ice and marine cores are often amenable to layer counting or anchoring to globally synchronous reference timescales (e.g., oxygen isotope "chronostratigraphy" in marine sediments, methane gas concentrations in ice cores), determining a reliable age-depth model for long lacustrine sediment sequences is generally more problematic. Because lake basins occupy a broad range of environments, each drilling location often contains a site-specific accumulation of terrigenous and biogenic sediment as well as a unique post-depositional alteration history influenced by non-climatic processes like tectonics and volcanism. Thus, aligning such records to external reference timescales (colloquially known as "tuning") requires a thorough investigation of how global climate events and more proximal geologic processes affect local paleoenvironmental proxy variability. Proving such relationships convincingly can be a formidable undertaking, but in the absence of other data, tuning is often the only means available to establish time constraints. As a result, such records are limited in their ability to address climatic questions that are dependent on the relative timing of events (e.g., Prokopenko et al., 2006; Nowaczyk et al., 2013; Stockhecke et al., 2014; Francke et al., 2016).

Therefore, when possible, absolute chronological data from radiometric and paleomagnetic dating techniques are highly desirable and generally serve as first-order constraints on age-depth models of sediment cores. The success and utility of such methods is dependent on factors such as the availability and quality of datable materials, the time range of the method, and the adherence to assumptions underpinning each technique within a given sediment sequence. When these factors align, the resulting independent chronologies allow for compelling investigations of forcing relationships (e.g., the radiocarbon- and tephra-based chronologies of Laguna Potrok Aike in Patagonia [Kliem et al., 2013] and Lake Petén Itzá in Guatemala [Kutterolf et al., 2016]). However, problems commonly arise when suitable dating materials are absent or the true age of the sediments is outside the applicable temporal range of a method: for instance, datable tephras are rare in most environments and the radiocarbon method is generally limited to the last 50 ka.

Currently, there exists a gap in comprehensively tested high-precision geochronological tools in the time interval between 50 and 780 ka, beyond the limit of radiocarbon dating and up to the most recent geomagnetic reversal (Brunhes–Matuyama), after which paleomagnetic reversal stratigraphy can be applied. Here, methods like uranium-thorium (U-Th), cosmogenic exposure, and optically stimulated luminescence (OSL) dating have potential (e.g., Roberts et al., 2018). However, these systems have mostly been underexplored in their broad application to lake sediments or have not been refined since improvements in instrumentation have opened new doors for sample selectivity. Ideally, data from multiple complementary chronological tools with different operating assumptions can be used to cross-validate one another (e.g., Colman et al., 2006; Shanahan et al., 2013), and in the process, reveal information about the nature of uncertainties and biases specific to each technique.

To this end, we present our efforts to U-Th date the carbonate-rich sediments from the deep drill core extracted in 2015 from Lake Junín, Peru. Our strategy for sample selection, tests for internal consistency that leverage stratigraphic coevality constraints, and use of other corresponding sedimentological, geochemical, and paleoecological data to inform our interpretations of the U-Th data can serve as a framework for future attempts to apply U-Th dating techniques to long cores. Our results also indicate that future work to establish or refine U-Th-based lake sediment chronologies must include deliberate tests that probe for possible open system behavior or excess "geologic scatter"—unresolved errors that can affect the accuracy and precision of dates due to unknown geologic complexities not accounted for in typical uncertainty calculations and corrections (Ludwig and Paces, 2002). Without a methodical exploration of U-Th data in context of other geologic information, age-depth models that contain single, standalone U-Th analyses that, at face value, seem like valid ages, may in fact hide the existence of geologic scatter and therefore be inaccurate.

The organization of this paper is as follows: We first provide a basic overview of the principles behind U-Th dating and review previous efforts to apply U-Th geochronology to lake sediments (Section 2.2). After describing the relevant background of Lake Junín (Section 2.2.3) and our methods for core sampling, U-Th geochemistry, and isotopic measurement (Section 5.2), we then present the results of 174 U-Th analyses from 55 unique samples (Section 5.3). Of these, only 72 analyses from 18 samples are used in the final chronology for the core. We explain our screening procedure for evaluating the validity of each U-Th date (Section 2.5), and then interpret our analyses alongside other sedimentological, geochemical, and paleoecological data to show that uranium remobilization, not detrital contamination, is the most likely cause for discrepancies in our data (Section 2.6). We then simulate the impact of detrital contamination and uranium remobilization on the isotopic evolution of our samples to further support this conclusion (Section 2.7). Using the U-Th age constraints that pass our criteria and radiocarbon dates from Woods et al. (2019), we then describe the construction of the age-depth model for the Lake Junín sediment record (Section 2.8). We end with a discussion on the uncertainties in U-Th age estimates learned from this study and propose considerations for future U-Th dating of lake sediments (Section 2.9).

Because terminology is important, hereafter, we distinguish between the terms *date* and *age*, adopting the convention followed by other geochronologists (e.g., Schoene et al., 2013; Dutton et al., 2017): a date is a number calculated from a decay equation and isotopic measurements, whereas an age is an interpretation of a date in the context of other information and represents a geologically meaningful time.

2.2 Background

Thus far, the application of U-Th dating in continental paleoclimate archives has been most visible and transformative in unrecrystallized corals and dense carbonate precipitates like cave stalagmites and groundwater vein calcites (e.g., Winograd et al., 1992; Cheng et al., 2000; Wang et al., 2001). In comparison, U-Th dating of lake sediments has historically been less straightforward. To place the challenges of our work in this context, in this section, we briefly describe the basic principles of U-Th dating, the geologic processes in lake sediments that can compromise the underlying assumptions of this dating system, and the strategies used by other studies to overcome or account for these issues.

2.2.1 Basic principles of U-Th dating

There are several "uranium-series disequilibrium" dating methods that make use of the decay chains of various actinide nuclides (e.g., ^{238}U, ^{235}U; see Bourdon et al., 2003). Unlike other notable radiometric chronometers such as uranium-lead or potassium-argon, which compare the concentrations of a parent nuclide to that of its stable daughter product, uranium-series disequilibrium dating schemes instead compare the activity—the number of disintegrations per unit time per unit mass of a material—of a parent nuclide to those of their series of unstable daughter products. These methods estimate time by measuring the degree to which different daughter isotopes along a decay chain are out of *secular equilibrium*, a steady state in which the activity of both the parent and daughter nuclides are equal (*i.e.*, the number of daughter nuclides forming is equal to the number of daughter nuclides decaying). Because the half-lives of the parent isotopes are much longer than that of all intermediate daughter products in these decay chains, a material containing the parent isotope that has remained unperturbed for several million years will have reached secular equilibrium (*i.e.*, the activity ratio of the parent nuclide to its daughter product will be equal to 1).

Disturbances to this equilibrium caused by various natural geochemical processes form the basis of uranium-series disequilibrium dating. For example, because of differences in the solubility of uranium and thorium complexes in natural waters of near-surface and surface environments, the highly soluble parent uranium is separated from its effectively insoluble daughter product thorium in a marine or lacustrine carbonate deposit. Once this separation occurs, the system will follow the laws of radioactivity, restoring equilibrium between the parent and daughter nuclides at a rate determined by their respective decay constants. Thus, the timing of carbonate formation is determined by measuring the extent to which daughter product growth has restored the system to secular equilibrium (*i.e.*, the extent to which the activity ratio of the parent nuclide and its daughter product has returned to unity). Using measurements of relevant activity ratios, a date can then be calculated from decay equations and constants.

Of the many uranium-series dating techniques available, in this paper, we use the more widely applied ^{230}Th-^{234}U-^{238}U disequilibrium dating method, for which "U-Th dating" commonly serves as shorthand (Fig. 2-1). U-Th dating has been most widely applied in carbonate minerals: not only are they nearly ubiquitous in most continental waters, but they also contain relatively higher amounts of uranium and are less prone to post-depositional alteration than other lacustrine precipitates, like halite. As previously mentioned, the conditions that increase the solubility and mobility of uranium tend also to decrease the solubility and mobility of thorium. In oxic environments, uranium generally assumes its highest oxidation state (U^{6+}) in the form of the highly soluble uranyl ion (UO_2^{2+}) which easily forms stable complexes with carbonate ions (CO_3^{2-}), further enhancing its solubility. UO_2^{2+} is then adsorbed onto or structurally incorporated into carbonate mineral host phases (Langmuir, 1978; Reeder et al., 2000, 2001; Kelly et al., 2003, 2006). In contrast, thorium is generally very insoluble and immobile in most aqueous environments where pH $>$ 3, with some exceptions (Chabaux et al., 2003). The solubility of both uranium and thorium increase significantly when forming complexes with organic ligands like humic and fulvic acids (Langmuir and Herman, 1980; Halbach et al., 1980; Murphy et al., 1999; Lenhart et al., 2000). Thus, in most conditions, except for those that are highly reducing or organic-rich, fluids are enriched in uranium and depleted in thorium, and this extreme fractionation is preserved when calcium carbonate forms from such waters.

Two equations take advantage of this behavior to form the backbone of U-Th dating. The first is the ^{230}Th age equation:

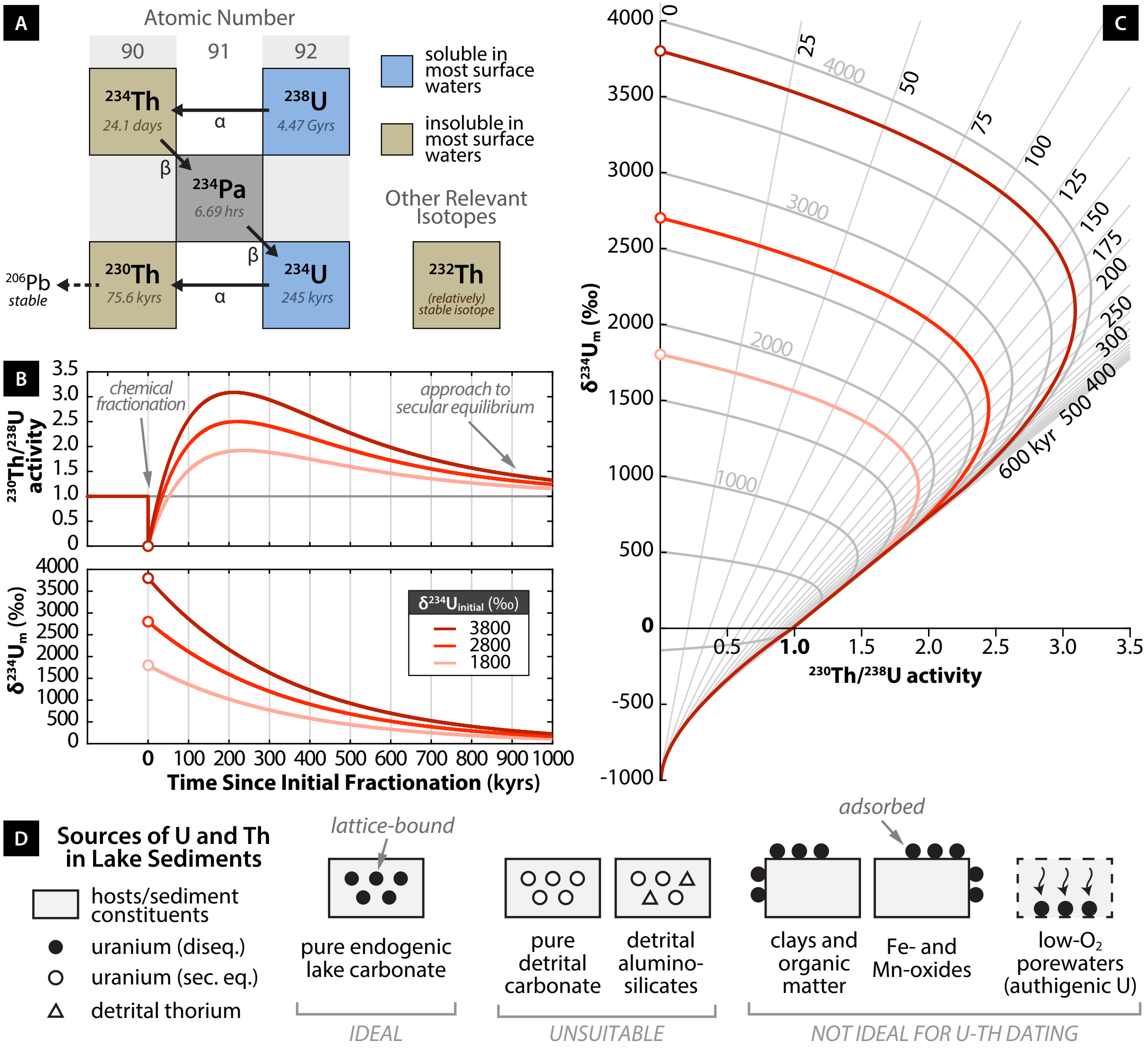

Figure 2-1: The basic principles of U-Th dating. [**A**] Schematic of the portion of the ^{238}U decay chain that is relevant for U-Th dating. The half-lives and type of particle emitted during radioactive decay (an α or β particle) of each isotope are shown. Ultimately, the decay chain ends with the stable ^{206}Pb. [**B**] and [**C**] Panels illustrating the evolution of ^{230}Th/^{238}U activity and measured δ^{234}U ($\delta^{234}U_m$)—the two ratios used for the calculation of U-Th dates—after initial fractionation. The three thick red-shaded lines represent different pathways towards secular equilibrium based on the value of $\delta^{234}U_{\text{initial}}$ (see legend in bottom of Panel B). Values shown are within the range of values observed in the Lake Junín sediments, but are otherwise arbitrary and selected purely for demonstration. Panel C plots the same curves in Panel B but in ^{230}Th/^{238}U activity-$\delta^{234}U_m$ space to show the graphical solution to the age equations. Hollow circles mark the initial isotopic composition of the sample. Straight gray lines represent solutions to the ^{230}Th age equation (Eq. 2.1, lines labeled in kyrs with black text) and curved gray contours represent solutions to the δ^{234}U equation (Eq. 2.2, some curves labeled with their $\delta^{234}U_{\text{initial}}$ in gray). The plot of data in ^{230}Th/^{238}U activity-$\delta^{234}U_m$ space originates from Edwards (1988). [**D**] Schematic of uranium and thorium sources in lake sediments. Black circles represent uranium in ^{230}Th/^{238}U disequilibrium whereas white circles represent uranium in secular equilibrium. To simplify, the detrital carbonate and aluminosilicate constituents represent bedrock-derived material of old age (>2 Ma). The placement of circles and triangles within or around boxes represents how uranium and thorium are associated with each host: bound within the crystal lattice or adsorbed to the substrate surface. The box furthest to the right represents the low-oxygen porewater uranium sink, where uranium changes from a soluble to insoluble valence state and accumulates authigenically.

$$\left[\frac{^{230}\mathrm{Th}}{^{238}\mathrm{U}}\right] - 1 = -e^{-\lambda_{230}t} + \left(\left[\frac{^{234}\mathrm{U}}{^{238}\mathrm{U}}\right] - 1\right)\left(\frac{\lambda_{230}}{\lambda_{230} - \lambda_{234}}\right)\left(1 - e^{-(\lambda_{230}-\lambda_{234})t}\right) \tag{2.1}$$

where square brackets around ratios indicate activity ratios; λ symbols are decay constants; and t is the date (Bateman, 1910; Broecker, 1963; see Edwards, 1988 and Ivanovich and Harmon, 1992 for derivation). The ^{234}U/^{238}U activity is more commonly expressed using delta (δ) notation, representing the deviation in parts per thousand (permil; ‰) of ^{234}U/^{238}U from secular equilibrium: δ^{234}U = ([^{234}U/^{238}U]−1) × 1000. From this equation, it is clear that measuring three key isotopes—^{238}U, ^{234}U, and ^{230}Th—allows us to uniquely solve for t (Fig. 2-1A).

The term in Eq. 2.1 involving δ^{234}U exists to account for the enrichment of ^{234}U over ^{238}U commonly observed in natural waters (Thurber, 1962). This disequilibrium is caused by the preferential leaching of ^{234}U during water-rock interactions due to its displacement inside the crystal lattice of the host mineral by the alpha recoil of its parent ^{234}Th (Kigoshi, 1971; Kronfeld, 1974; Fleischer, 1982; Chabaux et al., 2008). After solving for t using Eq. 2.1, we can use a second equation to determine the starting value of δ^{234}U at the time of fractionation (δ^{234}U$_{\mathrm{initial}}$):

$$\delta^{234}\mathrm{U_m} = \left(\delta^{234}\mathrm{U_{initial}}\right) e^{-\lambda_{234}t} \tag{2.2}$$

where the subscript m represents the present measured value. Thus, these two equations allow us to solve for two unknowns with the measurement of two isotopic ratios.

Fig. 2-1B shows the expected isotopic evolution of ^{230}Th/^{238}U activity and δ^{234}U$_{\mathrm{initial}}$ over time, provided the system remains closed. Fig. 2-1C shows the graphical solution to Eqs. 2.1 and 2.2: straight, sub-vertical lines represent solutions to the ^{230}Th age equation and curved lines emanating from the y-axis are solutions to the δ^{234}U equation. From this figure, two observations about this dating system can be made: (1) for a given analytical error, as the true age of the sample increases, so too does the error in the age estimate due to the increasing closeness of the age isolines; and (2) although both ^{230}Th/^{238}U and ^{234}U/^{238}U have not yet returned to their secular equilibrium values even after 1 Myrs, the age isolines eventually are so closely spaced that current analytical abilities cannot distinguish between a sample of a finite age and a sample of infinite age. This characteristic and current mass spectrometry techniques dictate the practical limit of U-Th dating at

∼700 kyrs (Stirling et al., 2000; Edwards et al., 2003; Cheng et al., 2016; Fig. 2-1A).

2.2.2 Previous work on U-Th dating of lake sediments

With all radiometric chronometers, a date is only interpretable as a meaningful age if the system meets the following criteria for *closed-system behavior*: (1) all decay products were absent at the time of formation, or can be corrected for if present; and (2) there was no gain or loss of any radionuclides after formation other than by radioactive decay. For U-Th dating of lake sediments, the most common obstacle is the lack of material that fulfill these criteria. Even carbonate-rich sediments remain difficult to date, as the carbonates often contain non-ideal constituents or have experienced post-depositional alteration due to various weathering, transport, and mixing processes common in lake basins (Fig. 2-1D).

Despite the challenge, geochronologists have devised ways to circumvent these issues. Table 2.1 is a list of lake sediment studies in which U-Th dating was applied, each with varying degrees of success. We distinguish between studies working with evaporites and carbonates, as these are the two most common materials used. Success has been limited primarily by the incorporation of detrital materials that introduce initial ^{230}Th, which increases uncertainties and, if not fully corrected for, potential inaccuracies. Detrital contamination is usually even more problematic for non-carbonate evaporites like gypsum or halite because these materials typically have very low amounts of uranium derived from precipitating waters. The most common detrital materials found in carbonates and evaporites are clay minerals (aluminosilicates and bulk limestone; Fig. 2-1D). Attempts to chemically separate detritus from bulk sediment have been made, but selective acid leaches meant to isolate endogenic material from the detrital component were found to also differentially fractionate the uranium and thorium isotopes in unpredictable ways (Bischoff and Fitzpatrick, 1991; Luo and Ku, 1991), making sequential acid leaching techniques for age determination ineffective in all but the most controlled experimental cases (Ku and Liang, 1984; Schwarcz and Latham, 1989).

Thus, most U-Th dating applications of lake sediments have applied corrections for detrital contamination by processing a series of coeval samples through total sample dissolution and then using “isochron” techniques. Here, the long-lived isotope ^{232}Th (Fig. 2-1A) acts as a tracer of contamination: assuming that the endogenic material contains no ^{232}Th or initial ^{230}Th, any ^{232}Th detected is attributed to the detrital component, and the accompanying amount of detrital ^{230}Th is assumed to occur at a particular proportion relative

Table 2.1: A list of sites and the associated studies which used U-Th dating to develop an age model for a lacustrine sediment sequence. Also indicated are other types of age constraints used for age model construction, separated into two categories: *absolute constraints* and *other tie points*. In these columns, '1' indicates that the chronological tool played a primary, first-order role in the age model, whereas '2' indicates that the tool played a second-order role, used only after application of first-order data. If no number appears beneath a column, this indicates that the chronological tool was not used to construct the age model at the site. The list of chronological tools in the table header reflects the tools used amongst the selected sites and is not meant to be a comprehensive of all possible tools.

				ABSOLUTE CONSTRAINTS					OTHER TIE POINTS			
					U-Th[a]							
Site	**Country**	**Duration**	**References**	^{14}**C**	*carb.*	*evap.*	*other*	**OSL**[b]	**pmag.**[c]	**tephra**[d]	**strata**[e]	**tuning**[f]
Lake Junín	Peru	~700 ka	this study	1	1							
Lake Igelsjön	Sweden	12 ka	Israelson et al. (1997)	1	1							
Babicora Basin	Mexico	65 ka	Metcalfe et al. (2002)	1			1[g]					
Salar de Atacama	Chile	106 ka	Bobst et al. (2001); Lowenstein et al. (2003)			1						
Lake Balikun	China	150 ka	Ma et al. (2004)		1				2			
Death Valley	USA	200 ka	Li et al. (1996); Ku et al. (1998)			1						
Searles Lake	USA	3 Ma	Peng et al. (1978); Bischoff et al. (1985); Lin et al. (1998)	1	1	1			1			
Qaidam Basin	China	4 Ma	Luo and Ku (1991); Phillips et al. (1993); Wang et al. (2013) and references therein	1		1			1			
Dead Sea	Israel	230 ka	Kaufman et al. (1992); Haase-Schramm et al. (2004); Stein and Goldstein (2006); Torfstein et al. (2015), references therein	1	1						1	1[h]
Bear Lake	USA	250 ka	Colman et al. (2006)	1	1				1			1[i]
Great Salt Lake	USA	280 ka	Balch et al. (2005)	1	1	1			1	1		
Lake Titicaca	USA	370 ka	Fritz et al. (2004, 2007)	1	1	1						1[j]
Lake Bosumtwi	Ghana	450 ka	Shanahan et al. (2013)	1	1			1	1		1	2[k]

---

[a] Applications of U-Th dating are separated into three categories based on material: carbonates ('carb.'), which includes minerals such as calcite and aragonite, and evaporites ('evap.'), which includes minerals such as halite and gypsum.

[b] 'OSL' refers to optically stimulated luminescence dating.

[c] 'pmag.' refers to the use of paleomagnetic excursions, reversals, and intensity to determine age constraints.

[d] 'tephra' refers to records that match tephras from the sediment sequence to well-dated tephras from other sites.

[e] 'strata' refers to matching stratigraphic units in the core to equivalent units in other well-dated records.

[f] 'tuning' refers to the alignment of proxy data to specific anchor points in the standardized timescales of external records ("wiggle matching").

[g] Diatom silica.

[h] The drill core from the Dead Sea Deep Drilling Project was also tuned to the LR04 benthic stack (Lisiecki and Raymo, 2005) and Soreq Cave (Bar-Matthews et al., 2003).

[i] For the deeper part of the core, lithologic units were tied to the Devils Hole oxygen isotope record (Winograd et al., 1992).

[j] Peaks in calcium carbonate content were tied to the Vostok CO_2 record (Petit et al., 1999).

[k] As a test of the age model, the dust record from Lake Bosumtwi was tied to that of EPICA Dome C (Lambert et al., 2008).

to ^{232}Th – an initial ^{230}Th/^{232}Th ratio.

For this reason, a sample with a higher measured ^{230}Th/^{232}Th or ^{238}U/^{232}Th ratio (more ^{238}U leads to more abundant ^{230}Th) is considered more "clean," while a sample with a lower measured ^{230}Th/^{232}Th or ^{238}U/^{232}Th ratio is considered "dirty" (colloquial terms used in the literature; e.g., Schwarcz and Latham, 1989; Przybylowicz et al., 1991; Stein and Goldstein, 2006). By plotting the isotope ratios of several analyzed portions of a single sample with varying amounts of detritus, an isochron line fit through those analyses can pinpoint the isotope ratios of the endogenic material, and thus provide a date. This approach is considered more rigorous than leaching methods, but is only applicable when there is a single, homogenized source of detritus with a consistent ^{230}Th/^{232}Th ratio forming one end member of the sample mixtures. Most studies listed in Table 2.1 apply this isochron method, but the process is labor intensive because at least three analyses are required for a date, and many more for one that is statistically rigorous (Powell et al., 2002).

In some cases where the measured ^{230}Th/^{232}Th ratio of sample material is sufficiently high, single-sample dates are possible by applying an initial ^{230}Th/^{232}Th correction that generously accounts for the full range of possible detrital ^{230}Th/^{232}Th ratios. The ^{230}Th age equation modified to correct for initial ^{230}Th is as follows:

$$\begin{aligned}\left\{\left[\frac{^{230}\mathrm{Th}}{^{238}\mathrm{U}}\right] - \left[\frac{^{232}\mathrm{Th}}{^{238}\mathrm{U}}\right]\left[\frac{^{230}\mathrm{Th}}{^{232}\mathrm{Th}}\right]_i \left(e^{-\lambda_{230}t}\right)\right\} - 1 = \\ - e^{-\lambda_{230}t} + \left(\left[\frac{^{234}\mathrm{U}}{^{238}\mathrm{U}}\right] - 1\right)\left(\frac{\lambda_{230}}{\lambda_{230}-\lambda_{234}}\right)\left(1 - e^{-(\lambda_{230}-\lambda_{234})t}\right) \quad (2.3)\end{aligned}$$

where i refers to the initial value at the time of fractionation (Edwards et al., 1987). For impure carbonates, this detrital correction is usually the largest contributor to the uncertainty of the final date, having greatest effect on samples with low uranium or low ^{230}Th/^{232}Th ratios. The impact of this correction decreases with the age of the sample: with time, radiogenic ^{230}Th builds up and any initial ^{230}Th decays away, making the proportion of radiogenic ^{230}Th to initial ^{230}Th more favorable. Single-sample dating has thus far only been successful in more recent studies where carbonates with high uranium concentrations (>3 ppm) are available and inductively-coupled plasma mass spectrometers allow for smaller amounts of material to be processed, making it easier to avoid detritus when sampling (e.g., Balch et al., 2005; Fritz et al., 2007; see Table 2.1).

Thus, the presence of initial ^{230}Th in sample materials has viable workarounds. However, less directly addressed is the issue of possible post-depositional gain or loss of uranium. In addition to clays, other sediment constituents like organic matter and Fe-Mn hydroxides serve as sources of uranium separate from endogenic materials; here, uranium is adsorbed to the mineral and solid surfaces of these impurities (Ames et al., 1983a,b,c; Porcelli et al., 1997; Ku et al., 1998; Schmeide et al., 2000; Chappaz et al., 2010; Fig. 2-8D). In theory, utilizing these other uranium sources for dating can be satisfactory if the uranium has remained immobile since their initial incorporation, as they are initially without ^{230}Th and would accumulate radiogenic ^{230}Th with time. Indeed, uranium associated with organic matter and clays enclosed in evaporites has been beneficial to the dateability of such low-uranium deposits (e.g., Ku et al., 1998). However, adsorbed uranium is far more susceptible to post-depositional remobilization than uranium bound within the crystal lattice of carbonates (Alam and Cheng, 2014). Furthermore, organic matter and clays can also adsorb additional uranium introduced to the materials via fluid flow, for instance when low-oxygen porewaters render uranium insoluble and cause it to accumulate authigenically (Fig. 2-1D; Yliruokanen, 1980; Bone et al., 2017).

Due to this capacity for organic matter to uptake uranium, there have been some attempts to date peats in highly organic-rich sediments that exhibit high uranium concentrations of 1–100 ppm (Van Der Wijk et al., 1986; Rowe et al., 1997; Geyh and Mu, 2005; Frechen et al., 2007), but open system behavior is commonly evidenced by age reversals or anomalous uranium isotope values in these materials. The sediment sequence at Lake Junín is interspersed with thick peat and organic-rich mud layers throughout its length, signaling that the lake has likely experienced considerable changes in lake level and redox conditions. In the following section, we provide further details about these sediments.

2.2.3 Background on the lake sediments from Lake Junín

Lake Junín (11.0°S, 76.2°W, 4100 m a.s.l.; Fig. 2-2) was targeted as a site for deep drilling because of its potential to yield the first continuous, absolutely dated record in the tropical Andes that spanned multiple glacial-interglacial cycles. Located on the high plateau between the eastern and western cordilleras of the central Peruvian Andes, this relatively shallow (<15 m) lake is the largest water body located entirely within Peru, occupying an area of ~300 km^2 fringed by marshlands and dense sedge mats (Wright, 1983). Bedrock

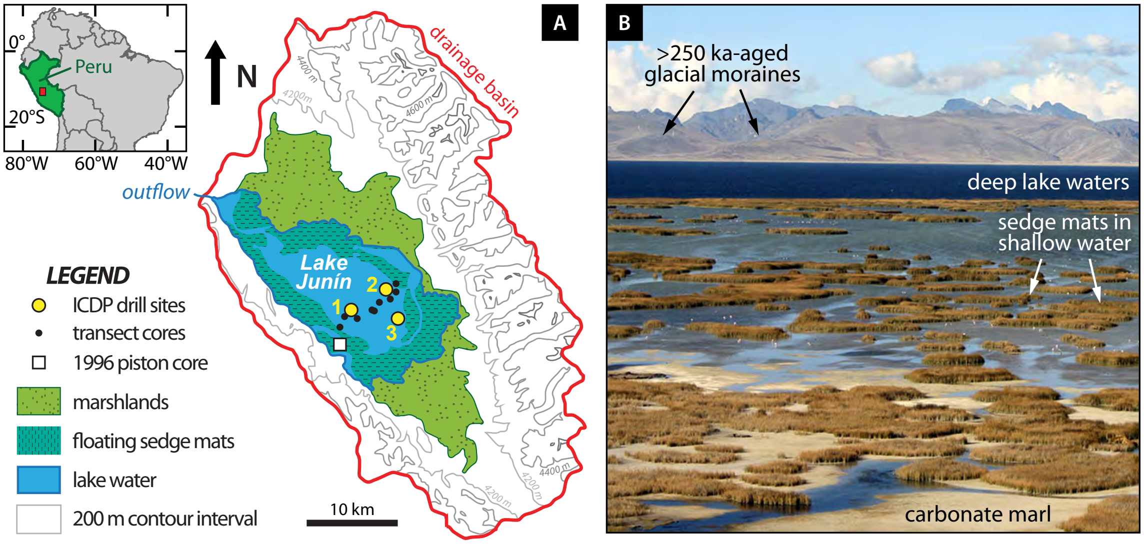

Figure 2-2: [**A**] Map of Lake Junín and its drainage basin, and the location of the three ICDP drill sites (yellow circles), the nine Livingstone core locations taken along a transect across the lake (black circles), and the 1996 piston core (white square; Seltzer et al., 2000). The composite splice for Lake Junín is composed of cores from Site 1 and two transect cores from the center of the basin (Hatfield et al., 2019). [**B**] More recently deposited carbonate silt found among the sedge mats fringing the lake margins. The carbonate silt is subaerially exposed during the dry season (June-July-August) when lake levels drop ∼1–2 m. For scale, small white specks in the shallow water are Chilean flamingos (∼1 m). Photograph taken by Charles Casey from the western shore, facing approximately northwest across the lake.

consists primarily of Paleozoic-Mesozoic marine carbonates, with some exposure of pre-Cambrian crystalline silicate rocks along the eastern cordillera (Cobbing et al., 1981). The lake owes its origin to >250-ka-aged coalescing glacial outwash fans that dam the northern and southern ends of the lake, respectively (Hansen et al., 1984). Moraine mapping and cosmogenic exposure ages from boulders on moraine crests indicate that the lake was not overridden by glaciers or ice at any time in the last 1 million years (Smith et al., 2005a, 2005b), making it one of the few studied lakes in the Andes that predates the maximum extent of glaciation.

Previously extracted short (∼20–25 m) cores spanning the last ∼50 kyrs revealed that the lake sediments consist of alternating packages of fine-grained glaciogenic silt and endogenic carbonate silt deposited at a high rate (0.2–1.0 mm yr^{-1}; Hansen et al., 1984; Seltzer et al., 2000). The carbonate silts are interpreted to have formed similar to the way such silts form in present day, in which springs and streams supersaturated in calcite enter the fringing wetlands along the western side of the lake and precipitate carbonate on rooted macrophytes (Flusche et al., 2005; Rodbell et al., 2012). Based on the modern carbonate production processes observed, it was hypothesized that a longer core would contain more carbonate-rich sections, coinciding with warm interglacial and interstadial periods when retreating piedmont glaciers allowed for the formation of marginal wetlands that isolated the basin center from detrital sediment input (Rodbell et al., 2012).

Proving such a temporal link between carbonate deposition, periods of reduced ice cover, and past warm intervals in a longer core would rest on the reliability of the age-depth model. Thus, we conducted a pilot study to determine if U-Th dating could be applied to bulk samples of the carbonate silts. Success would demonstrate than an independent U-Th-based chronology could support a long sediment record from this site, providing motivation for deep drilling. Sample material came from the 1996 piston core taken by G.O. Seltzer and D.T. Rodbell from the shallow western margin of the lake (Fig. 2-2A). The results from this initial test were encouraging: most of the U-Th analyses attempted on carbonates from the upper 10 m of the core were consistent with the chronology produced by ^{14}C ages (Fig. 2-3). The three outliers may have been influenced by open system behavior of mollusc shell fragments, which have been previously shown to post-depositionally uptake uranium (Blanchard et al., 1967; Kaufman et al., 1971; McLaren and Rowe, 1996). The preliminary results also revealed that Lake Junín carbonates have high uranium concentrations (0.3–2 ppm) and low detrital content, with ratios of radiogenic ^{230}Th to initial ^{230}Th that are 10 times greater than sediments from Lake Titicaca (Fritz et al., 2007) and the Great Salt Lake (Balch et al., 2005).

Following project approval, the uppermost ∼100 m of sediment was drilled and cored in eleven holes across three sites in August 2015. This paper focuses only on sediments recovered from Site 1, the deepest core extracted from the approximate depocenter of the lake. We work primarily from the PLJ-1 splice, which is comprised of core sections from four of the five holes at Site 1 and core sections from two Livingstone transect cores close to the lake depocenter (Fig. 2-2). More specifics regarding the coring operation and the subsequent generation of the PLJ-1 splice are described in Hatfield et al. (2019); hereafter, all references to depth in the Lake Junín core refer to the core composite depth below lake floor (CCLF). For complete information on the radiocarbon dates constraining the first ∼50 kyrs of the record, we refer the reader to Woods et al. (2019).

Here we briefly describe the stratigraphy of the PLJ-1 splice; a full description will be detailed in subsequent publications elsewhere. Broadly, the prediction that a long core

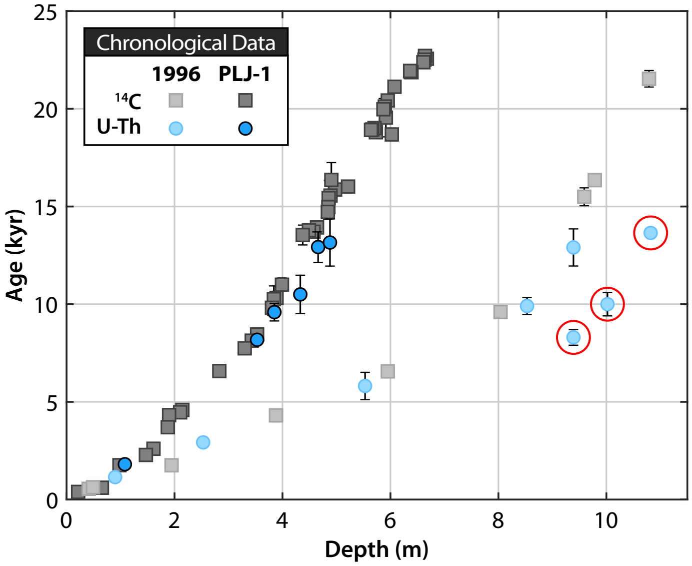

Figure 2-3: Comparison of radiocarbon (gray squares) and U-Th (blue circles) dates from the 1996 core and the PLJ-1 splice. Radiocarbon data are from Seltzer et al. (2000) for the 1996 core and Woods et al. (2019) for the PLJ-1 splice. Note that most U-Th data shown represent a mean of multiple analyses; see Table 2.3 for details. Circled in red are outlier U-Th analyses from the 1996 core that contained abundant mollusc shell fragments, and thus may have been affected by post-depositional uptake of uranium, biasing dates to be younger than the true age. Based on the PLJ-1 data, the inferred sedimentation rate (not normalized by dry bulk density) at the lake depocenter over the last 25 kyrs is ∼0.3 m kyr^{-1}, which is ∼50–60% slower than that of the 1996 core located on the western lake margin (Fig. 2-2).

from Lake Junín would also contain alternating packages of carbonate and glaciogenic sediment was correct: ∼10 m thick packages of cream-colored carbonate silt alternate with ∼10–15 m thick intervals of dark gray, fine-grained carbonate-rich glaciogenic silt throughout the length of the core until ∼85 m, where a thick package of carbonate-rich sand occurs (Fig. 2-4A). The mean grain size of this bed was incompatible with the drilling tools during core extraction, preventing deeper core recovery. Peat and organic-rich mud layers of ∼1- to 50-cm thickness punctuate both the carbonate and glaciogenic silt intervals and contain abundant microfossils that suggest that the peats represent times of wetland encroachment towards the lake center during lake level lowstands (Woods et al., 2019). Despite this interpretation, there is no stratigraphic evidence of any depositional hiatus or unconformity throughout the core, suggesting that the drill site has been submerged, however shallow in depth, for the duration of the record (Rodbell, Abbott, et al., in prep.).

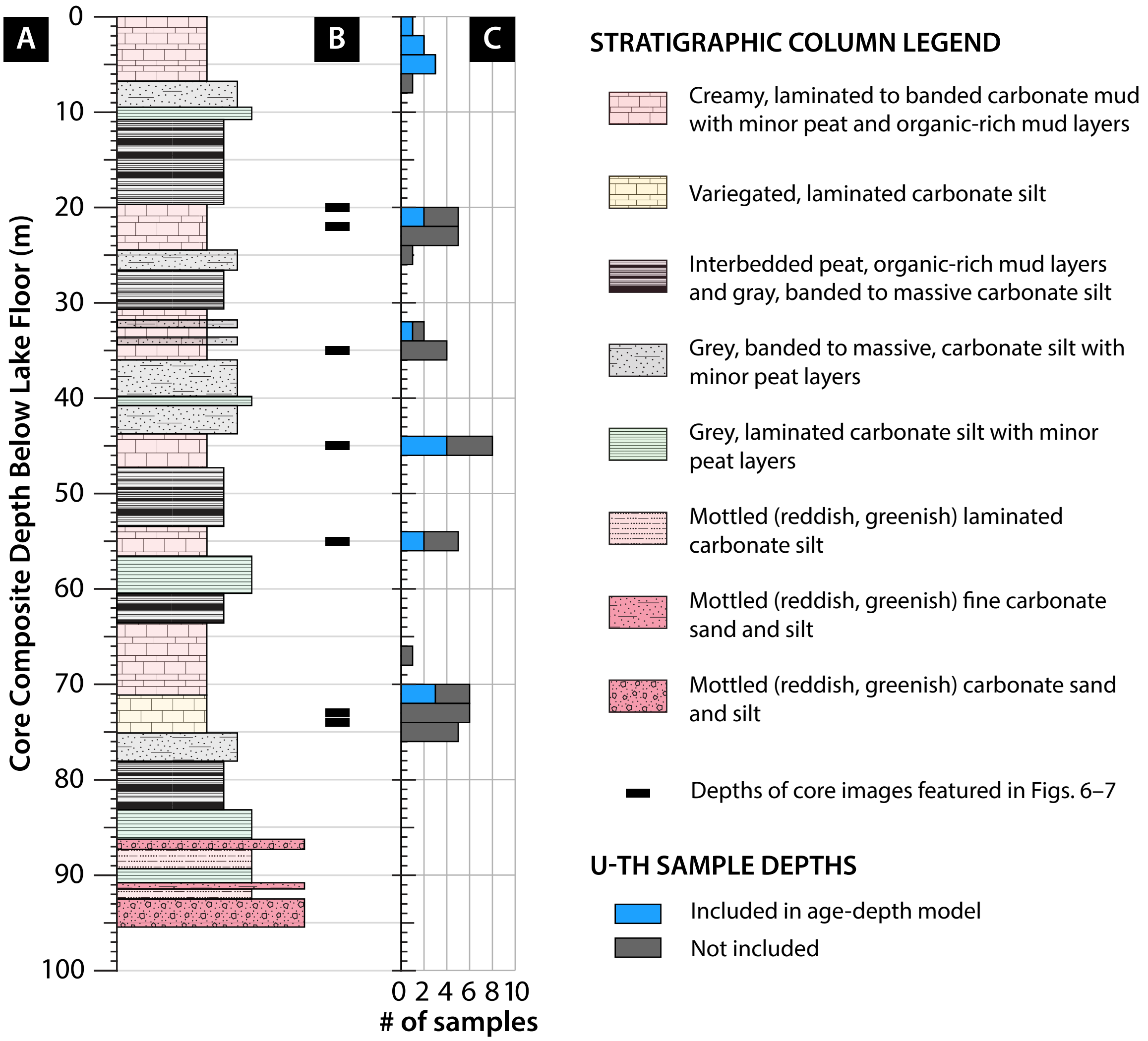

Figure 2-4: [**A**] Stratigraphic column of the PLJ-1 splice, described following the core description scheme proposed by Schnurrenberger et al. (2003). Lithologies in the stratigraphic column legend are listed in ascending order of mean grain size (smaller at the top, larger at the bottom). [**B**] Rectangular bars mark the depths of the cores featured in Figs. 2-6 and 2-7. [**C**] Stacked histogram of depths of samples collected for U-Th dating, in which blue represents samples that yielded dates included in the age-depth model and gray represents samples that yielded dates that were not included.

2.3 Methods

2.3.1 Core sampling for U-Th dating

Within the U-Th geochronology community, there is a common expectation that samples with the following characteristics, regardless of substrate type (speleothems, sediments, tufas, *et cetera*), have greater potential for success: light in color (considered an indicator of sample purity), non-porous, homogeneous (either as thin laminae or thicker intervals), and free of shell fragments and other detritus. We took advantage of the opportunity provided by modern mass spectrometry to process smaller amounts of material by making a deliberate effort to limit the amount of detritus included during the initial sampling stage.

Core splitting and sampling took place at the National Lacustrine Core Facility (LacCore) at the University of Minnesota, Twin Cities, in February 2016. After cores were split lengthwise and the centers were extracted with a plastic "U-channel" for paleomagnetic work, sampling for U-Th dating was given first priority on all cores. This order of operations ensured that the most ideal carbonates would be reserved for dating and not be under-utilized for other measurements where less ideal materials would suffice.

Cores were visually assessed for material that fulfilled the criteria described above. Once a carbonate section was identified, we used utility blades, knives from a fruit and vegetable carving set, and tweezers to cut and extract thin wafers of sediment ~0.2–0.5 cm in thickness (Fig. 2-5). In sections of core containing finely laminated carbonate sequences, we took care to isolate individual laminae, only sampling the cleanest parts and scraping away undesirable material when necessary. In addition, when possible, we sampled layers that appeared to have more detritus immediately adjacent to these cleaner laminae with the intention of using this material for possible isochron work. We examined smear slides during sampling in order to petrographically verify that samples identified by eye as being relatively detritus-free were as such, and made real-time adjustments in sampling strategy based on results. Fig. 2-4C shows the depths from which U-Th samples were taken and their relation to stratigraphic units. Sedimentary lithologies were defined following protocols by Schnurrenberger et al. (2003), including smear slide observations.

During sampling, we also documented the macro-scale sedimentological characteristics associated with each sample. After observing a variety of carbonate-rich sequences, we divided them into four lithological facies categories:

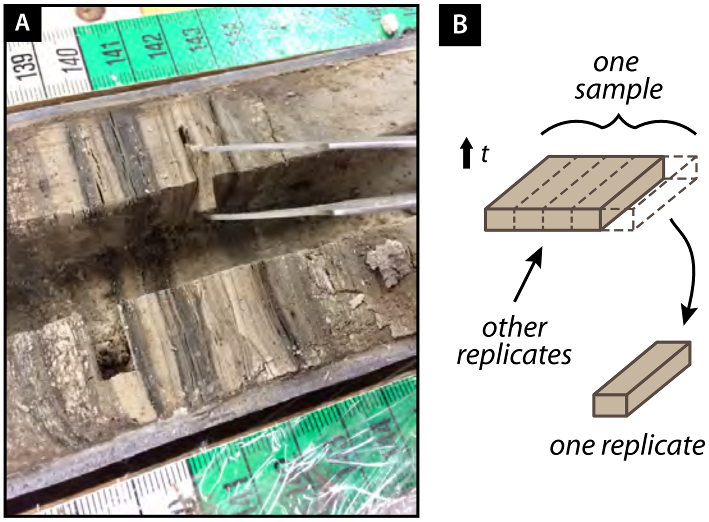

Figure 2-5: [**A**] The core sampling process for U-Th dating. Surgical straight edges and blades from a fruit carving knife set were used to cut out thin (∼0.2–0.3 cm) wafers of sediment, which were then extracted with tweezers. [**B**] One *sample* consists of a single wafer of sediment extracted as shown in Panel A. Replicate analyses are made on separate sections of the sediment wafer: rather than homogenizing the wafer into a powder and dating the powder multiple times, we date different sections of the sample in order to assess sample reproducibility.

- **C**ream-colored **m**assive **c**arbonates (**CMC**): cream-colored, massive, medium to thick (∼10–50 cm) bedded carbonate silts found in close association with gray, massive, banded or mottled silt, with some thin (∼1–2 cm thick) peat or organic-rich mud layers (Fig. 2-6)

- **R**ed-**g**reen **a**lternating (**RGA**): red and green laminated sets of carbonate silts that alternate in color every ∼5–20 cm, with some organic-rich peat laminae (Fig. 2-6)

- **C**ream-colored carbonates with **p**eat beds (**CP1**, **CP2**): Cream-colored, faintly banded carbonate silt interbedded with peat layers, with some associated with thick (∼30–50 cm) overlying peat beds that were laterally continuous across multiple holes at Site 1 (CP1), and others associated with thin (∼3–5 cm), laterally discontinuous peat beds (CP2) (Fig. 2-7)

Each sample extracted for U-Th dating was subsequently categorized into one of these four facies.

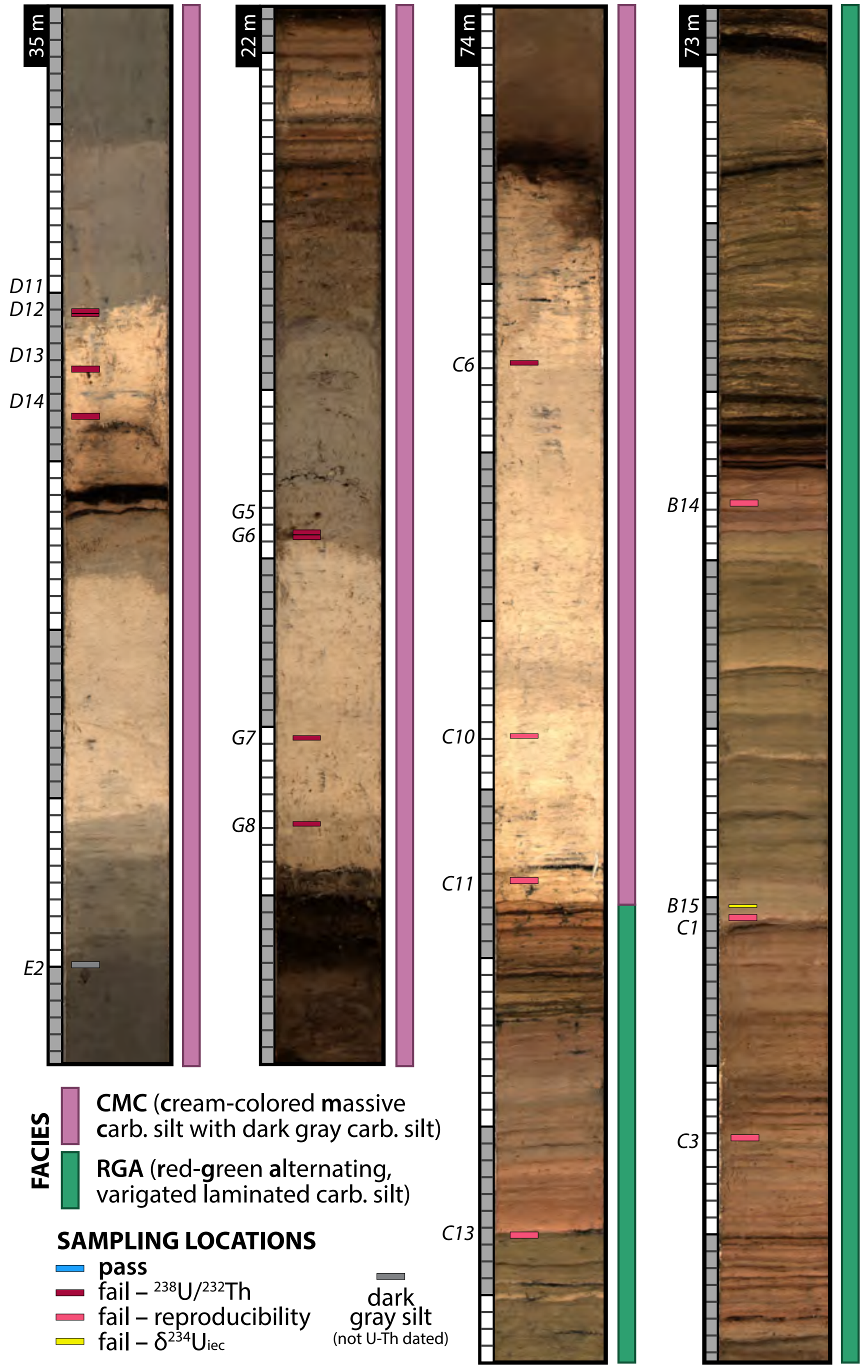

Figure 2-6: Core scanning images and U-Th sample locations of four selected cores that feature the CMC and RGA facies. The approximate corresponding CCLF is noted in the black rectangular box at the top left of each core image. The column of gray and white boxes appended to the left of each core image is a ruler representing alternating blocks of ten centimeters, mimicking the actual ruler used during scanning at LacCore's facilities. Small rectangles plotted on top of the core image represent sample locations and are labeled by sample ID and color-coded by threshold criteria result (see Section 2.5 and Fig. 2-8). The columns to the right of each core image represent the facies that is given to a sample collected in that depth interval; for example, for the third core image, samples C6, C10, and C11 are categorized as CMC, while C13 is categorized as RGA. Core scanning images were made using a Geotek MSCL-CIS at the National Lacustrine Core Facility (LacCore).

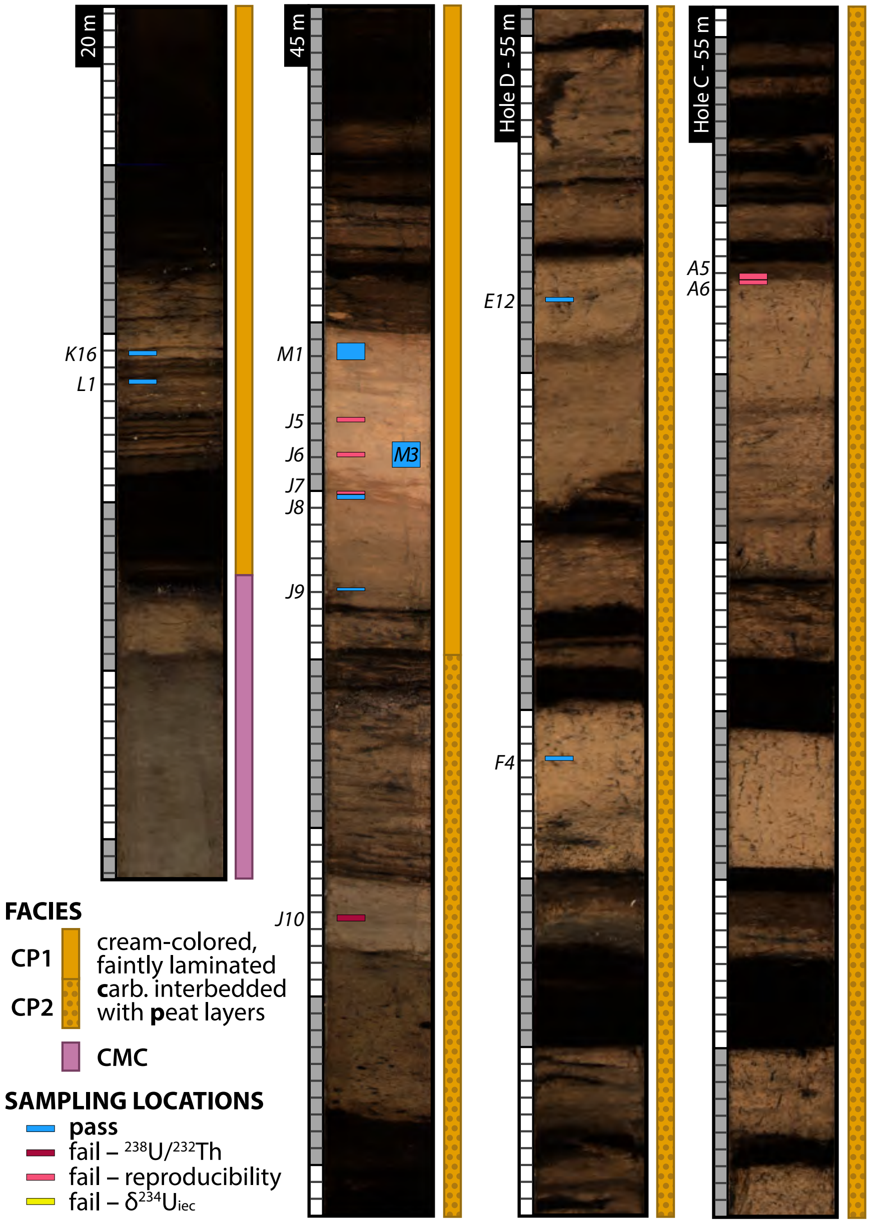

Figure 2-7: Core scanning images and U-Th sample locations of four cores that feature the CP facies, which is subdivided into CP1 and CP2 to differentiate between samples that are associated with thick (>10 cm) and laterally continuous peat layers (CP1) and those that are not (CP2). Note that the third and fourth images are of cores from the same CCLF but from different holes at Site 1, shown here to demonstrate the lateral discontinuity of some peat and carbonate beds. Holes at Site 1 were spaced approximately ∼20 m apart. Small rectangles plotted on top of the core image represent sample locations and are labeled by sample ID and color-coded by threshold criteria result (see Section 2.5 and Fig. 2-8). See caption in Fig. 2-6 for explanation of other symbology used in the figure.

2.3.2 Sample preparation and chemistry for U-Th dating

After core sampling, sediment wafers were frozen and then placed in a vacuum freeze drier to remove moisture from all material. Most samples retained their original wafer shape after this process. A small portion of each sample was then gently disaggregated for micro-scale sedimentological characterization under a picking microscope. We made qualitative observations on the following: color; hardness of bulk sediment (friable or compacted); and the relative abundance of mollusc shell fragments, ostracode valves, organic fibers (peat fragments, grasses, seed pods), sponge spicules, siliciclastic grains, or other mineral precipitates. For subsequent U-Th analyses, we manually removed mollusc shell pieces from the sample before dissolution, or avoided processing samples containing abundant mollusc shell fragments that could not be reliably removed. Otherwise, all analyses discussed are measurements on bulk samples containing all other aforementioned constituents.

Because U-Th column elusions are time and resource intensive, a small set of samples from different facies were screened for their uranium and thorium concentrations to determine which facies would most likely yield material viable for dating. Powders of ~2 mg were dissolved in dilute HNO_3, and analyses of uranium and thorium concentration were performed on a VG PQ2+ quadrupole ICP-MS and an Agilent 7900 ICP-MS at MIT. Samples with higher U/Th ratios were then identified as materials worth further processing as they are more likely to yield "clean" samples with high ^{230}Th/^{232}Th ratios (Section 2.2.2).

Replicate analyses were then processed through U-Th column elusions in batches of 5 to 15. When possible, we analyzed at least three replicates from each sample horizon. Here, we purposefully apportion different aliquots of the original sediment wafer for each replicate analysis in order to test the reproducibility of dates from stratigraphically coherent material (Fig. 2-5B). Note that this is an important difference from repeated analyses of a homogenized powder, which would only provide a measure of internal lab errors or the quality of sample homogenization. Our original intention in processing samples this way was not only to test for reproducibility, but also to build isochrons, for which it is necessary to analyze subsamples that span a range of detrital contamination levels.

After sample selection and preparation, sample dissolution was performed in a clean laboratory at MIT. Samples of 5–60 mg were dissolved in HNO_3 and spiked with a ^{229}Th-^{233}U-^{236}U tracer in Teflon beakers cleaned via a boiling-washing procedure with concentrated HNO_3, HCl, and aqua regia. Next, following methods described by Edwards et al. (1987) and Shen et al. (2002), uranium and thorium were co-precipitated with ~4–8 mg of

Fe oxyhydroxides and then separated using BioRad AG1-X8 anion exchange resin (100–200 mesh, 0.5 mL column volume). The isotopic compositions of the resulting uranium and thorium fractions were then measured on a Nu Plasma II-ES multi-collector ICP-MS at MIT. We introduced sample solutions through a CETAC Aridus II desolvating nebulizer system coupled to a PFA nebulizer with a 100 µL/min uptake capillary. Each uranium sample analysis was bracketed by a 5 ng/g solution of the CRM-112a standard (New Brunswick Laboratories). Each thorium sample analysis was bracketed by an in-house ^{229}Th-^{230}Th-^{232}Th standard in order to monitor mass bias and variable SEM yield. 2% HNO_3 solution blanks also bracketed each sample and standard analysis to determine the background signal. See Section 2.10.1 for details of U-Th measurements on materials from the 1996 core.

2.3.3 Estimating the initial ^{230}Th correction

As discussed in Section 5.3, the correction for initial ^{230}Th has a greater impact on impure sample materials, and so it follows that we must carefully consider this correction for the lake sediments at Lake Junín. Ten samples processed from the 1996 core yielded indeterminate ('infinite') dates, in which a unique solution for the ^{230}Th age equation could not be found after iteration. These samples all had ^{232}Th concentrations that were 20–200 times greater than other samples from the 1996 core that yielded calculable dates (2–7 ppm, compared to 0.04–0.1 ppm), forming a statistically distinct population. Similarly, these samples also had ^{238}U/^{232}Th ratios that were $\sim$50 times lower than that of other samples (0.3–0.6 ppm). These results suggest that the samples yielding indeterminate ages had high amounts of detrital contamination that contributed a significant amount of initial ^{230}Th at secular equilibrium with ^{238}U, thereby causing apparent infinite dates.

Assuming that the detrital component of the indeterminate samples of the 1996 core is representative of the isotopic composition of detrital material found in all sediments of the PLJ-1 splice, we calculated the average ^{230}Th/^{232}Th ratio of the indeterminate samples and used this ratio for the initial ^{230}Th correction in our calculations. This estimate has the effect of counting radiogenic ^{230}Th accumulated in these samples as detrital, but the depths of these samples suggest that their true age is no older than 30 kyrs and thus we do not expect an appreciable proportion of the ^{230}Th to be radiogenic.

The average ^{230}Th/^{232}Th atomic ratio of the indeterminate samples from the 1996 core is $7.9 \pm 0.9 \times 10^{-6}$. Our starting assumption is that this ratio is invariant through time, but it is entirely possible—if not expected—that the isotopic composition of detritus is variable due to changes in clastic transport or source regions. To account for these unknowns and other unknown unknowns, we apply an uncertainty of 50% to this average and use an initial ^{230}Th/^{232}Th atomic ratio of 8.0 ± 4.0 $\times 10^{-6}$ for U-Th data from the PLJ-1 splice.

2.3.4 Calculating weighted means and uncertainties of samples with replicate analyses

As previously mentioned, we attempted to analyze at least 3–5 replicates for each sample as a test of the reproducibility of unequivocally coeval material. We calculate a date for each individual replicate analysis using Eq. 2.1 and the initial ^{230}Th/^{232}Th ratio stated above. We then use these dates to calculate an error-weighted mean ($\bar{x}$) and uncertainty ($\sigma_{\bar{x}}$) of all replicate analyses in a sample, in which weights are equal to the inverse of the variance of each date:

$$\bar{x} = \frac{\sum^N x_i/\sigma_i^2}{\sum^N 1/\sigma_i^2}, \quad \sigma_{\bar{x}} = \sqrt{\frac{1}{\sum^N 1/\sigma_i^2}} \tag{2.4}$$

where N is the number of replicate analyses in the sample; x_i is the individual date of each replicate; and σ_i^2 is the variance of the individual dates of each replicate.

We then calculate the degree of agreement between replicate analyses to estimate an uncertainty that is appropriate for the observed scatter between dates. To do this, we calculate the Mean Square of Weighted Deviates (MSWD), a measure of the ratio of the observed scatter around the mean to the expected degree of scatter given the analytical uncertainties of each data point (McIntyre et al., 1966; Wendt and Carl, 1991). The value is essentially the chi-squared statistic (goodness of fit) divided by the number of degrees of freedom ($f = N - 1$), or the "reduced" chi-squared:

$$\mathrm{MSWD} = \frac{1}{f} \sum^N \frac{(x_i - \bar{x})^2}{\sigma_i^2} \tag{2.5}$$

The value of the MSWD tells us if the calculated uncertainties for each date are over- or underestimated based on the observed scatter in data. A value of ∼1 indicates that the observed scatter is equal to the predicted scatter; values less than 1 indicate that the observed scatter is less than is predicted by the uncertainties; and values greater than 1 indicate that the observed scatter is more than the predicted scatter. Samples with an MSWD much greater than 1 are considered to have excess "geologic scatter," suggesting possible biases in the calculated dates, perhaps due to a violation of the assumptions underpinning the system (e.g., open system behavior). Thus, for any sample with an MSWD > 1, we expand the uncertainties of the replicate analyses by a factor of $\sqrt{\text{MSWD}}$ and then recalculate the weighted means with these larger uncertainties using Eq. 2.4. The `IsoplotR` program by Vermeesch (2018) also includes this strategy as one option of treating data with excess geologic scatter (referred to as "overdispersion"). While the presence of excess scatter is non-ideal and raises concerns about the validity and practical use of such dates, the data still represent geologically meaningful information and thus should not necessarily be rejected outright without further consideration (and we will do much considering, starting in Section 2.5).

Using the MSWD as a black-and-white parameter to evaluate the validity of dates is generally discouraged, since the highest permissible MSWD is dependent on N (Wendt and Carl, 1991) and is often subject to interpretation (Powell et al., 2002; Ludwig, 2003). Thus, we calculate the probability of the observed scatter occurring given the uncertainties for each replicate analysis (a "probability of fit") by computing the chi-square cumulative distribution for $\text{MSWD}\times f$ (the chi-squared statistic) about f degrees of freedom (York, 1968).

Some samples only have 1–2 replicates; these were cases in which early replicate analyses yielded unfavorable results (*i.e.*, low $^{238}\text{U}/^{232}\text{Th}$ ratios) and were thus not further repeated in the interest of time and resources. For the remainder of this paper, our discussion of U-Th dates will refer to the weighted means and uncertainties (MSWD-adjusted) of samples rather than the individual dates of replicate analyses, unless otherwise noted.

2.3.5 Other corresponding data

We use other sedimentological, geochemical, paleoecological, and physical data to interpret and understand our U-Th data. We provide a list of these datasets in Table 2.2 and their intended use. More information regarding these methods of measurement can be found in the Supplementary Materials (Section 2.10.2) and other publications currently being prepared elsewhere.

Dataset	**Brief Methods**	**Purpose**
Elemental concentrations	sample dissolution, ICP-MS	Determine if there exists any relationship between U-Th data and concentrations of Ca and trace elements Mg, Sr, Al, Ti, P, V, Mn, and Fe. Measurements are made on same sample material used for U-Th dating.
Total inorganic and organic carbon	coulometry	Determine if there exists a relationship between U-Th data and carbon content. Only measurements made within 1 cm of the U-Th sample are paired with U-Th data.
Color reflectance	spectrophotometry on automated core logger	Determine if there exists a relationship between U-Th data and any spectral reflectance wavelength band. Only measurements made within 2.5 mm of the U-Th sample are paired with U-Th data.
Mineralogy	X-ray diffraction	Determine the mineral composition of the carbonate phases, and if there are discernible differences between endogenic and detrital carbonate.
Ostracode assemblages	picking and identification following Pérez et al. (2010) and Karanovic (2012)	Determine if there exists a relationship between U-Th data and ostracode color, taphonomy (number of broken vs. intact valves; adults vs. juveniles), or ecology (benthic vs. swimmer species, ornamentation).

Table 2.2: Other datasets used in this study for comparison with U-Th data.

2.4 Results

In total, we generated 174 U-Th dates from 55 bulk samples from the PLJ-1 splice. Uranium and thorium geochemical data as well as the number of replicates produced for each sample ($N = 3$–8) can be found in Table 2.3. Samples originate from each of the five high (>70%) $CaCO_3$ intervals that occurred every ~10–15 m in the core (Fig. 2-4C). All U-Th dates from the uppermost 5 m are broadly consistent with radiocarbon dates from terrestrial macrofossils and charcoal in the same depth interval (Fig. 2-3; Woods et al., 2019). A sample from ~6.5 m yielded an indeterminate date and had a $^{230}Th/^{232}Th$ atomic ratio of $7.7 \pm 0.2 \times 10^{-6}$, consistent with our estimate of the detrital $^{230}Th/^{232}Th$ ratio applied in corrections. Sample ^{238}U concentrations are variable and are generally 0.2–4.0 ppm (mean $= 1.5 \pm 1.2$ ppm, 1-σ); ^{232}Th concentrations are also variable, ranging 0.02–2.4 ppm (mean $= 0.6 \pm 0.5$ ppm, 1-σ).

For the deepest part of the core, the oldest U-Th dates suggest that the record is no older than ~800 ka. This observation is consistent with the absence of evidence of the Brunhes-Matuyama magnetic reversal (aged ~780 ka) in the paleomagnetic secular variation record (Hatfield et al., in prep.). However, the scatter of dates throughout the entirety of the core is, at first glance, alarming: at ~20–25 m, the first high-$CaCO_3$ section beyond the interval covered by radiocarbon, U-Th dates already span a range of ~200 kyrs (Fig. 2-8). The spread of dates increases with depth, reaching ~300 kyrs at the bottom of the record. As is, the scatter of data is too great to build any practical age-depth model, even after applying outlier analysis. Furthermore, all attempts to reduce scatter by building isochrons from replicate analyses and adjacent dirty-clean sample pairs failed (high MSWD and low probability-of-fit; Section 2.10.3).

Here, we arrive at the main crux of this paper. The scatter of data and the failure to build isochrons is clear evidence that at least some of the dated materials have not remained closed systems or do not otherwise satisfy the operating assumptions of U-Th dating. Despite this noise, is there a way to objectively assess the quality of each U-Th date, and subsequently curate the dataset without biases (avoid "cherry-picking")? In the following sections, we detail our approach to this question. At times, we will refer to specific U-Th samples by their sample name, which consists of an alphabetical letter A–P followed by a number 1–16 (Table 2.4).

2.5 Curation of U-Th data using threshold criteria

Noisy U-Th geochronological datasets are nothing new; in attempts to find clarity in uncertain data, a common practice is to apply some screening criteria based on uranium and thorium concentrations. For example, some studies dating corals and carbonate slope sediments have rejected dates that exceed a certain thorium concentration or do not meet a minimum uranium concentration because such dates tend to have larger corrections and errors (Robinson et al., 2002; Henderson et al., 2006; Skrivanek et al., 2018). However, picking the values for these thresholds can be subjective to an extent, especially if there is no clear separation between distinct populations within the data.

As a start towards better understanding the scatter in our data, we consider applying similar thresholds, first by examining the $^{238}U/^{232}Th$ ratio and the probability of fit of all dates for a given sample to a single weighted mean (Fig. 2-8A and B). $^{238}U/^{232}Th$ ratios ranged between <1 and 30 and probabilities of fit essentially spanned the full domain of possible values, from 0% to 99%. Between 20 and 60 m, we notice that the samples with the oldest dates all have ^{238}U/^{232}Th ratios that are <1, including those yielding indeterminate dates (Fig. 2-8A). One possible explanation for this observation is that these samples have initial ^{230}Th that has not been accounted for with our initial correction, which would bias dates to be older than the true age. The effect of this bias would be greatest in samples with low radiogenic ^{230}Th due to low uranium concentrations. (Note that we later discuss another explanation for these data in Section 2.7).

Regarding the probability of fit, deciding how low of a probability is acceptable is somewhat arbitrary; there is no broad consensus within the geochronology community on how best to treat such data, especially in circumstances in which the total number of subsamples is low (Ludwig, 2012), as is our case. However, most geochronologists would likely agree that samples with a probability of fit less than 1% (especially those much closer to 0%) exhibit an amount of excess scatter that is beyond recovery of practical information about the true age of the sample.

Thus, in the interest of not using too strong of a hand in curating the U-Th data to begin, we apply two conservative threshold criteria: the ^{238}U/^{232}Th ratio must be >1 and the probability of fit >1% (Fig. 2-8A and B). Of the 55 samples, 17 fail the ^{238}U/^{232}Th criterion and 22 fail the reproducibility criterion. Of the 17 samples that fail the ^{238}U/^{232}Th criterion, eight had more than one replicate analysis, and of those eight, five also fail the reproducibility criterion. In Fig. 2-8D, we show which criterion each sample fails; for the purposes of simplifying ensuing explorations into the dataset, the five samples that fail both aforementioned criterion are categorized as having failed the ^{238}U/^{232}Th criterion.

Next, we consider another screening approach adopted for U-Th dating of marine samples that involves $\delta^{234}\mathrm{U}_{\mathrm{initial}}$. Because the residence time of uranium in the ocean is very long (~400 kyrs; Ku et al., 1977), the δ^{234}U of seawater is thought to have remained relatively constant for at least the last 400 kyrs (Henderson, 2002; Henderson and Anderson, 2003). Thus, assuming that marine samples reliably preserve the δ^{234}U values of the waters in which they formed, dates from marine samples with δ^{234}U values that deviate significantly from modern values are considered potentially inaccurate due to diagenesis (Bard et al., 1991; Hamelin et al., 1991; Gallup et al., 1994). In contrast, the δ^{234}U of surface waters is very diverse and has been found to be sensitive to basin lithology, basin-specific weathering mechanics, riverine and groundwater inputs, and climate (e.g., Sarin et al., 1990; Kronfeld and Vogel, 1991; Plater et al., 1992; Kronfeld et al., 2004; Robinson et al., 2004; Durand et al., 2005; Grzymko et al., 2007; Chabaux et al., 2008). Although few

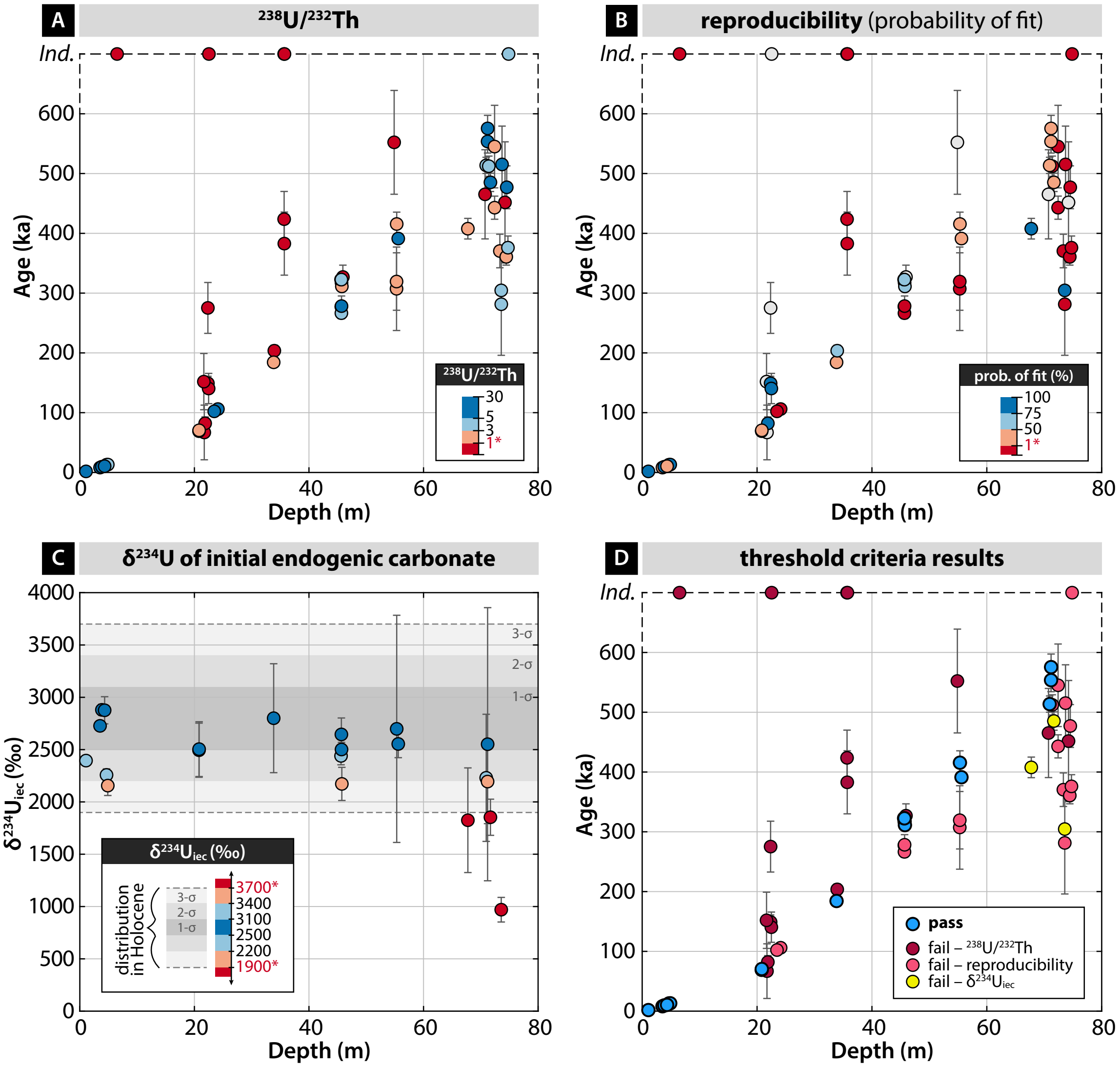

Figure 2-8: Step-by-step application of thresholding criteria: [**A**] ^{238}U/^{232}Th, [**B**] reproducibility, and [**C**] δ^{234}U of initial endogenic carbonate ($\delta^{234}U_{iec}$). [**D**] shows the data that pass and fail the three aforementioned criteria. Note that each point represents the weighted mean and standard deviation of multiple replicate analyses (see Table 2.3). In Panels A–C, blue/red colors represent values that are more/less ideal for U-Th dating. Values of thresholds are indicated by a red asterisk (*) in each legend. Samples that do not satisfy criteria and were thus subsequently eliminated are colored in dark red. Samples plotted along the uppermost dashed line labeled 'Ind.' refer to analyses that yielded incalculable U-Th dates or were infinite (indeterminate). In Panel B, analyses plotted in light gray are those with only one replicate analysis. Panel C only includes data that pass the ^{238}U/^{232}Th and reproducibility thresholds. Shaded gray areas represent the distribution of $\delta^{234}U_{iec}$ values observed in the Holocene, including data from the 1996 core. For Panel D, note that some samples failed both criteria for ^{238}U/^{232}Th and reproducibility; in these instances, the samples were categorized as having failed the ^{238}U/^{232}Th criteria. All error bars in each panel are 2-σ range. Depth refers to the composite core depth below lake floor (CCLF).

studies examine the long-term history of internal δ^{234}U variability in lakes and other surface waters (e.g., Kiro et al., 2018), the range of internal δ^{234}U variability observed in the aforementioned river and groundwater studies suggests that the internal δ^{234}U of lake waters should not vary significantly without dramatic changes in drainage basin organization. Since the lithology of a lake basin is invariant over the timescales relevant to this study, variability in δ^{234}U is driven by changes in hydrology. McGee et al. (2012) documented a 300‰ change in the δ^{234}U of lacustrine cave carbonates during the last deglaciation in Lake Bonneville (Utah, USA), which experienced a ∼2× change in precipitation.

Thus, we apply a third threshold criterion using the δ^{234}U of the initial endogenic carbonate ($\delta^{234}U_{\text{iec}}$) of each sample, which we calculate by correcting $\delta^{234}U_{\text{initial}}$ values for detrital uranium (see Section 2.10.4 for relevant equations). The average $\delta^{234}U_{\text{iec}}$ of all samples that yield dates verified by radiocarbon data (including data from the 1996 core) is 2800±300‰. If we compare this average to the $\delta^{234}U_{\text{iec}}$ values of the remaining 21 samples, we observe that three samples at ∼70–75 m have values that fall well below the average, even outside the range defined by three standard deviations from the mean (Fig. 2-8C). Because the magnitude of these differences is large, we suggest that these values are unlikely to reflect real changes in the δ^{234}U of the lake waters, and thus suspect the validity of these dates. Therefore, we mark these three samples as having failed the $\delta^{234}U_{\text{iec}}$ criterion (Fig. 2-8D).

While the remaining 18 dates form a visually pleasing line (Fig. 2-8D), this observation alone does not intrinsically prove that these remaining dates are accurate. However, the samples generally abide by the rules of stratigraphic order, which is behavior consistent with closed-system dates. Furthermore, the results of applying the threshold criteria may vaguely follow our theoretical expectations for normally distributed scatter about the mean. That is to say: if you were to ask someone to draw a line through the middle of the original scatter of points, the 18 samples that remain would not stray far from it.

2.6 Understanding the scatter

Having classified the U-Th data into categories that describe the main flaw of each nominally failed sample (Fig. 2-8D), we now explore the underlying causes for poor sample behavior and determine if the application of threshold criteria is justified. Essentially, we ask: Is there other evidence that supports our assertion that the threshold criteria failing samples have not remained closed systems? What is special about the 18 passing samples such that they exhibit fewer symptoms of open system behavior?

2.6.1 Detrital contamination

The first and most obvious hypothesis for poorly behaving dates is detrital contamination that is unaccounted for with the initial ^{230}Th/^{232}Th correction. As stated in Section 2.2.2, impure sample substrates have been the main obstacle in previous U-Th dating efforts in lake sediments, and there is no evidence to suggest that Lake Junín would be an exception. If detrital contamination does indeed play a large role in the scatter of our U-Th data, we can make certain predictions for how other sedimentological and geochemical data would respond. For example, we would expect that samples with lower $CaCO_3$ content would comprise the eliminated dates, especially those that failed the ^{238}U/^{232}Th criterion. We are able to test this hypothesis directly using co-located measurements of $CaCO_3$ content (weight %) as well as optical lightness from color reflectance spectra (Table 2.2 and Section 2.10.2). Optical lightness, defined here as the sum of spectra in the visible band of the electromagnetic spectrum (400–700 nm), has been shown to be a reasonable proxy for carbonate content in marine sediments (e.g., Nagao and Nakashima, 1992; Mix et al., 1995; Balsam et al., 1999). Data for the PLJ-1 splice also shows that $CaCO_3$ content >50% appears to scale with optical lightness (see gray circles in Fig. 2-9A). Because color reflectance data were measured on a finer and more regular sampling interval than carbon data, there are more optical lightness data that correspond to U-Th samples than $CaCO_3$ content measurements ($N = 46$ versus 29; Fig. 2-9).

From Fig. 2-9, we notice that all but one of our U-Th samples have >50% $CaCO_3$ content, with most passing dates having >70% $CaCO_3$ content. However, many data that failed threshold criteria occupy the same range in $CaCO_3$ content as passing data. Contrary to expectations, each of the five samples with the highest $CaCO_3$ content failed the threshold criteria (Fig. 2-9B). Likewise, the five samples with the highest optical lightness also failed (not the same five samples; Fig. 2-9C). Sample C10 is the most extreme case in this comparison, and as a visual check, we can see its sampling location in Fig. 2-6 and verify its optical lightness value relative to other samples. Again, there is no clear pattern between passing and failing U-Th dates and optical lightness; samples appear to exhibit the entire range of optical lightness values observed in the core. If anything, one could argue that the samples failing the ^{238}U/^{232}Th criterion tend to have higher optical lightness values compared to passing samples, behaving opposite to our predictions. The

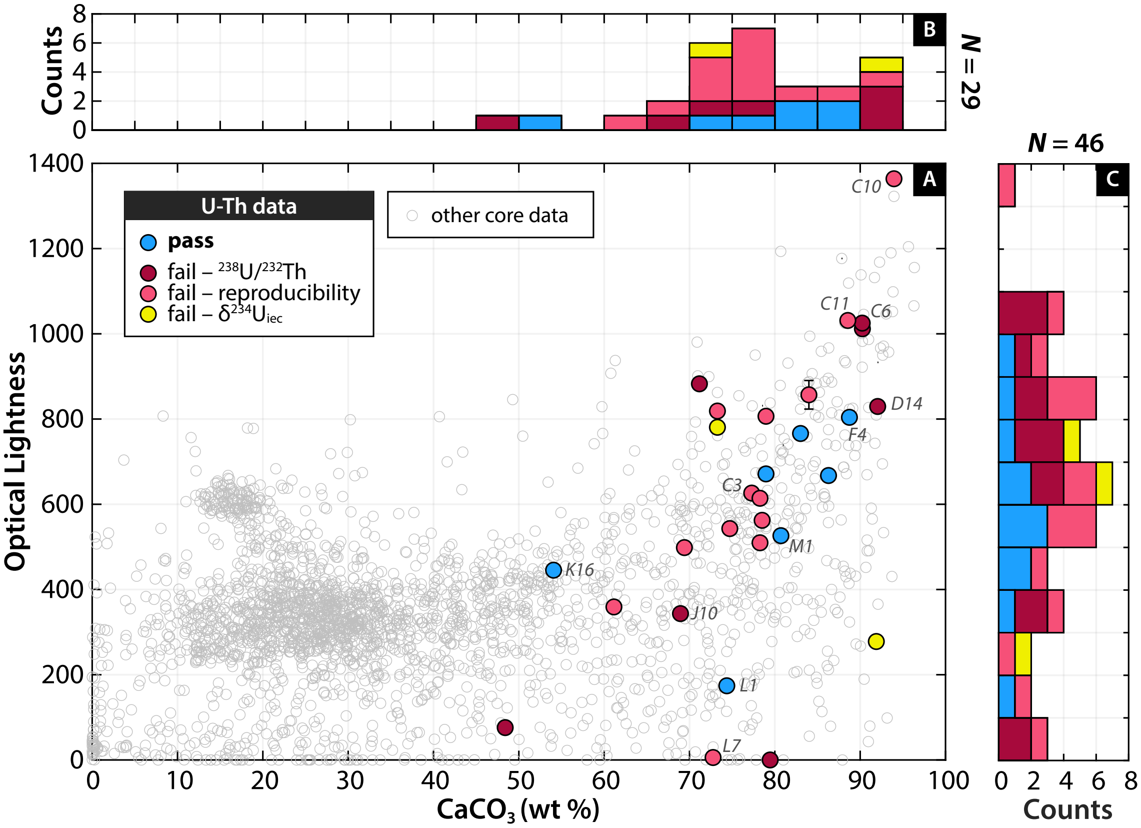

Figure 2-9: Cross-plot [**A**] and histograms of calcium carbonate content [**B**] and optical lightness [**C**], showing the distribution of these values for U-Th samples of each threshold criteria result. In Panel A, there are 29 colored circles which represent the U-Th samples that have both a corresponding $CaCO_3$ analysis (within 1 cm of the sample location) and a color reflectance measurement (within 2.5 mm of the sample location). Since color reflectance data were measured on a finer and more regular sampling interval than carbon data, there are more U-Th samples for which there is a corresponding color reflectance measurement ($N = 46$); thus, there are data plotted in the Panel C histogram that are not shown in Panels A and B. Empty circles with gray outlines represent other pairs of $CaCO_3$ and brightness data throughout the core and are only included if these data correspond to the exact same core depth. Note that this figure does not include any data from the upper 6 m of the core.

results are similar when we compare our data with grayscale or luminance (also known as L^*), another "lightness" parameter using the CIE L*a*b* color description system.

Based on these results, we speculate that a high proportion of bedrock carbonate in the detrital component could explain the high $CaCO_3$ content of failed samples; even the darkest gray silt sections in the core with high magnetic susceptibility had 20–50% $CaCO_3$ content. The uranium from this detrital carbonate would be at secular equilibrium (Fig. 2-1D) and would adversely impact our We compare the mineralogy of local carbonate bedrock to core sediments to see if mineralogical differences between these carbonates could be used to detect detrital contamination (Section 2.10.2). Unfortunately, the results show that there is no discernible difference between the carbonate bedrock and carbonate-bearing lake sediments, even when comparing different grain size groupings. All bedrock samples were dominated by low-Mg calcite, except one sample, which revealed the presence of dolomite. Low-Mg calcite was the dominant carbonate phase in all carbonate-bearing samples from the core, with no evidence of dolomite.

Despite this, elemental ICPMS concentration data support the prediction for detrital contamination in failed samples, in particular, those failing the ^{238}U/^{232}Th criterion. Fig. 2-10A is a biplot of the orthonormal principal component coefficients for Ca, Mg, Sr, Fe, Mn, Al, Ti, V, and P and the principal component scores for each sample. Here, the first principal component (PC1) has positive coefficients for elements that are markers for aluminosilicates (Fe, Mn, Al, and Ti) and explains $\sim$44.5% of the variance in concentration data. Samples failing the ^{238}U/^{232}Th criterion generally have positive PC1 scores, indicating that those samples tend to have relatively higher concentrations of these elements. Elemental concentration data from a sample of the dark gray carbonate silt also exhibits higher concentrations of these elements (sample E2; Fig. 2-6, core at 35 m). As most samples that failed the ^{238}U/^{232}Th criterion are of the CMC facies (Fig. 2-10B), these data are consistent with our visual observations of this facies, in which the lighter-colored carbonates visually appear to have semi-gradational boundaries with the surrounding dark gray glaciogenic silts, suggesting that these samples likely contain some fraction of this material. In addition, the sample with the highest PC1 score, D11, comes from a boundary between cream-colored carbonate and dark gray carbonate silt (Fig. 2-6).

Despite the clear relationship between high PC1 scores and ^{238}U/^{232}Th criterion failing samples, samples with low PC1 scores are not ubiquitously well-behaved, indicating that another factor is influencing our data. Interpreting the meaning of the second principal component (PC2) and the scores for other samples is less clear. PC2 distinguishes among samples that have high values for Mg, Sr, and Ca. Total organic carbon data suggest that samples with negative PC2 scores have higher organic carbon content, but there are not enough available corresponding carbon data to be convincing. Furthermore, there is no other distinguishable separation of U-Th data by threshold criteria result in the biplot.

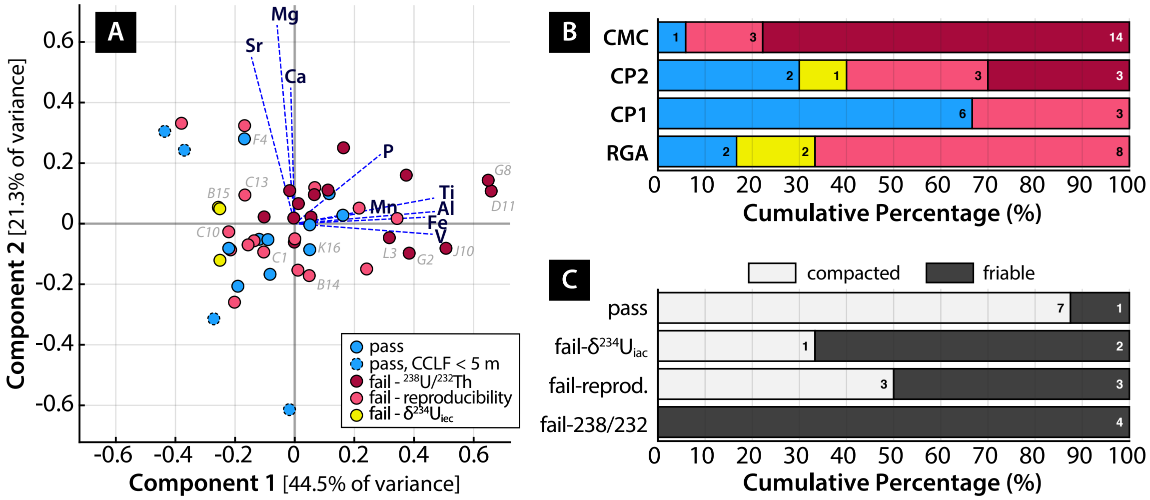

Figure 2-10: [**A**] Biplot of the orthonormal principal component coefficients for Ca, Mg, Sr, Fe, Mn, Al, Ti, V, and P concentrations (dashed blue lines, labeled by element) and the principal component scores for $N = 48$ samples (circles, color-coded by the threshold criteria result). Light gray labels are corresponding sample IDs of samples that are featured in other figures; we encourage the reader to follow these labels in order to connect these plots with others. [**B**] Bar chart showing, for each facies, the relative proportion of samples that are each of the four threshold criteria results. **CMC** is cream-colored massive carbonate silt (Fig. 2-6); and **CP1** and **CP2** are cream-colored carbonate silts interbedded with peat layers; and **RGA** is red-green alternating varigated carbonate silt (Fig. 2-7). See Section 5.2 for further details. The bar colors follow the legend of Panel A. Numbers within each bar represent the actual number of samples; for example, of the 18 samples categorized as the CMC facies (top row), 1 passed, 3 failed the reproducibility criterion, and 14 failed the ^{238}U/^{232}Th criterion. [**C**] Bar chart showing the relative proportion of samples that are compacted (light) versus friable (dark) for samples of each threshold criteria result. Note that we qualitatively assessed sediment hardness for only 21 samples. As with Panel B, numbers within each bar represent the actual number of samples. Note that Panels B and C do not include U-Th samples from the upper 6 m of the core.

2.6.2 Open system uranium remobilization

While the data comparisons presented thus far broadly confirm that samples with higher $CaCO_3$ content are more likely to yield well-behaved U-Th dates, there remain some inconsistencies with predictions for detrital contamination, mainly that the samples with the highest $CaCO_3$ content and optical lightness fail the threshold criteria, especially the ^{238}U/^{232}Th criterion. Regarding the other sample data, there were no patterns distinguishing passing samples from samples failing the reproducibility and $\delta^{234}U_{iec}$ criteria in Figs. 2-9 and 2-10A. This information leads us to consider the next probable cause for poor sample behavior: the remobilization of uranium after initial carbonate formation.

Using a qualitative assessment of sample hardness, we notice that passing samples were generally more compacted and dense, whereas failing samples were more friable and soft, especially those failing the ^{238}U/^{232}Th criterion (Fig. 2-10C). This observation fits our intuitive expectation that samples with less porosity would be more impervious to diagenesis or secondary deposition of uranium from porewater fluid flow (Fig. 2-1D).

We now refer back to the facies to which each sample is assigned for further insight. From Fig. 2-10B, it is clear that facies alone does not dictate how each U-Th sample behaves. Instead, there are some broad tendencies: most CMC samples failed the ^{238}U/^{232}Th criterion; most RGA samples failed the reproducibility criterion; and most of the passing samples originate from the CP facies (CP1 and CP2). In considering the reasons behind these patterns, we compare both facies and threshold criteria results with uranium concentration, total organic carbon (TOC), and a*, the red-green color reflectance of sediment, where +a* values are more red and -a* values are more green (Fig. 2-11). The red or green color of sediments has long been used as a qualitative indicator of *in situ* redox conditions, in which red colors signify oxidizing conditions and green-gray colors suggest reducing conditions, owing to the strong chromophores associated with ferric and ferrous iron (Tomlinson, 1916; Lyle, 1983).

Panels A–F in Fig. 2-11 (top half) compare the mean a* of all measurements within 5 cm of the U-Th sample to the mean point-to-point difference in a* across the same interval (a measure of the 'volatility' of a* around each sample). For example, having a mean difference of 2 units/cm in a* means that the a* value changes, on average, by a magnitude of 2 along every cm within the 10 cm range surrounding the U-Th sample. Such a value would indicate significant volatility in red-green color, given that the total range of mean a* observed in U-Th samples is ∼3. From these panels, we notice that the CP samples are more red and occupy a relatively narrow range of mean a* values, whereas the CMC samples tend to be less red and exhibit less volatility in red-green color (Fig. 2-11D, F), especially those failing the ^{238}U/^{232}Th criterion (Fig. 2-11C, E). These results are consistent with our qualitative observations of the CMC facies, in which the lighter colored carbonate occurs in ∼10–50 cm thick beds that are relatively uniform in color (Fig. 2-6).

Previous studies on sediments have interpreted changes in red-green color intensity as changes in the input of red iron-bearing materials (e.g., Giosan et al., 2002; Helmke et al., 2002; Ji et al., 2005), but because these iron-bearing minerals are highly sensitive to variations in redox environment, reductive diagenesis can subsequently alter sediment color to be more green (Lyle, 1983; König et al., 1999; König et al., 2000). Thus, here we

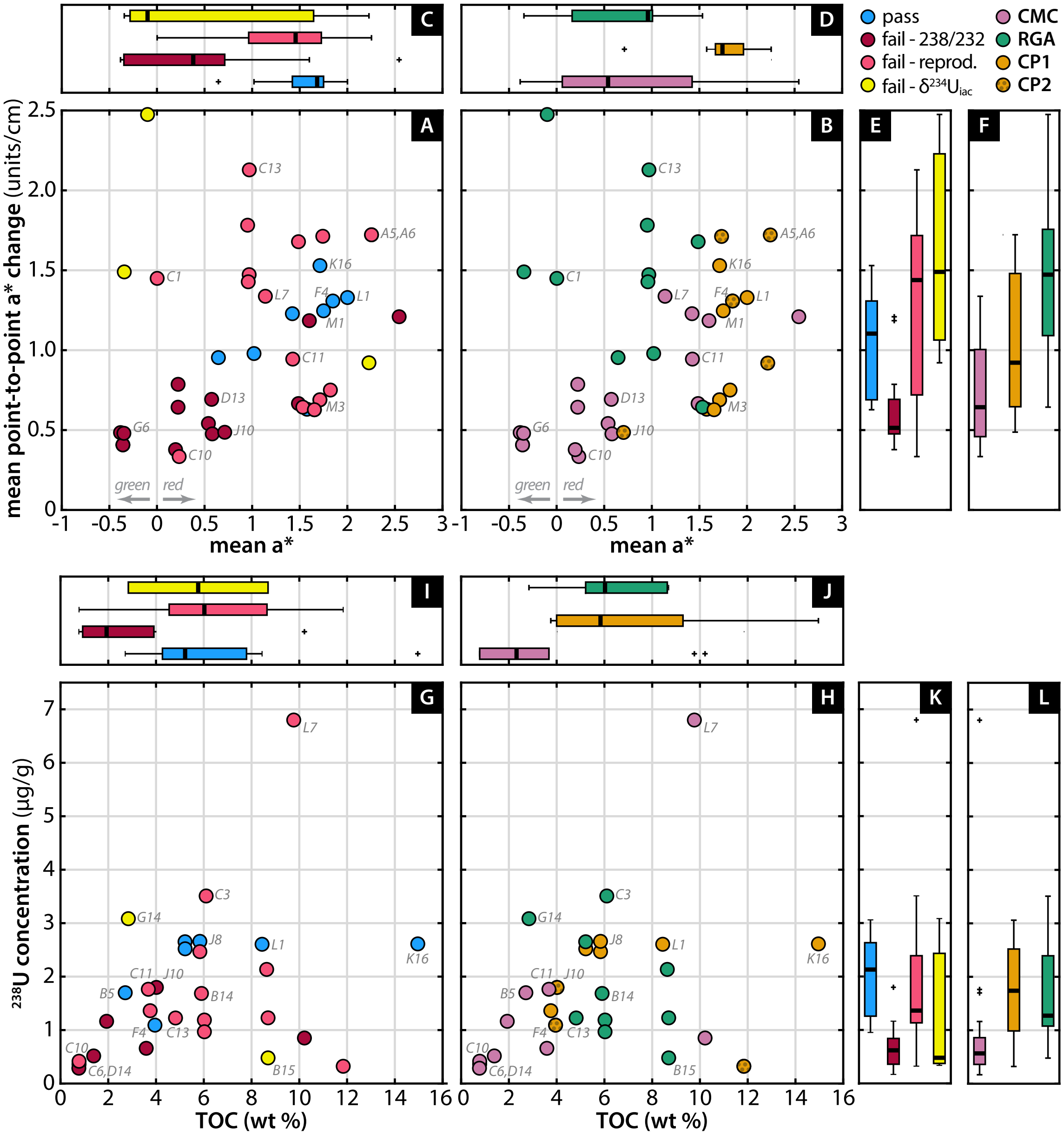

Figure 2-11: Cross-plots and box-and-whisker plots comparing the red-green color reflectance (a*; from the L*a*b* color space), total organic carbon (TOC) content, and ^{238}U concentration of U-Th samples and showing their relationship to threshold criteria result and facies. In all box-and-whisker plots, the thick central black line represents the median; the top and bottom edges of the box represent the 25th and 75th percentiles, respectively; the whiskers extend to the most extreme points not considered outliers; and the outliers are plotted as '+' symbols. A point is considered an outlier if it has a value >1.5x the interquartile range away from the 25th or 75th percentiles. The top half of the figure compares the mean a* of all measurements within 5 cm of the U-Th sample to the mean point-to-point difference in a* across the same interval. Note that there are some samples for which there is a ^{238}U concentration measurement but no corresponding TOC; thus, Panels K–L include data not shown in the cross-plots of Panels G–H. The bottom half of the figure compares TOC and ^{238}U concentration of each U-Th sample. Note that this figure does not include any data from the upper 5 m of the core.

propose that the difference in a* values between the CP and CMC samples is a reflection of diagenesis: the CP samples, being more red, have not been as altered by interactions with post-depositional reducing pore fluids and thus better preserve primary isotopic information to produce passing U-Th dates. In contrast, the CMC samples, which may have originally appeared more red like the CP samples, have been altered and as a result, have changed a more green color.

Consistent with this hypothesis is the observation that the CMC and ^{238}U/^{232}Th threshold failing samples generally have much lower ^{238}U concentrations and TOC compared to other samples (Fig. 2-11G–L). Consider the following scenario: a package of endogenic carbonate containing organic matter is deposited and submerged under oxygenated conditions. After burial, oxygenated porewaters then interact with the organic matter and begin to degrade it, removing from the sediments any uranium associated with the organic matter (Section 2.2.2; Fig. 2-1D). This degradation of organic matter may decrease the local pH of pore fluids such that it begins to alter the endogenic carbonate, leaching uranium originally bound within the crystal lattice. At some later point, the pore fluids are no longer recycled, and eventually all oxygen is depleted. The now reducing fluids then begin to reduce the surrounding sediment, shifting its color from red to more green. Any uranium that was removed from the carbonate into the pore fluid has now precipitated as authigenic uranium under these reducing conditions, but is no longer lattice-bound and is thus susceptible to further remobilization (Section 2.2.2; Fig. 2-1D). By the time we extract the core and measure the isotopic composition of these sediments, they are green (Fig. 2-11A–F), easy to physically disaggregate (Fig. 2-10C), and have low organic matter content and uranium concentrations (Fig. 2-11G–L).

If uranium loss has occurred from the CMC facies, preferential loss of ^{234}U may be expected, such that replicate analyses produce an inverse relationship between $\delta^{234}\mathrm{U}_{\mathrm{initial}}$ and ^{238}U concentration (e.g., Robinson et al., 2006). Indeed, such a relationship is observed for some CMC samples (Fig. 2-16). Furthermore, this proposed mechanism is compatible with the interpretations by Woods et al. (2019) for Lake Junín sediments of the last 50 ka, in which peat layers represent abrupt, ∼25–500 year periods of drought and lake low stands. Dramatic lake level changes would alter water table gradients and change groundwater discharge rates through littoral sediments. Thus, for the CMC facies, while detrital contamination is apparent given the elemental concentration data (Fig. 2-10), the initial ^{230}Th correction might have compensated to yield an accurate yet imprecise date, were it not for uranium loss.

As for why the CP facies seems not as affected by such pore fluids: we hypothesize that the thick peat beds associated with this facies act as a reductive barrier to the vertical movement of such oxygenated porewaters. This explanation is further bolstered by the observation that samples bounded on top by a thick (>10 cm) peat layer that is laterally continuous across multiple holes at the site (*i.e.*, the CP1 facies) yielded more passing dates with higher ^{238}U/^{232}Th and probability of fit (Fig. 2-10B and 2-7). The cream-colored carbonates of the CP1 facies also exhibit faint horizontal banding, possibly representing the preservation of primary fabric. In contrast, samples from the CP2 facies yielded comparatively less ideal U-Th data (Fig. 2-10B). Sedimentologically, the carbonates of the CP2 facies tend to be darker in color and more massive rather than banded in texture. Fig. 2-7 features two depth-equivalent core sections from different holes which were classified as the CP2 facies. Examining images of these two core sections, it is clear that the uppermost layer of peat is not laterally continuous. Samples E12 and F4 are the only two samples of this facies that pass the threshold criteria, and are arguably the most tenuous of the passing dates: E12 has a ^{238}U/^{232}Th ratio of 1.02 and F4 has a probability of fit only slightly above 1%, both borderline values.

Thus far, we have multiple lines of evidence that point towards uranium loss as an explanation for the broad behavior of CMC samples, and the basis for that theory can explain the acceptable behavior of the CP samples. As for the RGA samples, these sediments tend to exhibit higher a* volatility (Fig. 2-11D, F), as one would expect for samples of a facies defined by alternating beds of red and green laminae (Fig. 2-6). Contrary to the CMC samples, the red-green color of the RGA facies seems to be controlled by sediment composition, given that the laminae are well-defined and the boundaries between color changes are very distinct. The sediment color of RGA facies dulled noticeably a few hours after initial core cutting and exposure, suggesting that iron-bearing minerals again strongly influence color. To explain the general lack of reproducibility of U-Th data from RGA samples (Fig. 2-10C), we speculate that the green layers containing ferrous iron may be reactive enough to remobilize Fe-Mn hydroxides that complex with uranium (Chappaz et al., 2010), leading to open system behavior that manifests as poor reproducibility.

2.6.3 Ostracode and mollusc shells

As a demonstration of the utility of paleoecological data for U-Th data interpretation, we compare our U-Th sample data to measures of ostracode color and mollusc shell abundance.

During sample processing, we noticed that the color of ostracode shells often varied from sample to sample, ranging from translucent to dark gray or black. Because modern pristine ostracode shells are generally transparent and exhibit only trace pigmentation (Smith and Delorme, 2010), fossil ostracode shells with dark discoloration or coatings are generally thought to be altered and are thus avoided for geochemical analyses as a good practice (Holmes and Chivas, 2002). Many studies have made note of dark coatings on ostracode shells (e.g., Palacios-Fest et al., 2005; Wrozyna et al., 2012; Mackay et al., 2013), but there are few systematic studies that attempt to explain the origin and controls on ostracode discoloration or coatings (e.g., Ainsworth et al., 1990; Schwalb et al., 1995; Holmes, 1998).

The results of our comparison with ostracode shell color are broadly consistent with our hypothesis that the CMC facies has been altered by reductive diagenesis. Fig. 2-12 compares the threshold criteria result and facies with ostracode color, which we classified on a 7-point scale from translucent to black. Most CMC samples (5 out of 7) and all samples failing the $^{238}U/^{232}Th$ criteria had a higher proportion of darker shells. Sample B5, the only CMC sample that passed threshold criteria, has no ostracode shells with a color > 2. All other samples with different threshold criteria results and facies had ostracode assemblages comprised mainly of light-colored shells, with some exceptions.

Aside from color, there were no conclusive relationships between U-Th data and taphonomy (number of broken versus intact shells; adults versus juvenile counts) or ecology (benthic versus swimmer species; ornamentation). However, we noticed that most of the darker shells (color > 2) belonged to Darwinulidae, a family of benthic ostracodes that are considered an indicator of groundwater discharge. Schwalb et al. (1995) observed dark coatings on *Darwinula stevensoni* valves in Holocene sediments of Williams Lake (Minnesota, USA) and determined via wavelength- and energy-dispersive (WD/ED) spectrometry that the coatings were made of iron sulfide. They proposed that the coatings formed during periods of increased groundwater discharge, in which groundwater supplied additional Fe to the lake while reactive organic matter and sulfate led to reducing conditions that promoted iron sulfide formation. This mechanism is analogous to the one we propose to explain the behavior of U-Th data from the CMC facies. Future investigations should analyze the composition of the surface coatings with either WD/ED spectrometry or scanning electron microscope energy-dispersive X-ray (SEM-EDX) analysis.

Regarding mollusc shells, as discussed in Section 2.2.3, extensive attempts to U-Th date mollusc shells for paleo-sea level reconstructions have shown that this material does not remain a closed system after burial. We confirm that mollusc shells yield dates that are

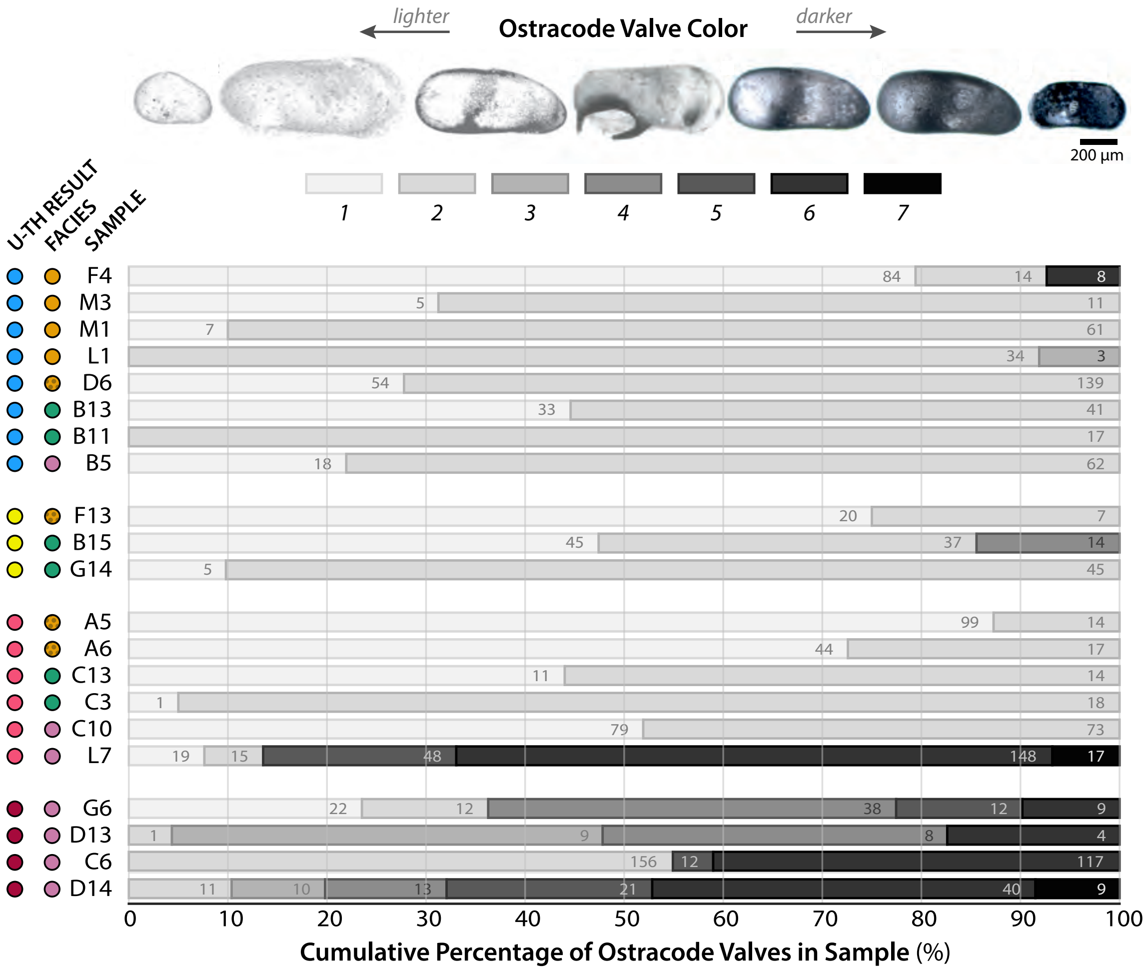

Figure 2-12: Relationship between ostracode color and U-Th data. Top row of microscope images of ostracode valves illustrate the coloration scale and are arranged from lightest to darkest on a scale of 1 to 7. The bar charts show the relationship between ostracode shell color, threshold criteria result, and facies for 21 samples. Each row in the chart represents ostracode count data from one sample. Rows of data are grouped together vertically by threshold criteria and then sorted within those groups by facies (see colored circles on the left). The length of bars in each row represents the relative proportion of shells in each sample that are of a particular color. The bar color represents the ostracode shell color. Numbers within bars indicate the actual number of valves of each color. From the microscope images (left to right): (1) Translucent (LV, Cyprididae, sample B5); (2) White (RV, Limnocytheridae, sample D14); (3) Partly light gray (RV, Darwinulidae, sample D14); (4) Light gray (RV, Limnocytheridae, sample C6); (5) Partly dark gray (RV, Darwinulidae, sample C6); (6) Dark gray (RV, Darwinulidae, sample C6); (7) Black (LV, Limnocytheridae, sample L7). LV: Left valve external view, RV: Right valve external view.

biased young in sample F14 (∼8200 ka), in which an analysis comprised purely of mollusc shell fragments yielded an age ∼3000 yrs younger that the surrounding bulk sediment (Table 2.4). Although we visually screened for and manually removed identifiable mollusc shell fragments from samples before processing, it is possible that smaller unidentified fragments remained; if differential amounts of mollusc shell fragments were included in replicate analyses, poorly reproducing U-Th data might be an expected result. There is some qualitative indication that the RGA facies is more abundant in mollusc shell fragments than other facies, but the results are not conclusive.

2.7 Modeling the effects of detrital contamination and uranium remobilization

We have examined various sedimentological and geochemical data to evaluate a few hypotheses for poorly behaved U-Th data. In this section, we simulate the uranium and thorium isotopic evolution of samples with various compositions and uranium loss/gain pathways, and compare these model results with the actual measured isotopic composition of our samples (Figs. 2-13 and 2-14). Based on these results, we posit that the balance of evidence from both modeling and the previous data comparisons (Section 2.6) favors uranium remobilization as the main explanation for the observed scatter, rather than substantial detrital contamination.

To model the effects of detrital contamination, we calculate the impact of mixing varying amounts of detrital material with pure endogenic carbonate. We also test the effects of varying the composition of the detrital material, changing the relative proportions of marine limestone and aluminosilicate. We assume that all detrital material is isotopically homogeneous and at secular equilibrium, in which $[^{230}\mathrm{Th}/^{238}\mathrm{U}]$ and $[^{234}\mathrm{U}/^{238}\mathrm{U}]$ are both equal to 1. The uranium and thorium concentrations of the detrital components are set to represent average values for marine limestone and the upper continental crust (Rudnick and Gao, 2003): U conc. = 2 ppm and Th conc. = 1 ppm for marine limestone, and U conc. = 2.7 ppm and Th conc. = 10.5 ppm for the aluminosilicate material. Our measurement of the uranium and thorium concentration of a dark gray silt sample that has ∼30% $CaCO_3$ content (sample E2; Fig. 2-6) suggests that using these values to simulate the detritus entering Lake Junín is not unrealistic. Although organic matter is a non-negligible constituent of our samples (1–16%; Fig. 2-11) and is likely a meaningful uranium source

(Fig. 2-1D), we chose to exclude TOC in our model as a necessary simplification for this exercise. As such, the modeling results should be treated as proofs of concept, rather than a serious attempt to precisely quantify the manner by which each deviating U-Th date occurs.

We focus on modeling two groups of data: samples from ∼20–23 m and samples from ∼70–75 m. Taking the passing U-Th dates within these groups at face value, these depth ranges correspond to samples with nominally true ages of ∼75 and ∼550 ka, respectively. The scatter of threshold criteria failing data at ∼20–23 m all originate from the CMC facies and are generally biased older relative to the passing dates, whereas the data at ∼70–75 mostly consists of the RGA facies and are biased younger (Fig. 2-15B).

2.7.1 Modeling results for ∼75 ka-aged samples

Fig. 2-13A compares our U-Th data from the first group (circles) to our simulations of isotopically evolving samples (colored lines) in ^{230}Th/^{238}U activity-δ^{234}U space. All models of samples are evolved for 75 kyrs. To orient the reader: the measured isotopic composition of the two passing samples in this depth range, K16 and L1, are marked by the pair of gray circles located adjacent to the pair of blue circles (see legend). The horizontal offset between the colored and gray circles represents the effect of the initial ^{230}Th correction, the magnitude of which is controlled by the ^{238}U/^{232}Th ratio (Eq. 2.3). The gray shaded region delineates the age range prescribed by the age-depth model (to be shown and discussed in Section 2.8); for our purposes here, we treat this range as the "true" age range of all samples shown. Thus, any colored circles that do not fall within the gray shaded region are samples that yielded apparent dates that are inconsistent with the true age of these sediments (see straight lines labeled by date). The goal of the subsequent exercises is to explore what pathways of isotopic evolution can explain the isotopic composition of these outlying data.

We first approximate the starting isotopic composition of a representative endogenic carbonate by reverse engineering the isotopic composition of the passing samples. K16 and L1 have an average uranium concentration of 2.6 ppm, carbonate content of ∼60%, and TOC of ∼10%. These values indicate that non-carbonate detrital material accounts for ∼30% of the sample composition. If we set the detrital end member to be made entirely of aluminosilicate material, we find that a sample consisting of the following material can roughly match the end isotopic composition of K16 and L1 after evolving for 75 kyrs:

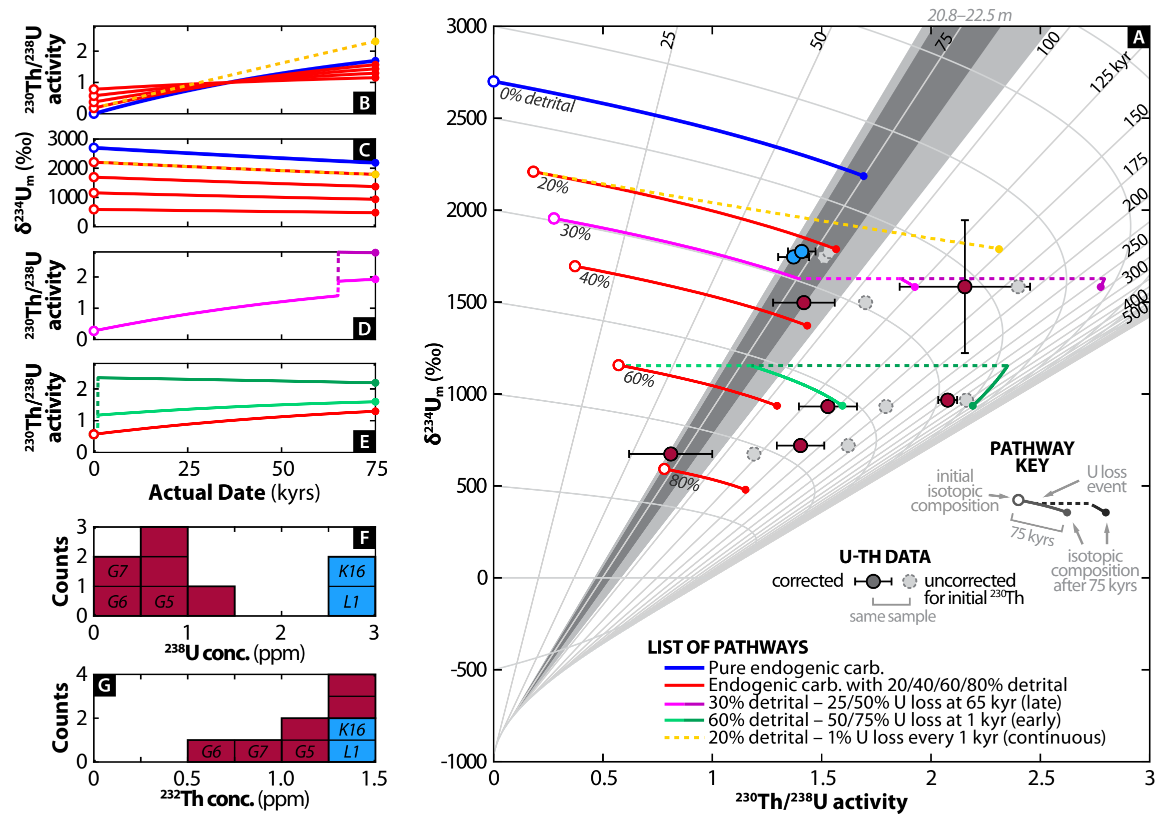

Figure 2-13: Possible pathways of uranium-thorium isotopic evolution that may explain the outlying data at ∼20–23 m. [**A**] Plot comparing U-Th data (circles; see legend) with possible pathways (colored lines) in δ^{234}U–^{230}Th/^{238}U activity space, following Fig. 2-1C. Corrected U-Th ratios (color-coded by threshold criteria result) are each paired with their corresponding uncorrected ratios (gray circles with dashed outlines). The gray triangular wedges represent the expected age range of samples from this depth range based on the age-depth model, where the dark gray area is the range of model means (red line in Fig. 2-15A) and the light gray area is the maximum and minimum of the uncertainty range (shaded gray area in Fig. 2-15A). Colored lines represent the isotopic evolution of sample material of mixed composition and uranium loss histories over 75 kyrs (see list of pathways and pathway key for symbology). The simulated samples are mixtures of two isotopically homogeneous end-members: pure endogenic carbonate and detrital material made of 30% limestone and 70% aluminosilicate material. The starting composition of the pure endogenic carbonate is 2.8 ppm ^{238}U and 2700‰ for δ^{234}U$_{\text{initial}}$. These calculations assume that the endogenic carbonate contains no initial ^{230}Th and that uranium loss occurs with no fractionation between ^{234}U and ^{238}U. [**B**] and [**C**] Change in the isotopic evolution as the proportion of detrital material increases (red lines). [**D**] and [**E**] Change in ^{230}Th/^{238}U activity after uranium loss. δ^{234}U is not shown because its evolution is no different from that without uranium loss (compare dashed yellow line with red line of same starting composition in Panel C). [**D**] and [**E**] ^{238}U and ^{232}Th concentrations of U-Th samples in this depth range. K16 and L1 are of the CP1 facies; all other U-Th data featured are of the CMC facies (see Fig. 2-15B).

20–30% detrital material and 70–80% endogenic carbonate with a starting composition of $\delta^{234}U_{\text{initial}} = 2700‰$ and uranium concentration = 2.8 ppm (Fig. 2-13A, colored lines labeled 20% and 30%; see legend). The blue pathway represents the isotopic evolution of a pure endogenic carbonate of this composition over the same amount of time, 75 kyrs: with no ^{232}Th, its initial ^{230}Th/^{238}U activity is zero and its final isotopic composition matches its true age. Adding detrital material to this pure endogenic carbonate increases the initial ^{230}Th/^{238}U activity and decreases the initial δ^{234}U of the sample (red pathways in Fig. 2-13B–C), causing the sample to yield an older apparent date after 75 kyrs (red pathways in Fig. 2-13A). Note that we tested the sensitivity of these simulations to the composition of the detrital material by varying the proportion of marine limestone, and found that this detail has a small impact compared to that of the total proportion of detrital material.

From the red pathways in Fig. 2-13A, it is clear that no amount of detrital material is able to explain the samples with high measured ^{230}Th/^{238}U activities, given the composition of the end members being mixed. Furthermore, the ^{232}Th concentrations of these samples place an inexact but actionable upper bound on how much detrital material is reasonable (Fig. 2-13G); for example, a 30% contribution of detrital material that is 50% limestone already produces a sample with ^{232}Th concentrations of $\sim$1.7 ppm. Thus, we invoke uranium loss to explain these data: yellow, pink, and green pathways in Fig. 2-13A illustrate the impact of continuous, late, and early uranium loss on the sample isotope composition (see legend and Fig. 2-13D–E). These samples are also the same low uranium CMC samples failing the ^{238}U/^{232}Th criterion described earlier. We cannot infer which of these uranium loss scenarios is most likely at work from isotopic measurements alone, but our hypothesis for the CMC samples described in Section 2.6.2 would favor early loss. In addition, the magnitude of uranium loss required to approach the isotopic composition of the outlying samples is similar to the difference in uranium concentration between passing and failing samples (Fig. 2-13F).

Note that these modeled uranium loss pathways are simplified to assume that loss occurs with no fractionation between ^{234}U and ^{238}U, but preferential leaching of ^{234}U is more likely closer to reality (Section 2.5).

2.7.2 Modeling results for $\sim$550 ka-aged samples

Fig. 2-14 features the U-Th samples from $\sim$70–75 m. At this age, the close spacing of the age isolines in this regime causes the area defining the “true” age range of these samples to occupy a much narrower area in ^{230}Th/^{238}U activity-δ^{234}U space (shaded gray area in Fig. 2-14B). Here, we start with a pure endogenic carbonate with a composition of δ^{234}U$_{\text{initial}}$ = 2700‰ and ^{238}U = 1.8 ppm, values selected via the same reverse engineering steps described in Section 2.7.1, but using the passing samples in this depth interval. Detrital contamination has much less impact on the accuracy of the dates at this age, as demonstrated by the fact that all the modeled pathways of samples with varied percentages of detrital material still ultimately end in the region defining the true age of the sediments (gray shaded region in Fig. 2-14B; see Section 2.2.2 for explanation). In order to produce samples with isotopic compositions that bias dates to be younger, we simulate the impacts of uranium gain.

Similar to detrital contamination, early uranium loss (or gain) has no effect on the final sample date at this age. Thus, in Fig. 2-14B, we only illustrate the impacts of late or continuous uranium gain (green and yellow pathways). In contrast to the pathways observed for ∼75 ka-aged sediments, here very small percent gains in uranium can have measurable impacts. For example, a 1% gain at 540 kyr can cause the sample date to be ∼100 kyrs younger (green pathway in Fig. 2-14B). Thus, the sensitivity of the apparent dates to small alterations in uranium in this regime, in combination with narrowly spaced age isolines, is likely the cause for the large spread of dates at this depth, as well as the poor reproducibility of replicate analyses (Fig. 2-8D). Because early uranium gain cannot explain the young bias of these samples, the hypothesis for post-depositional uranium uptake by gastropod shells seems less convincing; gains would have to be continuous and gradual, and it is unclear from where the continuous supply of uranium would come.

Note that although Figs. 2-13–2-14 do not explore compound gain or loss pathways, such scenarios are not outside the realm of possibility.

2.8 Conclusions: the age-depth model for the PLJ-1 splice

Through the use of threshold criteria that evaluate samples on the basis of their ^{238}U/^{232}Th ratio, reproducibility, and δ^{234}U$_{\text{iec}}$, we have conducted a methodical curation of the U-Th data that is justified by comparisons to other sedimentological, geochemical, and paleoecological datasets, as well as modeling of the isotopic evolution of simulated samples. As a result, we deem 18 of the 55 sample dates as satisfactory for use as age constraints. These passing samples generally come from sediments of the CP facies, which we hypothesize have experienced relatively less uranium remobilization because of the thick overlying peat

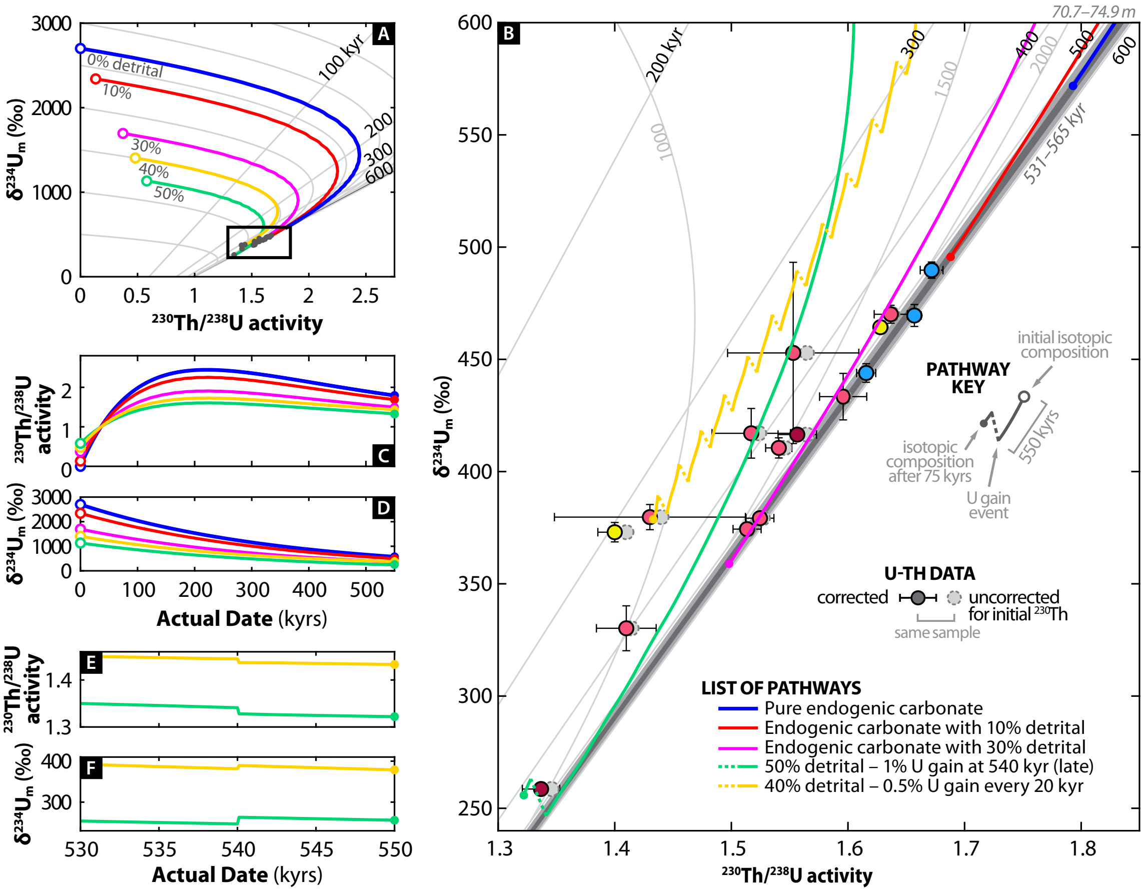

Figure 2-14: Possible pathways of uranium-thorium isotopic evolution that may explain the outlying data at ∼70–75 m. See caption in Fig. 2-13 for explanation of symbology. [**A**] Plot showing initial isotopic composition and evolution of pathways over 550 kyrs. [**B**] View of the isotopic evolution of samples within the extent represented by the rectangular box in Panel A. The gray triangular wedges representing the expected age range of samples from this depth range occupies a much narrower area in $^{230}Th/^{238}U$ activity-$\delta^{234}U$ space compared to Fig. 2-13. The starting composition of the pure endogenic carbonate is 1.8 ppm ^{238}U and 2700‰ for $\delta^{234}U_{initial}$. The detrital component has the same composition as that from Fig. 2-13, 30% limestone and 70% aluminosilicate material. These calculations assume that uranium gain occurs with a $\delta^{234}U$ ratio equal to the $\delta^{234}U_{initial}$ of the sample. [**C**] and [**D**] Change in isotopic evolution as the proportion of detrital material increases. [**E**] and [**F**] Change in isotopic evolution after uranium gain.

beds that act as reductive barriers to post-depositional fluid flow.

Fig. 2-15A shows the age-depth model for the PLJ-1 splice using these U-Th ages and radiocarbon data. The model was generated using the R-based Bayesian age-depth modeling software program called Bacon (v2.3; Blaauw and Christen, 2011). On average, the 95% confidence range of this model is ∼30 kyrs. Trachsel and Telford (2017) tested Bacon and other age-depth modeling routines (CLAM, OxCal, BChron) on a varved sediment sequence and found that they all produced mean age-depth models close to the truth, but each program has its own advantages and disadvantages. In the case of Bacon, the application of an accumulation rate prior forces sedimentation rates to be more smooth and linear than is possibly justified. Thus, while the alternating packages of carbonate and glaciogenic silt in the core hint at variability in sedimentation rates, this information is not utilized in the generation of the age-depth model. See Section 2.10.5 for details regarding the parameters and priors used for the model run.

Fig. 2-15A also compares the radiometric age-depth model to geomagnetic relative paleointensity (RPI) tie points made between the PLJ-1 normalized remanence record and well-dated RPI stacks (Hatfield, in prep.). Broadly, these data are consistent with age-depth model and provide further support for its validity. See Section 2.10.6 for details on the determination of the RPI tie points.

2.9 Considerations for future U-Th dating of lake sediments

When it comes to U-Th dating of lake sediments, there are no “silver bullets” or easy answers: no singular facies, carbonate content threshold, color, or any other sedimentological or geochemical data could predict the viability of a U-Th date with certainty in these sediments. In fact, samples that would conventionally be considered ideal were some of the most poorly behaved samples. One wonders what the outcomes might have been if only the nominally choicest samples had been processed, and the dateability of the entire core assessed from those results. Such decision making processes are the norm when less time and fewer resources are available.

Our concern for overlooked but dateable sediments in other records also extends in the opposite direction: other studies may be overly reliant on single-analysis U-Th dates that seem credible but have not been reproduced or tested with stratigraphic coevality

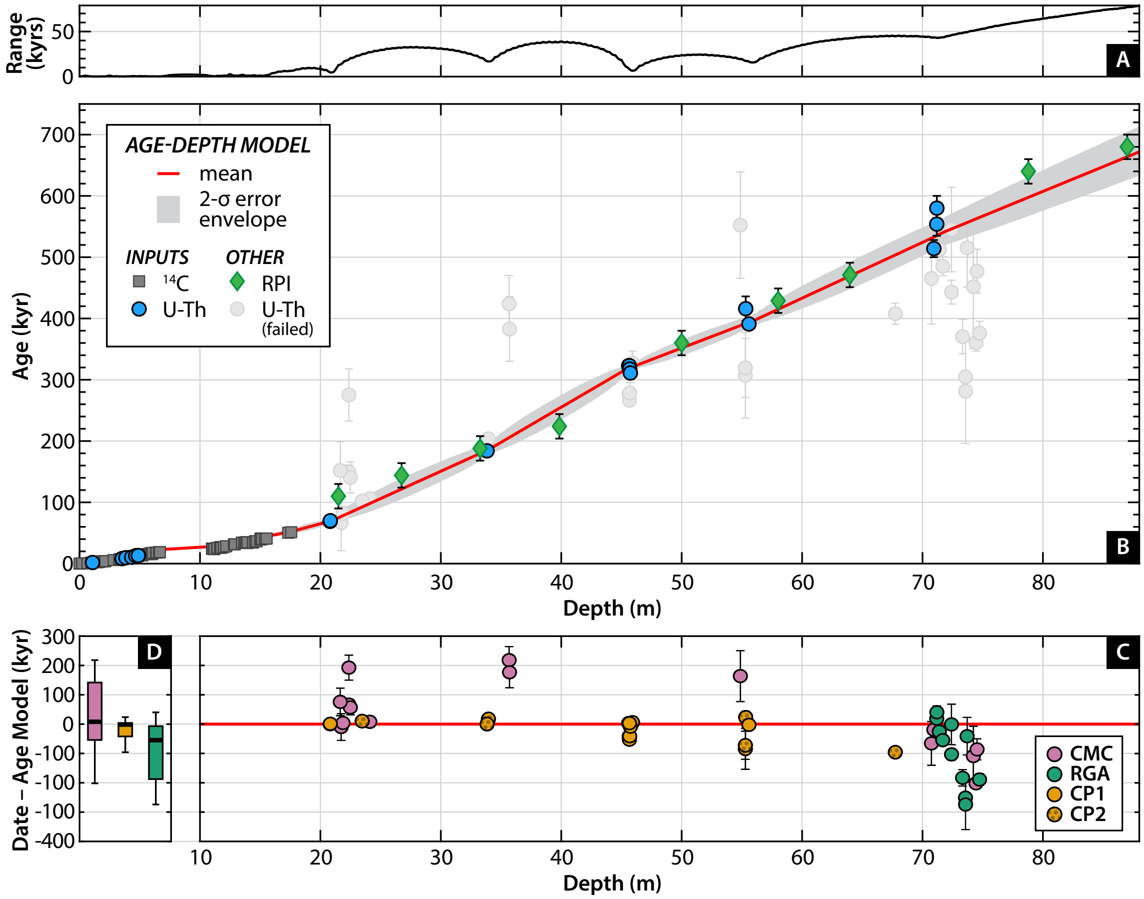

Figure 2-15: [**A**] and [**B**] Age-depth model for the PLJ-1 splice generated by Bacon (Blaauw and Christen, 2011) using radiocarbon (gray squares) and U-Th (blue circles) data. Red line represents the mean and gray shaded area is the 2-σ range error envelope. U-Th data that did not meet threshold criteria (light gray circles) and relative paleointensity (RPI) tie points (green diamonds) were not used as inputs for the age-depth model and are plotted as an overlay. Section 2.10.5 for additional information on the priors and posteriors of the model. Radiocarbon data are from Woods et al. (2019) and RPI data are from Hatfield et al. (in prep.). [**C**] Comparison of all U-Th dates and their departure from the age-depth model mean (thick red line at zero), color-coded by facies. See Fig. 2-8D to compare with data color-coded by threshold criteria result. [**D**] Box-and-whisker plots showing the distribution by facies of the difference between U-Th dates and the age-depth model mean; see caption of Fig. 2-11 for description of box-and-whisker plot symbology. All error bars shown are of 2-σ range. Analyses that yielded indeterminant U-Th dates or were infinite are not included in this figure.

constraints. The most glaring example of this can be demonstrated through the results from sample L7, which had the highest uranium concentration (7 ppm, 2 times higher than the next highest) and highest ^{230}Th/^{232}Th ratio out of all samples (Table 2.3). Because of this, individual analyses were rather precise, with 400–700 year uncertainties (2-σ) on $\sim$100 ka dates. On their own, these dates would be considered excellent, but only after replication is it revealed that none of the precise dates overlap with one another at the 2-σ level. Although a labor intensive strategy, there is no substitute for replication and reproducibility in assessing the quality of U-Th geochronological data.

Furthermore, while the threshold criteria ultimately decided which data would form the foundation of the age-depth model, it was the placement of geochronological data in context of other sedimentological and geochemical information that provided justification for these thresholds. These data comparisons also provide practical insights on what other characteristics to consider for future U-Th dating attempts on lake sediments: for instance, the aforementioned L7 sample contained some of the darkest ostracode shells categorized (see image of ostracode shell with color = 7 in Fig. 2-12).

Embracing the noise in our data has led to a richer understanding of the controls on uranium in these lake sediments. As our ability to resolve this noise increases as the analytical precision of measurements improves, subtle differences in the noise will become interpretable as information on paleoenvironmental processes themselves. This work demonstrates the beginnings of what is possible on this front. Although >150 analyses went into this work, we hope that this number does not intimidate those seeking to apply U-Th dating to their own lake sediment samples. Rather, we seek to showcase strategies for interpreting scattered geochronologic data of any size and encourage similar efforts where better geochronological control would have the most impact. As more high resolution datasets become paired with drill cores by default (e.g., scanning XRF, color reflectance, magnetic susceptibility), there will be more opportunities to use such additional data to test underlying working assumptions for geochronologic tools.

Of all the lessons learned, we hold the following as most important: for the determination of the age of lake sediments, geologic context—in the form of sedimentological observations, geochemical data, and paleoecological descriptions—is of equal importance to the numerical accuracy and precision of geochronological measurements.

Table 2.3: Average values of various U-Th data for each sample, calculated from replicate analyses. Samples that passed all threshold criteria (Section 2.5) are listed first; then all samples are sorted by depth (**CCLF**). All uncertainties listed are 2-σ. **N** is the total number of replicate analyses made for each sample. **MSWD** and **prob. of fit** fields are left blank if there is only 1 replicate analysis or marked with an asterisk (*) if any replicate analyses yielded infinite dates; samples marked with an * are considered to have failed the reproducibility criterion. **Weighted Mean Date** is reported relative to Before Present (BP), in which the present is defined as January 1, 1950. $\boldsymbol{\delta^{234}U_m}$ is the measured $\delta^{234}U$. Meaning of the abbreviations used for **facies** can be found in Section 5.2. For **threshold criteria result**, numbers indicate which threshold criterion each sample failed: 1 = $^{238}U/^{232}Th$; 2 = reproducibility; and 3 = $\delta^{234}U_{iac}$. See Table 2.4 for data associated with replicate analyses and Supplementary Materials for raw unrounded data.

Samp. ID	CCLF (m)	N	^{238}U (ng/g)	^{232}Th (ng/g)	MSWD	Prob. of Fit	Weighted Mean Date (yrs BP)	$[^{230}Th/^{238}U]$	$\delta^{234}U_m$ (‰)	$\delta^{234}U_{iac}$ (‰)	$^{238}U/$ ^{232}Th	$^{230}Th/$ ^{232}Th	Facies	Threshold Crite-ria Result
Passing Samples														
F9	1.080	3	2911±70	124±25	0.07	0.93	1810±200	0.0760±0.0027	2355.0±1.6	2395±19	24.1±4.6	28.9±4.5	–	pass
F14	3.530	4	697±58	25.2±5.5	1.38	0.25	8180±150	0.2822±0.0061	2639±11	2727±21	28.5±5.1	127±20	–	pass
F15	3.850	3	980±32	105±13	0.11	0.90	9600±500	0.3665±0.0073	2721±24	2880±53	9.39±0.91	54.5±4.3	–	pass
F16	4.330	2	1150±150	250±140	0.87	0.35	10500±1000	0.4251±0.0076	2630±120	2880±130	5.2±2.3	35±15	–	pass
C16	4.660	3	1580±250	243±32	0.17	0.84	12900±800	0.4181±0.0089	2085.3±3.8	2257±59	6.51±0.18	43.2±0.46	–	pass
D4	4.880	4	1970±71	497±18	0.03	0.99	13200±1200	0.4502±0.0046	1934.3±5.8	2156±95	3.965±0.053	28.34±0.38	–	pass
K16	20.806	5	2610±700	1430±350	0.11	0.98	69000±2000	1.512±0.017	1745±20	2490±260	1.824±0.047	43.8±1.0	CP1	pass
L1	20.823	5	2610±540	1300±380	2.77	0.03	70000±4000	1.535±0.067	1774.7±3.4	2500±260	2.04±0.14	49.6±1.7	CP1	pass
D6	33.839	5	1200±110	1000±160	2.06	0.08	184000±6000	2.176±0.075	1288±74	2800±520	1.211±0.096	41.9±4.7	CP2	pass
M1	45.599	4	2520±52	430±23	3.05	0.03	323000±3000	2.1303±0.0061	936.0±2.0	2440±85	5.87±0.21	198.7±7.6	CP1	pass
M3	45.660	5	1740±130	376±25	0.49	0.75	323000±2000	2.212±0.011	999.5±8.0	2650±160	4.63±0.21	162.8±7.5	CP1	pass
J8	45.686	3	2660±110	341±34	0.79	0.46	317500±1700	2.1828±0.0046	985.3±4.8	2501±68	7.83±0.46	271±16	CP1	pass
J9	45.741	3	3059±61	1179±24	0.59	0.56	311000±3000	1.9583±0.0064	807.5±3.1	2170±160	2.594±0.042	80.7±1.6	CP1	pass
E12	55.318	5	953±39	940±110	1.26	0.28	416000±20000	1.828±0.054	631±31	2700±1100	1.017±0.076	29.5±3.0	CP2	pass
F4	55.587	5	1092±80	120±3.6	3.32	0.01	391000±5000	2.0570±0.0064	816.9±4.1	2550±130	9.10±0.40	297±13	CP2	pass
B5	70.941	5	1699±34	364±17	1.00	0.41	514000±14000	1.6727±0.0098	489.7±3.6	2230±610	4.68±0.20	124.2±5.3	CMC	pass
B11	71.182	4	2650±170	353±34	1.70	0.16	554000±19000	1.6160±0.0082	443.9±4.1	2190±400	7.52±0.28	193.1±7.7	RGA	pass
B13	71.190	4	1318±84	134±13	1.69	0.17	580000±20000	1.6572±0.0059	469.5±4.9	2600±1300	9.88±0.41	260±11	RGA	pass

Table 2.3 continued from previous page

Samp. ID	CCLF (m)	N	^{238}U (ng/g)	^{232}Th (ng/g)	MSWD	Prob. of Fit	Weighted Mean Date (yrs BP)	[^{230}Th/^{238}U]	δ^{234}U$_{\mathrm{m}}$ (‰)	δ^{234}U$_{\mathrm{iac}}$ (‰)	^{238}U/ ^{232}Th	^{230}Th/ ^{232}Th	Facies	Threshold Criteria Result
P10	6.505	2	749±33	837±52	*	*	–	0.540±0.013	792.8±2.3	–	0.896±0.028	7.68±0.22	CP2	1,2
L3	21.649	1	619±12	1118±23	–	–	150000±50000	1.621±0.025	719.6±3.0	2200±1300	0.553±0.028	14.25±0.22	CMC	1
G1	21.725	1	851±17	1230±130	–	–	70000±50000	1.19±0.12	673.8±2.0	1340±660	0.69±0.11	13.1±1.9	CMC	1
G2	21.878	2	1164±23	1435±70	0.01	0.92	82000±11000	1.700±0.027	1497±11	2840±860	0.812±0.037	21.91±0.64	CMC	1
G5	22.364	1	635±13	1395±28	–	–	280000±40000	2.162±0.040	966.7±1.7	5200±4200	0.455±0.028	15.61±0.29	CMC	1
G6	22.367	4	351±58	692±81	0.04	0.99	149000±12000	2.40±0.33	1580±360	5300±4600	0.506±0.035	19.2±1.9	CMC	1
G7	22.486	3	418±9	829±17	0.05	0.96	140000±30000	1.794±0.033	932±21	3000±2200	0.504±0.028	14.36±0.19	CMC	1
G8	22.537	1	861±17	2362±48	–	–	–	1.986±0.035	621.9±3.9	–	0.365±0.028	11.50±0.20	CMC	1
M15	23.467	4	323±7	38.3±3	37.0	0.00	102000±3000	2.219±0.043	2302.9±7.0	3175±64	8.46±0.59	298±23	CP2	2
L7	24.105	7	6800±330	400±27	399	0.00	106000±5000	1.829±0.074	1687.6±3.8	2316±47	17.03±0.68	494±24	CMC	2
D7	33.954	2	838±18	997±46	0.24	0.63	204000±9000	2.331±0.020	1328±25	3500±940	0.840±0.028	31.1±0.92	CP2	1
D11	35.671	2	392±39	870±210	*	*	–	1.41±0.11	283.9±7.3	–	0.457±0.091	10.2±1.3	CMC	1,2
D12	35.673	2	262±47	440±22	*	*	420000±50000	2.080±0.024	806.1±1.5	4400±1900	0.60±0.14	18.7±5.9	CMC	1,2
D13	35.705	3	168±11	216±15	8.19	0.00	380000±50000	2.078±0.095	823±59	3900±1600	0.778±0.028	25.7±1.5	CMC	1,2
D14	35.733	2	287±6	291±12	*	*	–	2.663±0.040	1019.2±4.4	–	0.987±0.028	41.71±0.21	CMC	1,2
J5	45.640	4	1360±120	377±83	5.51	0.00	277000±5000	2.131±0.043	1002±40	2370±130	3.71±0.60	126±22	CP1	2
J6	45.661	3	1202±80	389±36	14.0	0.00	266000±9000	2.129±0.023	1016.9±5.4	2380±140	3.095±0.095	104.6±4.3	CP1	2
J7	45.683	2	2467±83	389.8±8.9	97.2	0.00	278000±17000	2.162±0.028	1027.3±1.1	2367±88	6.33±0.36	217.3±9.5	CP1	2
J10	45.921	1	1798±36	2117±42	–	–	327000±20000	1.977±0.016	789.8±0.8	2930±800	0.849±0.028	26.66±0.21	CP2	1
K1	54.873	1	659±13	654±13	–	–	550000±90000	1.798±0.014	571.8±1.4	3700±2100	1.000±0.028	28.76±0.23	CMC	1
A5	55.288	2	2360±140	1496±30	72.6	0.00	310000±70000	1.907±0.044	751±19	2290±380	1.578±0.071	47.8±1.0	CP2	2
A6	55.292	3	2520±190	1143±75	105	0.00	320000±50000	1.996±0.064	819.3±6.5	2400±370	2.202±0.028	69.8±2.0	CP2	2
F13	67.741	4	338±7	278±21	0.29	0.84	408000±17000	1.584±0.057	448±45	1820±500	1.219±0.082	30.7±3.1	CP2	3
B2	70.741	1	516±10	615±12	–	–	470000±70000	1.565±0.017	416.5±2.1	2300±1200	0.839±0.028	20.84±0.22	CMC	1
G13	71.394	4	734±15	159.6±6.0	*	*	512000±17000	1.597±0.020	433±10	2060±770	4.60±0.21	117.5±7.3	RGA	2
G14	71.679	2	3084±62	206.0±7.1	2.11	0.15	485000±15000	1.6282±0.0046	464.3±1.8	1850±170	14.98±0.64	387±17	RGA	3
H6	72.406	3	1188±89	887±33	*	*	550000±70000	1.527±0.012	379.2±2.9	2200±1700	1.34±0.12	33.3±1.6	RGA	2

Table 2.3 continued from previous page

Samp. ID	CCLF (m)	N	^{238}U (ng/g)	^{232}Th (ng/g)	MSWD	Prob. of Fit	Weighted Mean Date (yrs BP)	[^{230}Th/^{238}U]	$\delta^{234}U_m$ (‰)	$\delta^{234}U_{iac}$ (‰)	^{238}U/ ^{232}Th	^{230}Th/ ^{232}Th	Facies	Threshold Criteria Result
H7	72.409	4	968±51	607±47	*	*	443000±19000	1.546±0.011	410.5±4.5	1730±460	1.60±0.10	39.7±2.6	RGA	2
B14	73.327	4	1685±35	698±57	12.0	0.00	370000±30000	1.524±0.034	417±11	1420±620	2.43±0.20	58.7±5.2	RGA	2
B15	73.566	4	479±10	161±10	0.19	0.90	305000±5000	1.410±0.015	373.0±4.3	970±120	2.98±0.15	66.8±3.5	RGA	3
C1	73.573	4	1230±440	330±130	195	0.00	280000±90000	1.440±0.082	379.7±5.6	1270±460	3.8±0.66	87±13	RGA	2
C3	73.704	2	3508±71	673±20	8.62	0.00	520000±60000	1.514±0.012	374.4±2.5	1770±470	5.213±0.054	125.3±2.3	RGA	2
C6	74.222	1	361±7	422.6±8.5	–	–	450000±100000	1.346±0.016	258.6±2.8	1360±920	0.855±0.028	18.27±0.22	CMC	1
C10	74.444	8	417±37	275±31	3.69	0.00	361000±14000	1.565±0.057	453±40	1540±340	1.521±0.095	37.8±3.4	CMC	2
C11	74.529	2	1763±36	339±11	8.18	0.00	480000±40000	1.638±0.014	470.1±4.0	1980±330	5.202±0.088	135.3±3.5	CMC	2
C13	74.739	4	1226±42	356±32	7.11	0.00	376000±20000	1.414±0.026	330±10	1100±230	3.46±0.25	77.9±6.8	RGA	2
C14	74.851	2	2135±43	525±12	*	*	–	1.5881±0.0049	364.4±3.8	–	4.069±0.088	102.6±2.5	RGA	2

Table 2.4: U-Th data for replicate analyses of each sample. All uncertainties listed are 2-σ. **Rep. ID** refers to a unique identifier for each replicate analysis. Note that sample ‘F14(s)’ refers to an analysis of gastropod shells from the same horizon as F14. Reported errors for ^{238}U and ^{232}Th concentrations are estimated to be ±2% due to uncertainties in spike concentration; analytical uncertainties are smaller. **Date Uncorr.** indicates that no correction has been made for initial ^{230}Th. **Date Corr.** are corrected for initial detrital ^{230}Th assuming an initial ^{230}Th/^{232}Th of $8.0\pm4.0\times10^{-6}$ (Section 5.3), and are reported relative to Before Present (BP), in which the present is defined as January 1, 1950. Decay constants for ^{230}Th and ^{234}U are from Cheng et al. (2013a); decay constant for ^{238}U is 1.55125×10^{-10} yr^{-1} (Jaffey et al., 1971). See Eqs. 2.1–2.3 for equations for the calculation of dates. See Eq. 2.2 for the calculation of $\delta^{234}U_{\text{initial}}$ and Section 2.10.4 for the calculation of $\delta^{234}U_{\text{iac}}$.

Samp. ID	Rep. ID	^{238}U (ng/g)	^{232}Th (ng/g)	$\delta^{234}U_m$ (‰)	[^{230}Th/^{238}U]	^{230}Th/^{232}Th	Date Uncorr. (yrs)	Date Corr. (yrs BP)	$\delta^{234}U_{\text{initial}}$ (‰)	$\delta^{234}U_{\text{iac}}$ (‰)
Replicate Analyses of Passing Samples										
F9	F9(1)	2831±57	97.5±2.0	2356.7±1.1	0.07300±0.00060	33.67±0.29	2392±20	1830±280	2368.9±2.2	2391±13
	F9(2)	2940±59	147.4±3.0	2354.87±0.95	0.07805±0.00082	24.71±0.26	2560±27	1740±410	2366.5±2.9	2399±19
	F9(3)	2962±59	127.8±2.6	2353.5±1.1	0.07708±0.00082	28.36±0.30	2529±27	1820±360	2365.6±2.6	2394±16
F14	F14(1)	737±15	26.29±0.53	2635.37±0.68	0.28880±0.00099	128.59±0.49	8942±32	8410±270	2698.7±2.2	2725±15
	F14(2)	715±14	29.16±0.59	2640.01±0.82	0.2838±0.0016	110.42±0.62	8769±50	8160±310	2701.5±2.5	2732±17
	F14(3)	725±15	28.26±0.57	2652.8±6.3	0.2823±0.0014	114.98±0.57	8690±46	8110±290	2714.3±6.8	2743±21
	F14(4)	611±12	17.08±0.34	2625.96±0.69	0.27407±0.00084	155.78±0.42	8494±27	8080±210	2686.5±1.7	2707±12
	F14(s)	292±5.8	5.48±0.11	2636.3±3.6	0.1765±0.0012	149.3±1.3	5395±39	5110±150	2674.6±3.8	2688±11
F15	F15(1)	1000±20	119.7±2.4	2694.2±2.2	0.3748±0.0019	49.72±0.23	11524±61	9770±890	2769.5±7.3	2863±53
	F15(2)	997±20	99.0±2.0	2741.1±1.0	0.3624±0.0019	57.96±0.30	10980±61	9540±730	2815.9±5.9	2894±44
	F15(3)	944±19	96.9±1.9	2728.17±0.97	0.3621±0.0022	55.96±0.33	11010±70	9520±760	2802.4±6.1	2883±46
F16	F16(1)	1259±25	353.7±7.1	2546.1±1.6	0.4304±0.0049	24.33±0.28	13900±170	9600±2200	2616±17	2830±130
	F16(2)	1048±21	155.4±3.1	2717.5±6.4	0.4197±0.0025	44.96±0.22	12884±83	10700±1100	2801±11	2919±69
C16	C16(1)	1305±26	205.5±4.1	2084.2±2.5	0.4278±0.0024	43.12±0.23	16021±96	13300±1400	2163.6±9.0	2261±59
	C16(2)	1673±33	258.2±5.2	2088.26±0.47	0.4159±0.0023	42.78±0.22	15529±90	12800±1400	2165.2±8.4	2260±57
	C16(3)	1773±35	264.5±5.3	2083.6±3.8	0.4105±0.0023	43.69±0.23	15338±95	12700±1300	2159.8±9.0	2251±56
D4	D4(1)	1946±39	500±10	1930.39±0.61	0.4514±0.0034	27.87±0.20	17920±140	13100±2500	2003±14	2154±95
	D4(2)	2073±41	520±10	1929.5±2.5	0.4549±0.0033	28.78±0.21	18070±140	13400±2400	2004±14	2151±92
	D4(3)	1943±39	489.1±9.8	1935.47±0.82	0.4508±0.0038	28.44±0.24	17860±160	13200±2400	2009±14	2157±92

Table 2.4 continued from previous page

Samp. ID	Rep. ID	^{238}U (ng/g)	^{232}Th (ng/g)	$\delta^{234}U_m$ (‰)	[^{230}Th/^{238}U]	^{230}Th/^{232}Th	Date Uncorr. (yrs)	Date Corr. (yrs BP)	$\delta^{234}U_{initial}$ (‰)	$\delta^{234}U_{iac}$ (‰)
	D4(4)	1916±38	477.4±9.6	1942±1.2	0.4438±0.0040	28.28±0.25	17520±170	12900±2400	2014±14	2161±92
K16	K16(1)	3861±77	2049±41	1768±1.0	1.5022±0.0068	44.95±0.19	77570±470	68000±5100	2142±31	2500±240
	K16(4)	2258±45	1257±25	1750.7±2.2	1.520±0.017	43.35±0.48	79500±1200	69300±5500	2129±33	2510±250
	K16(5)	2357±47	1267±25	1713.3±1.9	1.506±0.016	44.48±0.48	80100±1200	70100±5400	2088±32	2450±240
	K16(6)	2293±46	1266±25	1746.5±1.9	1.524±0.017	43.81±0.48	79900±1200	69800±5500	2127±33	2500±250
	K16(7)	2290±46	1294±26	1746.9±1.8	1.509±0.017	42.39±0.48	78900±1200	68500±5600	2120±34	2510±260
L1	L1(2)	3570±71	1984±40	1780.6±1.1	1.6487±0.0075	47.09±0.21	87550±560	77700±5200	2217±33	2610±260
	L1(5)	2358±47	1113±22	1772.4±2.0	1.528±0.015	51.40±0.49	79200±1000	70700±4600	2164±28	2480±210
	L1(6)	2314±46	1106±22	1774.2±1.9	1.529±0.015	50.79±0.51	79200±1100	70600±4600	2166±28	2490±210
	L1(7)	2381±48	1115±22	1772.8±1.8	1.473±0.015	49.91±0.50	75350±1000	66800±4500	2141±28	2450±200
	L1(8)	2403±48	1171±24	1773.6±2.3	1.499±0.015	48.83±0.50	77100±1100	68300±4700	2151±29	2480±220
D6	D6(1)	1091±22	841±17	1347.5±1.2	2.209±0.013	45.48±0.27	193800±2600	180000±7900	2240±50	2840±420
	D6(2)	1070±21	806±16	1385.4±1.7	2.291±0.013	48.28±0.26	202300±2700	189400±7500	2364±50	2980±430
	D6(3)	1259±25	1141±23	1212.9±2.7	2.151±0.027	37.69±0.47	211600±6500	194000±12000	2100±69	2790±520
	D6(4)	1283±26	1104±22	1241.5±2.0	2.111±0.026	38.94±0.47	196100±5400	180000±11000	2061±62	2690±470
	D6(5)	1288±26	1103±22	1252.2±1.8	2.117±0.018	39.23±0.33	195000±3800	178700±9800	2074±58	2710±470
M1	M1(1)	2505±50	427.0±8.5	935.7±2.0	2.1324±0.0049	198.65±0.37	327100±3600	324300±3900	2337±26	2451±85
	M1(2)	2497±50	411.7±8.2	938.4±1.1	2.1321±0.0046	205.34±0.34	324700±3100	322000±3400	2328±23	2438±78
	M1(3)	2496±50	417.4±8.4	936.29±0.6	2.1351±0.0044	202.73±0.29	328400±2900	325600±3300	2347±22	2459±78
	M1(4)	2582±52	462.2±9.2	933.7±1.0	2.1213±0.0050	188.15±0.35	321600±3300	318600±3600	2295±24	2412±84
M3	M3(1)	1828±37	373.8±7.5	1004.66±0.81	2.2154±0.0051	172.03±0.31	324600±3200	321300±3600	2488±25	2635±99
	M3(2)	1820±36	384.4±7.7	1010.6±2.2	2.2234±0.0051	167.10±0.27	324900±3500	321600±4000	2504±29	2660±110
	M3(3)	1854±37	410.1±8.2	991.3±1.2	2.2034±0.0051	158.19±0.28	327600±3300	324100±3800	2474±27	2630±110
	M3(4)	1599±32	342.6±6.9	993.9±5.6	2.207±0.011	163.54±0.69	328000±8300	324500±8500	2484±61	2640±160
	M3(5)	1596±32	366.7±7.4	997.2±4.0	2.213±0.011	152.93±0.70	328700±7700	325000±8000	2496±58	2660±160
J8	J8(1)	2590±52	315.1±6.3	987.7±1.6	2.1837±0.0041	285.00±0.34	318300±2700	316300±2900	2412±20	2494±62
	J8(2)	2607±52	328.0±6.6	988.5±1.6	2.1862±0.0046	275.81±0.43	319300±3000	317200±3100	2420±22	2506±66
	J8(3)	2782±56	379.5±7.6	979.8±1.3	2.1785±0.0043	253.53±0.34	321100±2800	318900±3000	2410±21	2503±68

Table 2.4 continued from previous page

Samp. ID	Rep. ID	^{238}U (ng/g)	^{232}Th (ng/g)	$\delta^{234}U_m$ (‰)	[^{230}Th/^{238}U]	^{230}Th/^{232}Th	Date Uncorr. (yrs)	Date Corr. (yrs BP)	$\delta^{234}U_{initial}$ (‰)	$\delta^{234}U_{iac}$ (‰)
J9	J9(1)	3055±61	1156±23	810.79±0.64	1.9655±0.0064	82.48±0.25	320700±4500	313500±5900	1964±33	2190±160
	J9(2)	3058±61	1191±24	804.54±0.79	1.9548±0.0060	79.71±0.22	318700±4100	311200±5700	1936±31	2170±160
	J9(3)	3064±61	1192±24	807.1±1.3	1.9547±0.0058	79.79±0.20	316600±4000	309100±5700	1931±31	2160±160
E12	E12(1)	907±18	845±17	664.1±2.8	1.890±0.014	32.23±0.27	454000±31000	437000±34000	2280±220	3060±810
	E12(2)	913±18	821±16	663.9±2.8	1.880±0.012	33.20±0.21	436000±23000	419000±26000	2170±160	2870±650
	E12(3)	977±20	1053±21	606.4±3.5	1.779±0.035	26.22±0.52	397000±54000	373000±59000	1740±300	2500±1000
	E12(4)	991±20	1024±21	599.3±4.5	1.780±0.034	27.34±0.52	412000±60000	390000±64000	1800±340	2500±1100
	E12(5)	976±20	975±20	620.7±3.5	1.809±0.033	28.74±0.52	414000±56000	393000±60000	1880±330	2600±1100
F4	F4(1)	1006±20	116.2±2.3	818.5±2.1	2.0592±0.0054	283.16±0.61	394900±7100	393000±7200	2482±51	2560±110
	F4(2)	1003±20	115.9±2.3	811.9±2.2	2.0516±0.0049	281.86±0.51	396300±6800	394400±6900	2471±49	2550±110
	F4(3)	1140±23	122.3±2.4	822.0±1.1	2.0557±0.0044	304.29±0.52	385700±5000	384000±5100	2430±35	2503±83
	F4(4)	1157±23	122.1±2.4	813.5±1.8	2.0545±0.0057	309.03±0.78	397200±7400	395400±7400	2484±53	2560±120
	F4(5)	1154±23	123.2±2.5	818.6±1.9	2.0638±0.0064	306.99±0.87	400200±8300	398400±8400	2520±60	2600±130
B5	B5(1)	1693±34	352.7±7.1	494.4±2.1	1.6751±0.0050	127.68±0.30	503000±21000	499000±21000	2020±120	2150±270
	B5(2)	1702±34	393.9±7.9	488.2±1.1	1.6745±0.0052	114.89±0.33	536000±25000	532000±26000	2190±160	2340±360
	B5(3)	1687±34	355.4±7.1	488.7±2.5	1.6726±0.0087	126.04±0.63	525000±41000	521000±41000	2130±250	2250±540
	B5(4)	1690±34	354.2±7.1	490.6±2.2	1.6727±0.0088	126.71±0.65	514000±37000	510000±38000	2070±230	2200±480
	B5(5)	1721±34	362.0±7.3	486.7±3.6	1.6686±0.0098	125.93±0.69	519000±46000	515000±47000	2090±280	2210±610
B11	B11(1)	2501±50	331.3±6.6	447.3±1.2	1.6230±0.0041	194.52±0.37	567000±28000	565000±28000	2200±180	2290±370
	B11(2)	2501±50	318.5±6.4	445.21±0.84	1.6214±0.0043	202.18±0.46	576000±30000	574000±30000	2250±190	2330±400
	B11(3)	2787±56	389.2±7.8	445.3±2.8	1.6149±0.0048	183.58±0.47	538000±31000	535000±31000	2020±180	2100±380
	B11(4)	2819±56	374.2±7.5	437.9±1.9	1.6049±0.0053	191.98±0.59	540000±30000	537000±30000	1990±180	2070±370
B13	B13(1)	1280±26	131.9±2.6	468.4±1.1	1.6559±0.0041	255.10±0.46	588000±31000	587000±31000	2450±220	2520±450
	B13(2)	1218±24	116.1±2.3	471.6±4.9	1.6556±0.0059	275.87±0.65	558000±51000	557000±52000	2270±340	2330±710
	B13(3)	1401±28	145.5±2.9	471.25±0.86	1.6568±0.0036	253.31±0.46	568000±23000	567000±23000	2330±150	2400±320
	B13(5)	1372±27	141.3±2.8	466.9±3.0	1.6605±0.0053	256.07±0.72	645000±74000	644000±74000	2870±630	3000±1300

Replicate Analyses of Failing Samples

Table 2.4 continued from previous page

Samp. ID	Rep. ID	^{238}U (ng/g)	^{232}Th (ng/g)	$\delta^{234}U_{m}$ (‰)	[^{230}Th/^{238}U]	^{230}Th/^{232}Th	Date Uncorr. (yrs)	Date Corr. (yrs BP)	$\delta^{234}U_{initial}$ (‰)	$\delta^{234}U_{iac}$ (‰)
P10	P10(1)	726±15	800±16	794.4±1.5	0.543±0.013	7.83±0.18	38300±1000	-1000±25000	792±57	1130±360
	P10(2)	772±15	874±18	791.2±1.0	0.536±0.013	7.52±0.18	37700±1100	-3000±26000	785±59	1130±380
L3	L3(1)	619±12	1118±23	719.6±3.0	1.621±0.025	14.25±0.22	210400±8200	152000±47000	1100±150	2200±1300
G1	G1(1)	851±17	1230±130	673.8±2.0	1.190±0.120	13.1±1.9	121000±21000	67000±46000	810±110	1340±660
G2	G2(1)	1167±23	1485±30	1504.84±0.76	1.720±0.020	21.46±0.25	109200±2000	83000±16000	1900±86	2910±860
	G2(2)	1161±23	1386±28	1488.7±2.8	1.681±0.020	22.37±0.26	106600±1900	82000±15000	1875±79	2780±750
G5	G5(1)	635±13	1395±28	966.7±1.7	2.162±0.040	15.61±0.29	321000±25000	275000±43000	2100±260	5200±4200
G6	G6(1)	435.9±8.7	792±16	1041.8±2.3	1.902±0.025	16.62±0.22	195100±5800	150000±32000	1590±150	3200±1700
	G6(2)	315.3±6.3	614±12	1772.4±6.1	2.567±0.029	20.93±0.23	182200±4300	150000±21000	2710±160	5800±3400
	G6(3)	316.0±6.3	639±13	1777.8±1.8	2.586±0.031	20.30±0.24	184300±4600	151000±22000	2720±170	6100±3900
	G6(4)	336.2±6.7	721±14	1741.8±4.0	2.539±0.033	18.79±0.24	182500±4900	146000±24000	2630±180	6300±4600
G7	G7(1)	414.1±8.3	831±17	955.3±5.9	1.831±0.025	14.48±0.19	199500±6400	144000±43000	1440±180	3200±2200
	G7(2)	426.5±8.5	839±17	925.6±3.7	1.768±0.024	14.27±0.19	191400±5800	135000±44000	1360±170	2900±1900
	G7(3)	413.7±8.3	818±16	915.1±6.0	1.784±0.024	14.32±0.19	198100±6300	142000±44000	1370±180	3000±2000
G8	G8(1)	861±17	2362±48	621.9±3.9	1.986±0.035	11.50±0.20	–	–	–	–
M15	M15(1)	327.4±6.5	38.91±0.78	2306.98±0.78	2.2407±0.0058	299.35±0.64	105080±410	103470±910	3089.3±8.0	3193±58
	M15(2)	313.5±6.3	35.45±0.71	2310.06±0.98	2.2675±0.0057	318.39±0.64	106800±400	105280±870	3109.2±7.7	3208±56
	M15(3)	322.6±6.5	42.20±0.85	2300.3±1.5	2.1937±0.0065	266.23±0.65	102160±450	100400±1000	3053.5±8.9	3166±64
	M15(4)	327.3±6.5	36.66±0.73	2294.4±1.5	2.1731±0.0055	308.04±0.61	101030±380	99490±860	3038.2±7.6	3134±54
L7	L7(1)	6960±140	383.1±7.8	1690±1.4	1.8670±0.0044	538.4±2.5	110430±410	109510±620	2302.0±4.4	2337±21
	L7(2)	6430±130	372.4±7.6	1686.3±1.5	1.7499±0.0042	479.5±2.0	100410±370	99420±620	2232.4±4.4	2268±22
	L7(3)	7340±150	451.5±9.2	1691.47±0.64	1.9770±0.0046	510.6±1.9	120680±450	119670±680	2371.0±4.6	2411±24
	L7(4)	6460±130	392.9±8.0	1687.04±0.74	1.8028±0.0041	470.4±1.9	104900±360	103870±630	2261.7±4.2	2300±23
	L7(5)	6920±140	417.7±8.4	1692.2±1.5	1.8034±0.0041	474.2±1.3	104640±370	103620±630	2267.1±4.5	2305±23
	L7(6)	6590±130	388.6±7.8	1682.24±0.70	1.8101±0.0040	487.5±1.2	105840±350	104850±610	2261.5±4.0	2298±22
	L7(7)	6900±140	393.6±7.9	1684.15±0.78	1.7943±0.0047	499.6±1.4	104340±420	103370±640	2254.6±4.2	2290±22

Table 2.4 continued from previous page

Samp. ID	Rep. ID	^{238}U (ng/g)	^{232}Th (ng/g)	δ^{234}U$_{\mathrm{m}}$ (‰)	[^{230}Th/^{238}U]	^{230}Th/^{232}Th	Date Uncorr. (yrs)	Date Corr. (yrs BP)	δ^{234}U$_{\mathrm{initial}}$ (‰)	δ^{234}U$_{\mathrm{iac}}$ (‰)
D7	D7(1)	850±17	1029±21	1310.5±1.5	2.322±0.020	30.45±0.26	227500±5100	206000±13000	2344±89	3500±940
	D7(2)	825±17	965±19	1346.2±1.7	2.339±0.019	31.76±0.25	222000±4600	202000±13000	2378±85	3490±890
D11	D11(1)	365.0±7.3	725±64	289.1±1.1	1.330±0.110	10.7±1.3	–	–	–	–
	D11(2)	419.7±8.4	1025±21	278.7±2.1	1.493±0.039	9.71±0.26	–	–	–	–
D12	D12(1)	228.8±4.6	456.0±9.2	596.8±1.8	1.829±0.036	14.57±0.29	–	–	–	–
	D12(2)	294.8±5.9	424.9±8.5	806.1±1.5	2.080±0.024	22.91±0.26	447000±42000	424000±46000	2670±360	4400±1900
D13	D13(1)	161.4±3.2	204.2±4.1	862.8±2.5	2.168±0.018	27.20±0.22	467000±35000	448000±38000	3060±340	4700±1600
	D13(2)	161.8±3.2	210.5±4.2	851.3±1.8	2.087±0.022	25.46±0.27	378000±23000	354000±28000	2310±180	3600±1200
	D13(3)	180.4±3.6	233.1±4.7	755.1±2.2	1.979±0.021	24.31±0.26	399000±28000	375000±33000	2180±210	3400±1100
D14	D14(1)	291.2±5.8	299.1±6.0	1022.3±1.6	2.691±0.014	41.60±0.21	–	–	–	–
	D14(2)	282.0±5.6	282.1±5.7	1016.1±2.3	2.634±0.014	41.82±0.21	–	–	–	–
J5	J5(1)	1310±26	411.7±8.2	946.8±1.7	2.0688±0.0067	104.48±0.27	284200±3300	278500±4500	2078±27	2270±130
	J5(2)	1383±28	336.9±6.8	1031.87±0.62	2.1567±0.0078	140.58±0.54	277800±3300	273600±4000	2233±25	2390±110
	J5(3)	1238±25	285.7±5.7	1032.3±1.5	2.1597±0.0059	148.57±0.32	278800±2600	274800±3300	2242±21	2393±99
	J5(4)	1518±30	473.5±9.5	997.5±1.4	2.1404±0.0054	108.97±0.22	289100±2700	283600±3900	2221±25	2430±130
J6	J6(1)	1110±22	348.2±7.0	1019±1.9	2.1544±0.0089	109.03±0.40	283500±4100	278100±5000	2234±32	2440±140
	J6(2)	1247±25	402.2±8.0	1021±1.2	2.1230±0.0057	104.53±0.24	269200±2400	263400±3800	2147±23	2350±130
	J6(3)	1248±25	416.3±8.3	1010.8±1.6	2.1089±0.0061	100.38±0.25	268300±2600	262300±4100	2119±25	2330±140
J7	J7(1)	2526±51	383.5±7.7	1027.16±0.9	2.1421±0.0041	224.01±0.27	274000±1800	271400±2200	2209±14	2305±62
	J7(2)	2408±48	396.1±7.9	1027.4±1.1	2.1816±0.0047	210.61±0.33	291400±2300	288600±2700	2320±18	2429±72
J10	J10(2)	1798±36	2117±42	789.80±0.77	1.977±0.016	26.66±0.21	351000±14000	327000±20000	1990±110	2930±800
K1	K1(1)	659±13	654±13	571.8±1.4	1.798±0.014	28.76±0.23	568000±84000	552000±87000	2720±710	3700±2100
A5	A5(1)	2260±45	1479±30	737.1±1.3	1.938±0.013	47.01±0.31	379000±14000	366000±16000	2073±96	2520±380
	A5(2)	2464±49	1513±30	764.48±0.95	1.876±0.010	48.50±0.25	299700±6300	286700±9500	1717±46	2060±260
A6	A6(2)	2442±49	1117±22	812.2±1.9	1.9609±0.0081	68.09±0.28	316400±5600	307500±7400	1935±41	2210±200
	A6(3)	2376±48	1086±22	825.1±1.3	2.0697±0.0083	71.91±0.27	396900±9900	389000±11000	2477±76	2830±280
	A6(4)	2737±55	1227±25	820.6±2.2	1.9575±0.0087	69.31±0.28	307500±5600	298700±7300	1907±40	2170±190
F13	F13(1)	339.3±6.8	308.3±6.2	380.6±2.0	1.499±0.013	26.20±0.22	442000±36000	418000±40000	1240±150	1640±500

Table 2.4 continued from previous page

Samp. ID	Rep. ID	^{238}U (ng/g)	^{232}Th (ng/g)	$\delta^{234}U_m$ (‰)	$[^{230}Th/^{238}U]$	$^{230}Th/^{232}Th$	Date Uncorr. (yrs)	Date Corr. (yrs BP)	$\delta^{234}U_{initial}$ (‰)	$\delta^{234}U_{iac}$ (‰)
	F13(2)	339.2±6.8	265.6±5.3	467.8±2.6	1.606±0.015	32.57±0.30	417000±31000	398000±34000	1440±140	1830±460
	F13(3)	342.1±6.8	278.5±5.6	469.4±1.7	1.611±0.014	31.41±0.26	422000±29000	403000±32000	1460±140	1880±460
	F13(4)	330.7±6.6	260.6±5.2	472.6±1.8	1.621±0.013	32.66±0.27	434000±30000	416000±33000	1530±150	1940±480
B2	B2(1)	516±10	615±12	416.5±2.1	1.565±0.017	20.84±0.22	494000±68000	465000±75000	1550±340	2300±1200
G13	G13(1)	728±15	166.4±3.3	428.3±1.8	1.5828±0.0049	109.95±0.31	501000±22000	496000±22000	1740±110	1850±240
	G13(2)	727±15	163.0±3.3	426.5±2.1	1.5877±0.0052	112.52±0.32	533000±30000	528000±30000	1900±160	2020±360
	G13(3)	742±15	155.6±3.1	445.6±5.7	1.640±0.010	124.22±0.68	–	–	–	–
	G13(4)	737±15	153.6±3.1	445.3±2.1	1.6200±0.0082	123.40±0.60	566000±56000	563000±56000	2180±360	2310±770
G14	G14(1)	3066±61	211.1±4.2	465.4±1.8	1.6273±0.0046	375.25±0.92	477000±16000	476000±16000	1784±84	1820±170
	G14(2)	3101±62	201.0±4.0	463.2±1.0	1.6290±0.0037	399.07±0.58	493000±14000	492000±14000	1855±73	1890±150
H6	H6(1)	1115±22	918±18	364.6±1.7	1.648±0.016	31.79±0.30	–	–	–	–
	H6(2)	1288±26	891±18	378.4±2.9	1.523±0.012	34.95±0.27	547000±82000	532000±85000	1700±430	2100±1100
	H6(3)	1161±23	852±17	380.1±1.6	1.531±0.012	33.11±0.25	580000±110000	570000±120000	1900±690	2400±1700
H7	H7(1)	893±18	565±11	404.74±0.75	1.607±0.012	40.31±0.30	–	–	–	–
	H7(2)	1003±20	597±12	413.5±1.5	1.551±0.010	41.34±0.26	463000±31000	449000±33000	1470±140	1750±390
	H7(3)	988±20	675±14	405.4±1.7	1.5410±0.0110	35.85±0.26	466000±37000	449000±39000	1440±160	1770±460
	H7(4)	989±20	589±12	412.8±2.2	1.5452±0.0099	41.20±0.26	448000±28000	434000±30000	1400±120	1680±350
B14	B14(1)	1676±34	739±15	410.00±0.93	1.5156±0.0067	54.60±0.24	392000±12000	380000±14000	1200±47	1360±160
	B14(2)	1664±33	614±12	433.5±1.1	1.5425±0.0064	66.35±0.26	385000±11000	376000±12000	1251±43	1390±130
	B14(3)	1669±33	727±15	413.2±2.8	1.557±0.015	56.78±0.54	482000±57000	472000±58000	1570±270	1780±620
	B14(4)	1730±35	712±14	411.5±4.2	1.480±0.014	57.15±0.53	338000±18000	327000±19000	1035±58	1170±160
B15	B15(1)	477±10	155.4±3.1	373.5±1.9	1.4102±0.0058	68.70±0.30	314400±6400	304500±8300	882±21	968±82
	B15(2)	482±10	171.7±3.4	375.8±2.1	1.4136±0.0061	62.94±0.27	314900±6900	304000±9000	886±23	982±91
	B15(3)	471.0±9.4	149.8±3.0	375.3±3.6	1.416±0.011	70.72±0.55	318000±13000	309000±14000	897±37	980±100
	B15(4)	488±10	167.1±3.4	367.4±4.3	1.400±0.015	64.94±0.62	311000±16000	301000±17000	859±43	950±120
C1	C1(1)	1628±33	442.8±8.9	375.2±3.3	1.5121±0.0058	88.27±0.30	513000±35000	508000±35000	1570±160	1700±360
	C1(2)	1582±32	431.3±8.6	374.6±1.4	1.5083±0.0048	87.83±0.25	500000±22000	494000±23000	1509±98	1630±230
	C1(3)	865±17	276.2±5.5	385.3±5.4	1.389±0.012	69.06±0.55	283000±11000	273000±12000	831±31	911±93

Table 2.4 continued from previous page

Samp. ID	Rep. ID	^{238}U (ng/g)	^{232}Th (ng/g)	δ^{234}U$_{\mathrm{m}}$ (‰)	[^{230}Th/^{238}U]	^{230}Th/^{232}Th	Date Uncorr. (yrs)	Date Corr. (yrs BP)	δ^{234}U$_{\mathrm{initial}}$ (‰)	δ^{234}U$_{\mathrm{iac}}$ (‰)
	C1(4)	839±17	177.9±3.6	383.8±4.9	1.3509±0.0089	101.12±0.62	256800±6800	250000±7700	777±20	825±58
C3	C3(2)	3557±71	687±14	372.94±0.95	1.5058±0.0059	123.71±0.48	499000±26000	495000±26000	1510±110	1590±240
	C3(3)	3460±69	659±13	375.8±2.5	1.5228±0.0045	126.96±0.27	569000±40000	566000±41000	1850±220	1960±470
C6	C6(1)	361.3±7.2	422.6±8.5	258.6±2.8	1.346±0.016	18.27±0.22	490000±92000	450000±100000	930±280	1360±920
C10	C10(1)	381.9±7.6	267.9±5.4	414.3±1.6	1.525±0.010	34.51±0.22	398000±19000	379000±23000	1208±79	1490±290
	C10(2)	382.6±7.7	256.7±5.2	518.2±3.8	1.659±0.012	39.25±0.29	392000±21000	376000±23000	1497±100	1830±340
	C10(3)	379.9±7.6	218.5±4.4	515.5±1.9	1.6498±0.0099	45.53±0.27	384000±15000	370000±17000	1465±71	1740±250
	C10(4)	404.4±8.1	271.5±5.5	443.1±1.5	1.552±0.011	36.70±0.27	380000±18000	362000±21000	1232±74	1510±270
	C10(5)	431.3±8.6	277.9±5.6	427.2±1.6	1.530±0.011	37.71±0.27	379000±18000	361000±21000	1184±70	1440±250
	C10(6)	431.7±8.6	295.1±5.9	434.9±1.9	1.555±0.012	36.13±0.27	404000±23000	387000±25000	1296±94	1590±320
	C10(7)	483±10	325.0±6.5	433.1±2.6	1.528±0.012	36.02±0.28	364000±17000	345000±20000	1147±67	1400±250
	C10(8)	443.3±8.9	290.6±5.8	436.4±1.4	1.519±0.011	36.80±0.27	347000±14000	329000±17000	1104±55	1340±230
C11	C11(1)	1781±36	346.6±6.9	467.3±1.1	1.6278±0.0045	132.84±0.32	471000±14000	467000±14000	1747±71	1850±160
	C11(2)	1746±35	331.6±6.7	472.91±0.98	1.6480±0.0063	137.73±0.54	514000±26000	510000±26000	2000±150	2110±330
C13	C13(1)	1229±25	387.3±7.8	321.3±1.9	1.3946±0.0052	70.28±0.24	385000±11000	376000±12000	928±33	1015±98
	C13(2)	1281±26	378.0±7.6	322.1±1.5	1.3899±0.0048	74.77±0.22	374500±9000	366000±10000	904±27	983±84
	C13(3)	1214±24	322.1±6.5	341.3±2.6	1.4390±0.0098	86.11±0.58	424000±26000	417000±27000	1106±86	1190±190
	C13(4)	1180±24	334.8±6.7	336.1±3.6	1.434±0.011	80.24±0.59	429000±31000	421000±32000	1100±100	1200±230
C14	C14(1)	2133±43	516±10	367.09±0.91	1.5908±0.0047	104.35±0.25	–	–	–	–
	C14(2)	2136±43	533±11	361.7±1.2	1.5855±0.0049	100.87±0.26	–	–	–	–

2.10 Supplementary Materials

2.10.1 Methods of U-Th measurements on materials from 1996 piston core

U-Th measurements on materials from the 1996 core were performed at the University of Minnesota. For the first set of samples, processed in approximately 1999, mollusc shell fragments were removed prior to chemical processing. For the second set processed in 2011, mollusc shell fragments were not comprehensively removed. Sample preparation was identical to the procedures described in Section 2.3.2. Samples for the first set were analyzed on a Finnigan Element I using methods described in Shen et al. (2002). Samples for the second set were analyzed using a ThermoScientific Neptune multi-collector ICP-MS in peak-jumping mode using methods described in Shen et al. (2012) and Cheng et al. (2013a).

2.10.2 Methods of other datasets used to interpret U-Th data

Elemental concentration data. We measured 55 sediment samples for elemental concentrations of Ca, Mg, Sr, Al, Ti, P, V, Mn, and Fe. Samples of ∼1–2 mg in weight were dissolved and diluted in 3% HNO_3 and then measured on an Agilent 7900 ICP-MS at the MIT Center for Environmental and Health Sciences. Sample analyses were bracketed by a multi-element standard. Two measurements each were also made on two certified multi-element reference standards, PACS-2 and BCR-2. Data were corrected for blank intensities. Uncertainties for each element were determined by calculating the average percent difference between recommended values and measured values in PACS-2 and BCR-2, and then applying the larger percent difference on measured sample values. For example, the average percent difference between measured and recommended values in Mg (wt %) was 6% for PACS-2 and 2% for BCR-2; thus, all Mg measurements for samples were assigned an uncertainty of 6% of the measured Mg value. Of the 55 samples analyzed, 48 corresponded to U-Th analyses.

Total Inorganic Carbon/Total Organic Carbon. We measured weight percentage total carbon (TC) and weight percentage total inorganic carbon (TIC) by coulometry. For the measurement of TC, we combusted samples at 1000°C using a UIC 5200 automated furnace, and analyzed the resultant CO_2 by coulometry using a UIC 5014 coulometer. Similarly, we measured TIC by acidifying samples with 10% H_3PO_4 using an Automate acidification module and measured the resultant CO_2 by coulometry. We calculated weight percentage total organic carbon (TOC) from TOC = TC–TIC; weight percentage TIC was converted to percent calcite based on stoichiometry.

Color reflectance spectrophotometry. Color reflectance data were measured using a Geotek multi-sensor automated core logger (MSCL-XYZ) on split core sections at LacCore. To calculate sediment optical lightness, we took the sum total of light in the visible region of the electromagnetic spectrum, between 400 and 700 nm, following Balsam et al. (1999).

Mineralogy. In order to characterize the carbonate mineralogy of the drill core and to discern possible mineralogical differences between endogenic and detrital $CaCO_3$, 25 samples were selected from intervals with variable $CaCO_3$ abundance (0–85%) from throughout the core. In addition, 6 samples of carbonate bedrock from within the Junín drainage basin on both the eastern and western sides of the lake were also analyzed. All samples were pretreated with 35% H_2O_2 and 1M NaOH to remove organic matter and biogenic silica, respectively. Samples were then disaggregated with a solution of NaO_3P combined with ultrasonication, and then washed through 53 and 25 µm sieves to isolate fractions >53 µm, 25–53 µm, and, <25 µm. These fractions were then scanned on a Phillips PW 1840 diffractometer at 45 kW and 35 mA. Each subsample was scanned twice, wide scans were conducted at 0.6° (2Θ) per minute from 4.0–70° (2Θ) whereas narrow, more focused, scans were performed at 0.3° per minute from 28.0–31.0°.

Ostracode assemblage analysis. A total of 22 sediment samples corresponding to U-Th analyses were selected for ostracode analysis. One 0.25-g aliquot per sample was removed for most ostracode analyses. Prior to sieving, samples were gently disaggregated with three freeze/thaw cycles, since sediments were densely compacted. Then, samples were wet-sieved using a 63 µm sieve. Ostracodes were extracted with fine brushes, identified and enumerated with respect to numbers per 0.25 g dry sediment. Analysis was done using a Leica M80 stereo-microscope. Adult and juvenile intact and broken valves were differentiated. Broken valves were counted if >50% was encountered and when identification was still possible. Fossil ostracodes were identified down to family level following procedures described in Pérez et al. (2010) and Karanovic (2012).

Additionally, we made a brief sediment description that included information of other fauna, vegetation and minerals found in the observed sediment samples.

We calculated different ratios to facilitate taphonomy interpretations and for a better understanding of processes such as remineralization and reworking in samples. The broken:intact (B:I) ratio was calculated for each sample to identify samples with relatively high numbers of broken shells. Similarly the adult:juvenile (A:I) ratio was used to identify samples with a high number of adult valves, that could indicate transportation of the lighter juvenile valves to deeper waters. The nektobenthic:benthic (NB:B) was calculated to evaluate shifts in the relative abundance of bottom-swimming versus bottom-dwelling individuals.

Shell coloration was taken into account as well when enumerating ostracode shells. We were able to distinguish 7 different shell colorations: 1. Translucent, 2. White, 3. Partly light grey, 4. Completely light grey, 5. Partly dark grey, 6. Completely dark grey, 7. Completely black. Additionally, we used a Scanning Electron Microscope (SEM) TM3000 Hitachi with BSE Detector II for taking pictures of uncoated specimens to facilitate ostracode identification and to detect elements of ostracode shells using EDX analysis. All ostracode analyses were conducted at the Institut für Geosysteme und Bioindikation (IGeo) of TU-Braunschweig.

Comparison of other data to U-Th data. All comparisons between different datasets were carried out with MATLAB scripts written by CYC.

2.10.3 Failure to build isochrons

As mentioned in Section 5.3, determining dates from isochron plots failed (high MSWD and low probabilities of fit). We used the Isoplot program by Ludwig (2012) to generate isochron plots of various replicate analyses from bulk sample material, as well as analyses from adjacent clean-dirty sample pairs. The failure to build isochrons is further evidence of the existence of open system behavior occurring in these sediments. Figs. 2-18–2-28 show the results of our isochron building attempts.

2.10.4 Calculation of $\delta^{234}U_{iec}$

We assume that the detrital component has activity ratios essentially at secular equilibrium: $[^{234}\mathrm{U}/^{238}\mathrm{U}]_{\mathrm{det}} = 1.0 \pm 0.5$ and $[^{232}\mathrm{Th}/^{238}\mathrm{U}]_{\mathrm{det}} = 1.2 \pm 0.6$, following those used by Dutton et al. (2017). First, we calculate the fraction of uranium that is detrital in each sample (f_{det}):

$$f_{det} = [^{232}\mathrm{Th}]_{\mathrm{samp}} \times \frac{1}{[^{232}\mathrm{Th}/^{238}\mathrm{U}]_{\mathrm{det}}} \times [^{238}\mathrm{U}]_{\mathrm{samp}}$$

where brackets indicate activities, *samp* refers to the sample data, *det* refers to the detrital component. We then convert the initial [^{234}U/^{238}U] of the sample to $\delta^{234}U_{iec}$ with the following formula:

$$\delta^{234}\mathrm{U_{iec}} = \left(\frac{[^{234}\mathrm{U}/^{238}\mathrm{U}]^{\mathrm{init}}_{\mathrm{samp}} - [^{234}\mathrm{U}/^{238}\mathrm{U}]_{\mathrm{det}} \times f_{det}}{1 - f_{det}} - 1 \right) \times 1000$$

We propagate the uncertainties of the original measured $[^{238}\mathrm{U}]_{\mathrm{samp}}$, $[^{232}\mathrm{U}]_{\mathrm{samp}}$, and detrital activity ratios for the uncertainty of $\delta^{234}\mathrm{U_{iec}}$.

2.10.5 Parameters and priors used for Bacon age-depth model

We used the following parameters and priors for our Bacon age-depth model: `thickness` = 50 cm; `acc.mean` = 80 yr/cm; `acc.shape` = 2.0; `mem.strength` = 15; and `mem.mean` = 0.8. The age-depth model was generated by executing the following command:

```
   Bacon(core = "PLJ_dates_d234U_50", acc.mean = 80, acc.shape = 2, mem.mean
= 0.8, mem.strength = 15, thick = 50, ssize = 10000, burnin = 2000, suggest
= FALSE, depths.file = TRUE, yr.max = 800000, MaxYr=781000, d.max = 8800);
```

The Baconvergence test was run and yielded a Gelman and Rubin Reduction Factor of 1.031463, which fell below the 1.05 safety threshold and indicates robust mixing of Markov Chain Monte Carlo iterations.

Trachsel and Telford (2017) tested Bacon and showed that the `thickness` parameter (the segment length) had an unpredictable effect on the size of the error envelope. They also found that the impact of different values for `thickness` was dependent on `acc.shape`, the accumulation shape prior. As Blaauw and Christen (2011) did not explicitly make any recommendations for how to choose an appropriate value for `thickness`, Trachsel and Telford (2017) suggested that the length be shorter than the mean distance between dated intervals and to choose a value that allowed for faster model convergence.

As can be seen from Fig. 2-15, the chronological constraints of the PLJ-1 splice are not equally spaced. The average distance between radiocarbon data in the upper 20 m of the core is 24 cm; when considering all radiometric data (radiocarbon and U-Th), the average spacing is 72 cm.

Thus, we carried out a comparison of age-depth models generated using different lengths for the `thickness` parameter, keeping the accumulation shape prior constant. Fig. 2-17 shows that while the difference in the mean of the age-depth models does not vary by more than 8 kyr at any point in the record, there are 5–30 kyr differences in the width of the error envelope.

Unfortunately, there is no rule of thumb or other external information that can help us determine which length for the `thickness` parameter is most appropriate. At this point, the decisions for how to generate the age-depth model are, regrettably, more of an art. Thus, we collectively settled on using 50 cm as the length for the `thickness` parameter, for no other reason other than it seeming “reasonable.” We encourage others to use the chronological constraints generated in this study and others at Lake Junín to create better age-depth models with improved estimates of uncertainties.

2.10.6 Determination of relative paleointensity tie points

As paleomagnetic reconstructions perform best within intervals of high lithic flux (glacial periods in Lake Junín), the U-Th ages in Fig. 2-15A were first used to seat the paleomagnetic record during the carbonate-dominated interglacial sediments. Following interglacial anchoring, the Lake Junín normalized remanence record was compared to a regional RPI stack from the North Atlantic (Xuan et al., 2016) and the global paleointensity inversion PADM2M of Ziegler et al. (2011). The generally good agreement between these records and the Lake Junín normalized intensity record allowed additional tie points to be identified that improved the correlation between the PLJ-1 record and the two well-dated RPI targets. A somewhat arbitrary 10 ka uncertainty (2-σ) was prescribed to account for aliasing during the tuning process and the chronological uncertainty of the target stacks (see Hatfield et al., in preparation for further details). In general, the RPI picks center within the 2-σ error envelope of the PLJ-1 Bacon-derived age model, however, picks falling off the mean age-depth model likely infer variations in sedimentation rate between glacial-interglacial sediments (see Woods et al., 2019, for examples within the radiocarbon era) that might be expected in heterogeneous sedimentary environments but are not captured in the interglacial-only U-Th age-depth model (see Hatfield et al., in prep).

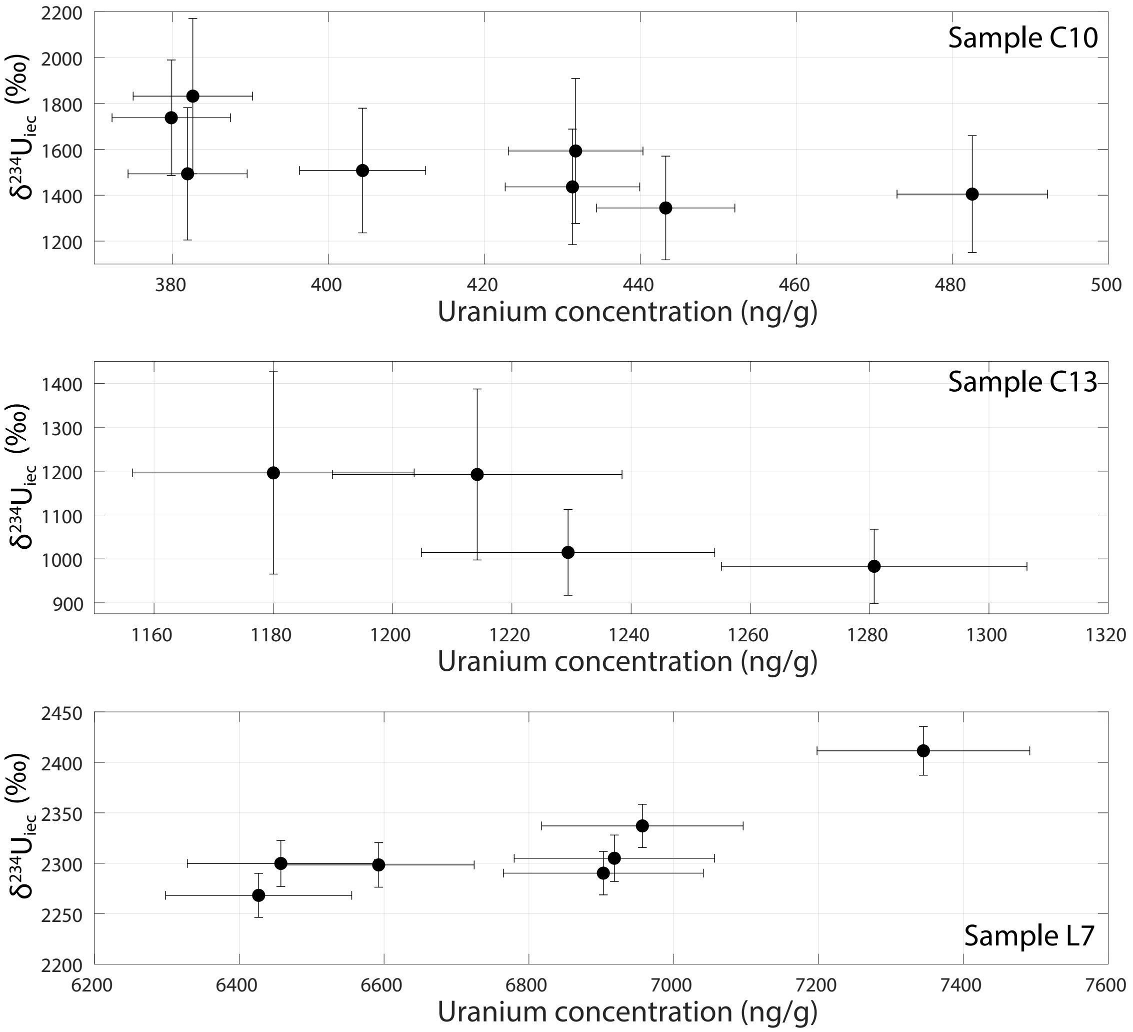

Figure 2-16: Comparison of uranium concentration and $\delta^{234}U_{iec}$ for three samples of the CMC facies: C10 (top), C13 (middle), and L7 (bottom). Samples C10 and C13 show some evidence of the inverse relationship between uranium concentration and $^{234}U_{iec}$, as would be predicted if there was preferential loss of ^{234}U (Robinson et al., 2006). However, L7—the sample with the highest mean uranium concentrations out of any sample analyzed—shows a trend that is more consistent with the expectations of preferential ^{234}U gain. All errors are at the 2-σ level.

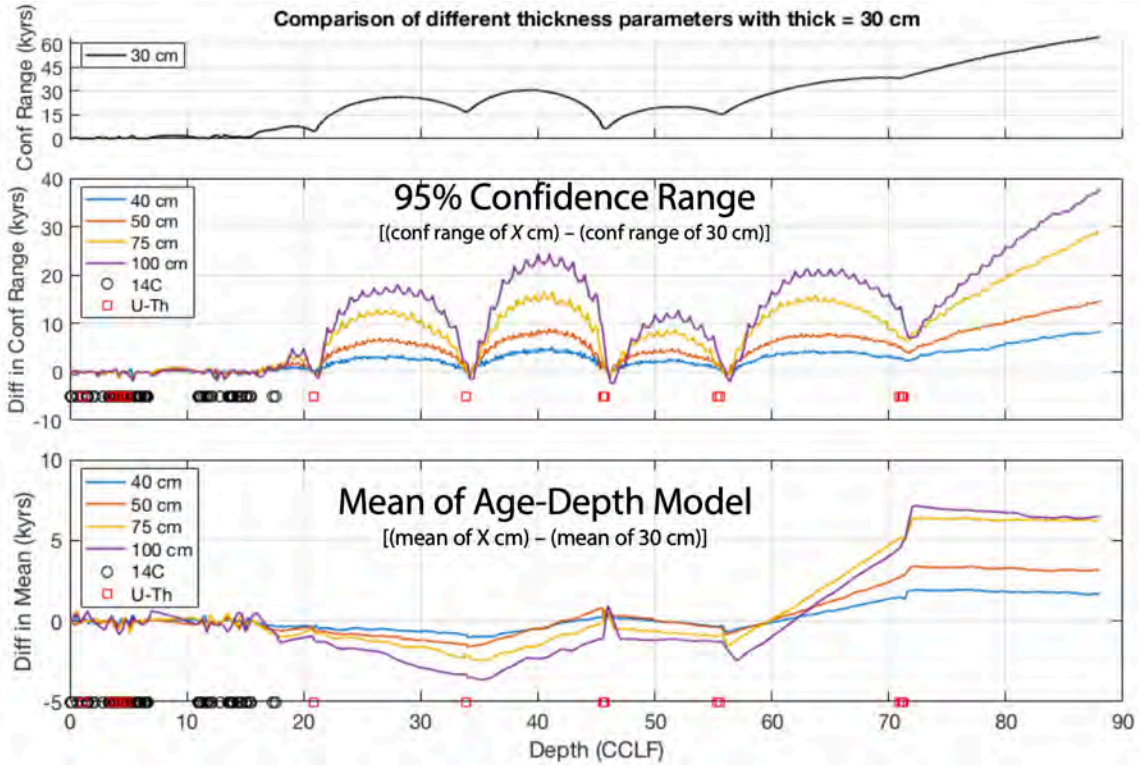

Figure 2-17: Comparison of the size of the 95% confidence range and mean of Bacon age-depth models run with varying lengths of the `thickness` parameter. Middle and bottom plots compare the age-depth models to the results of the model where `thickness` = 30 cm. The top plot shows the size of the 95% confidence range for the age-depth model where `thickness` = 30 cm.

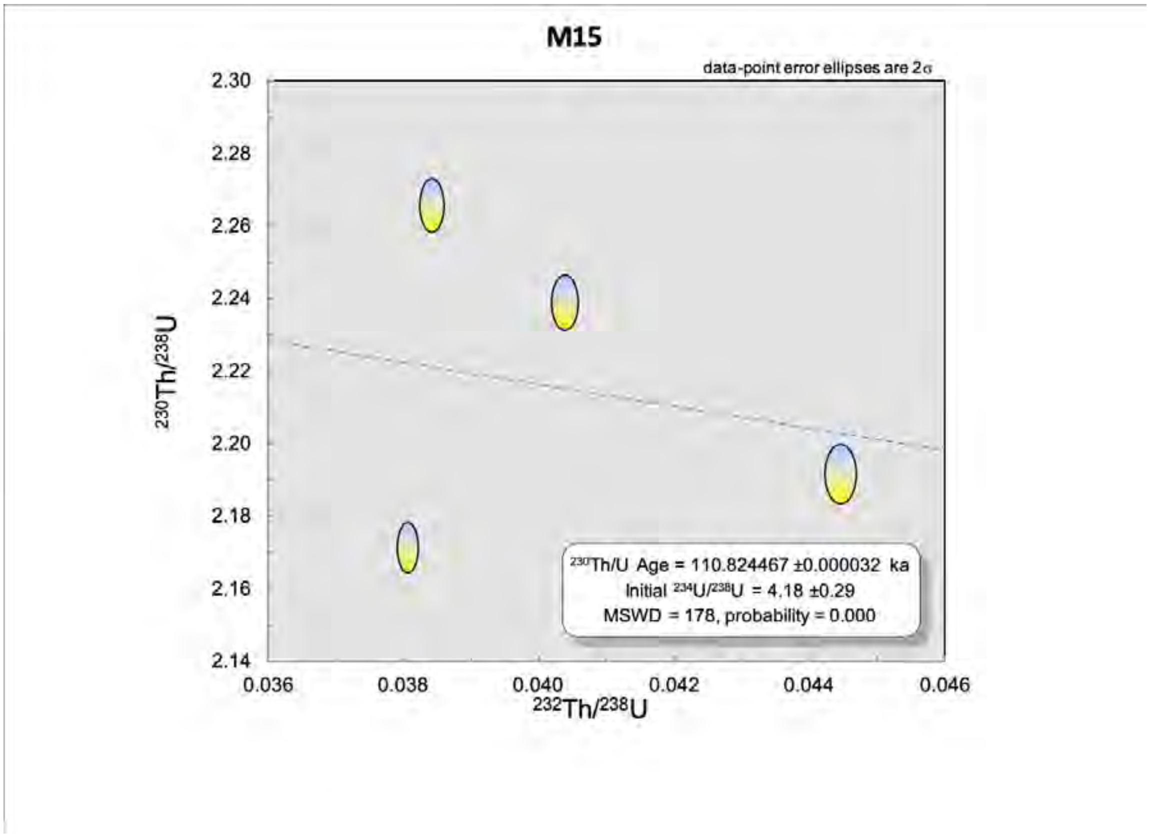

Figure 2-18: Isochron plot of analyses from sample M15.

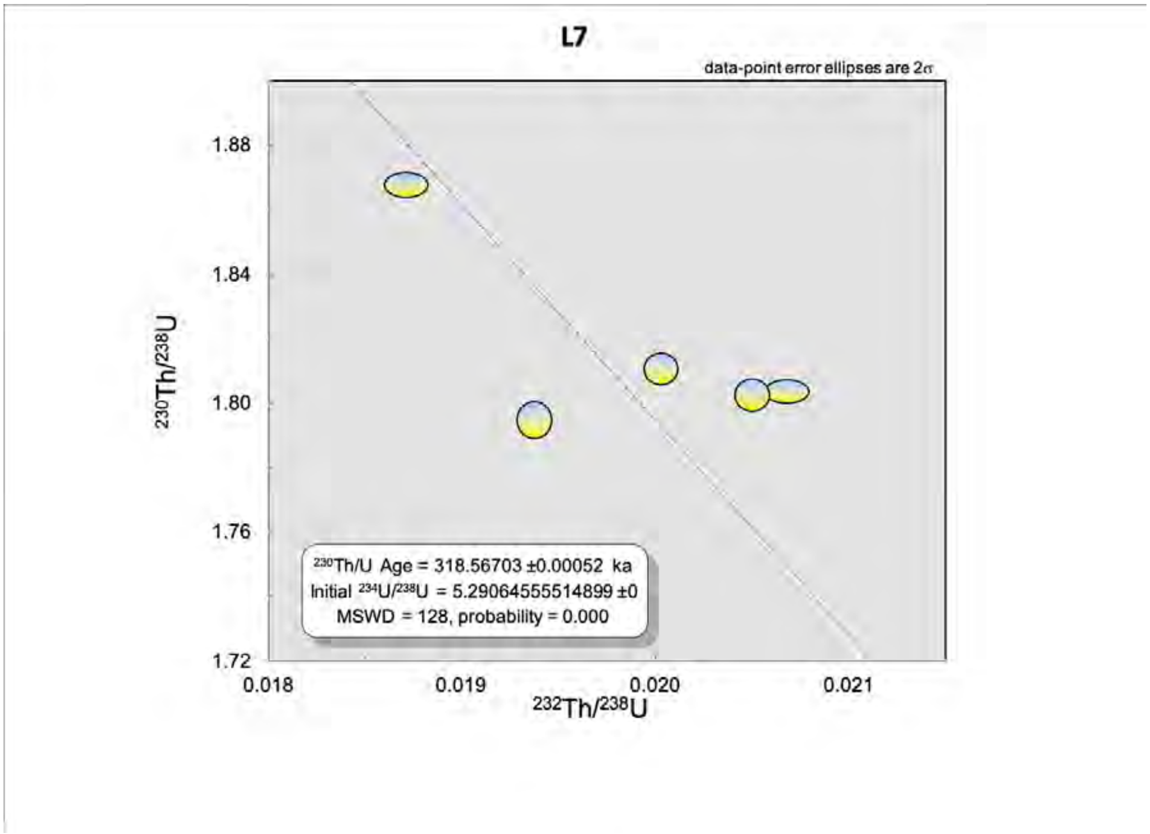

Figure 2-19: Isochron plot of analyses from sample L7.

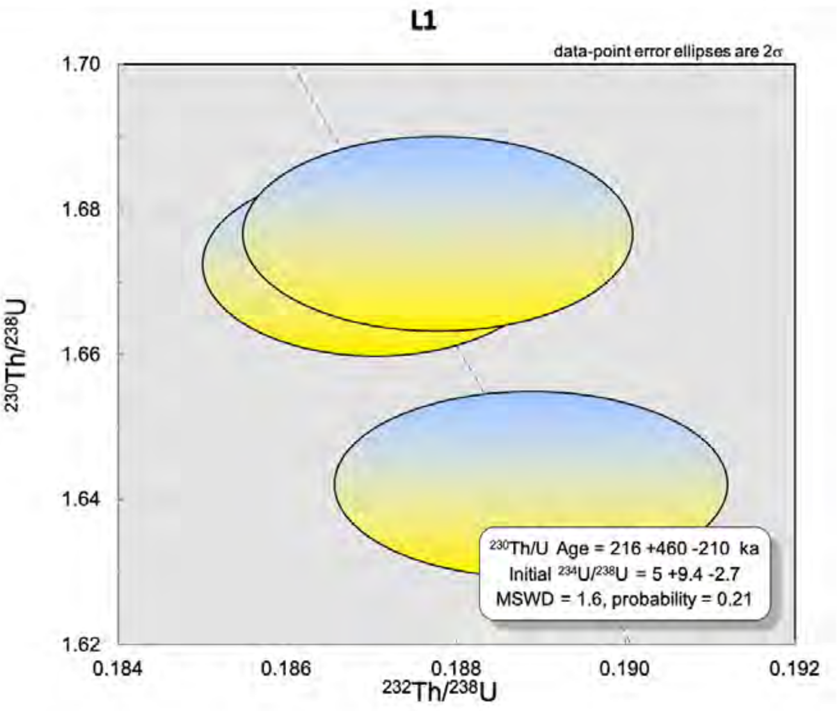

Figure 2-20: Isochron plot of analyses from sample L1.

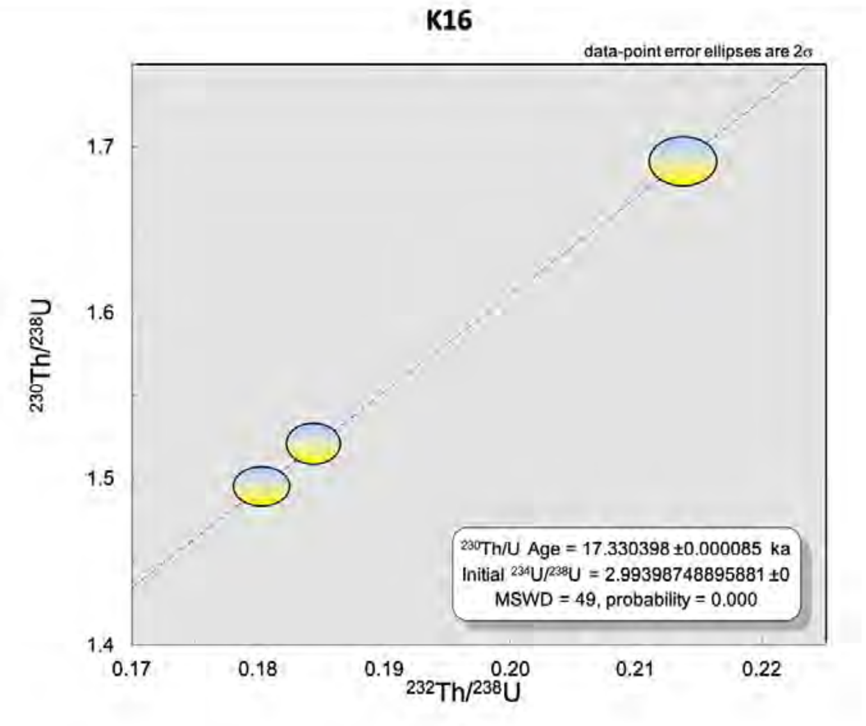

Figure 2-21: Isochron plot of analyses from sample K16.

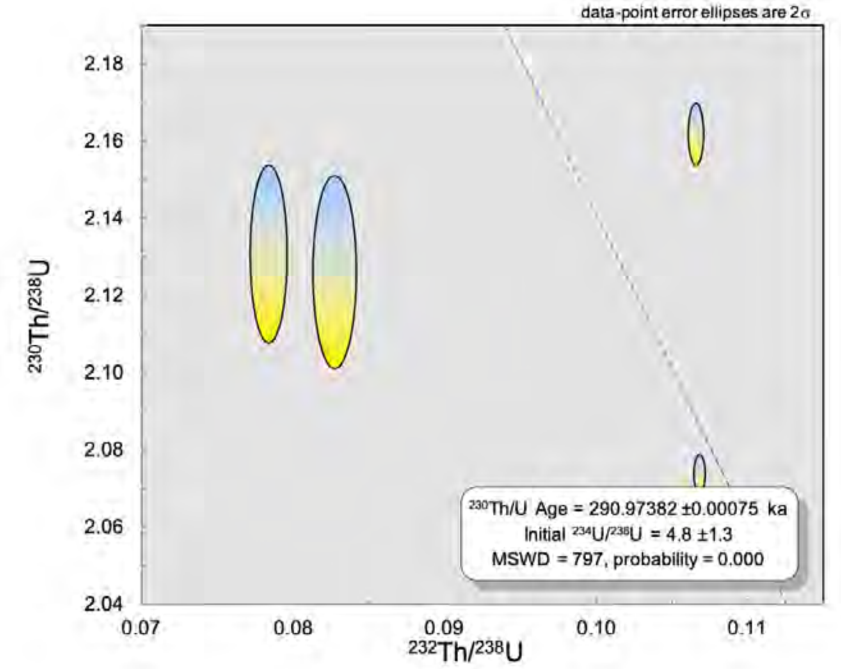

Figure 2-22: Isochron plot of analyses from samples J5 and J6.

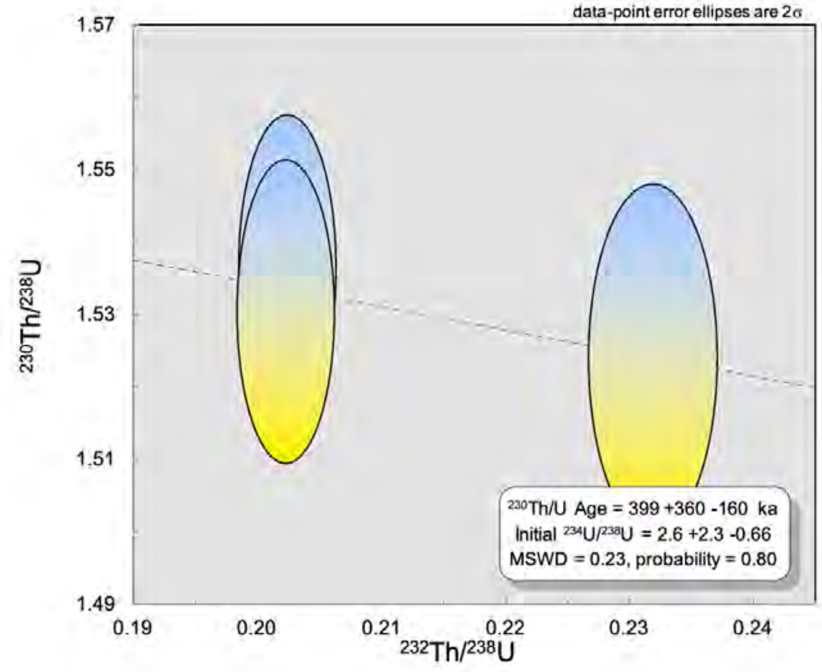

Figure 2-23: Isochron plot of analyses from sample H7.

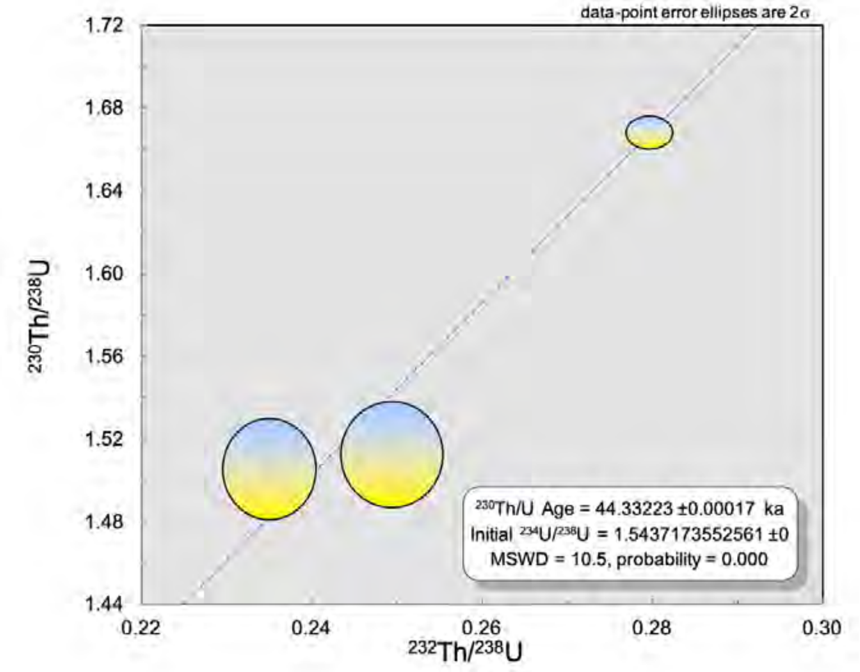

Figure 2-24: Isochron plot of analyses from sample H6.

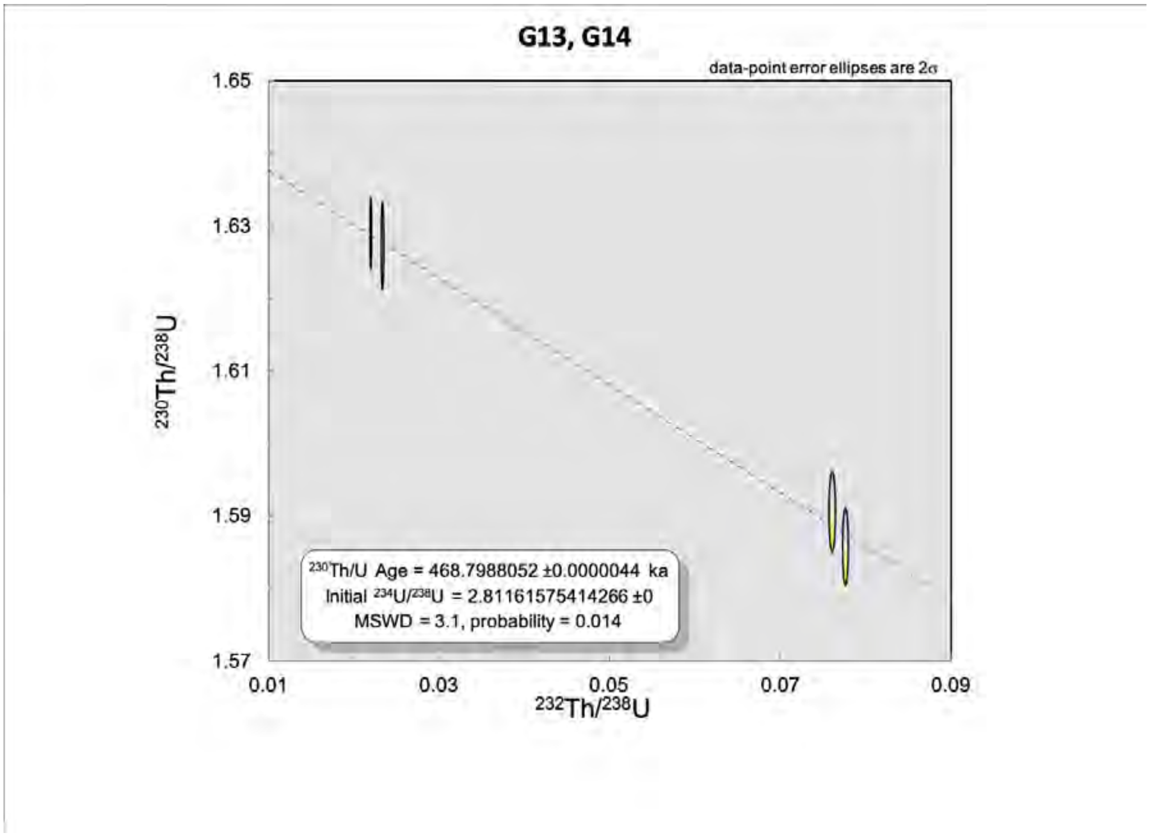

Figure 2-25: Isochron plot of analyses from samples G13 and G14.

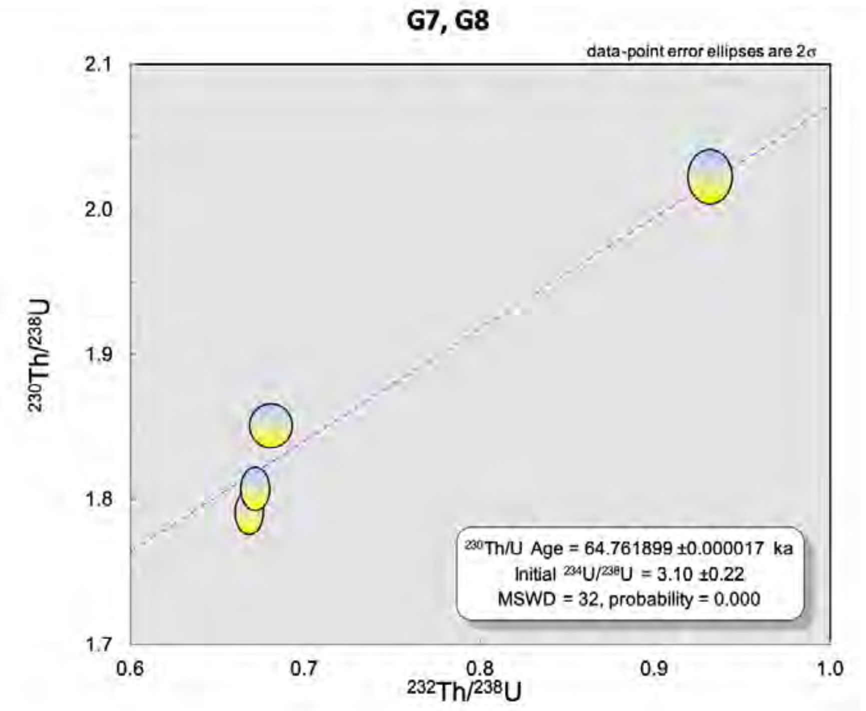

Figure 2-26: Isochron plot of analyses from samples G7 and G8.

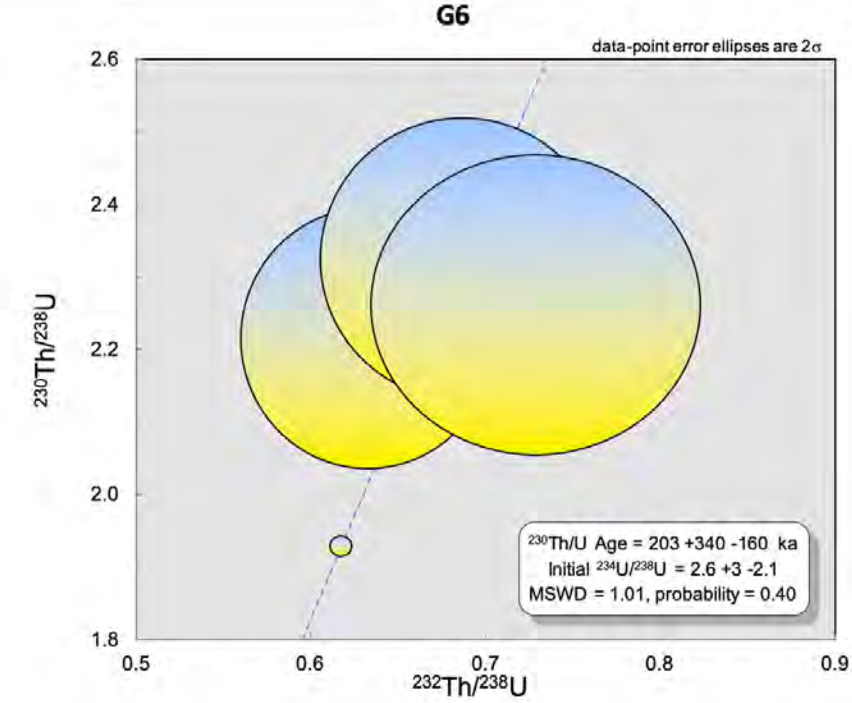

Figure 2-27: Isochron plot of analyses from samples G6.

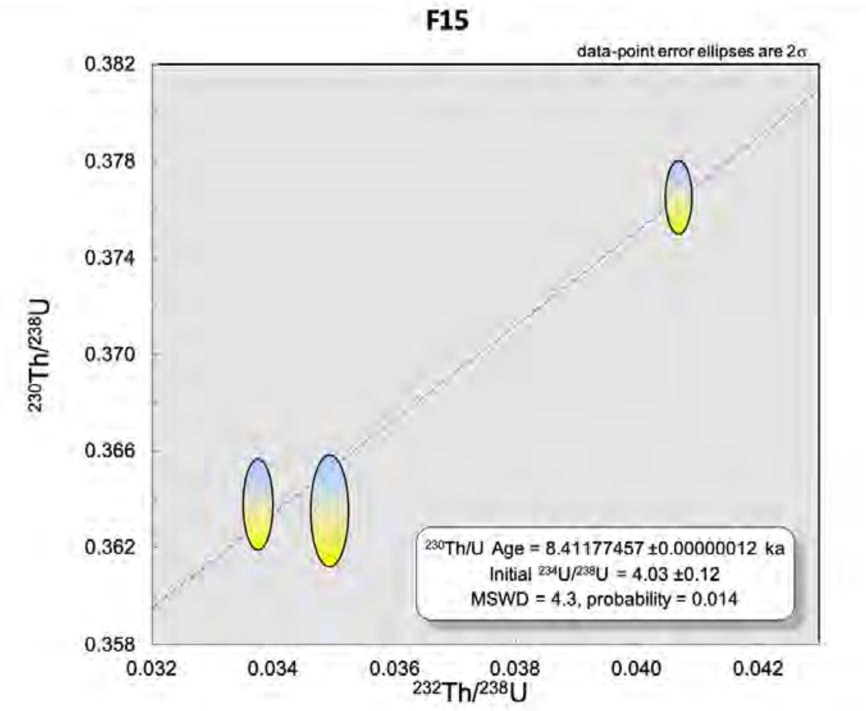

Figure 2-28: Isochron plot of analyses from samples F15.

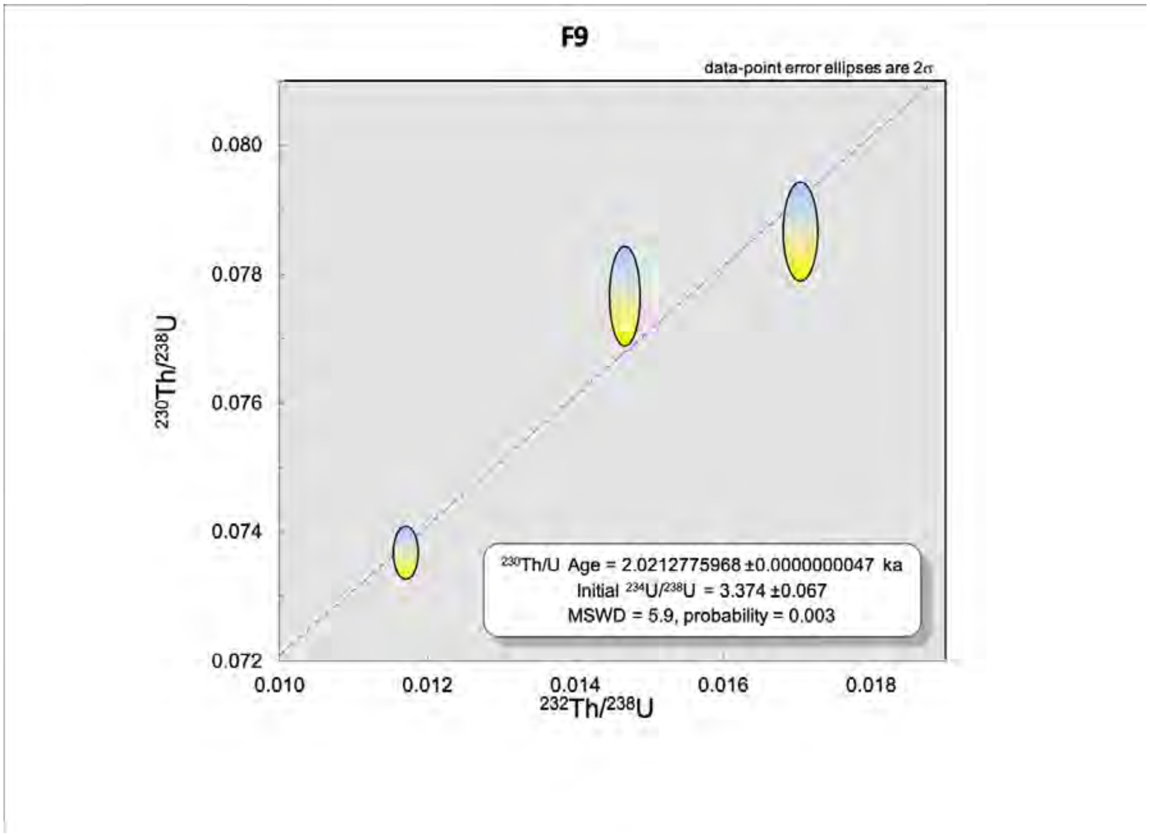

Figure 2-29: Isochron plot of analyses from samples F9.

Chapter 3

U-Th dating of tufas from Agua Caliente I, Laguna de Tara and Salar de Loyoques, northern Chile

3.1 Introduction

The South American summer monsoon (SASM) is the main source of precipitation for much of South America, impacting globally significant ecosystems ranging in diversity between the world's largest tropical rainforest in the Amazon basin to the world's driest desert in the Atacama (Nogués-Paegle et al., 2002; Jones et al., 2012). Future SASM changes are of particular concern in the Central Andes, where anomalous decreases in streamflow and water availability over the past three decades have rendered both human and ecological communities highly vulnerable to future anticipated climate change (Messerli et al., 1997; Aravena et al., 1999; Vicuña et al., 2012; Magrin et al., 2014; Morales et al., 2015). Despite societal significance, there is substantial uncertainty and poor agreement in climate model projections of future precipitation patterns over South America (Marengo et al., 2012; Rowell, 2012; Knutti and Sedláček, 2013; Shepherd, 2014). The short and sparse instrumental record and disagreement among reanalysis products make even more recent changes in the magnitude and spatial extent of SASM ambiguous (Grimm, 2011; Silva and Kousky, 2012).

To improve forecasts of future hydrological change in monsoonal regions, we must examine natural archives that record changes in precipitation during Earth's varied climatic past. Reconstructions of monsoon responses to past forcings and boundary conditions have been produced from compilations of pollen and lake level data (Qin et al., 1998; Kohfeld and Harrison, 2000; Yu et al., 2001; Bartlein et al., 2011) and used for data-based tests of climate model performance. Such proxy-model comparisons have revealed that models consistently underestimate past monsoon variations, but proxy data representation is heavily skewed towards the low- to mid-latitude regions of the Northern Hemisphere (Joussaume et al., 1999; Coe and Harrison, 2002; Braconnot et al., 2007, 2012; Roehrig et al., 2013; Perez-Sanz et al., 2014). Coverage in South America in both pollen and lake level compilations is much more sparse, making it impossible to determine whether models are adequately representing the magnitude and spatial extent of the SASM under past climate conditions (Figure 3-10) (Qin et al., 1998; Kohfeld and Harrison, 2000).

Furthermore, amongst the paleoclimate data that do exist in South America, there is little consensus on how precipitation responded to climate perturbations over the Pleistocene. In the Bolivian Altiplano of the Central Andes, sediment core records from the Titicaca-Uyuni basin suggest that lake levels mainly follow insolation and glacial-interglacial variations, with the wettest conditions occurring during austral summer insolation maxima and glacial periods (**?**). However, studies on preserved paleoshoreline deposits from the same basin suggest that North Atlantic cooling events are the primary drivers of wet conditions rather than insolation changes (Placzek et al., 2006b, 2013; Blard et al., 2011).

In this paper, we present new U-Th dating constraints on lake level variations from three small (<40 km^2), high-altitude closed-basin paleolakes on the Altiplano-Puna plateau of the Central Andes (23°S, 67°W; 4200–4300 meters above sea level). Because this area experiences a strong seasonal cycle, receiving 50 to 90% of its annual precipitation amount during austral summer (December-January-February, DJF; Nishizawa and Tanaka, 1983; Gandu and Silva Dias, 1998; Garreaud et al., 2003; Vuille and Keimig, 2004; Wade, 2014), the Altiplano-Puna region is ideally suited to represent a pure response to changes in the SASM (Figure 3-1A). In each of these basins, evidence for previous intervals of much wetter conditions is evident in spectacularly preserved paleoshorelines, which even a casual observer can identify via satellite imagery. Many of these paleoshorelines are encrusted with carbonate "tufa" deposits, which are essentially fossilized calcareous remains of algal reefs. Because modern analogues of tufa-forming organisms grow within the photic zone, the location of these tufa deposits approximates the elevation of past lake levels. Earlier radiocarbon (^{14}C) dating efforts to find the ages of these deposits have been limited due to a lack of terrestrial organic matter and large uncertainties in the reservoir effect in these lake basins. Thankfully, due to high U concentrations and low detrital Th content, we are able to apply U-Th dating techniques to these materials. By U-Th dating these tufas and other lacustrine carbonates, we can pair an age to a quantitative constraint for the magnitude of lake area expansion calculated from differential GPS (dGPS) measurements of the elevations of shoreline features.

These data are the first results from a planned north-south transect of six lake basins spanning the subtropics of the Central Andes (20-33°S; Figure 3-1B) aimed at filling a key geographical gap between existing lake level chronologies in the tropics and mid-latitudes, as well as providing valuable constraints on past spatial variations in SASM extent. The paper is organized as follows: In Section 3.2, we summarize current knowledge on the modern climate of the Altiplano-Puna plateau. In Section 3.3, we describe previous work that demonstrates past linkages between local summer insolation and North Atlantic cooling events to hydrological changes in South America and the Central Andes. We discuss the setting of the lake basins in our study in Section 3.4 and describe our methods for U-Th dating and mapping ancient shorelines in Section 3.5. The results and implications of our findings are discussed in Sections 3.5–3.7. Finally, we outline the future direction of this research (for instance, a water balance model to provide quantitative constraints on precipitation and evaporation changes) and other possible avenues in Section 3.8.

3.2 Modern climate of the Altiplano-Puna plateau

The Altiplano and Puna plateaus of the Central Andes are arid to semi-arid internally-drained basins situated between cordilleras to the east and west. Together, they form the second highest continental plateau in the world (average elevation 3700 m), stretching for 1800 km and varying between 350 and 400 km in width (Isaks, 1988; Allmendinger et al., 1997; Kay and Coira, 2009). Mean annual temperatures from the few available weather stations on the plateau average to 9°C after elevational differences are normalized (Blard et al., 2011). Based on modern δ^{18}O of rainfall data from the IAEA-GNIP database, average δ^{18}O values of precipitation on the plateau are -12.1 ± 6.1‰ VSMOW (-41.7 ± -24.0 VPDB; IAEA/WMO, 2015). Despite the overall aridity of the region (<200 mm yr^{-1} precipitation in the south and ∼1000 mm yr^{-1} in the north; Garreaud et al., 2003; Vuille and Keimig, 2004), the plateau is the main source of water for the neighboring hyper-arid Atacama Desert resting at the base of the western flank of the Andes. Evaporation rates decrease while precipitation rates increase from west to east across the Andes such that open water bodies are generally only observed at elevations greater than 4000 masl (Magaritz et al., 1989; Vuille and Baumgartner, 1993; Aravena et al., 1999). This observed west-to-east gradient in rainfall across the Central Andes and within the plateau is consistent with an eastern continental moisture source (Garreaud et al., 2003). Moist, cool air from the Pacific ocean rarely reaches the plateau due to coastal topography and a thermal inversion layer over the subtropical southeast Pacific caused by large-scale subsidence (Rutllant and Ulriksen, 1979).

As mentioned earlier, rainfall over the Altiplano-Puna plateau is highly seasonal and heavily influenced by the behavior of the SASM. Similar to other classic monsoon systems

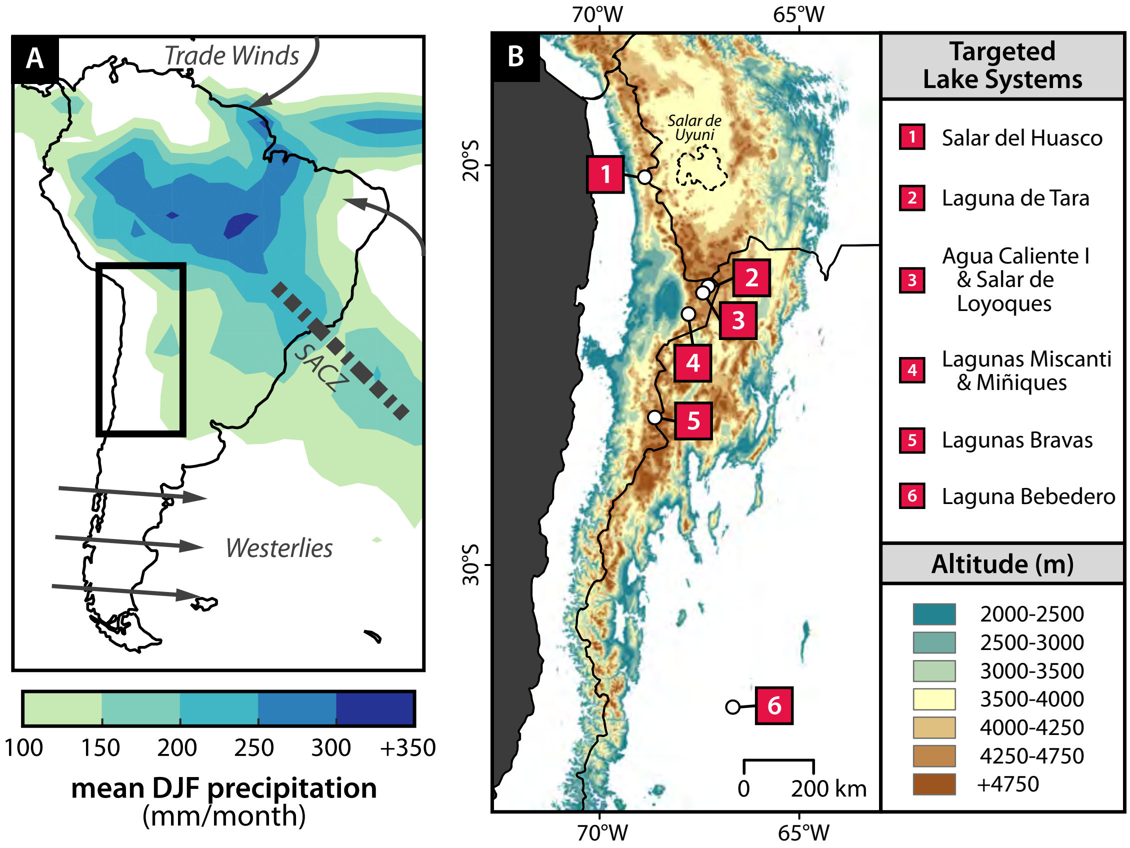

Figure 3-1: [**A**] Austral summer (DJF) precipitation in South America. The box shows the region highlighted in panel B, which lies on the western and poleward edge of monsoon rains. Data are from the CPC Merged Analysis of Precipitation (CMAP) from 1979-2015. [**B**] Sites involved in a planned meridional transect of closed-basin lakes, and other lakes mentioned in the text.

(e.g., the Indian summer monsoon), large-scale upper tropospheric circulation of the SASM is driven by seasonally-varying differential sensible heating of land and ocean that then triggers moist atmospheric processes which redistribute energy via latent heat transfer (Zhou and Lau, 1998; Vera et al., 2006; Marengo et al., 2012). Throughout most of the year, dry air from the subtropical Pacific is brought over the plateau by prevailing subtropical westerly winds, resulting in very low precipitation rates. During austral winter, the SASM is at its weakest, and South America receives most of its rainfall north of the equator in line with the location of the local Intertropical Convergence Zone (ITCZ), centered at ∼5°N. While the local ITCZ is north of the equator, the interior of the continent undergoes its dry season.

During austral summer at the peak of the SASM, a southward shift of the ITCZ strengthens the easterly trade winds that advect moisture from the tropical Atlantic ocean onto the continent, causing heavy convective precipitation in the southern Amazon basin and northern Argentina (Figure 3-1A). These summertime convective thunderstorms involving cumulonimbus clouds (Houze, 1997) release latent heat (condensational heating) over the Amazon basin that causes the formation of the Bolivian High, an upper-troposphere high-pressure cell (Lenters and Cook, 1997; Garreaud et al., 2003; Garreaud et al., 2009). This warm upper-level anti-cyclonic circulation cell channels mid- and upper-level easterly winds over the Central Andes, which provide the moist continental lowland air necessary for the generation of deep convection on the plateau (Garreaud et al., 2003; Vuille and Keimig, 2004; Falvey and Garreaud, 2005). Deep, moist convection is then triggered by destabilization of the local lower troposphere via solar-driven sensible heating of the plateau surface (Garreaud, 1999; Vuille, 1999), releasing moisture and latent heat as afternoon and early evening rainfall (Fuenzalida and Rutllant, 1987; Garreaud and Wallace, 1997).

The Bolivian High is also associated with the formation of a low-pressure system centered over the Gran Chaco region of Argentina (Chaco Low, ∼25°; Seluchi et al., 2003), which steers low-level (below ∼1500 m altitude) easterly winds flowing over the Amazon southwards along the eastern slope of the Andes, funneling moisture from the Amazon basin into the subtropics (Saulo et al., 2000; Marengo, 2004; Garreaud et al., 2009). Enhanced specific humidity in the lower troposphere of these subtropical continental lowlands appears correlative with wet conditions in the southern part of the Altiplano-Puna plateau, but a causal link between these two conditions, and why the neighboring lowlands do not matter for conditions on the northern Altiplano-Puna plateau, is unclear (Garreaud et al., 2003; Vuille and Keimig, 2004).

While interannual and decadal-scale fluctuations in precipitation over the Amazon basin are well-studied, such variations are <15% of the region's annual mean rainfall amount (Garreaud et al., 2009). In contrast, year-to-year precipitation variations over the Altiplano-Puna plateau are very strong, alternating between severe drought and very wet summer conditions (e.g., 11 mm to 277 mm in consecutive rainy seasons; Garreaud and Aceituno, 2001; Garreaud et al., 2003). Interannual and decadal-scale precipitation on the plateau shows strong connections with Pacific sea surface temperature (SST) patterns, with a warm eastern equatorial Pacific (El Niño-like conditions) corresponding to drier conditions (e.g., Lenters and Cook, 1997; Vuille, 1999; Vuille et al., 2000; Garreaud et al., 2003). During El Niño years, the anomalously warm eastern equatorial Pacific Ocean causes a warming of the troposphere above, causing large-scale, upper-level zonal flow to take on a more westerly direction. This strengthening of westerly winds across the Central Andes transports dry air from the western slopes of the Andes, thus bringing about a dry spell (Garreaud and Aceituno, 2001; Garreaud et al., 2003; Vuille and Keimig, 2004). An opposite response occurs during most La Niña episodes: anomalously cool eastern Pacific SSTs cool the tropical troposphere and decrease meridional temperature gradients, resulting in a poleward shift of weakened westerly winds over the Central Andes, allowing greater westward penetration of moist air.

Interestingly, there is no evidence for a tropical Atlantic influence on austral summer rainfall in the Altiplano-Puna plateau on modern interannual timescales (Vuille et al., 2000). However, given the short and often incomplete instrumental record in the Central Andes, it is possible that Atlantic teleconnections may only play a role in Central Andes precipitation on longer timescales.

3.3 Previous Work on Past Changes in the SASM

Records of millennial climate variations from South America are comparatively scarce, but those that do exist show clear climatic shifts contemporaneous with Greenland during the last glaciation (e.g., Lowell et al., 1995; Arz et al., 1998; Behling et al., 2000; Lamy et al., 2000; Peterson et al., 2000; Peterson and Haug, 2006). Oxygen isotope records from various speleothems in South America (e.g., Cruz et al., 2005, 2007; Wang et al., 2004, 2006, and 2007; Mosblech et al., 2012; Cheng et al., 2013b; Stríkis et al., 2015) suggest that SASM precipitation was influenced by not only changes in local summer insolation, but also abrupt millenial-scale North Atlantic cooling events (e.g., Bard et al., 2000) which had a significant impact on the interhemispheric temperature difference (Shakun et al., 2012). These anomalously cool North Atlantic events are called Heinrich events, and are associated with marine deposition of iceberg-derived coarse-grained sediments. The South American speleothem records suggest that periods of SASM intensification coincide with Heinrich events by showing more negative δ^{18}O values during these periods, which is interpreted to indicate increased rainout upstream. Although these δ^{18}O speleothem records are robust and possess excellent temporal resolution and precision in ages, the magnitude and spatial pattern of these precipitation changes cannot be gleaned from such proxies.

Lake records from the Central Andes have already proven to be a powerful and necessary complement to these South American speleothem records. The shoreline-based records from the Titicaca-Uyuni lake basin in Bolivia suggest that lake levels were primarily driven by Heinrich events (Placzek et al., 2006b, 2013; Blard et al., 2011), and corresponding hydrologic modeling suggests that a $\sim$2–3 factor increase in precipitation relative to present rates was necessary to maintain the lake at its highstand, called the Tauca phase, during Heinrich Event 1 (H1; $\sim$18–14.6 ka). Increased Central Andes rainfall associated with H1 is also observed in paleowetland deposits showing elevated groundwater tables (Quade et al., 2008), fluvial terraces and pack-rat middens showing increased stream discharge (Latorre et al., 2006; Nester et al., 2007; Gayo et al., 2012), and glacial moraines showing substantial ice cover expansion (Smith and Delorme, 2010). In a sediment record from Laguna Miscanti (Figure 3-1B) spanning the last $\sim$22 ka (Grosjean et al., 2001), two periods of higher lake levels during the last deglaciation are inferred from aquatic pollen assemblages and sediment lithology. Unfortunately, large ^{14}C reservoir effects for aquatic organic materials of 2200–4000 years greatly limited the chronology of this record.

In this study, we aim to not only lay the foundation for quantifying past precipitation changes, but also test the two contradictory interpretations of the Titicaca-Uyuni lake system. The past extent of lake stages prior to >25 ka in this system is disputed due to complex basin geometry and uncertainty over past sill elevations (Placzek et al., 2013; **?**). By examining these pluvial events in smaller, simpler paleolake basins, we can assess how consistent our reconstructed lake level histories are with each interpretation of the Titicaca-Uyuni lake level record.

3.4 Study Area

Our study area focuses on three neighboring lake basins in northern Chile, located south of Salar de Uyuni (Figure 3-1B): Agua Caliente I (23.13°S, 67.41°W), Salar de Loyoques (23.25°S, 67.29°W), and Laguna de Tara (23.04°S, 67.28°W) (Figure 3-2). The landscape is dominated by large volumes (>10,000 km^3) of primarily silicic ignimbrites extruded between 10–1 Ma (Quade et al., 2015). Mean annual temperatures of 0°C and annual precipitation rates of 150–180 mm/yr make this area a very cold and dry place (Dirección General de Aguas, 1987). At present, freshwater springs breaching the surface a few tens of meters above the modern lake or salar feed these lakes; surface flow of water is confined to such spring discharges. Agua Caliente I is also fed by thermal springs in the southwest part of the basin, as is implied by its namesake. An inactive stream channel located at the foot of converging alluvial fans from opposite sides appears to link the Agua Caliente I basin with Salar de Loyoques, but no such surficial linkages exist with Laguna de Tara, its neighbor to the north.

3.5 Materials and Methods

3.5.1 Field sampling and shoreline mapping

In order to obtain constraints on past lake water elevations, we identified, sampled, and recorded the present-day elevation of sequences of tufa formations and lacustrine carbonate deposits that provide information on paleowater depths. When combined with paleoshoreline observations and geochronologic tools such as ^{14}C and U-Th dating, this strategy is successful in reconstructing lake level histories in both large and small lake basins (e.g., Oviatt et al., 1994; Benson, 1994, 1995; Placzek et al., 2006b). When sampling, we focused primarily on deposits associated with shoreline features, but we also sampled material from road cut and stream channel exposures. When the entire thickness of a unit could not be sampled, we took samples from the top (outer part) and bottom (inner part) of deposits to capture the entire duration of lake episodes. Our sampling approach also took advantage of several cross-cutting relationships and disconformities to find the relative timing of distinct depositional events.

We collected precise location and elevation data of shoreline features and samples using a Trimble Geo 7x handheld device, a high-accuracy Global Navigation Satellite System (GNSS) receiver. After post-processing with proprietary software, we are able to achieve horizontal and vertical location measurements of submeter accuracy (Section 3.9.1 and Figure 3-12). For shoreline features, we measured the elevations of the crests of gravel barriers, the base of incised alluvial fan scarps, and the tops and bottoms of abrasional platforms, following methods described by Chen & Maloof (in revision). We also drove through the stream channel connecting the Agua Caliente I and Salar de Loyoques basins, taking regular dGPS elevation measurements of the channel bottom (thalweg) to estimate the potential overflow (sill) elevation.

The locations and elevations of the highest shoreline features in each basin were then

Figure 3-2: Annotated satellite imagery of the three lake basins examined in our study. Dashed lines serve as a guide to the reader to identify the modern extent of lakes and salars within each lake basin.

used for paleolake area calculations, which were determined with geographic information systems (GIS), satellite imagery, and a digital elevation map (DEM) (Section 3.9.2).

3.5.2 U-Th dating of shoreline tufas and other lacustrine deposits

Tufa and other lake carbonate samples were slabbed along the axis of primary growth or deposition and cleaned with ultrapure water prior to sampling. Using a vertical milling machine with a tungsten carbide-tipped drill bit, we drilled carbonate powders weighing 2–10 mg from these slabbed surfaces, targeting areas with primary textures and the least amount of siliciclastic detritus and post-depositional chemical or physical alteration. For Bolivian Altiplano lake carbonates, Placzek et al. (2006a) found that white-colored carbonates tended to have lower initial Th content compared to material with faint pink or orange coloration; thus, we also preferentially sampled white-colored material.

Preparation of these aliquots for U-Th dating was then performed in a clean laboratory at MIT. Aliquots were dissolved in HNO_3 and spiked with a ^{229}Th-^{233}U-^{236}U tracer in Teflon beakers cleaned via a boiling-washing procedure with concentrated HNO_3 and HCl. Next, following methods described by Edwards et al. (1987) and Shen et al. (2002), U and Th were co-precipitated with ~4 mg of Fe oxyhydroxides and then separated using BioRad AG1-X8 anion exchange resin (100-200 mesh, 0.5 mL column volume). The isotopic compositions of the resulting U and Th fractions were then measured on either a Thermo Scientific Neptune Plus multi-collector ICP-MS at Brown University or a Nu Plasma II-ES multi-collector ICP-MS at MIT. At both locations, we introduced sample solutions through a CETAC Aridus II desolvating nebulizer system coupled to a PFA nebulizer with an 100 μL/min uptake capillary. Each U sample analysis was bracketed by a 5 ng/g solution of the CRM-112a standard (New Brunswick Laboratories). Each Th sample analysis was bracketed by an in-house ^{229}Th-^{230}Th-^{232}Th standard in order to monitor mass bias and variable SEM yield. 2% HNO_3 solution blanks also bracketed each sample and standard analysis to determine the background signal. One sample set of chemistry was analyzed at MIT in peak-jumping mode on the ion counter following methods by Shen et al. (2002). See Steponaitis et al. (2015) for more details on the mass spectrometry procedure used at Brown University.

Total procedural blanks were included with each batch of 5–10 samples and were on average 0.2 ± 0.2 fg ^{230}Th, 1.2 ± 2.0 fg ^{234}U, 1.8 ± 0.9 pg ^{232}Th, and 8.7 ± 8.2 pg ^{238}U. These averages do not include anomalous blanks, which had high values of 4.8 fg ^{230}Th, 11 fg ^{234}U, 47 pg ^{232}Th, and 107 pg ^{238}U. However, even with such large blanks, the magnitude of the blank correction for ages we trust in our study was at most 5%. Data with ^{230}Th/^{232}Th ratios >100 ppm (atomic ratio) and <5% blank correction were deemed acceptable. Replication is necessary and planned for samples where blank corrections were higher than 5%. After making blank, background, tail, mass bias, and yield corrections, we calculated U-Th ages using the ^{238}U half-life measured by Jaffey et al. (1971) and the ^{230}Th and ^{234}U half-lives determined by Cheng et al. (2013a). All ages were calculated with an estimate of the detrital ^{230}Th/^{232}Th atomic ratio, $(4.4 \pm 2.2) \times 10^{-6}$.

In the initial project stages prior to any U-Th dating of material, we pre-screened samples to determine which sample materials would be most viable for U-Th dating. In lacustrine settings, the initial ^{230}Th/^{232}Th is often high (e.g., Haase-Schramm et al., 2004; Israelson et al., 1997), causing samples with even modest concentrations of ^{232}Th to have large age corrections. Thus, samples with low ^{232}Th concentration are considered more favorable for U-Th dating. Sample powders of ~2 mg were dissolved in dilute HNO_3, and analyses of ^{238}U and ^{232}Th concentration were performed on a VG PQ2+ quadrupole ICP-MS at MIT. A ^{238}U/^{232}Th ratio of 100 was our threshold for acceptable material for U-Th dating.

3.5.3 Determination of mineralogy and stable isotope composition of carbonates

For mineralogical determination, powders weighing 1–3 mg were drilled from the same sample locations used for U-Th dating and non-destructively analyzed using attenuated total reflectance Fourier transform infrared (ATR-FTIR) spectroscopy on a Perkin Elmer SpectrumOne at Harvard University. Some of these same powders were used to determine the stable isotope composition of samples. The δ^{13}C and δ^{18}O of carbonates were measured at the University of Arizona (UofA) and at the Woods Hole Oceanographic Institution (WHOI). At UofA, measurements were performed on a KIEL-III automated carbonate preparation device coupled to a Finnigan MAT 252 gas-ratio mass spectrometer. Powdered samples of ~0.1–0.2 mg were dissolved in dehydrated phosphoric acid at 70°C. The 2-σ uncertainty of isotope ratio measurements, based on repeated measurements of carbonate standards NBS-18 and NBS-19, is ± 0.22‰ for δ^{18}O values and ± 0.16‰ for δ^{13}C values. At WHOI, stable isotope measurements were made on a Thermo Scientific MAT 253 mass spectrometer. Powdered samples of 3.5–5.5 mg were introduced into a custommade, automated acid reaction and gas purification line built for carbonate clumped isotope analysis (see Supplementary Materials in Thornalley et al. 2015 for method details). We repeatedly analyzed NBS-19 carbonate standards to determine the precision of the isotope ratio measurements, which is ± 0.26‰ for $\delta^{18}O$ values and ± 0.12‰ for $\delta^{13}C$ values at 2-σ uncertainty. Each reported measurement is an average of 3-4 replicate analyses of a particular sample; thus, the measurements made at WHOI may be more representative of the average $\delta^{18}O$ and $\delta^{13}C$ value of each drilled location in a sample.

As a preliminary step towards investigating the microfacies of these lacustrine carbonate deposits, one large format (40 mm × 60 mm) thin section was prepared at Spectrum Petrographics (Vancouver, WA) and examined with an Olympus BX51 light polarizing microscope.

3.6 Results

Field work and sample collection occurred in 2009, 2010, and 2015. In Agua Caliente I, samples span an elevational range of 0 to ~25 m above the modern salar. In Salar de Loyoques, the elevational range of samples is 0 to ~70 m above the modern salar. In Laguna de Tara, samples are 10–30 m above the modern salar. See Table 3.1 for the elevation of the modern salar or lake in each basin.

3.6.1 Observed tufa varieties and other lacustrine carbonates

Of the three lake basins in this study, Agua Caliente I contained the most unique types of calcareous tufa and lacustrine carbonate. Figure 3-3 is a schematic representation of the elevational relationship between paleoshoreline features, different tufa varieties, and other

Lake Basin Name	**Modern Salar/Lake Elev.** (m)	**Highest Shoreline Elev. Above Modern** (m)	**Modern Area** (km^2)	**Ancient Area** (km^2)	**Factor Increase**
Agua Caliente I[†]	4219	34	6.6	26.9	4
Salar de Loyoques[‡]	4182	70	10.7	201	19
Laguna de Tara	4322	30	36	179	5

Table 3.1: Table of modern and ancient lake areas for each basin. [*]Ancient area calculations are for lake highstands. [†]Calculation of the ancient lake highstand is based on the assumption that Agua Caliente I did not overflow into Salar de Loyoques. The present-day elevation of the sill is below that of the highest paleoshoreline in Agua Caliente I. [‡]The modern day lake area of Salar de Loyoques includes the modern day lake area of Agua Caliente I.

lake carbonate deposits in Agua Caliente I. We now describe the morphology and character of each type of deposit observed in the field.

Encrusting floret tufa.—By volume, this porous, whitish-beige-colored tufa variety is the most abundant lacustrine carbonate observed, covering many surfaces ∼5–28 m above the modern lake throughout the basin (∼4223 and 4246 m elevation; Figure 3-4A). These deposits vary in thickness from 3 to 20 cm and appear thickest on smooth, hard substrates such as boulders on hills made of exposed volcanic bedrock (Figure 3-4B). Frequently, multiple sequentially-formed encrustations separated by disconformities can be found on large boulders, with cumulative thicknesses of up to 50 cm. Neighboring boulders are often cemented together by this deposit.

Where coating boulders thickly, the encrustations can vary laterally in thickness by several centimeters, forming broad, mound-like, domal buildups that tend to be thickest towards the boulder tops. In cross-section, the tufa has the appearance of closely-packed “floret”-like growths of uniform thickness radiating away from their nucleation surface (Figure 3-4C). Preservation of this growth structure varies basin wide and between sequentially-deposited encrustations on a singular boulder.

The boulder encrustations are primarily found in the northern and eastern parts of the basin where small bedrock hills are located. Interestingly, the deposits are most thickly developed on the lakeward side of these hills, even when elevation data indicates that the landward side of hills must also have been in contact with lake waters. In the southern part of the basin where there are no such hillsides and the bathymetric slope is much shallower, the encrusting floret tufa assumes a thinner, more flat-lying, tabular shape with more uniformity in lateral thickness (Figure 3-4D). These tufa also tend to be more porous and weathered, incorporating a larger amount of detrital sediment. These differences in porosity and morphology within a single tufa variety may reflect different wave energy environments, in which the more tabular-shaped tufas indicate higher-energy wave conditions (James and Bourque, 1992), possibly due to larger fetch and a shallower wave run-up slope.

Although lateral discontinuities are present, the floret tufas do not exhibit any laminations in their internal structure in any location. A thin section taken along the growth axis of an encrusting floret tufa shows dark microbial peloids (microcrystalline carbonate grains) forming radially-oriented branching structures that are surrounded by micrite (microcrystalline calcium carbonate) containing tiny growth-oriented filaments and dark lenticular tube-like cyanobacterial-algal microfossils (Figure 4-2D). Trapped detrital materials consisting of skeletal ostracod (benthic micro-crustaceans encased in a calcitic bivalved

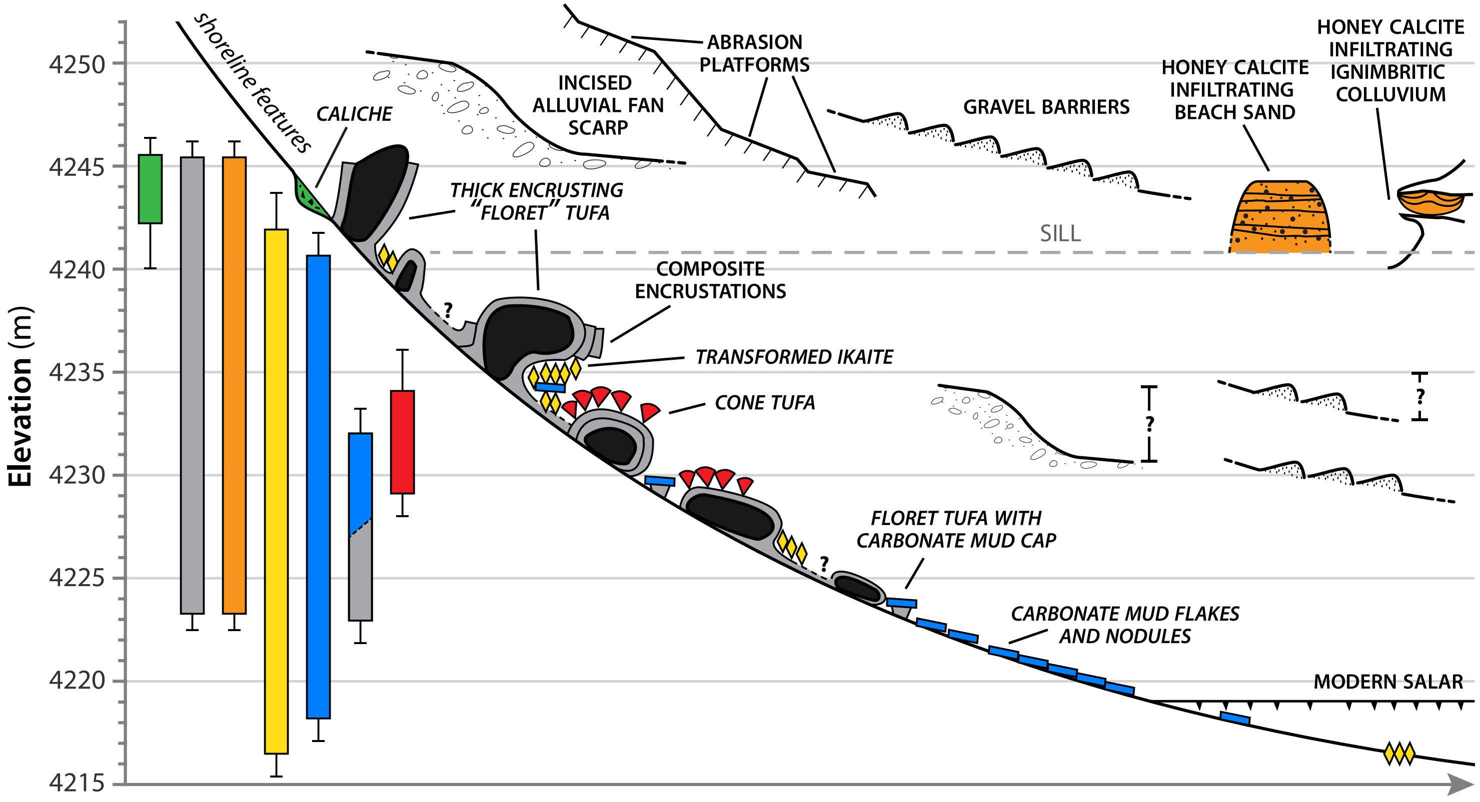

Figure 3-3: Schematic representation of the elevational relationship amongst paleoshoreline features, tufa varieties, other lake carbonate deposits, and overflow points (sills) in Agua Caliente I. The morphology of the tufa varieties are simplified, and their complex internal structures are not illustrated. Colored bars on the left represent the elevational range where each tufa and lake carbonate variety is observed: green = caliche; gray = floret tufa; orange = honey calcite cement; yellow = transformed ikaite; blue/gray = floret tufa with carbonate cap; blue = carbonate mud flakes and nodules; red = cone-shaped tufa.

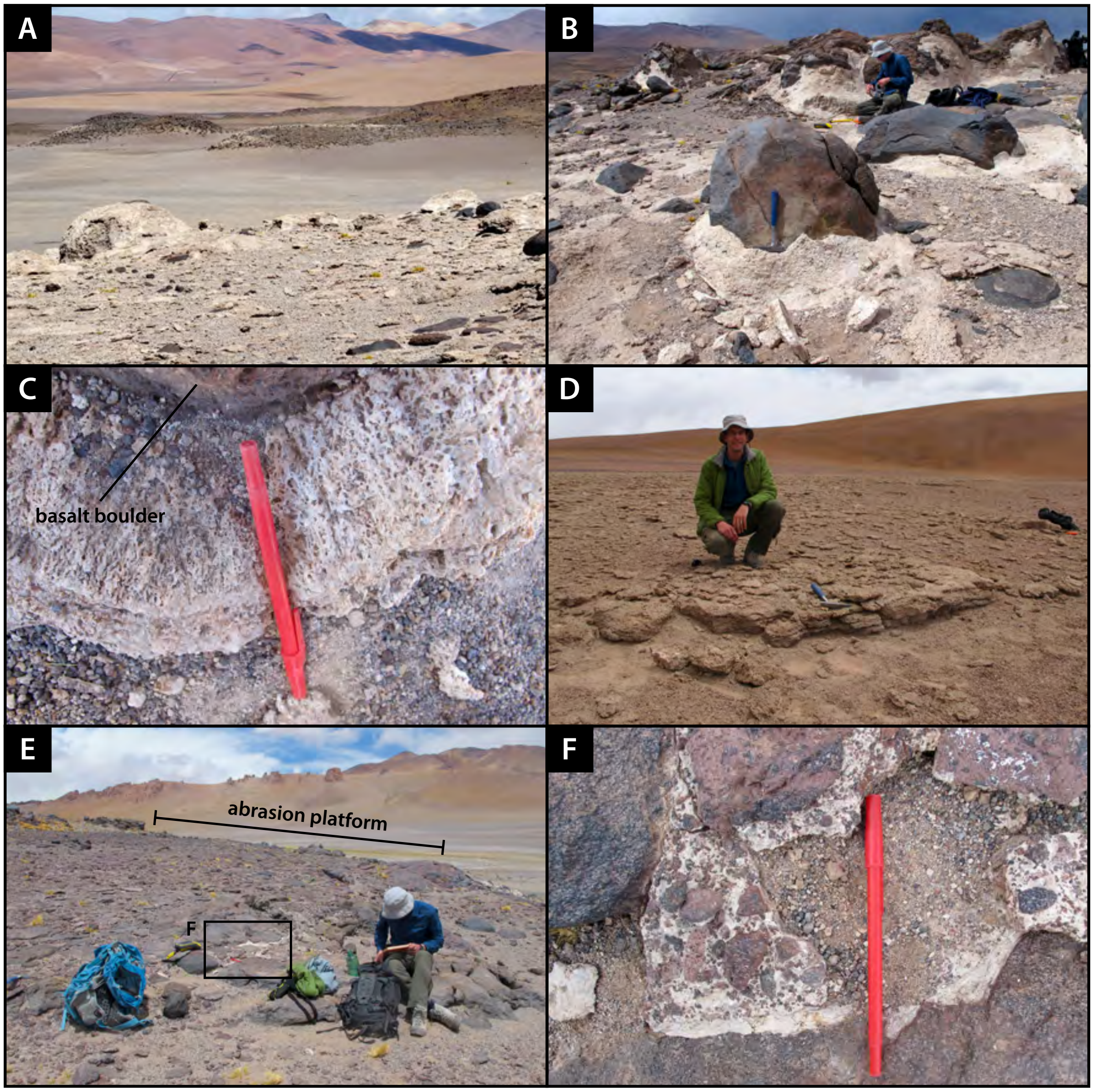

Figure 3-4: Photographs of encrusting floret tufa and caliche observed in Agua Caliente I. [**A**] Photo looking northeast from a tufa-encrusted bedrock hillside in the northern part of the basin. By volume, most tufa in this basin is of the floret variety. [**B**] The floret tufa drapes over all hillside surfaces, including boulders. [**C**] A close-up, cross-sectional view of a thick deposit of floret tufa coating a basalt boulder, showing a faint radial fabric. [**D**] The morphological expression of the floret tufa in the southern part of the basin, where the slope is more gently inclined and no basalt boulders are present. Here, the floret tufa geometry appears more tabular. [**E**] An abrasion platform carved into a hillside of exposed volcanic bedrock in the northern part of the basin. The platform is ~33 m in length, measuring from the top of the platform (4247.2 ± 0.8 m) to the bottom (4245.9 ± 0.8 m). Here, exposed caliche is observed at the base of the platform. [**F**] A close-up photo of the caliche observed at the location shown in Panel E. The carbonate crust only penetrates a few centimeters before reaching sand. Red pen is 15.5 cm in length.

shell) fragments and possibly carbonate fecal pellets are also observed in intact primary pore spaces (Figure 4-2E).

CALICHE.—A matrix-supported conglomerate can be found as a calcified crust in depressions between boulders of volcanic bedrock in flat or gently-sloping areas at the base of abrasion platforms (Figure 3-4E) and at the tops of bedrock hills at ~4242-4246 m elevation. The carbonate matrix binding poorly sorted, sub-rounded volcaniclastic pebbles and sand is fine-grained and patchy in color, from white to light brown (Figure 3-4F). The carbonate is also concretionary, forming coatings around grains and clasts. Accumulations of volcaniclastic sand and silt often cover the crust, which seems to be only a few centimeters thick. We hypothesize that these deposits are caliches (i.e., a soil carbonate formed by meteoric waters) based on these observations; however, stable isotope analysis is needed to confirm its origin.

CONE TUFAS.—Reef-like colonies of cone-shaped tufas that are ~10–20 cm in height and diameter are found along a narrow range of elevations (~4229–4234 m) in the basin. These cone tufas have a fan-like internal growth fabric of concentric bands linked by radially-oriented structures stemming from a narrow, mat-type holdfast. In some places, we find cones on top of floret tufa buildups, growing from holdfasts embedded in the uppermost layer of the floret tufa encrustation (Figure 3-5A). Cone spacing is irregular: some groups of cones appear to grow from holdfasts directly adjacent to one another to form an aggregate cone composed of 4+ smaller individual entities, whereas other cones are distributed more evenly across the substrate such that only their wide tops make contact. A gently undulated surface results from numerous cone tufas joining at their tops. Large gaps between cones have often been infiltrated with platey carbonate mud deposits.

In other locations, cone tufas are found on sandy substrate and do not form prominent reef-like colonies. This observation may reflect preservation issues rather than real differences in the megastructure of the cone tufas. We also observe that the aspect ratio of cones is variable. For instance, in the southernmost part of the basin where the bathymetric slope is more shallow, the cones tend to be shorter and wider (bowl-shaped). Like the tabular-shaped floret tufas, shorter and wider cones may also be indicate that the southern part of the basin was host to a higher-energy wave environment (James and Bourque, 1992). Due to their external geometry, these cone tufas may also indicate that water roughness was lower than the roughness of the preceding wave environment in encrusting floret tufa.

Conical tufas with clear biological textures are also described in the Uyuni basin of the Bolivian Altiplano (Rouchy et al., 1996) and the Miocene Ries Crater lake in Germany

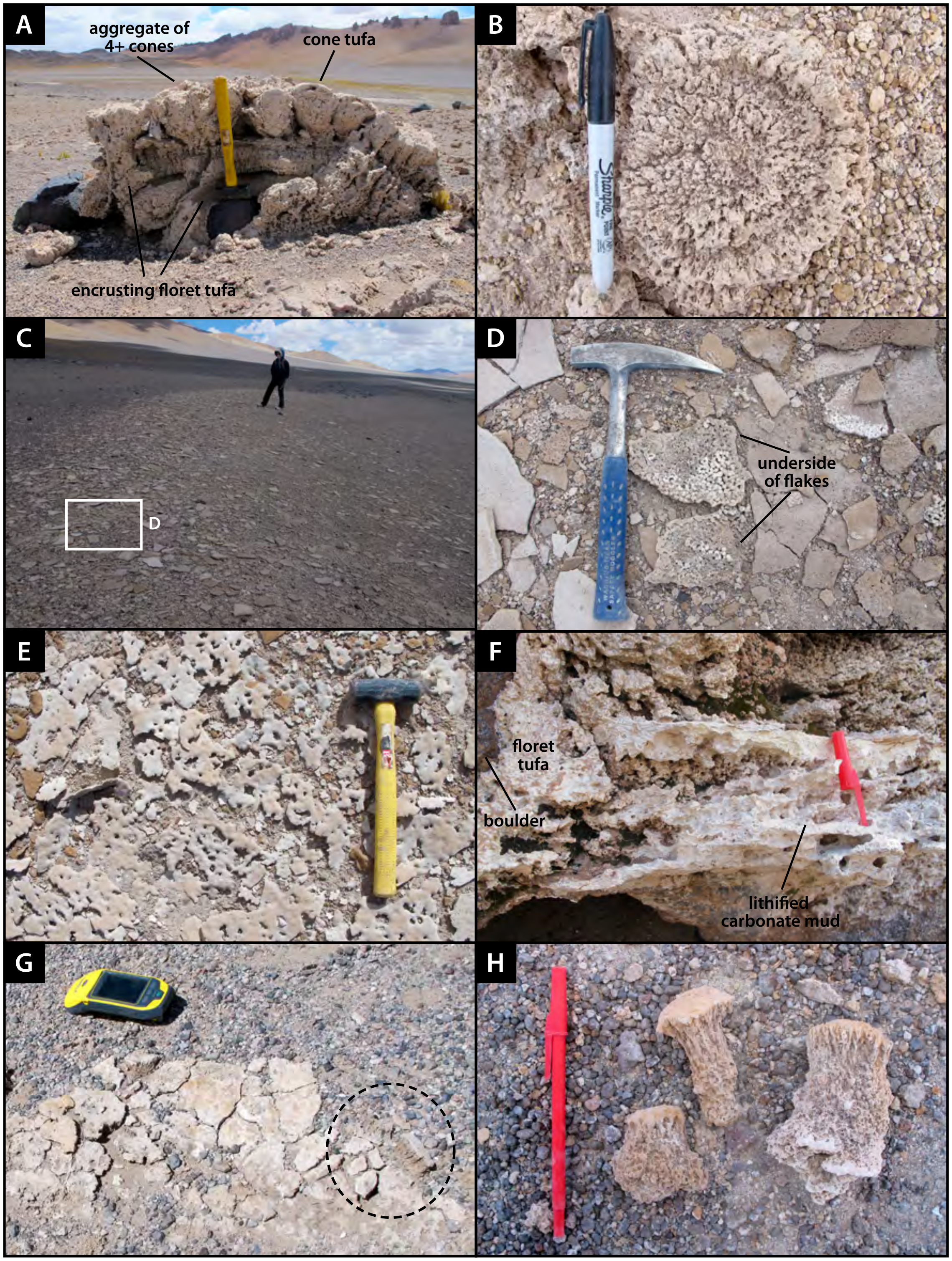

Figure 3-5: (Caption on the top of next page.)

Figure 3-5: (Figure on previous page.) [**A**] Photo of cone-shaped tufas on top of two distinct deposits of encrusting floret tufa. [**B**] Top-down view of a cone tufa, showing concentric growth structure. [**C**] Lighter-colored carbonate mud flakes stand out against darker volcaniclastic material, tracing a contour line of elevation. [**D**] The two flakes to the right of the hammer have been flipped over, showing that some undersides of mud flakes exhibit wiggly, possibly microbial textures. [**E**] Nodular forms of carbonate mud. [**F**] Layers of platey carbonate in association with encrusting floret tufa. [**G**] A continuous layer of carbonate mud capping floret tufa. Dashed circle highlights a few overturned pieces showing that the floret tufa is directly underneath. [**H**] A closer view of the carbonate-capped floret tufas, which look like mushrooms.

(Riding, 1979; Arp, 1995), but their external morphology and size differ from the cones observed in our study area. Regardless, we interpret the cones to also be of algal origin due to their structure.

PLATEY CARBONATE MUD FLAKES AND NODULES.—Broken plates of lighter-colored lithified carbonate marl stand out against the darker backdrop of volcaniclastic materials, and are often found tracing continuous elevational contour lines between 4218 and 4231 m elevation (Figure 3-5C). Sometimes, the undersides of these flakes exhibit a wiggly embossment, possibly of microbial origin (Figure 3-5D). In other locations, the lithified carbonate mud is more nodular in form (Figure 3-5E). It is unclear what conditions cause one morphology to form over the other, but the carbonate nodules often contain dendritic manganese oxide stains and tend not to incorporate much detrital material compared to the platey flakes, suggesting that the nodule morphology may be a result of carbonate replacement, rather than lithification, of muds and lake sediment. However, the nodular carbonates are rich with ostracod remains <1 mm in size, and may even be entirely ostracod-supported, suggesting that primary material in these carbonates still exists, even if they have been diagenetically altered.

Platey carbonates are also observed in association with other tufa varieties at elevations up to 4242 m (Figures 3-5F). Clear sedimentological cross-cutting relationships indicate that most, if not all, platey carbonates found in these areas were deposited at a time during or after the formation of encrusting floret and cone tufas. This temporal relationship is perhaps best demonstrated by the mushroom-like carbonates consisting of floret tufa capped by lithified carbonate mud (Figure 3-5G & H). When slabbed to expose a cross-sectional surface, these samples show that the carbonate capping material fills gaps between floret growths. Although this particular field relationship is apparent, we note that these platey carbonate flakes and nodules are diachronous, with some deposits likely forming more recently than others, especially those at lower elevations closer to the modern lake.

We also found platey carbonate nodules in Salar de Loyoques.

Transformed ikaite.—Aggregates of elongate prismatic crystal blades of calcium carbonate are found at many elevations in Agua Caliente I, from 4216 to 4242 m. Based on their crystal habit, these deposits are interpreted as being pseudomorphs of the metastable mineral ikaite, $CaCO_3{\cdot}6H_2O$ (Swainson and Hammond, 2001). Modern naturally-occurring ikaites are found mainly in marine environments (e.g., Buchardt et al., 1997, 2001) and less commonly in continental lacustrine and spring settings (e.g., Bischoff et al., 1993b; Oehlerich et al., 2013), but they are always observed in strict association with near-freezing water temperatures. When waters are warmed to temperatures above $\sim$4°C, ikaite crystals rapidly decompose to calcite plus water within minutes to hours (Suess et al., 1982; Jansen et al., 1987), producing a fragile, highly porous crystal mesh due to $\sim$70% volume loss during transformation (Shearman and Smith, 1985; Larsen, 1994). Thus, early diagenetic precipitation of a carbonate cement is needed to preserve the original ikaite crystal habit (Selleck et al., 2007). Transformed ikaites similar in morphology and setting to those observed in our study area include the thinolites described in the Lahontan and Mono Lake basins in the western United States, where they are interpreted to have formed at or below the sediment-water interface (Dunn, 1953; Shearman et al., 1989; Council and Bennett, 1993; Bischoff et al., 1993b, 1993a). Thus, the elevation of a transformed ikaite represents a minimum constraint on the elevation of lake level at the time of its formation.

In Agua Caliente I, transformed ikaites manifest as aggregates of irregularly arranged 0.5- to 10-cm-long pyramidal crystals and are generally found filling spaces that may have been eroded hollows within the floret tufa (Figure 3-6A & B). Carbonate-cemented detrital grains fill many gaps between individual prisms. In many instances, transformed ikaites are also found growing on top of and below deposits of platey carbonate. Thus, it is apparent that ikaite formation occurred during or after the deposition of the floret tufas and platey carbonates in these areas. However, like the platey carbonate mud flakes and nodules, the formation of the transformed ikaites in this basin is not necessarily synchronous. We also found one occurrence of a friable and highly porous transformed ikaite thinly buried beneath sediment at 4216 m elevation in the modern salar.

Transformed ikaites were also found at Salar de Loyoques and Laguna de Tara. In Salar de Loyoques, the pyramidal crystals tend to be better preserved and larger in diameter, exhibiting square prismatic morphology in some instances (Figure 3-6C). Although weathered on the outside, the insides of these transformed ikaites are very white and

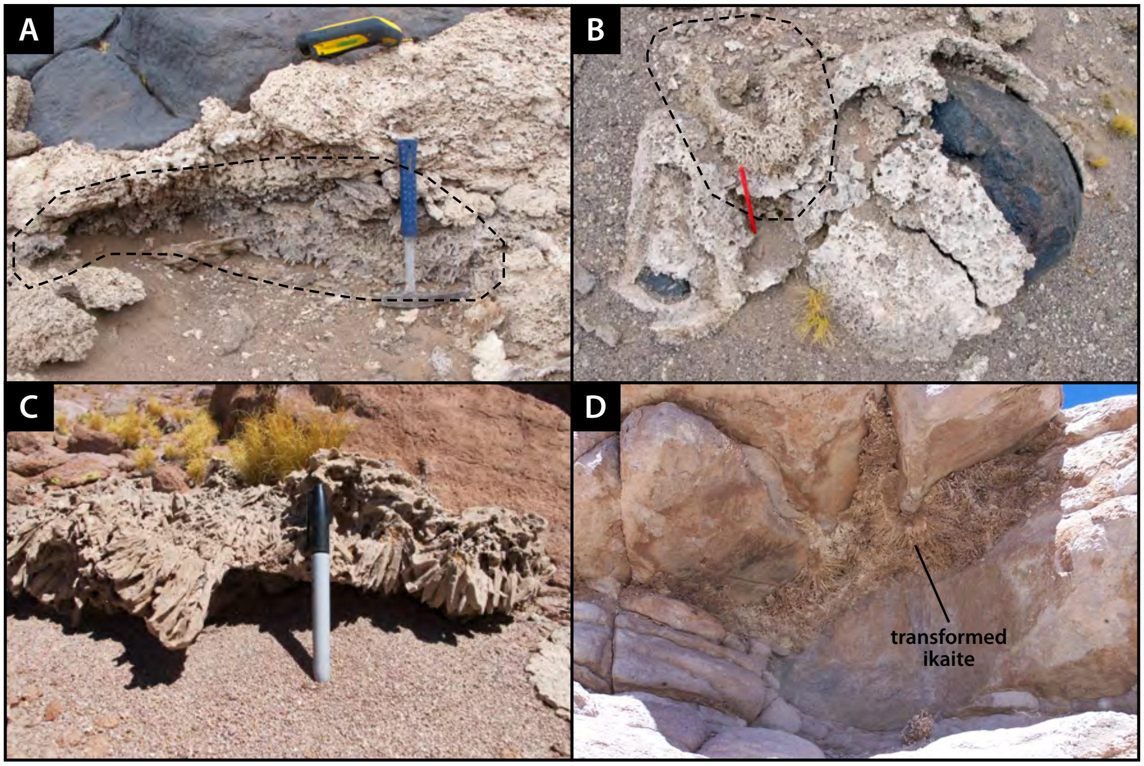

Figure 3-6: Photographical field context of the ikaite pseudomorphs observed in Agua Caliente I (A, B), Salar de Loyoques (C), and Laguna de Tara (D).

micro-crystalline. Interestingly, some transformed ikaites contain abundant ostracod remains. We also observe small, <2-mm-sized transformed ikaites embedded in carbonate nodules with sigmoidal crystal habit, exhibiting both square-prismatic and pyramidal faces. In Laguna de Tara, transformed ikaite is best preserved between crevices on the undersides of exposed bedrock overhangs (Figure 3-6D). Here, a secondary carbonate cement obscures the characteristic prismatic crystal habit of ikaite (Figure 3-8A). A slabbed surface reveals that the transformed ikaite crystals are white in color with few detrital grains, whereas the carbonate cement is pink and full sand-sized detrital material. The pink color of the cement likely comes from the pink-colored ignimbrite unit in which the Laguna de Tara basin sits. Transformed ikaites were the only variety of lacustrine carbonate collected from Laguna de Tara.

Honey calcite cement.—The origin of this carbonate phase, observed only in Agua Caliente I of the three basins in this study, is perhaps the most unique of all the encountered varieties of lacustrine carbonate in our study area. The honey calcite is named so because of its golden cloudy-translucent color. We describe it in more detail in Chapter 4.

3.6.2 U-Th dating of tufas and other lacustrine deposits

Our preliminary U-Th age dataset consists of 47 ages of carbonate deposits from Agua Caliente I (35 out of 47), Salar de Loyoques (6 out of 47), and Laguna de Tara (7 out of 47) (Table 3.2 & 3.3). Spectra from ATR-FTIR spectroscopy indicate that all lacustrine carbonates examined thus far from Agua Caliente I and Laguna de Tara are composed of calcite; mineralogical analyses have not yet been run for samples from Salar de Loyoques. High U concentrations ranging between 1 and 22 μg/g (average 7.1 ± 5.6 μg/g) and high ^{230}Th/^{232}Th ratios between 60 and 50,000 ppm (atomic ratio; average 3,100 ± 7,900 ppm) allow us to date deposits in our study area at high precision, with 2-σ uncertainties <200 years at 10–20 ka and <1000 years at 115 ka. These U concentrations are >2 times greater than the U concentrations of lacustrine carbonates from paleolakes in the Bolivian Altiplano (Placzek et al., 2006a).

Of these data, the most robust ages come from the honey calcite cement in Agua Caliente I (Figure 3-7A–E). We refer the reader to Chapter 4 for more details.

Unfortunately, we are not able to reliably reproduce an age for the encrusted floret tufa due to the pervasive infiltration of the honey calcite cement (Figure 4-2F). We obtained 15 U-Th ages from various spots on slabbed specimens of encrusting floret tufa that differ in their proportions of honey calcite and tufa. Although we do not know the exact fractional contribution of each phase in the sample powders, we can guess at their relative proportions through a qualitative assessment of the color of the drilled location. The sample that best isolates the floret tufa phase yields a U-Th age of 23,415 ± 64 yr BP with a high U concentration of ∼15 μg/g (Figure 3-7D; 4233.5 ± 0.8 m elevation). All other sample powders are mixtures with greater proportions of the honey calcite cement and yield ages that fall between this age and the 15.2–15.6 kyr BP age of the isolated honey calcite cements. Based on this data, the ∼23.5 kyr BP age for the encrusted floret tufa at this elevation should be considered a minimum age.

We also obtained U-Th ages from a carbonate nodule capping a floret tufa, a transformed ikaite, and pristine white carbonate within caliche from Agua Caliente I. However, such ages have not been reliably replicated yet due to possible sample heterogeneities or a low ^{230}Th/^{232}Th ratio (∼150 ppm atomic). The carbonate nodule has the highest U concentration for any sample measured thus far in Agua Caliente I, at ∼20 μg/g. Two preliminary ages from the caliche suggest that it is a more recently formed deposit (mid- to late-Holocene).

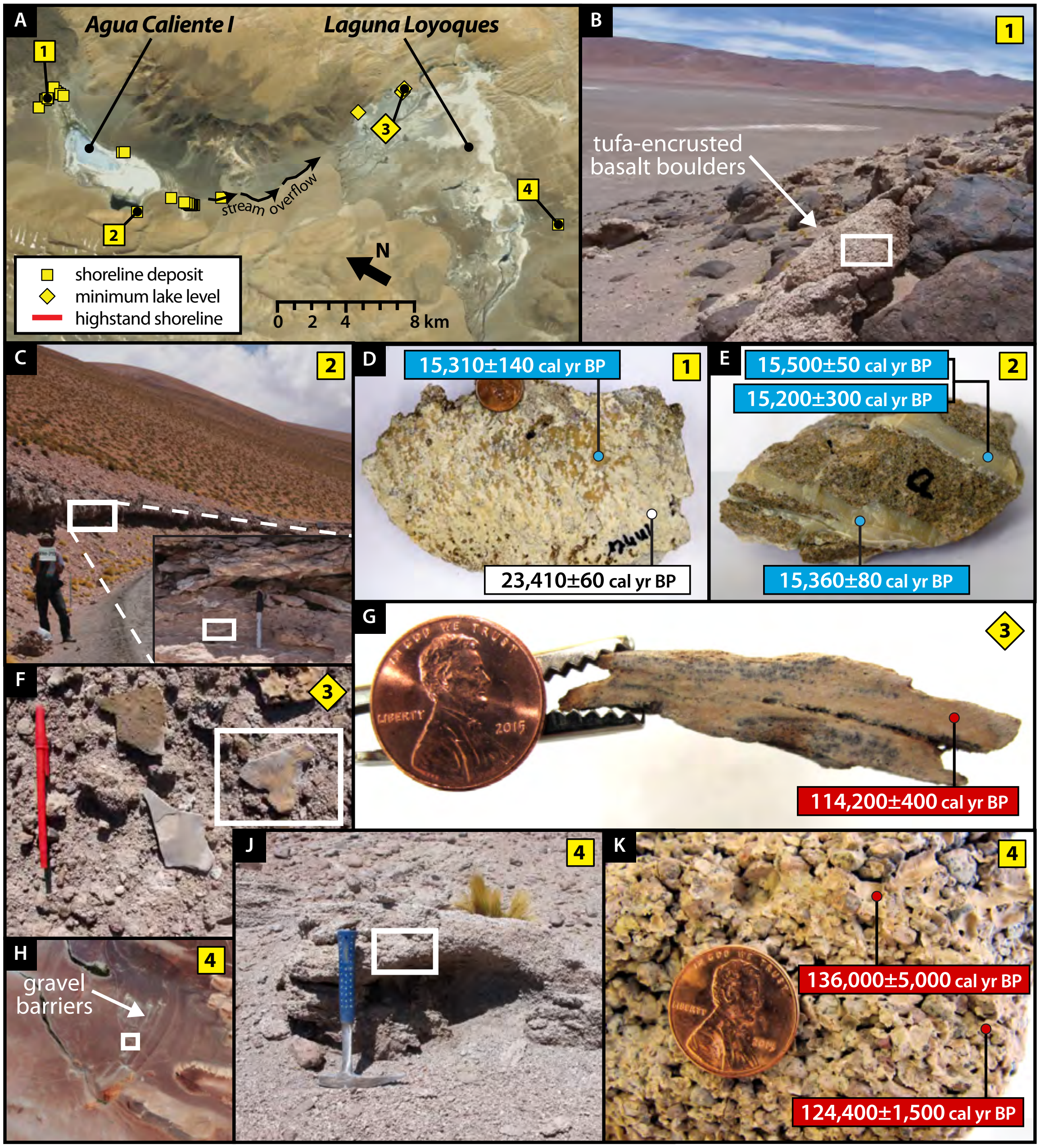

Figure 3-7: [**A**] Aerial imagery of Agua Caliente I and Laguna Loyoques, showing location of carbonate samples collected in January of 2015 and an approximate outline for the lake highstands, based on imagery and field observations. Numbered sites indicate locations of samples featured in Panels B-G. [**B**] Field photo of tufa-encrusted basalt boulders at Site #1. White box indicates the location of sample featured in Panel D. [**C**] Field photo of road cut exposing lacustrine carbonate material at Site #2. White boxes indicate location of sample featured in Panel E. [**D**] Cross-section of slabbed hand sample of tufa collected at location featured in Panel B, showing two phases of carbonate growth/deposition and their respective U-Th ages. [**E**] Hand sample of lacustrine carbonate (calcite) material and associated U-Th ages. [**F**] Field photo of platey carbonate found at Site #3. White box is [**G**], which is a cross-sectional view of the sample with its U-Th age. [**H**] Aerial imagery of gravel barriers at Site #4. White box indicates location of [**J**], which shows an outcrop of carbonate-cemented beach rock. White box indicates sampling location for [**K**], where carbonate cements were U-Th dated. The isochron method for calculating U-Th ages will need to be applied for the beach gravel cements in [K].

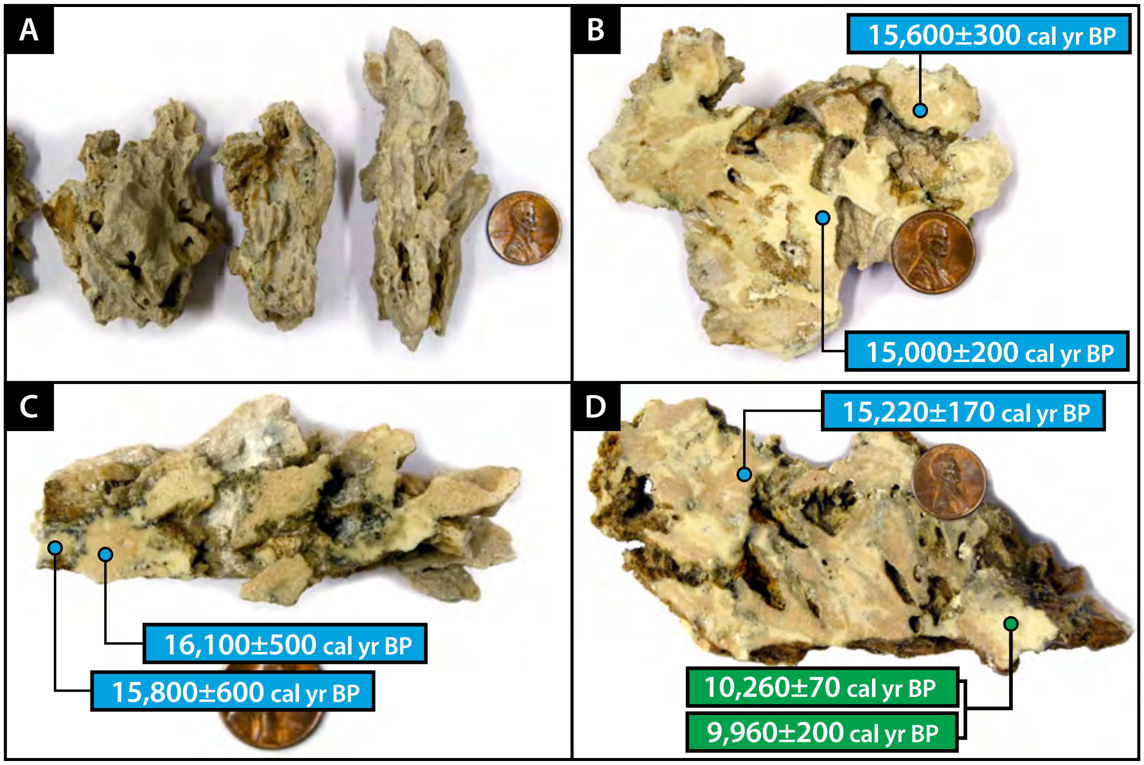

Figure 3-8: [**A**] Transformed ikaites from Laguna de Tara, showing that the prismatic crystal habits are obscured by a secondary cement. The remaining panels show U-Th ages from various spots on slabbed transformed ikaites. The transformed ikaite crystals are white, whereas the carbonate cements are pink due to incorporation of pink ignimbritic detrital material. Each sample shown was collected from different elevations: [**B**] 4334 m, [**C**] 4349 m, and [**D**] 4352 m. Note that elevations were measured with a Garmin GPS, not the Trimble Geo 7x. The elevation of the modern lake is ~4322 m according to Google Earth.

In Laguna de Tara, all U-Th ages are from three samples of transformed ikaite spanning an elevational range of ~20 m (4334–4352 m elevation). Of all the tufa varieties in this study, these samples have the lowest ^{230}Th/^{232}Th ratios (60 to 550 ppm, atomic ratio). The ^{230}Th/^{232}Th ratios of the pink cements were consistently 25–50% lower than adjacent carbonate cements, consistent with the observation that these cements incorporate a significant amount of pink ignimbritic detrital material. For the two samples lowest in elevation, the U-Th ages fall within the range of 15 and 16 kyr BP for both the transformed ikaite crystals and the surrounding cements (Figure 3-8B, C). The highest sample yields an age of around ~10.0–10.3 kyr BP for the transformed ikaite and ~15.2 kyr BP for the cement (Figure 3-8D).

With the available geochronological data, it is unclear if the cement and transformed ikaites in the highest two samples formed simultaneously, or if the cement arrived shortly after ikaite formation. If their formation was coincident, it may suggest that carbonate replacement of the original ikaite occurred while the crystals were still below the sediment-water interface. The replicated ~10.0–10.2 kyr BP age for the transformed ikaite at lower elevation suggests that there are multiple stages of ikaite formation in this basin. The U-Th age for the cement in this sample is closely aligned with the age of the cements for the other two samples, suggesting that cement formation may have occurred simultaneously over the 20-m elevational range covered by these samples. More replication of ages is needed to determine the precise sequence of carbonate deposition in Laguna de Tara.

In Salar de Loyoques, we obtained U-Th ages from transformed ikaites (Figure 3-6C), platey carbonate nodules (Figure 3-7F & G), and carbonate cements from beach gravels (Figure 3-7H–K). The transformed ikaites are very clean, with high ^{230}Th/^{232}Th ratios (>10,000 ppm atomic). Similar to the carbonate nodule in Agua Caliente I, the carbonate nodule dated in Salar de Loyoques has a high U concentration of ~22 µg/g. Our preliminary U-Th ages fall between 110 and 140 kyrs BP, but these data have not yet been reliably replicated. More work is needed to determine if age discrepancies within samples are due to true sample heterogeneities, incorrect assumptions for the initial detrital Th correction, or problems with procedural blanks or cross contamination in chemistry. The age from the beach gravel cement will be of particular interest, given that it was sampled from a gravel barrier located ~70 m above the modern salar. Furthermore, the beach gravel cement is one of the few lacustrine carbonate samples in our study that is directly associated with a paleoshoreline feature, making its age a robust indicator of the timing of lake expansion in this basin. We anticipate using the isochron method for obtaining a U-Th age of the beach gravel cement material due to its low ^{230}Th/^{232}Th ratio.

We briefly describe differences in the $\delta^{234}U_{\mathrm{initial}}$ values of lake carbonates between the basins in Section 3.9.3.

3.6.3 Stable isotope composition of deposits

Table 3.4 lists the stable isotope compositions of samples from Agua Caliente I and Laguna de Tara. In Agua Caliente I, the δ^{13}C and δ^{18}O of encrusting floret tufas, transformed ikaites, and the honey calcite cement fall within a narrow range of values: +0 to +3‰ (VPDB) for δ^{13}C and +1.0 to +2.5‰ (VPDB) for δ^{18}O (Figure 3-11). The platey carbonate nodules are the only samples that yield negative δ^{13}C values (-3 to -1‰, VPDB). The stable isotope composition of material that sampled both the honey calcite and encrusted floret tufa phases generally fall within a 'mixing line' between two end member compositions, with some nuances. The transformed ikaites from Laguna de Tara occupy an even narrower range of values: +2.5 to +3.5‰ (VPDB) for δ^{13}C and +0.6 to +1.1‰ (VPDB) for δ^{18}O. We do not yet have information on the stable isotope composition of the carbonate in the caliche or cone tufas from Agua Caliente I, nor for any samples from Salar de Loyoques.

Based on the negative δ^{18}O values for modern precipitation (IAEA/WMO, 2015) and nearby groundwater (Rissmann et al., 2015), the positive δ^{18}O values of the carbonates analyzed thus far are an indication of lacustrine origins.

3.6.4 Paleoshoreline features and magnitude of lake area changes

We refer the reader to Section 3.9.4 for details regarding the paleoshorelines features examined in our study. In each basin, the elevations of the highest of these paleoshorelines were used for paleolake area calculation. Table 3.1 lists our estimates for modern lake and paleolake areas for our three lake basins (see Figure 3-14 for area outlines on a map). Agua Caliente I and Laguna de Tara experienced ∼4–5 factor increases in lake area associated with 30–35 m elevational increases in lake level. The expansion observed in Salar de Loyoques was much greater: Based on the elevation of the highest gravel barrier identified in the southern part of this basin via satellite imagery, Salar de Loyoques increased in area by a factor of ∼19 relative to present, rising 70 m and merging with the Agua Caliente I lake basin. Of further note: Paleoshoreline evidence of this large paleolake in Salar de Loyoques only exists on the eastern margin of the basin. The contour of elevation representing this lake overlaps alluvial fans showing no evidence of lake incision all along the southern and western parts of the lake (Figure 3-14). Thus, accumulation of these alluvial fans must have occurred after the lake in Salar de Loyoques regressed to lower elevations.

3.7 Discussion

3.7.1 Relative temporal constraints on lake carbonate and paleoshoreline formation in Agua Caliente I

As of yet, there are not enough U-Th age constraints to determine the exact sequence of carbonate and paleoshoreline formation in Agua Caliente I. However, some relative constraints can be made purely from field observations. For example, at least two generations of encrusting floret tufa must be older than the cone tufas (Figure 3-5A), and the honey calcite, which is likely synchronous throughout the basin, must be younger than both of these tufa varieties (Figures 4-2 & 4-1). Our U-Th ages confirm this relative relationship between the honey calcite and the floret tufa (Section 3.6.2). All ikaites observed thus far formed after the encrusting floret tufas (Figure 3-6A & B), and the nodular carbonate caps are clearly younger than their floret tufa counterparts (Figure 3-5G & H). However, it is clear that not all ikaites in the basin are the same age: The honey calcite cement can be found in association with some transformed ikaite formations and not others. Likewise, the various carbonate mud flakes and nodules throughout the basin are most likely diachronous.

In relation to various paleoshorelines, reworked floret tufas with carbonate caps were found on top of a gravel barrier in the northeast part of the basin (Section 3.9.4). When linking paleoshoreline features with specific tufa or carbonate deposits, we must remember that the abrasional platforms and alluvial fan incisions represent the cumulative occupation of a lake at that elevation; the lake could have risen to the elevation of those features multiple times in the past. The gravel barriers most likely represent regressive or fluctuating lake levels, since constructional transgressive features are rarely preserved due to reworking of sediments upon inundation. One observation of interest is that the cone-shaped tufas occupy the same elevational range as the lower sets of gravel barriers and the lower alluvial fan incision with residual salt deposits (Figure 3-3 & Section 3.9.4). It is possible that these features are synchronous.

Only further careful U-Th dating of samples with clear stratigraphical relationships and additional field observations will clarify the temporal relationship of carbonate and shoreline features in this lake basin.

3.7.2 U-Th ages of tufa and carbonate deposits and their implications for past lake level changes

Due to the ambiguous temporal relationships between deposits as described above and the lack of independent age constraints on paleoshoreline landforms, linking the U-Th ages of tufa and carbonate deposits to a paleolake area is challenging. Although the encrusting floret and cone-shaped tufas are likely of algal origin, the absolute water depth of tufa formation is uncertain given that it is extremely difficult, if not impossible, to identify a modern analogue of the species of algae responsible for forming the tufa. The elevational range of the encrusting floret tufa is also quite large at ∼20 m, and it is unclear if each generation of floret growth covered part or the whole of this range (Figure 3-3). Although potentially useful as a paleosalinity indicator, species identification of the ostacod shells found in floret tufa pore spaces (Figure 4-2G & H) and within carbonate nodules may not be helpful for interpreting paleowater depths, given that a single species can be found in a wide range of depths in both lacustrine and marine settings (e.g., Benson, 1984; De Deckker, 2002).

There is also evidence for lake level fluctuations that are not captured by a shoreline carbonate deposit. For instance, reworked pebble-sized pieces of tufa with the honey calcite cement were found at the base of the alluvial fan incision in the southeast (Section 3.9.4 and Figure 3-13D), indicating that water levels must have risen to that elevation at some point after ∼15 ka, a period from which we have yet to find material. We must recognize that carbonate and tufa formation represent a discontinuous record and are not only dependent on lake levels, but also influenced by factors such as the concentration of calcium and carbonate in lake waters and groundwater inputs; salinity; mean annual and seasonal temperatures; biological productivity and nutrient supply; and other lake chemistry characteristics (Gierlowski-Kordesch, 2010).

Consider the observation that biologically-mediated tufas are not conspicuously forming in Agua Caliente I today, even though a lake clearly exists in the basin. At least two conditions are necessary for tufa development: (1) the existence of an algal or bacterial mat, and (2) sufficient concentrations of calcium and carbonate ions to allow for microbially-induced precipitation of carbonate during photosynthesis (Golubic, 1973), as well as trapping of clastic carbonate particles. It is possible that tufa formation in this basin occurs only when the waters from the hot springs in the southwest, where the only obvious signs of modern microbial activity occur, mix with the waters from the freshwater springs in the north. In Pyramid Lake, Nevada, similar mixing zones between nutrient-rich thermal spring waters and alkaline lakes are prime areas of microbialite formation (Arp et al., 1999). Presently, the waters from the hot springs and the spring-fed lake are separated into two sub-basins. Although we have no water chemistry data to test our hypothesis, it is possible that the spring-fed lake and thermal spring waters possess the condition that is lacking in the other water body that is necessary for tufa development. Thus, when these two water bodies combine, tufas may be able to form. This hypothesis is consistent with the fact that no tufas of clear biological origin have been found thus far in Salar de Loyoques and Laguna de Tara, basins for which we have not yet found any evidence for past or present hot spring activity. However, we know that calcium carbonate concentrations in the lake must have been high enough in the past for ikaite and carbonate nodule formation. These observations support the idea that the hot springs in Agua Caliente I is unique, long-lived, and critical for tufa formation. If the hot springs were to shut off, higher lake levels may not necessarily induce tufa formation. Other confounding factors such as salinity and temperature could prevent tufa formation even if the thermal spring and lake waters are able to mix.

We must also consider that the role of the presently inactive stream channel and sill elevation remains unclear, given that we have not found deposits in Agua Caliente I that date to >100 ka, nor material in Salar de Loyoques with ages from the last 30 ka. There is strong evidence showing that the sill elevation between these two basins has changed over the last 200 ka: According to satellite imagery, accumulation of alluvial fans has occurred since the regression of the large >100 ka lake in Salar de Loyoques (Section 3.6.4 and Figure 3-14). The stream channel incision at the foot of these younger, converging alluvial fans is the most recent change to the sill elevation. At its present elevation of 4240.5 ± 1.1 m (Figure 3-3 & Section 3.9.4), the sill is lower than some encrusting tufa deposits in Agua Caliente I. Observations and elevational measurements of the stream channel base indicate that channel incision occurred via flow into the Salar de Loyoques basin (Section 3.9.4); however, our current body of evidence is not sufficient to prove that a higher lake in the Agua Caliente I basin overflowed into Salar de Loyoques to create this channel, and we do not know to what elevation Salar de Loyoques would have filled from such an overflow. Thus our estimate of the highstand lake area for Agua Caliente I, which assumes no overflow, is a minimum estimate of lake expansion.

Despite these uncertainties, we are still able to make reasonable assumptions on lake level changes in each basin. The carbonate cements from the beach gravels in Salar de Loyoques are perhaps the only dateable material that is in direct association with a paleoshoreline feature; thus, we are certain that the lake that existed at some point before 100 ka represents a large lake ∼19 times the size of the water bodies currently occupying the Salar de Loyoques and Agua Caliente I basins. Both the tufa formations and transformed ikaites provide a minimum bound on former lake levels, with ikaites growing at or directly beneath the sediment-water interface and algal reefs forming at or below the water surface.

In Laguna de Tara, U-Th ages for the transformed ikaite crystals and surrounding cements align with H1 and the earliest Holocene, shortly after the Younger Dryas (YD;

Figure 3-9D). During both of these periods, Laguna de Tara expanded to at least 5 times its modern area. In Agua Caliente I, the honey calcite cement also yields U-Th ages that coincide with H1. Although the nature of this phase is complex, our present working hypothesis is that the honey calcite is a "spray-zone" deposit precipitating from lake waters that intermittently spray over the tufa formations, beach sands, and gravels via wave action (Section 4). Although the exact water level represented by these deposits is unclear, the area of the H1 lake in Agua Caliente I must have been at least 1.5–2 times the area of the modern lake, based on the elevation of the lowest occurrence of the honey calcite cement. The ∼23.5 ka minimum age from the best isolated encrusting floret tufa material may indicate the presence of a higher lake during H2 and may be related to the uppermost paleoshoreline features observed in Agua Caliente I, but more U-Th age replication is necessary before drawing these conclusions.

Although the expansion observed in Salar de Loyoques is impressive, we note that we must calculate the ratio between the lake area and corresponding drainage basin area for each lake before making comparisons. This ratio normalizes lake systems by their size and is directly proportional to total annual precipitation (Hudson and Quade, 2013).

3.7.3 Comparison with shoreline and sediment core records from the Titicaca-Uyuni and Miscanti lake basins

The H1 and possible H2 lake level increases in the Agua Caliente I and Laguna de Tara basins coincide with the Tauca highstand and Sajsi lake stage in the Titicaca-Uyuni basin, which is recorded in both lake sediment records (Baker et al., 2001) and shoreline studies (Placzek et al., 2006b, 2013; Blard et al., 2011; Figure 3-9C). The ∼10.0–10.3 kyr BP age of transformed ikaite crystals in the highest sample from Laguna de Tara suggest that the lake was also larger shortly after the YD. No robust U-Th ages from Agua Caliente I dating to around the YD are available, though some preliminary U-Th dating of transformed ikaite from Agua Caliente I may have formed at this age. Our preliminary data further support the finding that the highest lake levels on the Altiplano-Puna plateau coincided with Heinrich events, not maxima in local summer insolation. It is of great interest to determine if the lake highstand in Salar de Loyoques coincided with H11 or with one of the two highest maxima in summer insolation over the last 200 ka. It is possible that the dominance of influence by Heinrich events in the last 100 ka is due to the modulating effect of eccentricity on the amplitude of precessional insolation changes, which has been small

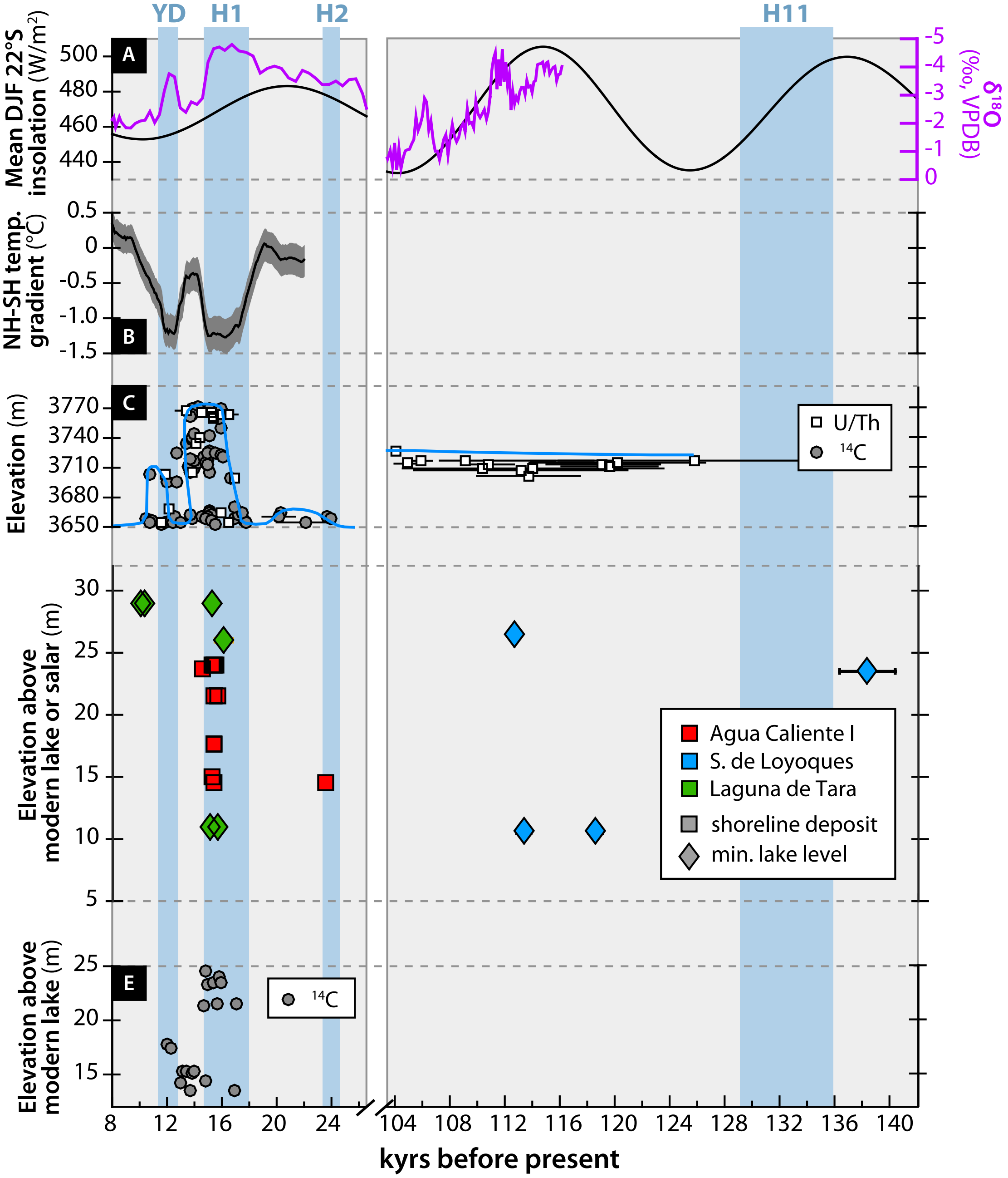

Figure 3-9: [**A**] Mean DJF insolation at 22°S (black; Laskar et al., 2004) and the $\delta^{18}O$ record Botuverá Cave (purple; Cruz et al., 2005; Wang et al., 2007). [**B**] Interhemispheric temperature gradient, with uncertainty (Shakun et al., 2012). [**C**] Lake level history for the Poopo, Coipasa, and Uyuni basins in southern Bolivia (15-22°S; Placzek et al., 2006b). [**D**] Preliminary U-Th dates of shoreline tufa (squares) and other lacustrine deposits (diamonds) from Agua Caliente I (red), Salar de Loyoques (blue), and Laguna de Tara (green) (22-23°S), plotted against their elevation relative to the modern lake or salar. [**E**] Laguna Bebedero ^{14}C dates of shoreline tufas (33°S). Period for H11 is defined by Cheng et al. (2009).

over this interval of time.

We present these conclusions tentatively, for there are several caveats to acknowledge. As discussed previously, the tufa formations and other shoreline deposits may not necessarily capture every lake level fluctuation that occurs in a basin. The growth of algal or microbial mats and subsequent preservation of such organisms as tufa formations may only occur under a limited set of conditions involving temperature, salinity, dissolved inorganic carbon and calcium ion concentrations, *et cetera*. Such caveats and uncertainties provide motivation for further work combining shoreline studies with continuous records from lake sediment cores.

Assuming that these Central Andes lakes are truly only responding to Heinrich Events, contrasting records at lower elevations which are affected by both precessional insolation cycles and these millenial-scalecold events, then the following question arises: Why? One possibility is that the Central Andes may only be sensitive to the most extreme southward displacements of the ITCZ, given that it is located at the modern day southern edge of SASM. Indeed, Heinrich Events and other cold North Atlantic events that dramatically increase the interhemispheric temperature gradient are associated with the largest shifts in ITCZ position (Donohoe et al., 2013; McGee et al., 2014). A second possibility is that these lake level changes are responses to changes in Southern Hemisphere westerly jet dynamics. Chiang et al. (2014) suggest that North Atlantic cooling may cause weakened and more zonally symmetric Southern Hemisphere subtropical westerly winds, which also move poleward. This weakening and poleward shift of the subtropical westerly finds then allows for more convection and advection of moisture onto the Altiplano-Puna plateau.

3.8 Conclusions

Our preliminary U-Th data and shoreline mapping suggests that lake levels in Agua Caliente I and Laguna de Tara were significantly higher than present levels during H1. Agua Caliente I may have also been higher during H2, but further replication of U-Th ages is needed. In Salar de Loyoques, we have evidence for a large lake that incorporated the Agua Caliente I lake basin existing at some time before 100 kyrs ago. Further U-Th dating will determine if this lake corresponds to local summer insolation highs or H11. With increases in lake level coinciding with H1, we have extended the known region of SASM influence southwards from the Titicaca-Uyuni lake system.

We have yet to take full advantage of the numerous observed field relationships between different tufa varieties in Agua Caliente I. Applying U-Th dating to carbonates with clear stratigraphical relationships will allow us to develop a more nuanced picture of lake level changes in these basins. After better understanding these field relationships and their implication for past lake levels, as well as further replicating U-Th ages, the next step will be to develop basin-specific water balance models to determine the magnitude of precipitation and evaporation changes that would be necessary to create such large lakes. We plan to follow and adapt the methods described in other papers for GIS watershed analysis (Hudson and Quade, 2013) and the water balance model (Blard et al., 2009; Placzek et al., 2013). Such a model will need to pay special attention to the impacts of groundwater flow into and out of the basins. Temperature constraints necessary to determine evaporation rates will be gleaned from studies on local glaciers and possibly pollen records, as well as experimental clumped isotope analyses on the lake carbonates in our study. Such quantitative constraints on past rainfall will be useful for proxy-model comparisons of general circulation models that are currently used for future projections of precipitation under a warming climate. Although there remain many unknowns, we feel confident that applying the these same methods to a series of 6 lakes along a north-south transect in northern Chile will ultimately allow us to create a spatio-temporal map of water balance changes over the late Pleistocene.

There are also several potential avenues for geomorphology-inclined research pertaining to the paleoshorelines and alluvial fans in these basins, which we describe in Section 3.9.5. We also plan to conduct radiocarbon (^{14}C) analyses on lake carbonate materials from Agua Caliente I and Laguna de Tara to constrain the reservoir effect in these basins, which will be useful for any future work on lake sediment cores.

Acknowledgements

We thank Rick Kayser at MIT and Soumen Mallick at Brown University for their help with mass spectrometry; Ashling Neary for running the ATR-FTIR carbonate mineralogy measurements; Elena Steponaitis, Irit Tal, and Ben Hardt for lab chemistry assistance; and Tim Grove and Ben Mandler for petrographic scope assistance. Weifu Guo assisted C.Y.C. in making the stable isotope measurements at WHOI. Discussions with Kristin Bergmann, Adam Hudson, and Elena Steponaitis on tufa microfacies interpretation were insightful. We also thank Kim Huppert, Roger Fu, Justin Stroup, Francisco (Pancho) Gonzales, Héctor Orellana, and Marty Pepper for field assistance. Claudio Latorre and Blas Valero Garces both provided crucial advice on conducting field work in Chile. This work was supported by the NSF Graduate Research Fellowship, MIT Ida Green Fellowship, MIT EAPS Grayce B. Kerr Fellowship, MIT EAPS Callahan-Dee Fellowship, MIT EAPS Student Research Fund, MIT International Science and Technology Initiatives (MISTI), WHOI Ocean Ventures Fund, and the Comer Science and Education Foundation.

Table 3.2: Locations and descriptions of tufa and other lacustrine carbonate samples from Agua Caliente I, Salar de Loyoques, and Laguna de Tara. **Sample Name** is the original name of the sample and is referred to in the text of the paper. Corresponding **ID numbers** are referenced in figures. Reported coordinates and elevations of samples from Agua Caliente I and Salar de Loyoques were measured using the Trimble GEO 7x device. Coordinates and elevations of samples from Laguna de Tara were measured using a less precise Garmin GPS device. Mineralogy was determined using ATR-FTIR spectroscopy. Empty spaces indicate that a measurement has not yet been made for that attribute on that sample.

Sample Name	**ID No.**	**Latitude** (°)	**Longitude** (°)	**dGPS Elev.** (m)	**Vert. Prec.** (m)	**Mineralogy**	**Description**
Agua Caliente I							
AD10-225(B)	1	-23.084303	-67.401078	4233.5	0.8	calcite	white porous tufa
AD09-98(D)	2	-23.083391	-67.407970	4240.6	0.8		white porous tufa
AD10-233a(A)	3	-23.174139	-67.399202	4243.0	0.9	calcite	honey calcite
AD10-233a(A)	4	-23.174139	-67.399202	4243.0	0.9	calcite	honey calcite
AD10-233a(B)	5	-23.174139	-67.399202	4243.0	0.9	calcite	honey calcite
AD10-225(A)	6	-23.084303	-67.401078	4233.5	0.8	calcite	honey calcite in tufa
CYC15-049(A)	7	-23.160174	-67.397851	4242.7	0.9		honey calcite cementing beach sand
AD09-98(A)	8	-23.084021	-67.406679	4234.0	2.0	calcite	mixture of honey calcite and white tufa
AD09-98(A)	9	-23.084021	-67.406679	4234.0	2.0	calcite	mixture of honey calcite and white tufa
AD09-98(B)	10	-23.084021	-67.406679	4234.0	2.0		mixture of honey calcite and white tufa
AD09-98(C)	11	-23.084021	-67.406679	4234.0	2.0		mixture of honey calcite and white tufa
AD10-228(A)	12	-23.085568	-67.402128	4236.6	0.8	calcite	mixture of honey calcite and white tufa
AD10-228(C)	13	-23.085568	-67.402128	4236.6	0.8	calcite	mixture of honey calcite and white tufa
AD10-228(D)	14	-23.085568	-67.402128	4236.6	0.8		mixture of honey calcite and white tufa
AD09-95(A)	15	-23.083391	-67.407970	4240.6	0.8	calcite	mixture of honey calcite and white tufa
AD09-95(B)	16	-23.083391	-67.407970	4240.6	0.8	calcite	mixture of honey calcite and white tufa
AD09-95(C)	17	-23.083391	-67.407970	4240.6	0.8	calcite	mixture of honey calcite and white tufa
AD09-95(D)	18	-23.083391	-67.407970	4240.6	0.8		mixture of honey calcite and white tufa
AD09-95(E)	19	-23.083391	-67.407970	4240.6	0.8		mixture of honey calcite and white tufa
AD09-100(A)	20					calcite	mixture of honey calcite and white tufa
AD09-100(B)	21						mixture of honey calcite and white tufa
AD09-221(A)	22						mixture of honey calcite and white tufa

Continued on next page

Table 3.2 – continued from previous page

Sample Name	**ID No.**	**Latitude** (°)	**Longitude** (°)	**dGPS Elev.** (m)	**Vert. Prec.** (m)	**Mineralogy**	**Description**
AD10-226(A)	23	-23.082755	-67.401042	4237.2	3.6	calcite	ikaite pseudomorph
AD10-226(A)	24	-23.082755	-67.401042	4237.2	3.6	calcite	ikaite pseudomorph
AD10-226(B)	25	-23.082755	-67.401042	4237.2	3.6		ikaite pseudomorph
AD09-99(A)	26	-23.084264	-67.406469	4228.8	0.8	calcite	platey carbonate nodule
AD09-99(B)	27	-23.084264	-67.406469	4228.8	0.8		platey carbonate nodule
AD09-221(B)	28					calcite	platey carbonate nodule
AD09-96(A)	29						platey carbonate nodule(?)
AD09-96(A)	30						platey carbonate nodule(?)
AD09-96(B)	31					calcite	platey carbonate nodule(?)
CYC15-016A(A)	32	-23.085533	-67.400864	4244.8	0.9		white, clean calcite infilling(?)
CYC15-016B(A)	33	-23.085533	-67.400864	4244.8	0.9		white, clean calcite infilling(?)
AD09-101(A)	34					calcite	ambiguous
Salar de Loyoques							
CYC15-047(A)	35	-23.301139	-67.264143	4251.0	1.7		carbonate cementing beach gravel
CYC15-047(B)	36	-23.301139	-67.264143	4251.0	1.7		carbonate cementing beach gravel
CYC15-025AA(A)	37	-23.202370	-67.270781	4192.6	1.0		ikaite pseudomorph
CYC15-025AA(B)	38	-23.202370	-67.270781	4192.6	1.0		ikaite pseudomorph
CYC15-022A(A)	39	-23.202575	-67.272532	4205.5	1.1		ikaite pseudomorph
CYC15-021A(A)	40	-23.202267	-67.272589	4208.5	2.5		platey carbonate nodule
Laguna de Tara							
AD10-246(A)	41	-23.030042	-67.347418	4334	–	calcite	ikaite pseudomorph
AD10-246(B)	42	-23.030042	-67.347418	4334	–	calcite	ikaite pseudomorph
AD10-245(A)	43	-23.029639	-67.348633	4349	–	calcite	ikaite pseudomorph
AD10-245(B)	44	-23.029639	-67.348633	4349	–	calcite	ikaite pseudomorph
AD10-244(A)	45	-23.027097	-67.352499	4352	–	calcite	ikaite pseudomorph
AD10-244(A)	46	-23.027097	-67.352499	4352	–	calcite	ikaite pseudomorph
AD10-244(C)	47	-23.027097	-67.352499	4352	–	calcite	ikaite pseudomorph

Table 3.3: U-Th dating results of carbonates examined in this study. In the ID number column, a '$*$' symbol indicates that the powder dated is a mixture of two phases of carbonate and does not represent an age linked to a specific geologic or hydrologic event. A '†' symbol indicates that the reliability and interpretation of the age as being representative of a specific event is unclear due to factors such as ambiguous sample context, high blank corrections, or low ^{230}Th/^{232}Th ratios, and requires further investigation and replication. [a]Reported errors for ^{238}U and ^{232}Th concentrations are estimated to be ±1% due to uncertainties in spike concentration; analytical uncertainties are smaller. [b]δ^{234}U = ([^{234}U/^{238}U]$_{\text{activity}}$ - 1) × 1000. [c][^{230}Th/^{238}U]$_{\text{activity}}$ = 1 - $e^{\lambda_{230}T} + (\delta^{234}U_{\text{measured}}/1000)[\lambda_{230}/(\lambda_{230} - \lambda_{234})](1 - e^{-(\lambda_{230}-\lambda_{234})T})$, where T is the age. "Uncorrected" indicates that no correction has been made for initial ^{230}Th. [d]Ages are corrected for detrital ^{230}Th assuming an initial ^{230}/^{232}Th of $(4.4\pm2.2)\times10^{-6}$. [e]δ^{234}U$_{\text{initial}}$ corrected was calculated based on ^{230}Th age (T), i.e., $\delta^{234}\text{U}_{\text{initial}} = \delta^{234}\text{U}_{\text{measured}} \times e^{\lambda_{234}T}$, where T is the corrected age. [f]B.P. stands for "Before Present" where the present is defined as January 1, 1950 C.E. Decay constants for ^{230}Th and ^{234}U are from Cheng et al. (2013a); decay constant for ^{238}U is 1.55125×10^{-10} yr^{-1} (Jaffey et al., 1971).

ID No.	^{238}**U** (ng/g)[a]	^{232}**Th** (pg/g)[a]	δ^{234}**U** (‰)[b]	^{230}**Th**/^{238}**U** (activity)	^{230}**Th**/^{232}**Th** (ppm atomic)	Age (yr) (uncorrected)[c]	Age (yr) (corrected)[d]	δ^{234}**U**$_{\text{initial}}$ (‰, corrected)[e]	Age (yr B.P.)[f] (corrected)
Agua Caliente I									
1	15100 ± 300	30900 ± 1100	1241.7 ± 1	0.4433 ± 0.001	3440 ± 100	23550 ± 60	23520 ± 60	1326.9 ± 1.1	23410 ± 60
2$*$	9700 ± 190	62000 ± 1300	1192.4 ± 0.9	0.3829 ± 0.0011	951 ± 7	20570 ± 70	20490 ± 80	1263.4 ± 1	20380 ± 80
3	4000 ± 80	1900 ± 200	1262.9 ± 1.3	0.3 ± 0.005	10100 ± 1200	15300 ± 300	15300 ± 300	1318.7 ± 1.7	15200 ± 300
4	4030 ± 80	3330 ± 120	1281.2 ± 1.2	0.3082 ± 0.0009	5930 ± 180	15620 ± 50	15610 ± 50	1339 ± 1.2	15500 ± 50
5	4080 ± 80	16500 ± 800	1272.7 ± 1.2	0.3052 ± 0.0013	1200 ± 50	15520 ± 70	15470 ± 80	1329.5 ± 1.3	15360 ± 80
6	3183 ± 19	6765 ± 5	1273 ± 3	0.304 ± 0.002	2400 ± 20	15450 ± 140	15420 ± 140	1329 ± 3	15310 ± 140
7	4320 ± 90	141000 ± 3000	1137.5 ± 1.8	0.2776 ± 0.0017	135.2 ± 0.8	14990 ± 100	14500 ± 200	1185 ± 2	14400 ± 200
8$*$	7602.6 ± 1.8	181350 ± 160	1227 ± 2	0.3536 ± 0.0014	246.7 ± 1.1	18570 ± 80	18270 ± 170	1292 ± 3	18160 ± 170
9$*$	5120 ± 100	72000 ± 2000	1217.4 ± 1.2	0.318 ± 0.005	357 ± 10	16700 ± 300	16500 ± 300	1275.4 ± 1.7	16400 ± 300
10$*$	4210 ± 80	10200 ± 400	1220.6 ± 1.6	0.285 ± 0.006	1870 ± 80	14800 ± 300	14800 ± 300	1273 ± 2	14600 ± 300
11	4520 ± 90	11800 ± 500	1227 ± 1	0.2954 ± 0.0012	1790 ± 70	15320 ± 70	15290 ± 70	1281.1 ± 1.1	15180 ± 70
12$*$	3920 ± 30	16834 ± 13	1252 ± 3	0.311 ± 0.003	1213 ± 10	16010 ± 180	15960 ± 180	1310 ± 3	15850 ± 180
13	5780 ± 120	38000 ± 800	1233.1 ± 1	0.2998 ± 0.0007	724 ± 2	15520 ± 40	15430 ± 60	1288 ± 1.1	15320 ± 60
14	5030 ± 100	11800 ± 400	1233.4 ± 0.9	0.2992 ± 0.001	2020 ± 60	15490 ± 60	15450 ± 60	1288.3 ± 1	15340 ± 60
15$*$	7922.6 ± 1.8	21910 ± 20	1279 ± 2	0.3203 ± 0.0013	1942 ± 14	16290 ± 70	16260 ± 80	1339 ± 2	16150 ± 80
16	2420 ± 40	11025 ± 11	1260 ± 5	0.308 ± 0.006	1140 ± 16	15800 ± 300	15700 ± 300	1317 ± 5	15600 ± 300
17$*$	8570 ± 170	18000 ± 400	1253 ± 1.2	0.3366 ± 0.0008	2542 ± 16	17390 ± 40	17360 ± 50	1315.9 ± 1.3	17250 ± 50
18	4980 ± 100	2600 ± 300	1262.8 ± 0.9	0.3028 ± 0.0013	9200 ± 1200	15470 ± 70	15460 ± 70	1319.1 ± 0.9	15350 ± 70
19$*$	3560 ± 70	6200 ± 300	1245 ± 0.9	0.3113 ± 0.0013	2830 ± 150	16060 ± 70	16040 ± 70	1302.7 ± 1	15930 ± 70
20$*$	1260 ± 20	22200 ± 20	1268 ± 6	0.314 ± 0.008	298 ± 5	16000 ± 400	15800 ± 400	1326 ± 7	15700 ± 400

Continued on next page

Table 3.3 – continued from previous page

ID No.	^{238}**U** (ng/g)	^{232}**Th** (pg/g)	δ^{234}**U** (‰)	^{230}**Th**/^{238}**U** (activity)	^{230}**Th**/^{232}**Th** (ppm atomic)	Age (yr) (uncorrected)	Age (yr) (corrected)	δ^{234}**U**$_{\text{initial}}$ (‰, corrected)	Age (yr BP) (corrected)
21†	7470 ± 150	80600 ± 1700	1234.3 ± 0.9	0.3282 ± 0.0011	483 ± 3	17080 ± 60	16940 ± 90	1294.7 ± 1	16830 ± 90
22∗	16857 ± 5	271700 ± 200	1195.6 ± 1.8	0.3137 ± 0.001	323.8 ± 1.2	16590 ± 60	16380 ± 120	1252.1 ± 1.9	16270 ± 120
23†	2059 ± 15	10718 ± 9	1193 ± 3	0.269 ± 0.003	864 ± 7	14110 ± 150	14040 ± 160	1242 ± 3	13940 ± 160
24†	2190 ± 40	18600 ± 800	1172.3 ± 2	0.24 ± 0.02	450 ± 40	12700 ± 1100	12600 ± 1100	1215 ± 4	12500 ± 1100
25†	2450 ± 50	21400 ± 400	1162.9 ± 1.2	0.3944 ± 0.001	715 ± 3	21560 ± 60	21450 ± 90	1235.4 ± 1.3	21340 ± 90
26∗	20654 ± 5	735400 ± 600	1206.7 ± 1.7	0.3345 ± 0.0012	156.2 ± 0.6	17670 ± 70	17200 ± 200	1267 ± 2	17100 ± 200
29	2015 ± 13	12172 ± 12	1189 ± 3	0.277 ± 0.003	765 ± 6	14570 ± 150	14490 ± 150	1239 ± 3	14380 ± 150
30∗	8610 ± 170	138000 ± 3000	1171.7 ± 1.2	0.2693 ± 0.0009	266.1 ± 1.8	14270 ± 50	14060 ± 120	1219.1 ± 1.3	13950 ± 120
31†	10900 ± 200	69200 ± 1700	1183.5 ± 1.2	0.2819 ± 0.0015	708 ± 11	14890 ± 90	14810 ± 100	1234 ± 1.3	14700 ± 100
32†	13500 ± 300	600 ± 300	1212.8 ± 1.1	0.1464 ± 0.0004	50000 ± 20000	7420 ± 20	7420 ± 20	1238.5 ± 1.1	7310 ± 20
33†	14800 ± 300	6500 ± 700	1197.3 ± 1.6	0.1098 ± 0.0006	4000 ± 400	5560 ± 30	5560 ± 30	1216.2 ± 1.6	5450 ± 30
34∗	254 ± 8	5812 ± 6	1226 ± 9	0.315 ± 0.012	230 ± 5	16400 ± 700	16100 ± 700	1283 ± 10	16000 ± 700
Salar de Loyoques									
35†	1550 ± 30	263000 ± 5000	723 ± 6	1.33 ± 0.03	125.2 ± 0.7	139000 ± 5000	137000 ± 5000	1063 ± 18	136000 ± 5000
36†	1520 ± 30	196000 ± 4000	708.8 ± 1.6	1.252 ± 0.006	153.6 ± 0.8	126500 ± 1100	124500 ± 1500	1007 ± 5	124400 ± 1500
37†	5690 ± 110	7800 ± 200	752.1 ± 1.4	1.214 ± 0.003	14100 ± 300	114900 ± 500	114900 ± 500	1040 ± 2	114800 ± 500
38†	5430 ± 110	10400 ± 300	766.3 ± 1.3	1.259 ± 0.003	10470 ± 150	120200 ± 500	120100 ± 500	1076 ± 2	120000 ± 500
39†	10100 ± 200	167000 ± 3000	705.2 ± 1.3	1.324 ± 0.01	1272 ± 12	140000 ± 2000	140000 ± 2000	1047 ± 6	140000 ± 2000
40†	21700 ± 400	293000 ± 6000	713.4 ± 1.3	1.1825 ± 0.002	1389 ± 4	114500 ± 300	114300 ± 400	985 ± 2	114200 ± 400
Laguna de Tara									
41†	2956 ± 19	46380 ± 40	889 ± 3	0.25 ± 0.002	265.7 ± 1.9	15340 ± 160	15110 ± 200	928 ± 3	15000 ± 200
42†	2500 ± 50	87600 ± 1800	930.8 ± 1.4	0.2694 ± 0.0008	122.1 ± 0.3	16200 ± 50	15700 ± 300	972.9 ± 1.6	15600 ± 300
43†	2836 ± 19	157290 ± 140	890 ± 3	0.276 ± 0.003	82.9 ± 0.8	17000 ± 200	16200 ± 500	932 ± 3	16100 ± 500
44†	3720 ± 70	263000 ± 5000	921 ± 1.3	0.2802 ± 0.0008	62.92 ± 0.13	16980 ± 50	15900 ± 600	963 ± 2	15800 ± 600
45†	18009 ± 7	166420 ± 190	1041.1 ± 1.7	0.1886 ± 0.0006	339.7 ± 1.4	10490 ± 40	10360 ± 70	1072 ± 1.8	10260 ± 70
46†	10700 ± 200	55700 ± 1700	1031.4 ± 1.3	0.182 ± 0.003	554 ± 16	10150 ± 190	10070 ± 200	1061.1 ± 1.5	9960 ± 200
47†	3300 ± 70	65700 ± 1300	954 ± 1.6	0.2637 ± 0.0012	210.5 ± 1.1	15630 ± 80	15330 ± 170	996.2 ± 1.7	15220 ± 170

Table 3.4: Stable isotope data of samples from Agua Caliente I and Laguna de Tara. See Table 3.2 for ID number references. See Section 3.6.3 for a description of the method of data acquisition.

ID **No.**	δ^{13}**C** UofA (‰)	± **1** σ	δ^{18}**O** UofA (‰)	± **1** σ	δ^{13}**C** WHOI (‰)	± **1** σ	δ^{18}**O** WHOI (‰)	± **1** σ
Agua Caliente I								
1	0.34	0.03	1.56	0.03	0.58	0.01	1.21	0.02
3	1.75	0.01	1.60	0.01	1.91	0.01	1.83	0.04
4	1.75	0.01	1.60	0.01	1.91	0.01	1.83	0.04
6	2.47	0.00	2.09	0.04	2.41	0.01	2.03	0.01
8	2.16	0.01	2.03	0.04	2.24	0.02	1.96	0.02
9	2.16	0.01	2.03	0.04	2.24	0.02	1.96	0.02
10					2.62	0.00	1.67	0.02
12	1.99	0.04	1.76	0.03	2.53	0.26	1.55	0.04
15	2.00	0.05	1.24	0.07	2.00	0.07	1.05	0.11
16					2.00	0.00	1.41	0.01
20	2.35	0.00	1.38	0.03	2.17	0.02	1.81	0.01
22	1.14	0.02	1.25	0.05				
24	3.06	0.02	1.70	0.06	2.89	0.01	1.51	0.02
26	-1.28	0.02	1.74	0.04	-1.43	0.09	1.85	0.05
27	-2.35	0.02	2.34	0.07	-2.28	0.01	2.36	0.02
28					-1.45	0.02	2.19	0.02
31	1.92	0.02	2.42	0.04	1.57	0.06	2.03	0.04
34	1.96	0.01	2.34	0.02	2.26	0.24	2.29	0.03
Laguna de Tara								
41	3.21	0.01	1.02	0.04				
43	2.61	0.01	0.67	0.06				
45	2.80	0.02	0.77	0.05				
46	2.80	0.02	0.77	0.05				
47	2.63	0.05	0.78	0.01				

3.9 Supplementary Materials

3.9.1 Differential GPS measurements of shoreline features and sample locations

A GPS receiver (rover) calculates distance using the travel time and velocity of radio signals from orbiting satellites. These radio signals may be delayed by atmospheric disturbances in the troposphere such as cloud cover or charged particles in the ionosphere. Discrepancies between satellite and receiver clocks, varying levels of satellite connectivity, and inaccurate monitoring of satellite positions also can lead to errors. We use dGPS to correct for these errors by relying on the coordination of two receivers: a stationary base station and a roving receiver making dGPS measurements. The coordinates of the known locations of base stations serve as local points of reference, which then are used for differential correction of rover data in post-processing. The base stations run around the clock collecting data on their location, quantifying drift by comparing their current measured GPS location with its single known location. In post-processing, the proprietary Trimble Pathfinder Office software differentially corrects rover data according to this calculated amount of drift at the time of measurement by comparing time stamps between rover and base station data.

For the differential correction of all dGPS data collected in Agua Caliente I and Salar de Loyoques, we used hourly data from a Scripps Orbit and Permanent Array Center (SOPAC) base station in Cordoba, Argentina, located ∼950 km air distance away from the site. This base station is the closest station to our field site for which data is easily accessible through the proprietary software. For the 197 dGPS measurements taken, the estimated post-processed accuracy of the 197 dGPS measurements taken falls between 0.8 and 1.0 m for 57.9% of data; 1.0 and 2.0 m for 33.0% of data; and >2.0 m for 9.1% of data. See Figure 3-12A for histogram of estimated post-processed accuracy of all dGPS measurements. All dGPS measurements were made in the WGS84 datum (EGM96 geoid), with elevations reported relative to mean sea level (MSL).

3.9.2 Calculation of modern lake areas and paleolake areas

We used ESRI ArcGIS 10.2 software to determine the area of modern lakes and paleolakes. Using the dGPS elevation measurements and satellite imagery of the highest paleoshoreline features in each basin, we generated contour lines of elevation from the 1-arc second (∼30 m) digital elevation model from the Shuttle Radar Topography Mission (SRTM DEM) and used these outlines as approximations of the perimeter of highstand paleolake areas, accounting for the ∼3.5 m average difference between dGPS elevation measurements and the 30-m SRTM DEM (3-12). The following contour lines of elevations are used to represent the highstands of each lake basin: 4248 m for Agua Caliente I; 4253 m for Laguna de Tara; and 4270 m for Salar de Loyoques. To estimate the outline of the modern lake in each lake basin, we identified 'flat patches' within the SRTM DEM, taking advantage of the fact that the SRTM DEM records water surfaces as horizontal planes. These outlines for paleolake highstands and modern lakes were then used for lake area calculations, using an equal-area conic projection centered on South America.

In the future, we plan to apply the methods described in Hudson and Quade (2013) to better estimate modern lake areas. Our current methods use the lake areas of 2009 (the year of the SRTM) to represent modern.

3.9.3 Differences in $\delta^{234}U_{\mathrm{initial}}$ values of lake carbonates between basins

The carbonates from Agua Caliente I analyzed thus far vary within a narrow range of $\delta^{234}U_{\mathrm{initial}}$ values, from 1180 to 1340 ‰ (average = 1280 ± 40‰). In Salar de Loyoques, the $\delta^{234}U_{\mathrm{initial}}$ values of carbonates also fall within a narrow range between 980 and 1080‰ (average = 1040 ± 30‰). In Laguna de Tara, $\delta^{234}U_{\mathrm{initial}}$ values range between 930 and 1070‰ (average = 990 ± 60‰).

Unpaired student t tests of the $\delta^{234}U_{\mathrm{initial}}$ values in each basin indicate that Agua Caliente I $\delta^{234}U_{\mathrm{initial}}$ values are statistically distinct from the other two basins, suggesting that the Agua Caliente I basin's water source spends a statistically significant different amount of time interacting with bedrock before entering the lake. The difference in $\delta^{234}U_{\mathrm{initial}}$ value between samples from Salar de Loyoques and Laguna de Tara is not statistically significant.

3.9.4 Paleoshoreline features in Agua Caliente I and Salar de Loyoques

We measured the elevations of various paleoshoreline features in Agua Caliente I and Salar de Loyoques. In Agua Caliente I, the best preserved features were located in the northeastern corner of the basin. At least three distinct abrasion platforms in volcanic bedrock hillsides are present between 4244 and 4252 m elevation. The elevation of the base of the alluvial fan scarp varies between 4243 and 4245 m. Satellite imagery of the fan incision in the northwest part of the basin shows that there is a noticeable amount of salt deposit “staining” the landscape at ∼4235 m, suggesting that the water levels may have fluctuated at approximately that elevation for a long enough duration to leave such salt deposits. At the base of the incised alluvial fan scarp in the southeast, we found pebble-sized pieces of reworked white tufas with the honey calcite cement (Figure 3-13), suggesting that a lake must have existed at this elevation at some point after the deposition of the honey calcite.

Three separate sets of gravel barriers occupy a narrow range of elevations. The highest set consists of at least 6 individual barriers that occupy a narrow, ∼3 m range of crestal elevations (4244–4247 m) across a lateral distance of ∼200 m. The relief of these gravel barriers is minimal, with crestal heights of <0.5 m relative to lows between individual barriers. Although these barriers are obvious in satellite imagery, the individual crests of gravel barriers are only distinguishable on the ground by the relative abundance of pink disk-shaped ignimbritic cobbles, which are more abundant on crests. Cross-sectional exposure of these gravel barriers via the channel of spring discharge reveals that beach cobbles and pebbles are oriented lake wards for at least several meters below the surface.

The lowest set of gravel barriers, clustering around ∼4230 m elevation, are more prominent in relief (∼3 m). These barriers also contain reworked floret tufas with the nodular carbonate cap. Unfortunately, we did not examine the intermediate set of gravel barriers, but we estimate their elevation to be approximately 4233–4235 m based on satellite imagery and the DEM (Section 3.9.2). It is possible that this set of barriers should be grouped with the lowest set of barriers.

For our measurements of the base of the inactive stream channel connecting the Agua Caliente I and Salar de Loyoques basins, the highest elevation measured was 4240.5 ± 1.1 m. We tentatively call this elevation the “sill” or spillover elevation for Agua Caliente I. Taking advantage of color differences between different alluvial fans along the length of this inactive stream channel, it appears that the direction of flow is predominantly from northwest to southeast based on the color of entrained materials into the channel, i.e., from Agua Caliente I to Salar de Loyoques. This observation is consistent with the monotonically decreasing elevation of the stream channel base towards the southeast, as well as an alluvial fan feature at the juncture of the stream channel and the Loyoques basin. However, recent human bulldozing activity at both ends of the stream channel make it difficult to entirely rule out a pathway of water into Agua Caliente I. The relationship between the elevations of the sill, the paleoshoreline features, and the tufa and other carbonate deposits found within Agua Caliente I is illustrated in Figure 3-3.

In Salar de Loyoques, constructional paleoshoreline features are only well-preserved within two embayments in the southeast part of the basin. At least 9 individual gravel barriers exist, spanning an elevational range of 4225–4270 m across a distance of ~1.3 km. Faint traces of gravel barriers in the northern part of the basin are between 4191–4192 m elevation.

3.9.5 Potential avenues for future geomorphological research

The following are potential pathways for future geomorphological research in these lake basins:

- The U-Th ages of shoreline deposits could be compared to optically simulated luminescence (OSL) of beach gravels and detrital material beneath the caliche, as well as cosmogenic ^{3}He exposure dating of the abrasion platforms of basalt. Any statistically significant difference between such dating results could constrain "growth" rates of the encrusting floret and cone-shaped tufa deposits, or help calibrate the OSL and ^{3}He exposure dating systems.

- Due to color differences in different volcanic deposits in the Laguna de Tara basin, the cumulative amount of along-shore transport is recorded by lighter-colored ignimbritic deposits settling over darker colored sediments of basaltic composition in the northwest and southeast parts of the basin. Given basin geometry and an average wind speed and direction, process-based modeling could determine the cumulative amount of time that the lake occupied the elevation of these paleoshorelines based on the cumulative amount of along-shore transport indicated by such deposits.

- The alluvial fans in the western and southernmost parts of Salar de Loyoques formed after the regression of the large lake that existed at some time before 100 ka. Once a robust U-Th age is determined for the carbonate cements of the beach gravels, we can calculate a lower bound on the accumulation rate of these fans.

Sample Name	Elev. (m)	Lon. (°W)	Lat. (°S)	δ^{18}O (‰)	δD (‰)	Description
AD09-103	4238	67.4081	23.0885	2.6	-31	spring, ACI
AD10-222	–	67.4002	23.0867	-7.6	-77	main outflow channel of ACI
AD10-229	4225	67.4173	23.1473	0.6	-36	steaming hot spring, SW corner of ACI
AD10-240	4329	67.3353	23.0100	-7.6	-77	small spring, L. de Tara
AD10-243	4332	67.3388	23.0180	-9.1	-83	major creek flowing into NW corner of Tara

Table 3.5: Table of δ^{18}O and δD values of various waters from Agua Caliente I (ACI) and Laguna de Tara. Elevations and coordinates were measured with a a handheld Garmin GPS.

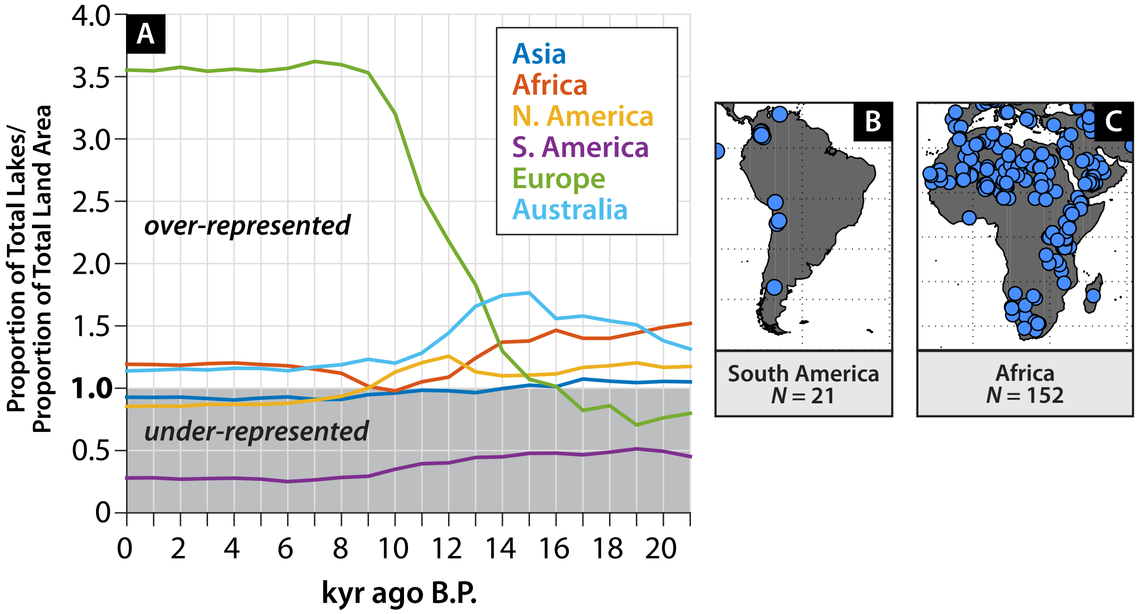

Figure 3-10: [**A**] Data representation by continent in the Global Lake Status Database (Qin et al., 1998; Kohfeld and Harrison, 2000). A value of 1.0 indicates that a continent has the same data density as the global average for that timestep. [**B**] and [**C**] Comparison of lakes with status information in the database from the past 30 ka in South America and Africa, respectively.

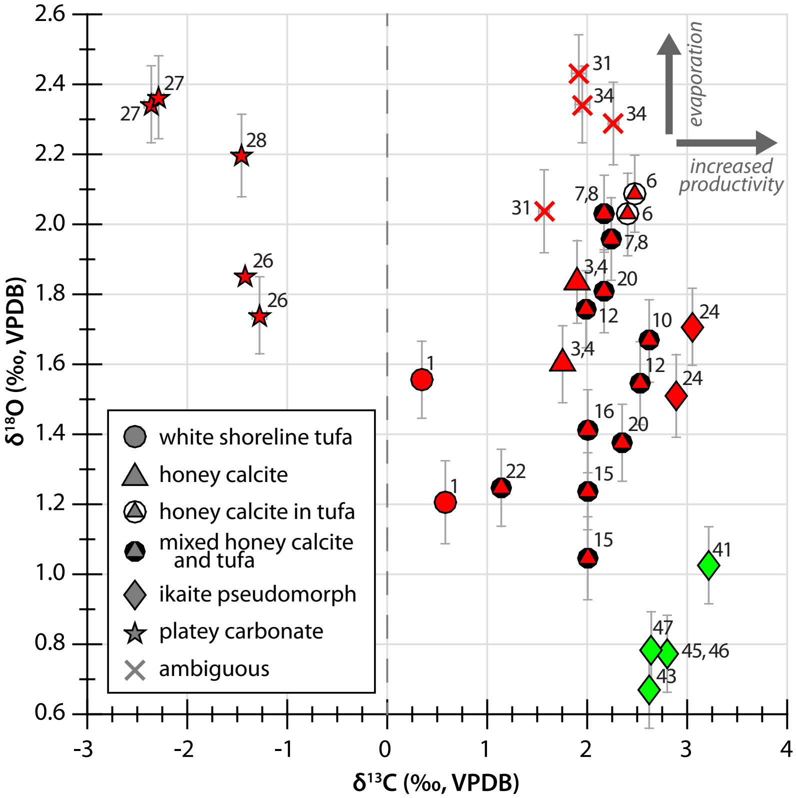

Figure 3-11: Cross-plot of δ^{13}C and δ^{18}O values of carbonates samples from Agua Caliente I (red) and Salar de Loyoques (green). Numbers correspond to the ID number of the sample (see Table 3.2). Error bars indicate 2-σ uncertainty. See Table 3.4 for stable isotope values.

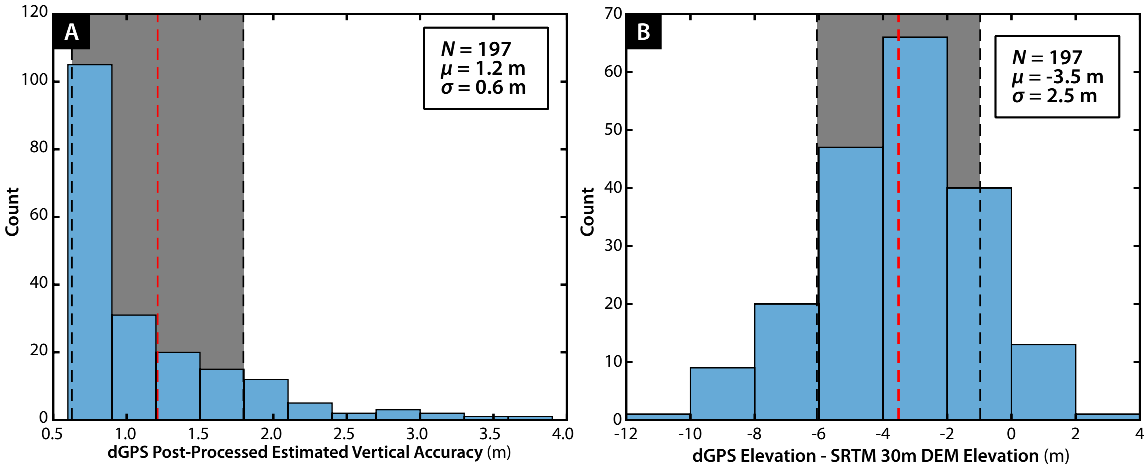

Figure 3-12: [**A**] Histogram of the estimated post-processed vertical accuracy of all dGPS measurements from Agua Caliente I and Salar de Loyoques. Mean accuracy is ± 1.2 m (1-σ). [**B**] Histogram comparing all dGPS elevation measurements from Agua Caliente I and Salar de Loyoques to the SRTM 30 m DEM. Mean difference is -3.5 ± 2.5 m. Red dashed lines represent the mean, with the gray shaded areas and black dashed lines representing one standard deviation from the mean.

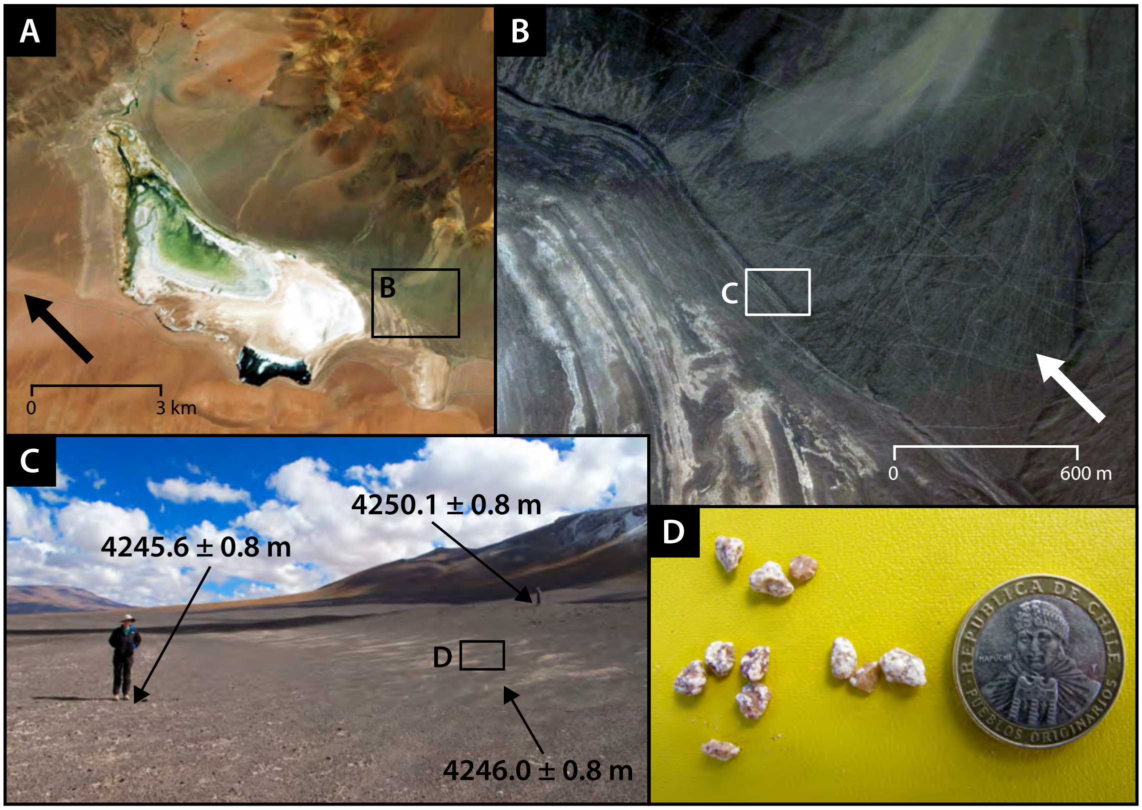

Figure 3-13: Panels showing the location of reworked pieces of tufa with honey calcite, which were found in the float of the scarp of an incised alluvial fan [**B**] in the southeast corner of the Agua Caliente I lake basin [**A**]. [**C**] Kim Huppert stands at the base of the scarp while Justin Stroup stands at the top. The elevational difference between the base and top of the scarp is ∼4.5 m. [**D**] Photo of the reworked pieces of tufa with honey calcite. Chilean peso for scale is 2.7 cm in diameters.

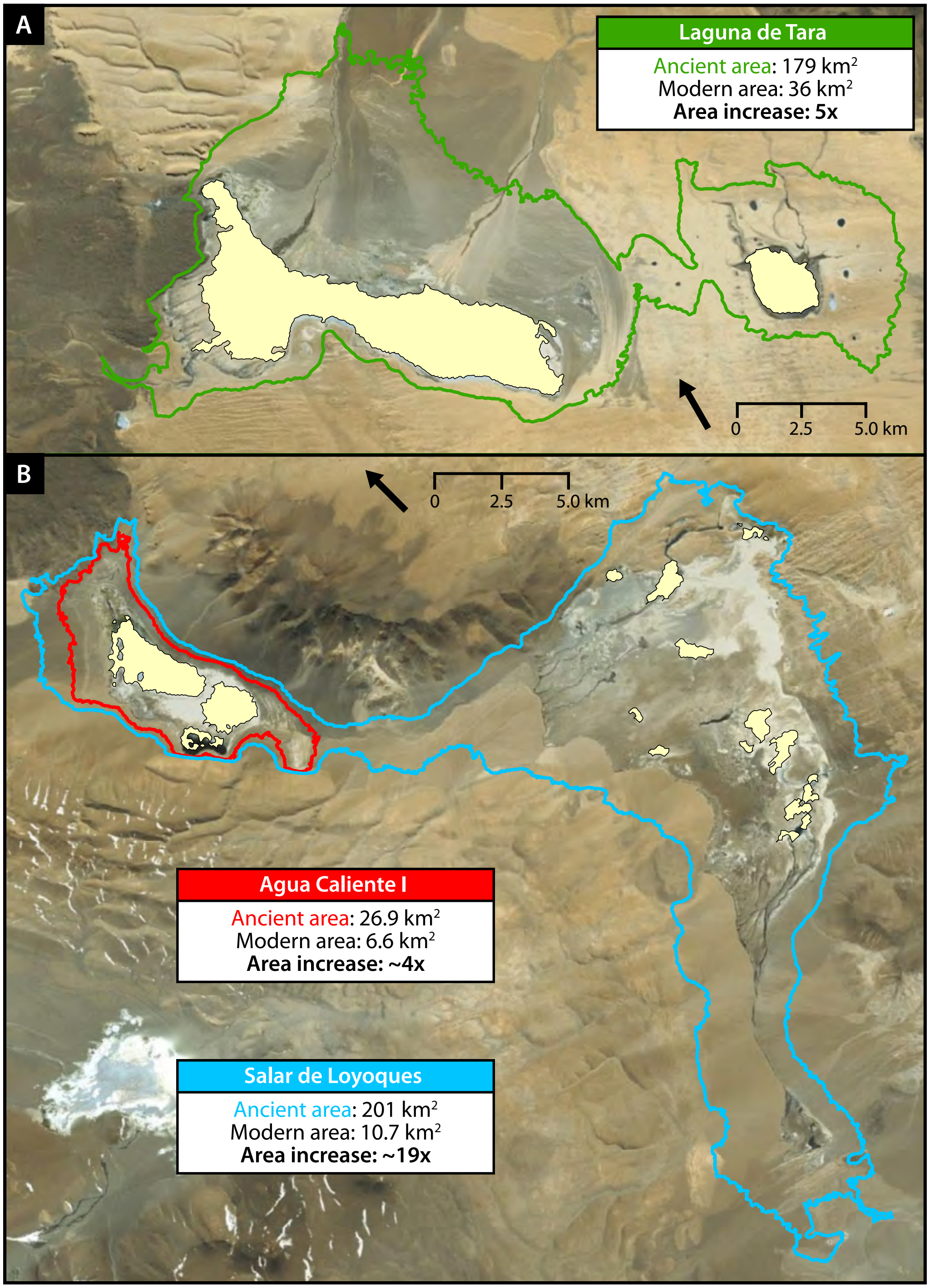

Figure 3-14: [**A**] Comparison of the maximum areal extent of Laguna de Tara (green line) to modern day extent of the lake (cream yellow polygons). [**B**] Comparison of the maximum areal extent of Agua Caliente I (red line) and Salar de Loyoques (blue line) to modern day extent of the lake (cream yellow polygons). The outline for Agua Caliente I is drawn under the assumption that no overflow occurred into the Salar de Loyoques.

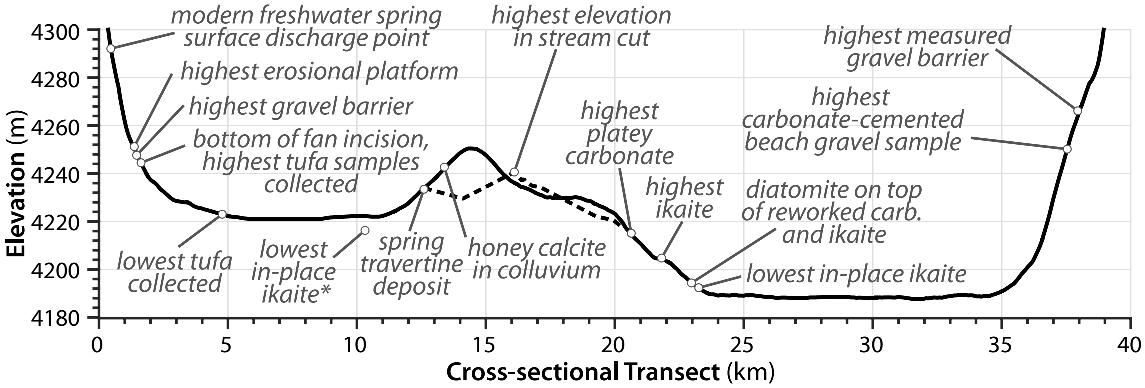

Figure 3-15: Cross-sectional transect of the Agua Caliente I and Salar de Loyoques basins, showing the elevations of major paleoshoreline features and lacustrine carbonate samples. The actual distance listed on the x-axis is not meaningful.

Chapter 4

Honey calcite: gravitational drip cements of lacustrine origin preserve evidence of rapid, large-magnitude lake level fluctuations

4.1 Introduction

Porous carbonate build-ups of lacustrine origin called “tufas” are widespread in desert landscapes, but determining the age of their formation, and thus the timing of the lakes that formed them, has been notoriously difficult. Early researchers attempting to date such deposits with carbon-14 techniques remarked on their internal complexity, noting that multiple carbonate deposition events were often present on sub-centimeter scales (Broecker and Orr, 1958; Kaufman and Broecker, 1965). Because identification of such composite or altered samples was not always obvious, and radiometric dating tools at the time could not operate on sample sizes smaller than the scale of cross-cutting relationships, tufas were generally considered problematic for geochronological purposes. These sentiments were further ingrained as subsequent research revealed the problem of carbon reservoir effects in precipitated carbonates, and even moreso when initial promise for U-Th dating techniques was dampened by difficulties with detrital constituents in tufas (Ku and Liang, 1984).

Here, we report the existence of a distinct carbonate cement found in close association with tufas and other lake deposits that may reignite optimism for geochronological control of these materials. This "honey calcite" is named for its golden color and cloudy translucency, and is documented in two geographically disparate Pleistocene-aged lake basins in northern Chile and the southwestern United States. We suspect its occurrence in closed-basin lake tufa and shoreline deposits is more common than previously known. We show that U-Th dates of this deposit are reproducible and stratigraphically coherent, suggesting that the data are viable as geologically meaningful and interpretable age constraints. The significance of this deposit is even more compelling when considering its morphology: it appears within cracks and void spaces as a gravitational "dripstone" or pendant cement characterized by thickening along the undersides of tufa or other substrates. This morphology is considered a classic indicator of the vadose zone, where cements of uneven thickness precipitate from excess droplets of saturated water and are therefore orientated parallel to the gravity vector (Müller, 1971; Longman, 1980; Schoelle and Ulmer-Schoelle, 2003).

Because of the diagnostic morphology, field context, and the lateral and elevational extent of the cement, we interpret the honey calcite to represent a "spray-zone" deposit formed by high-magnitude lake level fluctuations. The presence of fine laminations in the cement and U-Th ages suggest that these fluctuations may be rapid, occurring on century to decadal timescales. We present U-Th geochronological data, petrographic analysis, and stable isotope results to support our argument. At the site in northern Chile, the duration of fluctuations captured by the honey calcite is confined to the last ∼1000 years of Heinrich Event 1 (18–15 ka). We speculate that this may suggest that the time immediately preceding the termination of this north Atlantic winter cooling period was characterized by high variance (unstable) and large magnitude local climate change, similar to findings by Bakke et al. (2009) from high-resolution northern Atlantic marine sediments and Pigati et al. (2019) from desert wetlands during the Younger Dryas cold period.

4.2 Field and Geologic Context

The most pristinely preserved instance of honey calcite found thus far is from Agua Caliente I (23.13°S, 67.41°W, 4200 meters above sea level; Figs. 3-2 and 3-7A) in northern Chile. In this basin, the cement is observed in two distinct situations: (1) coating the exterior of or infiltrating primary void spaces within porous tufas and (2) cementing sands and gravels of colluvium or gravel barrier deposits. In all observed cases, the honey calcite is dense (non-porous), hard, and crystalline.

For (1), throughout the basin, the honey calcite is found associated with the encrusting floret and cone-shaped tufas (see orange vertical bar in Fig. 3-3). In these contexts, the honey calcite appears thickest along the exterior sides of cones (Figure 4-1) and other surfaces that were exposed at the time of honey calcite deposition. Fig. 4-2 features petrographic images of the honey calcite infiltrating an encrusted floret tufa sample collected from ∼14 m above the modern salt flat. The sample shared a contact with an igneous bedrock boulder and was cross-sectionally slabbed along a plane normal to the contact surface. Fig. 4-2B shows a gradient in the amount of honey calcite present: there exists more cement along the outer parts of the sample compared to the inner parts. Petrographic analysis of this thin section made along this plane show the characteristic pendant morphology of the honey calcite, especially when infilling larger primary pore spaces in the outer part of the floret tufa (Figure 4-2J–K). Fine laminations of a few tens of micrometers thick are also discernible, in which layers are bounded by a fine layer of dark micritic material. Despite the laminations, the bladed crystals comprising the honey calcite appear to grow across multiple laminae (Figure 4-2K).

For (2), along a road cut exposing colluvium at the southern margin of the lake basin (4243.0 ± 0.9 m elevation; Figure 4-3), we find honey calcite cements up to 1 cm in thickness predominantly coating the undersides of cracks. The cements are only found within a resistant belt of outcrop that is laterally continuous at roughly the same elevation for ∼100 m, though their own presence throughout this resistant layer is not uniform throughout. Like that observed within void spaces of tufa, the honey calcite here is laminated and hangs as smooth and broad overlapping pendants from the roof of cracks. Where the cements do not entirely fill spaces within cracks, a thin <1-mm-thick veneer of opaque white carbonate coats the bottom of these cements where exposed to air.

The honey calcite also occurs as sub-horizontal discontinuous "sheets" upon and incorporating detrital sediment. In one location at 4242.7 ± 0.9 m elevation, the honey calcite fully infiltrates sediment within a spit-like formation to form sub-horizontal layers of honey calcite-supported beach sands. In another location, the honey calcite forms around lenses of silt-sized particulate sediments, but leaves fenestral pore spaces between overlapping sub-horizontal sheets.

Another key observation is that, in hand sample, the honey calcite appears to have three packages differentiable by color, in which the oldest package is darkest yellow in color and

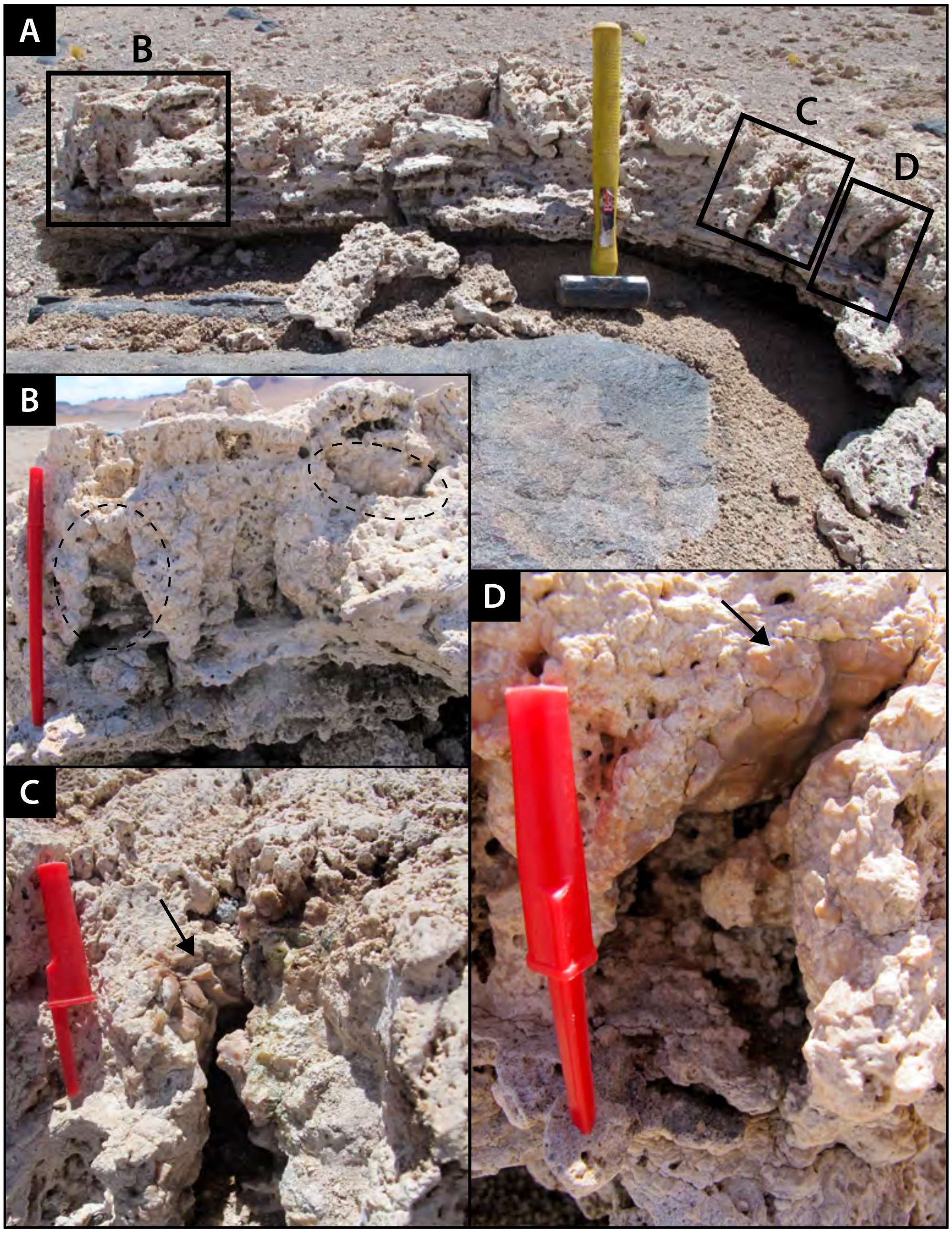

Figure 4-1: Field photographs showing that, in the context of shoreline tufas, the honey calcite appears thickest along the sides of cone-shaped tufas where primary gaps and spaces between cones exist. [**A**] Cone-shaped tufas on top of encrusting floret tufa on a volcanic boulder at 4233.9 ± 1.5 m elevation. Panels [**B**], [**C**], and [**D**] are close-up photographs of locations where thicker deposits of honey calcite are found, indicated by ovals of black dashed-lines and arrows. Red pen is 15.5 cm in length; pen cap is 6.5 cm.

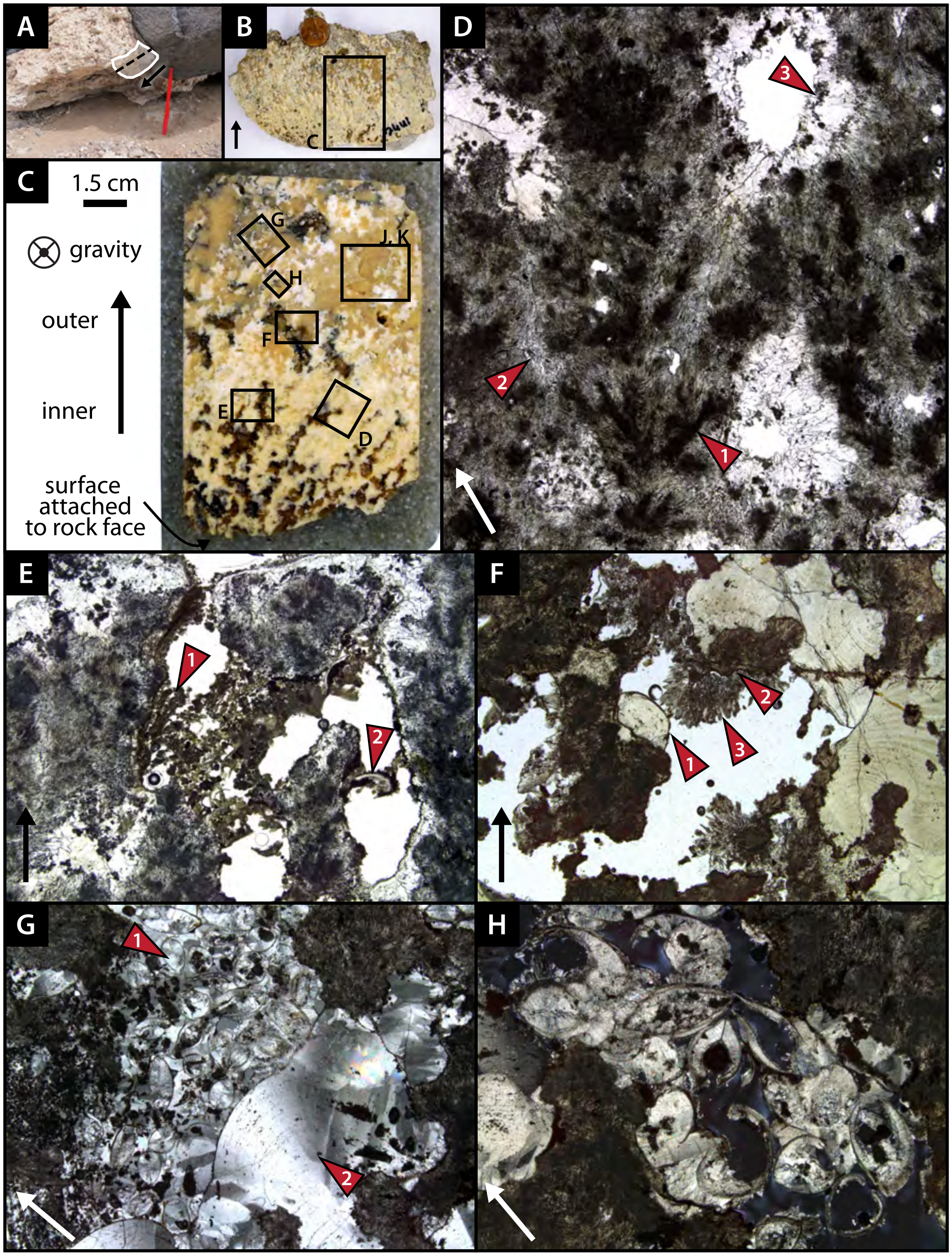

Figure 4-2: (Caption and Panels J and K on the following page.)

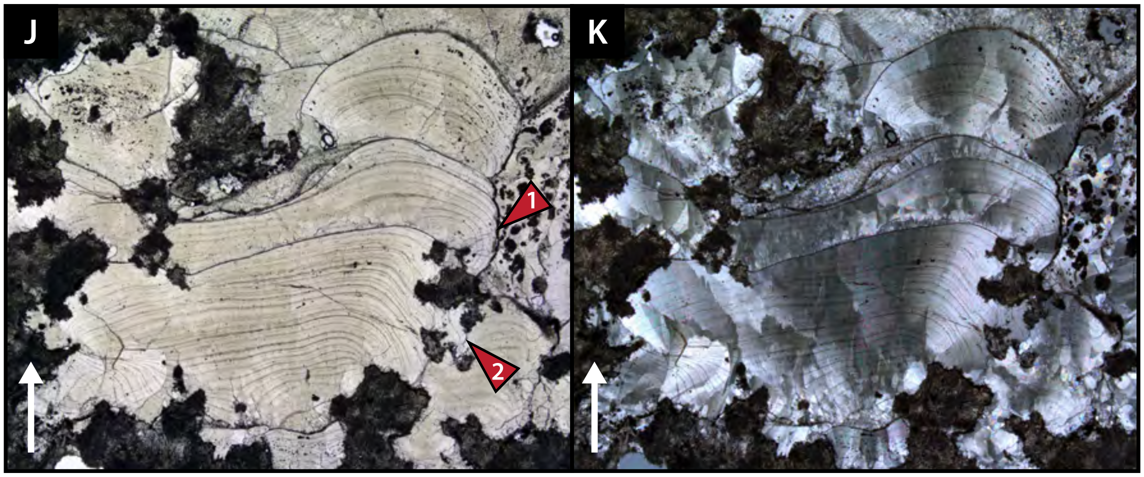

Figure 4-2: An examination of the two distinct phases of carbonate formation in Agua Caliente I, as seen in sample AD10-225 (ID #1 and #6). [**A**] Photograph showing the field context of the sample. AD10-225 was attached to a volcanic boulder in the area indicated by the shaded region outlined in white. The dashed black line indicates the orientation of the planar surface pictured in [B] and the thin section in [C]. The black orientation arrow is pointing radially away from the tufa-boulder contact in the direction of growth. This orientation arrow appears in all other panels of this figure. Red pen is 15.5 cm in length. [**B**] Flat slabbed surface of AD10-225 with U.S. penny (∼1.9 cm in diameter) for scale, showing two distinct carbonate phases: a dense, honey-colored, translucent calcite, and a porous, opaque white material. The box represents the approximate area made into a thin section (40 mm × 60 mm). [**C**] Close-up of the sample embedded in resin, showing the location of areas featured in remaining thin section panels. The thin section plane is oriented parallel to the growth direction. Note that in this panel and all others, gravity is oriented parallel to the vector going into and out of the page. [**D**] Thin section photomicrograph in plane polarized light showing that the white porous carbonate phase consists of dark, branching, microbial peloids (1) surrounded by micrite containing thin, growth-oriented filaments and dark, lenticular tube-like cyanobacterial-algal microfossils (2). The honey calcite phase is most easily observed filling or coating primary pore space (3). [**E**] Photomicrograph in plane polarized light showing trapped detritus in primary pore space (1). Trapped materials include skeletal fragments of ostracods (2), microbial peloids, and possibly carbonate fecal pellets. [**F**] Photomicrograph in plane polarized light. The honey calcite possesses fine-scale layering and most obviously fills primary pore space (1), but it also infiltrates the previously-deposited white porous carbonate phase (2). There are few places where the white porous phase is untouched by the honey calcite (3). [**G**] and [**H**] Photomicrographs in cross polarized light showing good preservation of ostracod shells (1), which have been infilled by honey calcite. The honey calcite frequently exhibits an undulose extinction pattern (2). [**J**] and [**B**] Photomicrographs in plane and cross polarized light, respectively, showing that the honey calcite exhibits pendant-like morphology in areas where it fills primary pore space. The morphology suggests that the honey calcite phase is a gravitational cement. Thin, micrometer thick layers are separated by bands of thin, dark-colored micritic material.

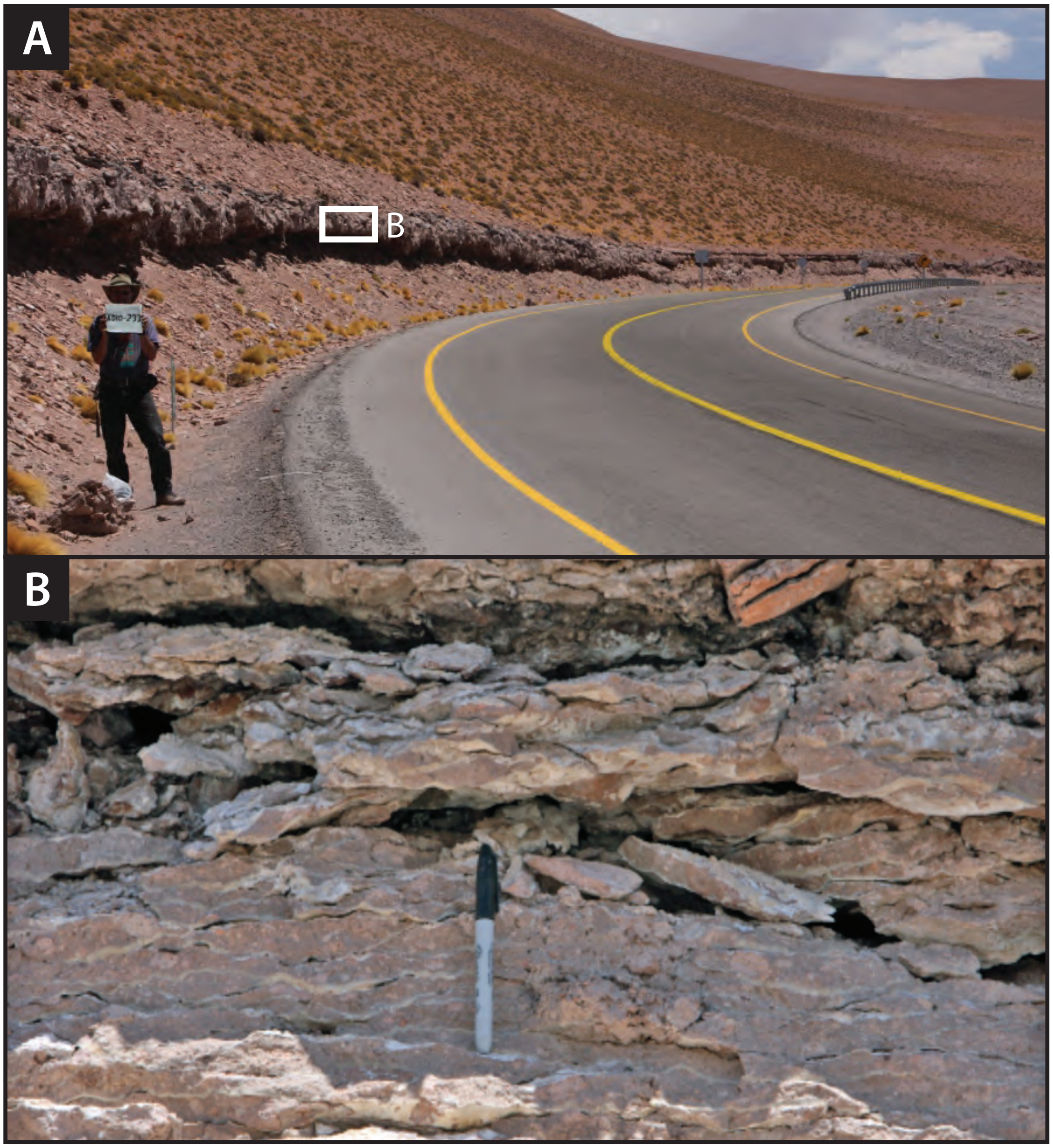

Figure 4-3: [A] Image of sample location AD10-233, where a road cut exposes an outcrop of honey calcite cementing colluvium made of ignimbritic and igneous materials. [B] Closer-up view of the outcrop with a Sharpie marker for scale.

the youngest package is a translucent white color. These three differently-colored packages of honey calcite are observable elsewhere in the basin, such as within tufas. On top of the outermost layer, a thin veneer of opaque white carbonate can be found.

4.3 Stratigraphic coherence of U-Th geochronological results

The preparation and chemical procedure for U-Th dating of these deposits is described in previous chapters. We drilled powders from the tops and bottoms (start and end) of the three distinct honey calcite packages across multiple samples from both the road-cut outcrop as well as from a thick honey calcite deposit found along the outside of a cone-shaped tufa. The initial ^{230}Th/^{232}Th ratio used to correct the data for detrital contamination was determined by calculating dates for a broad range of initial ^{230}Th/^{232}Th ratio values and deciding which ratio brought the U-Th data into stratigraphic coherence. After running these tests, a initial ^{230}Th/^{232}Th ratio of 4.5 ± 3.0 ppm atomic was chosen.

Fig. 4-4 shows an example of U-Th data from a sample from the road-cut outcrop. Here, the dates fall in stratigraphic order.

Fig. 4-5 combines all U-Th dates from honey calcite in Agua Caliente I and displays them as “camel” plots, or probability density functions. With some exceptions, the vast majority of the U-Th dates from the tops and bottoms of the three honey calcite packages are consistent with the constraints of stratigraphic order. When comparing the mean ages of dates grouped together by coevality (same layer), the data indicate that the depositional period of the honey calcite occurs at the end of HE1 for $\sim$1000 years.

We hypothesize that the good behavior of U-Th dates owes itself to the purity of the honey calcite; the cement contains few inclusions and peloidal grains. Our observations of the extent of honey calcite infiltration from thin section also explains the lack of reproducible data from the encrusting floret tufas: the honey calcite has penetrated the original underlying tufa to a degree that makes isolating the floret tufa phase on its own practically impossible (Figs. 4-2F, 4-6).

4.3.1 Origins of the honey calcite cement

Our current working hypothesis for the origin of the honey calcite cement is that it is an upper-littoral “spray-zone” deposit, precipitating from lake waters that intermittently spray over the tufa formations, beach sands, and gravels. This hypothesis is consistent

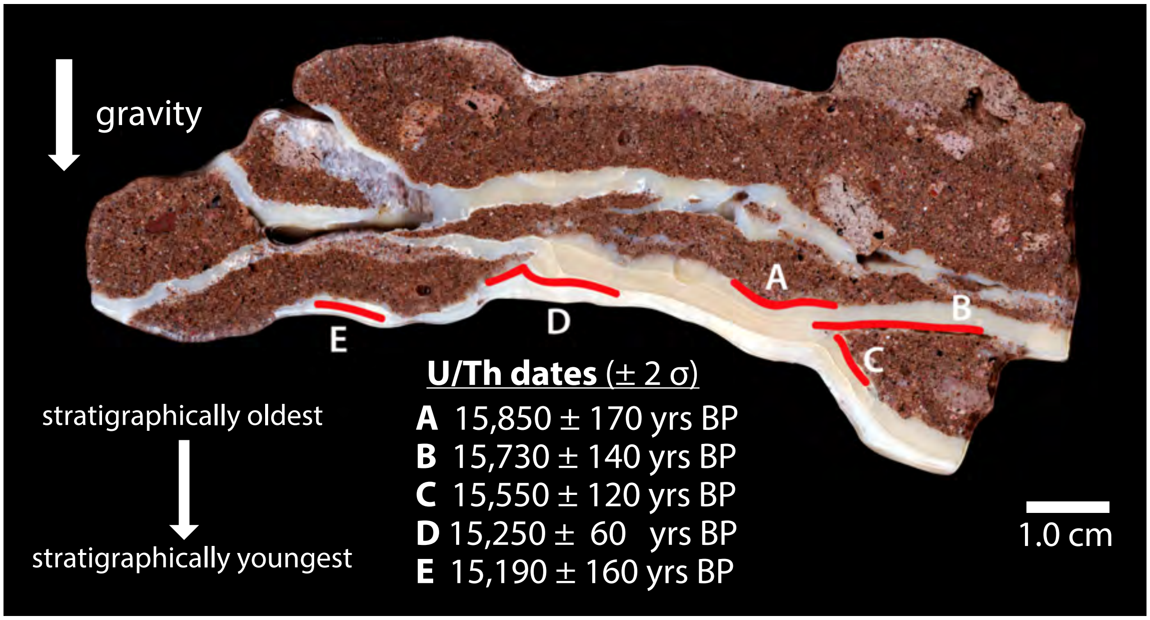

Figure 4-4: U-Th dates from sample AD10-233-10. Locations of drilling are indicated with red lines and are annotated by alphabetical letter in order of stratigraphically oldest to youngest (i.e., A is the oldest layer drilled).

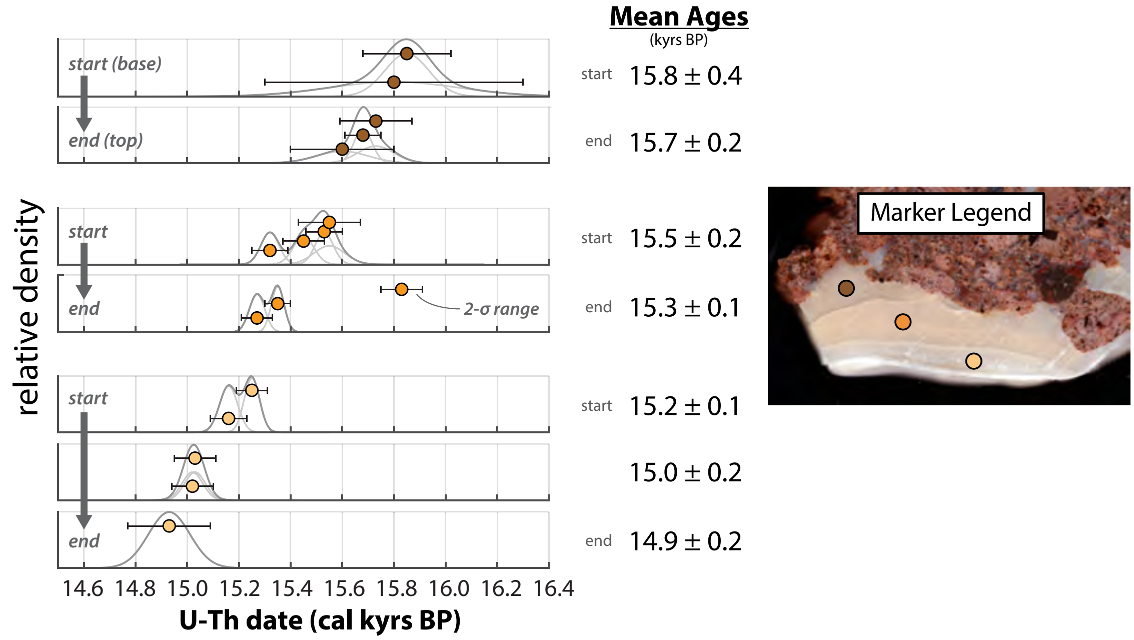

Figure 4-5: Camel plot diagram of all U-Th dates from honey calcite at sample sites AD10-233 and CYC15-019. Each date is represented by a circle color-coded by honey calcite package (see 'Marker Legend' on the right). Top two rows show data from the start and end (top and bottom) of the innermost, stratigraphically oldest honey calcite package; middle two rows show data from the start and end of the middle honey calcite package; and the bottom three rows show data from the start, middle, and end of the outermost honey calcite package. Error bars represent the uncertainty of each date (2-σ range). Each date is then represented by a probability density function, in light gray. The dark gray curve represents the cumulative probability density function of dates in each row. The mean and standard deviation of dates in each row is listed to the right of each plot.

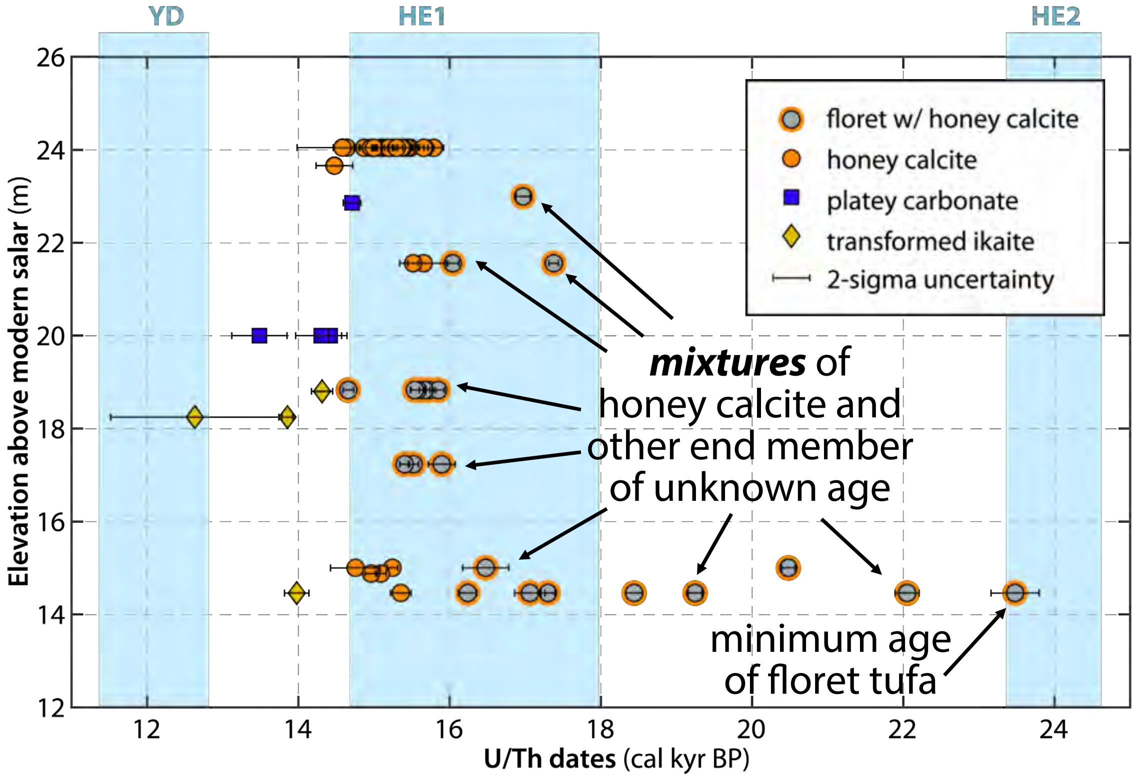

Figure 4-6: Comparison of U-Th dates of different tufa and carbonate deposits at different elevations in Agua Caliente I.

with the following observations:

1. The smooth laminations, lack of inclusions and peloidal particles, and positive δ^{13}C values indicate that the honey calcite was physio-chemically deposited, rather than biologically formed. Inorganic precipitation could have been assisted by evaporation of spray waters, raising the carbonate saturation state of the fluid to encourage precipitation of the cement.

2. The pendant morphology observed in both the floret tufa and the road cut of exposed colluvium suggests that the honey calcite is a gravitational cement reflecting vadose conditions (Müller, 1971; James and Choquette, 1984). Such pendant, microstalactic-like morphologies are observed in Holocene beach sediments and ancient limestones elsewhere, and are interpreted as indicators of supratidal environments, areas where seawater regularly splashes but does not submerge (e.g., Inden et al., 1996; Schoelle and Ulmer-Schoelle, 2003).

3. If the honey calcite were a spray deposit, we would expect the cement to be thickest where spray waters would accumulate most, on the outer tops and exterior sides of surfaces. We observe that the honey calcite cement more completely fills the pore spaces in the outer part of floret tufas (Figure 4-2B–C), leaving open primary pore space filled with trapped detritus in the inner part of the tufa (Figure 4-2E). The honey calcite also is also thickest along the sides of cones (Figure 4-1).

4. Both the positive δ^{18}O value and the ubiquitous presence of the honey calcite throughout the lake basin strongly point towards a lacustrine origin for this deposit. The $\delta^{234}\mathrm{U}_{\mathrm{initial}}$ value of the honey calcite is very similar to that of other lacustrine deposits in the basin, suggesting that the source of the honey calcite cannot have been purely groundwater.

5. Good preservation of delicate ostracod remains, which have also been infiltrated by the honey calcite cement (Figure 4-2G–H), and the lack of dissolution textures at the contact between separate phases are strong indications that the honey calcite cement is syn-sedimentary cement, rather than a cement formed via dissolution and reprecipitation of the original encrusting floret or cone-shaped tufas.

6. Some evidence suggests that the honey calcite cements are greater in percent abundance at lower elevations than at higher elevations. Figure 4-2F shows that the honey calcite does not merely coat the surface of the floret tufa, but also infiltrates

it, causing the original white porous material to take on a more beige-colored appearance. Samples collected at lower elevations tend to be more completely infiltrated by the honey calcite cement, with few white-colored areas. More field observations are needed before this observation can be confirmed.

7. The abrasion platforms on volcanic bedrock hillsides indicate that significant wave-eroding action must have been present at some point in the past, despite the small fetch length of the lake.

Such gravitational cements have also been described in beachrock settings in the marine environment, which may be materials that have yet to be taken advantage of in terms of geochronological control. Reconstructions of past sea level could benefit from finding a new type of material for dating.

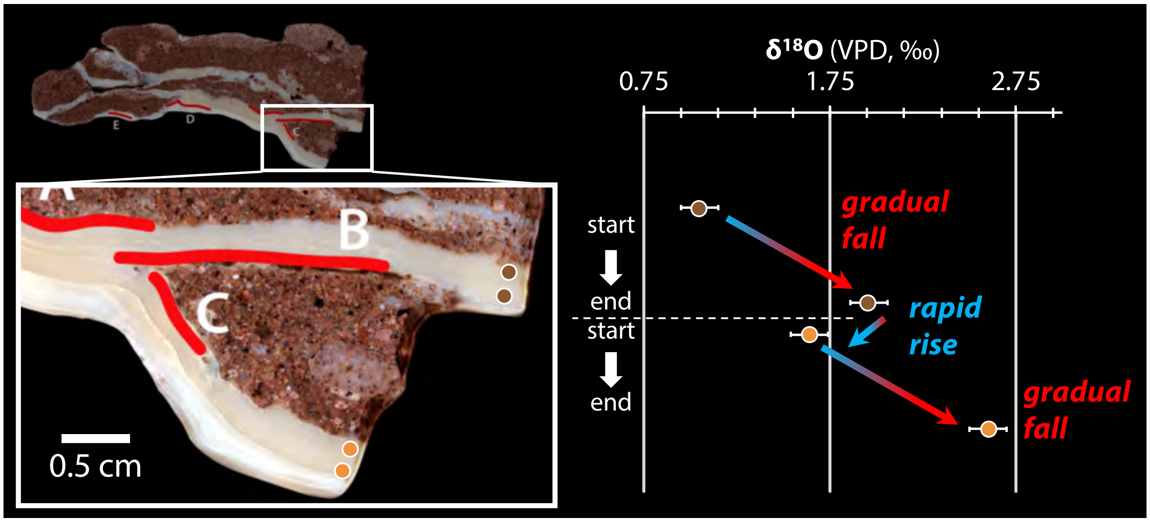

Figure 4-7: δ^{18}O data from sample AD10-233-10. Image on left shows the location of drill holes; plot on right compares the δ^{18}O values in stratigraphic order. Note that the vertical axis does not represent depth quantitatively. Annotations on plot to the right represent the current working hypothesis for the behavior of lake levels at the time of honey calcite formation.

Chapter 5

U-Th dating of tufas from the Miscanti-Miñiques-Pampa Varela lake system, northern Chile

5.1 Geologic Setting

Lagunas Miscanti and Miñiques are two high-altitude (∼4000–4200 meters above sea level) permanent shallow lakes located in the Altiplano-Puna plateau of northern Chile (Fig. 5-1). Together with Pampa Varela, these basins fall immediately to the east of a major northeast-striking fault that separates the Andean cordillera from the lower elevation pre-cordillera to the west. The basin lithology consists primarily of ignimbrite and other clastic igneous rocks associated with the now dormant volcanoes that share the same name as these two water bodies below them (Fig. 5-1B). In the present day, the water budget is predominantly driven by groundwater flow from a large catchment area (∼320 km^2) and evaporation (Valero-Garcés et al., 1996). Today, this lake system is part of the Los Flamencos National Reserve and is maintained by the Indigenous Atacameños people in Socaire in partnership with the National Forest Corporation of Chile (CONAF).

Previous work on lake sediments and tufa deposits in the basin has indicated that these basins experienced higher lake levels at some time during the last deglaciation and Holocene (Grosjean et al., 1995; Valero-Garcés et al., 1996, 1999; Grosjean et al., 2001). In a sediment record from Laguna Miscanti spanning the last ∼22 ka (Grosjean et al., 2001), two periods of higher lake levels during the last deglaciation are inferred from aquatic

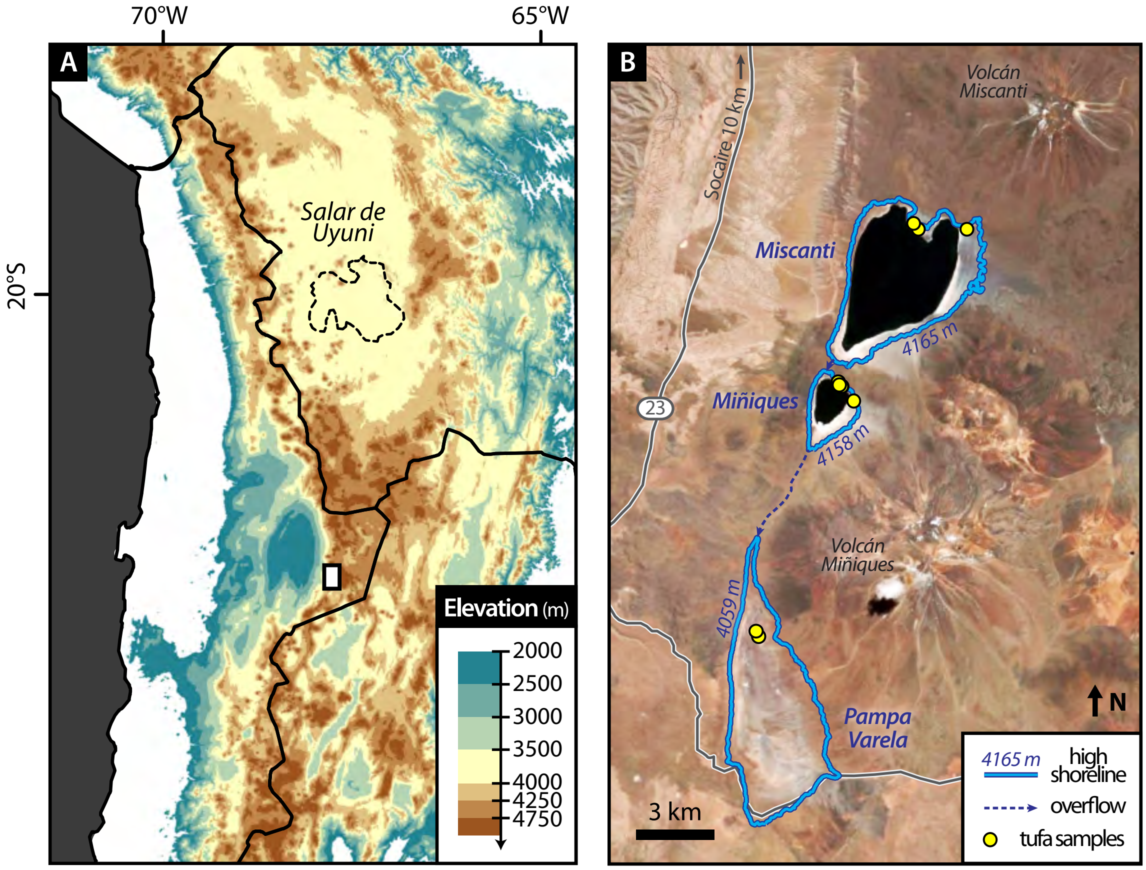

Figure 5-1: [**A**] Overview map of the Altiplano-Puna plateau in the central Andes. White rectangle marks the location of the Miscanti-Miñiques-Pampa Varela (MMPV) lake system. [**B**] Satellite imagery of the MMPV lake system. Blue outlines are contours of elevation that approximate the high shoreline in each sub-basin. Contour outline were generated using the SRTM DEM. Dark blue dashed lines with arrows trace the pathway of overflow in between each sub-basin. Yellow circles mark the locations of tufa samples discussed in this paper. This site is approximately ∼10 km from the town of Socaire in northern Chile.

pollen assemblages and sediment lithology. Unfortunately, interpretation of these records was hampered from poor chronological control due to a reservoir effect of unconstrained magnitude on radiocarbon dates. Since terrestrial material suitable for radiocarbon dating was non-existent in the core, radiocarbon dates were made on aquatic organic matter and bulk carbonates formed in waters with $^{14}C/^{12}C$ ratios that may have been out of equilibrium with that of the atmosphere. This is especially a likely scenario in the active volcanic setting of the central Andes, in which volcanic CO_2 is present in groundwaters. Slow recharge times are also typical in modern lakes in this area and contribute to the reservoir effect. Modern measurements from the nearby Laguna Lejía suggest that the modern reservoir effect is ∼2000 years for aquatic organic matter and as high as ∼8000 years for carbonates (Grosjean et al., 1995).

In this chapter, we continue our exploration of the link between Heinrich Events and the hydroclimate of the Altiplano-Puna plateau of the Central Andes by U-Th dating lacustrine tufa deposits in the Miscanti-Miñiques-Pampa Varela (MMPV) lake basin system. Various studies in this region—including work on carbonate-encrusted paleoshorelines showing lake expansions (Bills et al., 1994; Sylvestre et al., 1999; Placzek et al., 2006a, 2006b; Placzek et al., 2009; Blard et al., 2011; Placzek et al., 2013; Chen et al., unpublished data), cave stalagmites indicating increased rainfall amounts (Kanner et al., 2012), paleowetland deposits showing elevated groundwater tables (Quade et al., 2008), fluvial terraces and rodent middens showing increased stream discharge (Latorre et al., 2006; Nester et al., 2007; Gayo et al., 2012), and glacial moraines showing substantial ice cover expansion (Smith and Rodbell, 2010)—all indicate that this region experienced the wettest conditions of the last deglaciation during Heinrich Event 1 (∼15–18 ka). The regional synchroneity of these wet phases is so prominent that the local phenomenon is often revered to as a “Central Andean Pluvial Event” (CAPE).

Because Miscanti and Miñiques overflow into the Pampa Varela basin upon breaching the elevations of their sills, the timing of the lake creating the high shoreline in Pampa Varela represents the hydrologic maximum of the drainage basin.

5.2 Methods

We mapped paleoshorelines and collected carbonate samples over two days in May 2016. We used a Trimble GEO 7x handheld receiver to collect precise location and elevation data of shoreline features and tufa samples, which yields sub-meter accuracy after differential correction using proprietary software.

Carbonate samples were then prepared for U-Th dating following the same procedures described in the previous chapter. We used an initial $^{230}\mathrm{Th}/^{232}\mathrm{Th}$ ratio of 4.5 ± 3.0 ppm atomic for the calculations of dates. Petrographic images of thin sections were made using a Zeiss AX10 microscope.

Several powders drilled from tufas were also analyzed for their mineralogy using a Nicolet iS50 attenuated total reflectance Fourier transform infrared (ATR-FTIR) spectrometer at the Center for Nanoscale Systems at Harvard University. To test the reliability of the results, we prepared three mixtures consisting of known proportions of clean calcite and aragonite standards and determined if the measurements could accurately reconstruct these relative proportions. Measurements of these mixed standards were all within 5% of true proportions of calcite and aragonite.

5.3 Results

5.3.1 Geologic and geomorphic context of tufa deposits

Due to the short time on site, we were unable to survey the basins and their tufa deposits comprehensively, and thus recognize that this work is limited by our sampling. Regardless, we report our findings on the most conspicuous deposits, generally located on the northern parts of each basin (Fig. 5-1B, yellow circles). This spatial distribution may be related to pathways of groundwater flow and spring discharge: in both Miscanti and Miñiques, warm spring waters are observed seeping into the modern lake along the northern shoreline.

In Miscanti, the high shoreline in the north is mainly expressed as a salient wave-cut terrace eroded into igneous bedrock (Fig. 5-2A). The promontory in the north-central part of the coastline consists of a broad platform with outcrops of smoothed basalt boulders on its lakeward edge. These boulders act as the substrate for a thick (∼20–35 cm) and laterally continuous (∼200 m) deposit of tufa (Fig. 5-2B) that runs parallel to the paleoshoreline. Although much of this tufa remains *in situ* (Fig. 5-2C), it is very porous and friable; as a result, many fragments of tufa are found in float in the surrounding area. The extent of this re-deposition of tufa is illustrated by the color contrast between the eroded pink-beige tufa and dark purple-brown basalt, which is easily observable in both the field (Fig. 5-2B, see ‘tufa in float’) and satellite imagery.

In contrast, the smaller Miñiques basin does not have any broad platforms. Here, tufa deposits are found encrusting basalt boulders along the more steeply sloping bedrock hillsides (Fig. 5-2D). In Pampa Varela, the only instances of *in situ* tufa that we encountered were found encrusting boulders in protected spaces (*e.g.*, undersides of boulders).

In all three basins, pebble- to cobble-sized fragments of tufa were found redeposited at the crests of the constructional gravel berms at the high and intermediate shorelines. In fact, in the northeastern corner of Miñiques, an cross sectional exposure reveals that a

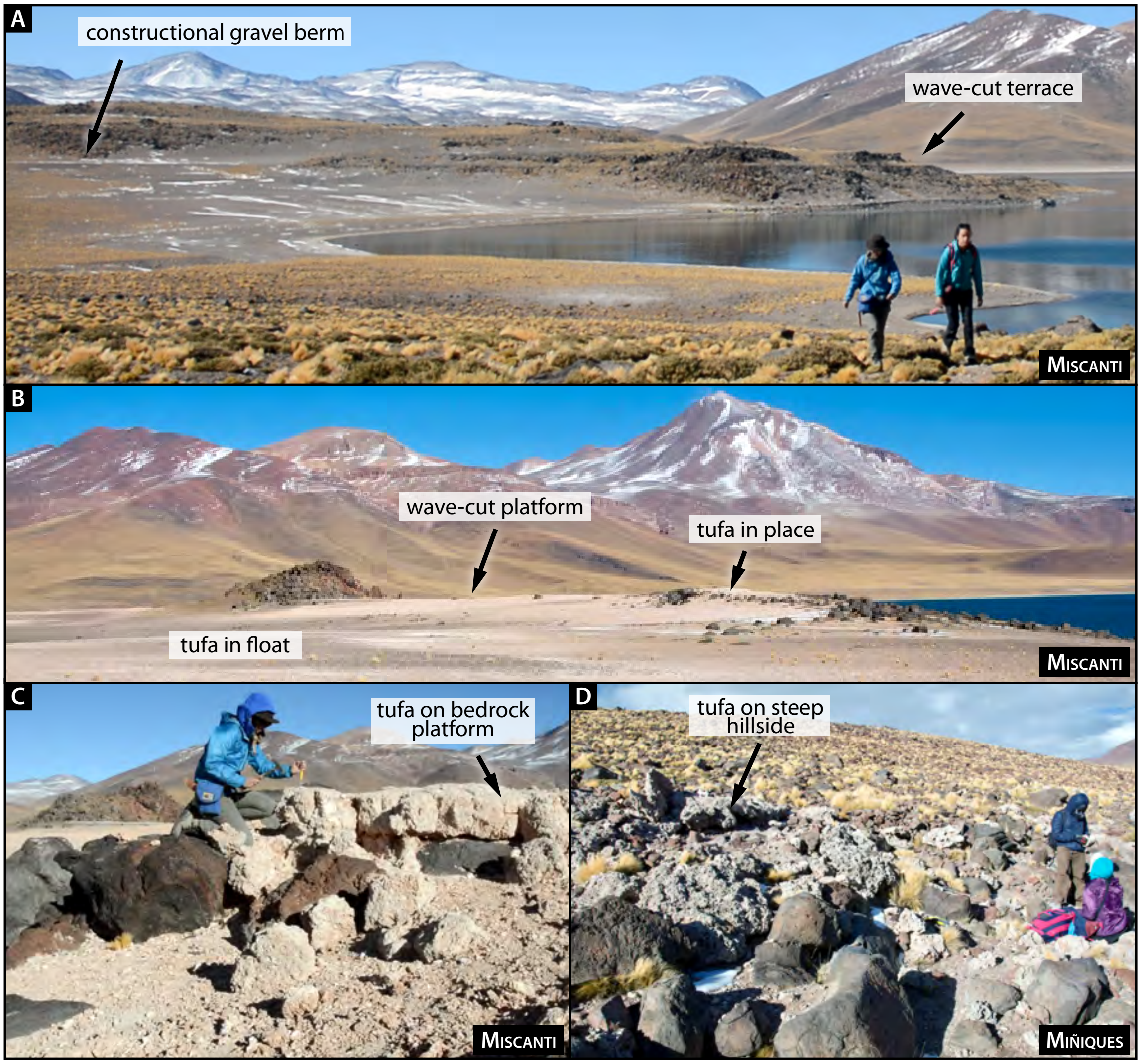

Figure 5-2: Field photographs of paleoshorelines and tufa deposits. [**A**] In the northwest embayment of Miscanti, the high shoreline is expressed as a distinct wave cut terrace eroded into basalt bedrock (dGPS elev. = 4164±1.0 m) and a constructional gravel berm. Photo taken looking east. [**B**] The promontory in the north-central coastline of Miscanti. The outer, lakeward edge of this platform has outcrops of smooth basalt boulders that are coated with a thick (∼20–30 cm) and laterally continuous (∼200 m) deposit of tufa (see 'tufa in place'); pieces of this tufa can be found on the landward, backshore side of this platform in float. The extent of this redeposition of tufa is illustrated by the contrasting colors of the pink-beige tufa and the dark purple-brown of the basalt (see 'tufa in float'). Photo taken looking southeast. [**C**] Close up view of the thick tufa deposit coating bedrock featured in Panel B as 'tufa in place'. Note the same bedrock headland in the backgrounds of Panel B and C. [**D**] In Miñiques, tufa is found on top of more steeply-sloping hillsides of bedrock boulders.

∼10–15 cm thick layer made entirely of eroded tufa fragments lies at the crest of the high shoreline gravel barrier. In many instances, the hydrodynamical differences between tufa fragments and other clastic igneous rocks created a 'highlighting' effect, whereby geometry of berms was accented in color by the spatial distribution of the tufa fragments. These observations indicate that there was at least one occurrence of higher lake levels after the original formation of the tufa deposits.

5.3.2 Characteristics of various tufa facies

The tufas in the MMPV lake basin system can be broadly categorized into two categories: (1) fibrous mats and (2) carbonate cement encrustations. We now describe these two facies categories in Figs. 5-3–5-5.

The fibrous mat tufa facies consists of fine and elongate calcite crystals that are arranged radially relative to the surface of the substrate (Figs. 5-3B and C). The thick, continuous deposit of porous tufa described in Fig. 5-2B and C consists primarily of this facies. These tufas are not well-lithified and are highly weathered, with many exhibiting clear signs of recrystallization and/or diagenesis (Fig. 5-3B, white arrows). In exposed cross sections of outcrop, different beds of fibrous tufa with slightly varied macro-scale morphology are discernible, with some exhibiting a more splayed, feather-like fabric and others exhibiting a more classic radial growth fabric. On a sub-centimeter scale, banding can be observed within the tufas and appears to be related to porosity. In plan view, weathered surfaces exhibit closely packed polygonal shapes, suggesting that the internal structure of these tufas consists of a composite of smaller inverted cone shapes of varying sizes. In thin section, abundant diatoms are observed oriented parallel to the fabric of these tufas.

The cements are the second most common form of carbonate deposition in the tufa deposits. These ∼1–3 mm thick cements are generally isopachous, finely laminated and are found indiscriminately coating various substrates. They are most well-preserved when coating cobbles of clastic igneous rocks (Fig. 5-4). The coatings vary in color from being beige to mostly translucent white.

Another common substrate of the carbonate cements are the remains of charophyte algae. Many tufas found *in situ* in Miñiques exhibited excellent structural preservation of macroscopic charophyte algae of the order Charales, commonly known as "stoneworts" (Fig. 5-5). Charales are morphologically complex filamentous green algae and are found in shallow, calm, fresh and brackish waters worldwide (Wood and Imahori, 1959; Bold

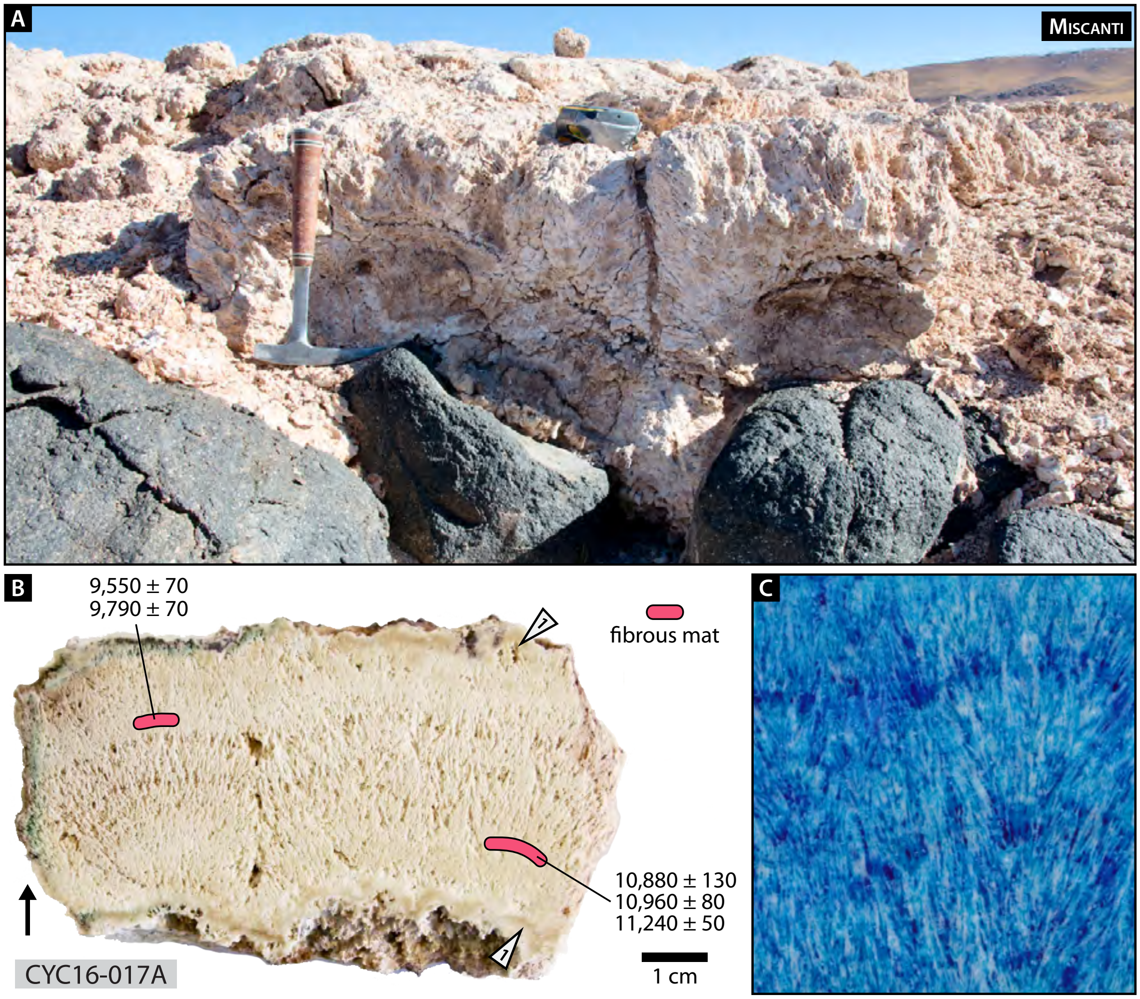

Figure 5-3: The fibrous mat carbonate facies. [**A**] Outcrop photo, close up view of tufa on bedrock platform from Panels B and C in Fig. 5-2. Hammer is ∼33 cm tall. [**B**] Cross-sectional view of a sample of the fibrous mat facies (CYC16-017A, found in float). Pink shapes indicate the drilling locations of powder used for U-Th dating. Annotated dates are in units of years before 1950. Uncertainties are 2-σ range. White arrows labeled '1' mark areas which have been recrystallized, which are the exposed surfaces of the sample. Arrow represents the direction of stratigraphic up. [**C**] Close up view of internal structure of the sample.

and Wyynne, 1978). Living charophytes are found at the sediment-water interface today (Fig. 5-5A). Finding a direct modern analogue of fossil tufas is very uncommon; if the depth constraints on the modern occurrence of charophytes could be determined, this information would allow for better interpretations of the paleolake level represented by the tufa deposits.

A carbonate-encrusted sample of charophyte algae was found in float in Miscanti, but we were not able to locate the corresponding *in situ* outcrop in this basin.

5.3.3 Results of U-Th dates on tufa deposits

The uranium concentrations of these deposits were between 10 and 300 ppm, ∼2–3 orders of magnitude higher than concentrations observed in tufa deposits from the Bolivian Altiplano (Placzek et al., 2006a) and elsewhere in northern Chile (Chen et al., unpublished). In several instances, tufas are comprised of both the fibrous mat facies and carbonate cements. In these situations, we are able to leverage the incontrovertible constraints of cross-cutting relationships and stratigraphic order to test the viability of our U-Th dates. For example, the cement in sample CYC16-025A featured in Fig. 5-5D has clearly formed around both the charophyte algae as well as the fibrous mat (see white triangle labeled '3'), and thereby

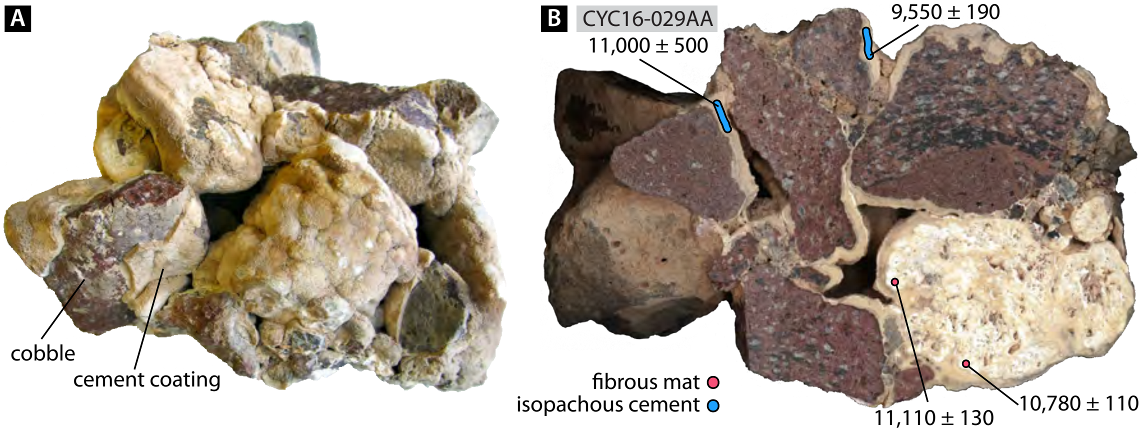

Figure 5-4: The cement encrustations facies. [**A**] Hand sample consisting of large pebbles and cobbles that are coated in a ∼1–3 mm thick rind of isopachous carbonate cement. [**B**] Exposing a cross section of the sample featured in Panel A (CYC16-029AA) reveals that one cobble is made not of igneous rock, but rather a fibrous mat tufa. The cement has infiltrated the pore spaces of the fibrous mat tufa cobble.

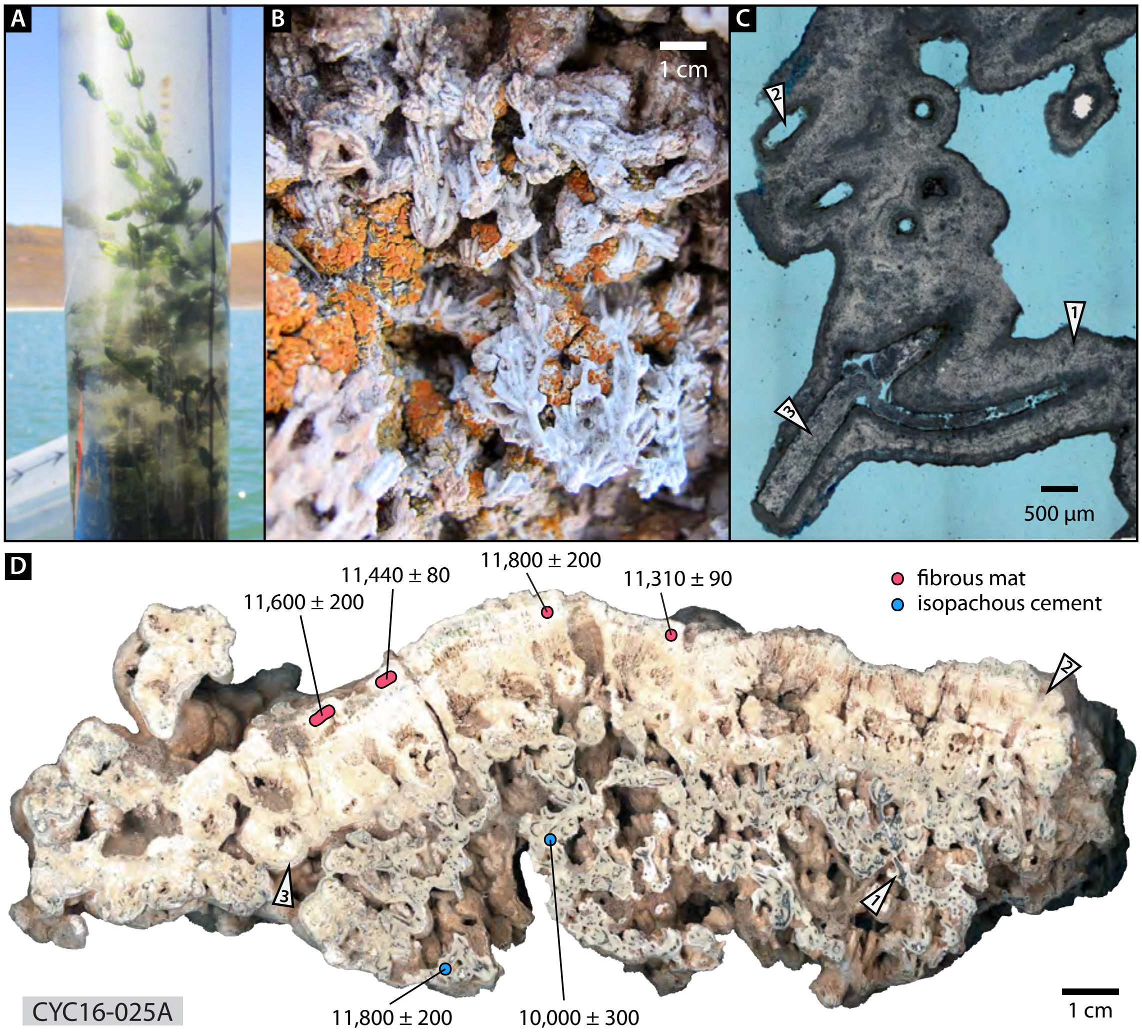

Figure 5-5: Preservation of charophyte algae by carbonate cement. [**A**] Modern living charophytes living at the sediment-water interface, extracted during sediment coring from Miniques in April 2013. Photo taken by Matías Frugone. [**B**] Pristine charophyte preservation by carbonate encrustation on the hillside in the Miniques basin featured in Panel D of Fig. 5-2. [**C**] Petrographic thin section image of a carbonate-encrusted charophyte tufa sample. 1: Isopachous, radial calcite cement with many inclusions. The area immediately surrounding the original charophyte is darker due to a higher proportion of dark microbial peloids. 2: Holes indicate locations where the charophyte used to be. 3: This area is either the primary preservation of the original carbonate skeleton of the charophyte, or a secondary infilling. The carbonate here contains an abundance of diatoms. [**D**] Hand sample of a carbonate-encrusted charophyte algae associated with a ∼2 cm thick fibrous mat tufa. 1: An instance in this sample of a well-preserved charophyte stem. 2: Fine layers in the fibrous mat tufa. 3: The isopachous cement is coating the fibrous mat, indicating that the formation of the cement occurred after the formation of the fibrous mat.

constrains its formation to be after that of the fibrous mat. For the cements, we are also able to test the reproducibility of coeval layers within a sample.

Fig. 5-3B shows analyses from two separate layers in a fibrous mat tufa sample. Here, we observe that the dates within each layer are not reproducible—as in, the analytical uncertainties calculated from measurements do not overlap with one another. We also notice that the dates from the stratigraphically older layer are older than the dates from the stratigraphically younger layer. Note that while the existence of layers implies a sequence in time, because each layer in these fibrous mat tufa samples is delineated by a change in porosity rather than any layer representing a depositional hiatus, it is possible that the entire thickness of the sample formed within a narrow window rather than over a long enough period of time to allow for U-Th dates to differentiate between the top and bottle of the sample.

Fig. 5-4B shows analyses from carbonate cements coating cobbles of igneous rock and one fibrous mat tufa. The uniform color and thickness of the cement surrounding these cobbles suggests that all the cement in this hand sample formed at the same time. However, the two analyses of the cement from different locations in the sample yield dates that differ by ∼1.5 kyrs and do not overlap in uncertainty. In addition, one of the dates on the fibrous mat tufa cobble are inconsistent with stratigraphic order constraints. The latter observation could be explained by the fact that the cement has infiltrated most of the pore spaces in the fibrous mat tufa, so much so that attempts to isolate powder from the original fibrous mat cobble is not practically feasible, similar to the effect of the honey calcite in Agua Caliente I.

Fig. 5-5 shows analyses from a sample that exhibits cross-cutting relationships between fibrous mat tufa and cements encrusting a charophyte algae. Here again, the two dates on the isopachous cement do not overlap in uncertainty. Analyses along the uppermost part of the fibrous mat tufa are all within the same ∼500 year range but some analytical uncertainties of analyses do not overlap.

These results can be explained a number of different ways: (1) It is possible that the formation of the cement occurred very slowly, such that small differences in the location of drilling can lead to large differences in calculated dates; (2) the initial ^{230}Th/^{232}Th ratio used for the calculation of dates does not adequately account for the true amount of initial ^{230}Th in these samples; (3) there exists hydrogenous Th in the lake system that was incorporated into the tufa at the time of formation; and/or (4) these tufas have not remained closed systems with respect to uranium.

Some data from fibrous mat tufas in both Miscanti and Pampa Varela support the hypothesis for open system behavior (Fig. 5-6). In sample CYC16-018A, powders were drilled from the bottom and top of the sample in an attempt, originally, to determine the duration of tufa formation, especially given that this sample formed directly on top of bedrock. Again, the analyses along seemingly coeval locations yield dates that do not overlap in uncertainty. However, we notice that dates of powders drilled from portions that appear altered (recrystallized) have elevated $\delta^{234}U_{initial}$ values and low uranium concentrations (Fig. 5-6B), a pattern that is consistent with uranium loss.

We also observe elevated $\delta^{234}U_{initial}$ values in analyses from the outermost part of the sample CYC16-038A from Pampa Varela (Fig. 5-6C and D). These analyses yielded dates that were old and inconsistent with stratigraphic order constraints.

Thus, we have good evidence to suggest that these analyses shown in gray in Fig. 5-6 have experienced uranium loss and should not be considered data that represent any geologically meaningful event. However, there are still inconsistencies in the remaining data, primarily the lack of reproducibility of dates from coeval layers and lack of adherence to the constraints imposed by stratigraphic order. Here, dates from coeval layers span a range of ~5–10 kyrs or more, as opposed to data previously shown in Figs. 5-3–5-5, which only span a range of <2 kyrs.

Fig. 5-7 plots all U-Th analyses from tufa samples in the MMPV lake system. The scatter of dates of samples of the fibrous mat facies in Pampa Varela makes it difficult to make many interpretations on the timing of tufa formation in this basin. We are only able to say with confidence that a lake of deglacial age once existed in Pampa Varela. In contrast, there is more coherence in data from Miscanti and Miñiques: We notice that the fibrous mats in both basins generally occupy the same ~3-kyr-long time range. There also exists dates of carbonate cement encrusted charophytes in both basins between ~16–13 kyr ago. Other carbonate cements yield dates that are consistent with those from fibrous mat tufas, with some dates being younger than the youngest fibrous mat data, consistent with stratigraphic relationships.

Thus, there is evidence from U-Th dating that there existed a higher lake levels from 16–9 ka, broadly consistent with the CAPE I and CAPE II intervals. However, time intervals in this plot with no data do not necessarily prove that higher lake levels did not exist during these times: again, we are limited by our sampling bias. In other words, the absence of data does not prove the absence of a lake.

Future work (imminently) will compare these results to past data from the Miscanti

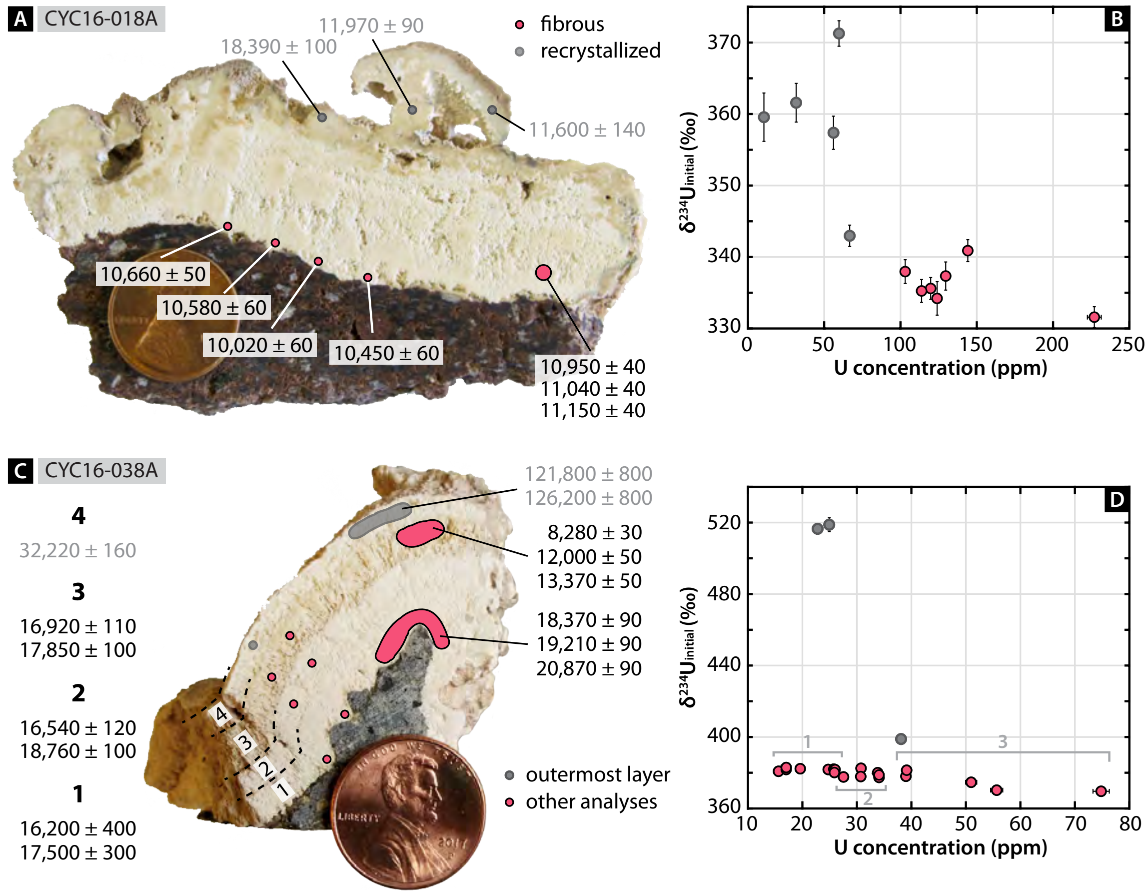

Figure 5-6: Evidence of open system behavior from analyses of recrystallized portions of tufa [**A**, gray] and the outermost layer of porous tufa [**C**, gray]. All dates are in units of years before 1950. Dates listed on the left side of Panel C correspond to the layers annotated on the sample (1–4, 1 being stratigraphically the oldest). [**B**] and [**D**] Comparison of $\delta^{234}U_{initial}$ and uranium concentration of samples featured in Panels A and C, respectively. Note that there are analyses featured in these panels that are not shown in the sample images; additional analyses come from different cross-sectional exposures of the same sample. In Panel D, the groups labeled 1–3 correspond approximately to analyses from layers 1–3 in Panel C.

sediment core and attempt to provide another estimate of the reservoir correction of this lake.

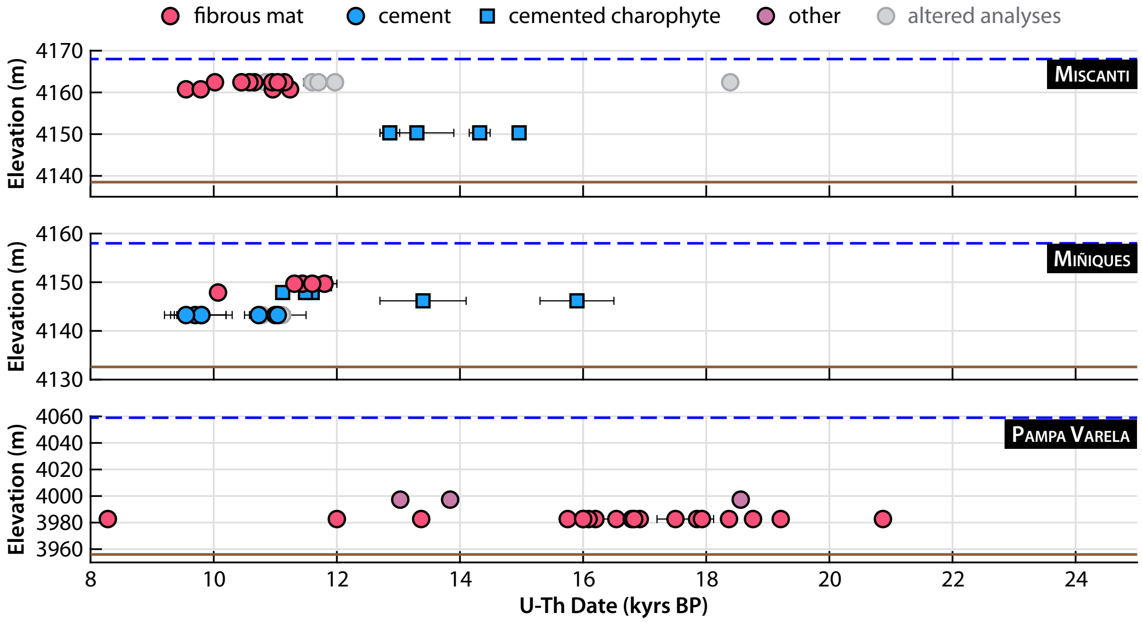

Figure 5-7: Summary of U-Th dates on tufas from Miscanti (top), Miñiques (middle), and Pampa Varela (bottom), plotted against elevation of sample location. Dashed blue line marks the elevation of the highest shoreline in each basin. Solid brown line marks the elevation of the modern lake or lowest point in the basin. Errors bars are 2-σ. See legend above all plots for symbology.

Appendix A

Appendix Tables

Table A.1: U-Th data associated with Chapters 3–5. Reported errors for ^{238}U and ^{232}Th concentrations are estimated to be ±1% due to uncertainties in spike concentration; analytical uncertainties are smaller. $\delta^{234}\text{U} = ([^{234}\text{U}/^{238}\text{U}]_{\text{activity}} - 1) \times 1000$. Ages are corrected for detrital ^{230}Th assuming an initial $^{230}\text{Th}/^{232}\text{Th}$ of 4.5 ± 3.0 ppm atomic. $\delta^{234}\text{U}_{\text{initial}}$ corrected was calculated based on ^{230}Th age. B.P. stands for "Before Present" where present is defined as January 1, 1950 in the Common Era. Decay constants for ^{230}Th and ^{234}U are from **?**; decay constant for ^{238}U is 1.55125×10^{10} yr^{-1} (Jaffey et al., 1971).

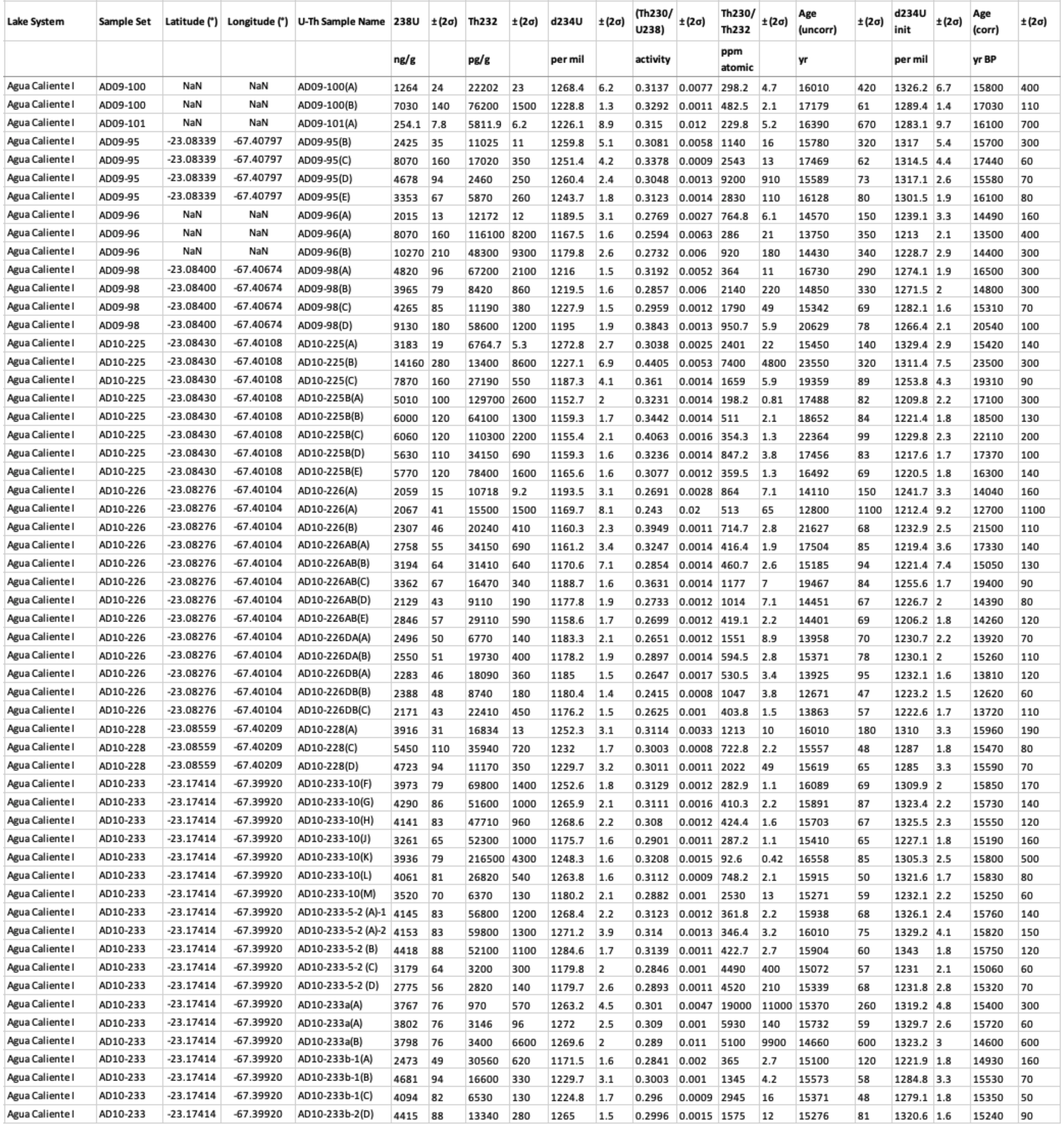

Lake System	Sample Set	Latitude (°)	Longitude (°)	U-Th Sample Name	238U	±(2σ)	Th232	±(2σ)	d234U	±(2σ)	(Th230/ U238)	±(2σ)	Th230/ Th232	±(2σ)	Age (uncorr)	±(2σ)	d234U init	±(2σ)	Age (corr)	±(2σ)
					ng/g		pg/g		per mil		activity		ppm atomic		yr		per mil		yr BP	
Agua Caliente I	AD09-100	NaN	NaN	AD09-100(A)	1264	24	22202	23	1268.4	6.2	0.3137	0.0077	298.2	4.7	16010	420	1326.2	6.7	15800	400
Agua Caliente I	AD09-100	NaN	NaN	AD09-100(B)	7030	140	76200	1500	1228.8	1.3	0.3292	0.0011	482.5	2.1	17179	61	1289.4	1.4	17030	110
Agua Caliente I	AD09-101	NaN	NaN	AD09-101(A)	254.1	7.8	5811.9	6.2	1226.1	8.9	0.315	0.012	229.8	5.2	16390	670	1283.1	9.7	16100	700
Agua Caliente I	AD09-95	-23.08339	-67.40797	AD09-95(B)	2425	35	11025	11	1259.8	5.1	0.3081	0.0058	1140	16	15780	320	1317	5.4	15700	300
Agua Caliente I	AD09-95	-23.08339	-67.40797	AD09-95(C)	8070	160	17020	350	1251.4	4.2	0.3378	0.0009	2543	13	17469	62	1314.5	4.4	17440	60
Agua Caliente I	AD09-95	-23.08339	-67.40797	AD09-95(D)	4678	94	2460	250	1260.4	2.4	0.3048	0.0013	9200	910	15589	73	1317.1	2.6	15580	70
Agua Caliente I	AD09-95	-23.08339	-67.40797	AD09-95(E)	3353	67	5870	260	1243.7	1.8	0.3123	0.0014	2830	110	16128	80	1301.5	1.9	16100	80
Agua Caliente I	AD09-96	NaN	NaN	AD09-96(A)	2015	13	12172	12	1189.5	3.1	0.2769	0.0027	764.8	6.1	14570	150	1239.1	3.3	14490	160
Agua Caliente I	AD09-96	NaN	NaN	AD09-96(A)	8070	160	116100	8200	1167.5	1.6	0.2594	0.0063	286	21	13750	350	1213	2.1	13500	400
Agua Caliente I	AD09-96	NaN	NaN	AD09-96(B)	10270	210	48300	9300	1179.8	2.6	0.2732	0.006	920	180	14430	340	1228.7	2.9	14400	300
Agua Caliente I	AD09-98	-23.08400	-67.40674	AD09-98(A)	4820	96	67200	2100	1216	1.5	0.3192	0.0052	364	11	16730	290	1274.1	1.9	16500	300
Agua Caliente I	AD09-98	-23.08400	-67.40674	AD09-98(B)	3965	79	8420	860	1219.5	1.6	0.2857	0.006	2140	220	14850	330	1271.5	2	14800	300
Agua Caliente I	AD09-98	-23.08400	-67.40674	AD09-98(C)	4265	85	11190	380	1227.9	1.5	0.2959	0.0012	1790	49	15342	69	1282.1	1.6	15310	70
Agua Caliente I	AD09-98	-23.08400	-67.40674	AD09-98(D)	9130	180	58600	1200	1195	1.9	0.3843	0.0013	950.7	5.9	20629	78	1266.4	2.1	20540	100
Agua Caliente I	AD10-225	-23.08430	-67.40108	AD10-225(A)	3183	19	6764.7	5.3	1272.8	2.7	0.3038	0.0025	2401	22	15450	140	1329.4	2.9	15420	140
Agua Caliente I	AD10-225	-23.08430	-67.40108	AD10-225(B)	14160	280	13400	8600	1227.1	6.9	0.4405	0.0053	7400	4800	23550	320	1311.4	7.5	23500	300
Agua Caliente I	AD10-225	-23.08430	-67.40108	AD10-225(C)	7870	160	27190	550	1187.3	4.1	0.361	0.0014	1659	5.9	19359	89	1253.8	4.3	19310	90
Agua Caliente I	AD10-225	-23.08430	-67.40108	AD10-225B(A)	5010	100	129700	2600	1152.7	2	0.3231	0.0014	198.2	0.81	17488	82	1209.8	2.2	17100	300
Agua Caliente I	AD10-225	-23.08430	-67.40108	AD10-225B(B)	6000	120	64100	1300	1159.3	1.7	0.3442	0.0014	511	2.1	18652	84	1221.4	1.8	18500	130
Agua Caliente I	AD10-225	-23.08430	-67.40108	AD10-225B(C)	6060	120	110300	2200	1155.4	2.1	0.4063	0.0016	354.3	1.3	22364	99	1229.8	2.3	22110	200
Agua Caliente I	AD10-225	-23.08430	-67.40108	AD10-225B(D)	5630	110	34150	690	1159.3	1.6	0.3236	0.0014	847.2	3.8	17456	83	1217.6	1.7	17370	100
Agua Caliente I	AD10-225	-23.08430	-67.40108	AD10-225B(E)	5770	120	78400	1600	1165.6	1.6	0.3077	0.0012	359.5	1.3	16492	69	1220.5	1.8	16300	140
Agua Caliente I	AD10-226	-23.08276	-67.40104	AD10-226(A)	2059	15	10718	9.2	1193.5	3.1	0.2691	0.0028	864	7.1	14110	150	1241.7	3.3	14040	160
Agua Caliente I	AD10-226	-23.08276	-67.40104	AD10-226(A)	2067	41	15500	1500	1169.7	8.1	0.243	0.02	513	65	12800	1100	1212.4	9.2	12700	1100
Agua Caliente I	AD10-226	-23.08276	-67.40104	AD10-226(B)	2307	46	20240	410	1160.3	2.3	0.3949	0.0011	714.7	2.8	21627	68	1232.9	2.5	21500	110
Agua Caliente I	AD10-226	-23.08276	-67.40104	AD10-226AB(A)	2758	55	34150	690	1161.2	3.4	0.3247	0.0014	416.4	1.9	17504	85	1219.4	3.6	17330	140
Agua Caliente I	AD10-226	-23.08276	-67.40104	AD10-226AB(B)	3194	64	31410	640	1170.6	7.1	0.2854	0.0014	460.7	2.6	15185	94	1221.4	7.4	15050	130
Agua Caliente I	AD10-226	-23.08276	-67.40104	AD10-226AB(C)	3362	67	16470	340	1188.7	1.6	0.3631	0.0014	1177	7	19467	84	1255.6	1.7	19400	90
Agua Caliente I	AD10-226	-23.08276	-67.40104	AD10-226AB(D)	2129	43	9110	190	1177.8	1.9	0.2733	0.0012	1014	7.1	14451	67	1226.7	2	14390	80
Agua Caliente I	AD10-226	-23.08276	-67.40104	AD10-226AB(E)	2846	57	29110	590	1158.6	1.7	0.2699	0.0012	419.1	2.2	14401	69	1206.2	1.8	14260	120
Agua Caliente I	AD10-226	-23.08276	-67.40104	AD10-226DA(A)	2496	50	6770	140	1183.3	2.1	0.2651	0.0012	1551	8.9	13958	70	1230.7	2.2	13920	70
Agua Caliente I	AD10-226	-23.08276	-67.40104	AD10-226DA(B)	2550	51	19730	400	1178.2	1.9	0.2897	0.0014	594.5	2.8	15371	78	1230.1	2	15260	110
Agua Caliente I	AD10-226	-23.08276	-67.40104	AD10-226DB(A)	2283	46	18090	360	1185	1.5	0.2647	0.0017	530.5	3.4	13925	95	1232.1	1.6	13810	120
Agua Caliente I	AD10-226	-23.08276	-67.40104	AD10-226DB(B)	2388	48	8740	180	1180.4	1.4	0.2415	0.0008	1047	3.8	12671	47	1223.2	1.5	12620	60
Agua Caliente I	AD10-226	-23.08276	-67.40104	AD10-226DB(C)	2171	43	22410	450	1176.2	1.5	0.2625	0.001	403.8	1.5	13863	57	1222.6	1.7	13720	110
Agua Caliente I	AD10-228	-23.08559	-67.40209	AD10-228(A)	3916	31	16834	13	1252.3	3.1	0.3114	0.0033	1213	10	16010	180	1310	3.3	15960	190
Agua Caliente I	AD10-228	-23.08559	-67.40209	AD10-228(C)	5450	110	35940	720	1232	1.7	0.3003	0.0008	722.8	2.2	15557	48	1287	1.8	15470	80
Agua Caliente I	AD10-228	-23.08559	-67.40209	AD10-228(D)	4723	94	11170	350	1229.7	3.2	0.3011	0.0011	2022	49	15619	65	1285	3.3	15590	70
Agua Caliente I	AD10-233	-23.17414	-67.39920	AD10-233-10(F)	3973	79	69800	1400	1252.6	1.8	0.3129	0.0012	282.9	1.1	16089	69	1309.9	2	15850	170
Agua Caliente I	AD10-233	-23.17414	-67.39920	AD10-233-10(G)	4290	86	51600	1000	1265.9	2.1	0.3111	0.0016	410.3	2.2	15891	87	1323.4	2.2	15730	140
Agua Caliente I	AD10-233	-23.17414	-67.39920	AD10-233-10(H)	4141	83	47710	960	1268.6	2.2	0.308	0.0012	424.4	1.6	15703	67	1325.5	2.3	15550	120
Agua Caliente I	AD10-233	-23.17414	-67.39920	AD10-233-10(J)	3261	65	52300	1000	1175.7	1.6	0.2901	0.0011	287.2	1.1	15410	65	1227.1	1.8	15190	160
Agua Caliente I	AD10-233	-23.17414	-67.39920	AD10-233-10(K)	3936	79	216500	4300	1248.3	1.6	0.3208	0.0015	92.6	0.42	16558	85	1305.3	2.5	15800	500
Agua Caliente I	AD10-233	-23.17414	-67.39920	AD10-233-10(L)	4061	81	26820	540	1263.8	1.6	0.3112	0.0009	748.2	2.1	15915	50	1321.6	1.7	15830	80
Agua Caliente I	AD10-233	-23.17414	-67.39920	AD10-233-10(M)	3520	70	6370	130	1180.2	2.1	0.2882	0.001	2530	13	15271	59	1232.1	2.2	15250	60
Agua Caliente I	AD10-233	-23.17414	-67.39920	AD10-233-5-2 (A)-1	4145	83	56800	1200	1268.4	2.2	0.3123	0.0012	361.8	2.2	15938	68	1326.1	2.4	15760	140
Agua Caliente I	AD10-233	-23.17414	-67.39920	AD10-233-5-2 (A)-2	4153	83	59800	1300	1271.2	3.9	0.314	0.0013	346.4	3.2	16010	75	1329.2	4.1	15820	150
Agua Caliente I	AD10-233	-23.17414	-67.39920	AD10-233-5-2 (B)	4418	88	52100	1100	1284.6	1.7	0.3139	0.0011	422.7	2.7	15904	60	1343	1.8	15750	120
Agua Caliente I	AD10-233	-23.17414	-67.39920	AD10-233-5-2 (C)	3179	64	3200	300	1179.8	2	0.2846	0.001	4490	400	15072	57	1231	2.1	15060	60
Agua Caliente I	AD10-233	-23.17414	-67.39920	AD10-233-5-2 (D)	2775	56	2820	140	1179.7	2.6	0.2893	0.0011	4520	210	15339	68	1231.8	2.8	15320	70
Agua Caliente I	AD10-233	-23.17414	-67.39920	AD10-233a(A)	3767	76	970	570	1263.2	4.5	0.301	0.0047	19000	11000	15370	260	1319.2	4.8	15400	300
Agua Caliente I	AD10-233	-23.17414	-67.39920	AD10-233a(A)	3802	76	3146	96	1272	2.5	0.309	0.001	5930	140	15732	59	1329.7	2.6	15720	60
Agua Caliente I	AD10-233	-23.17414	-67.39920	AD10-233a(B)	3798	76	3400	6600	1269.6	2	0.289	0.011	5100	9900	14660	600	1323.2	3	14600	600
Agua Caliente I	AD10-233	-23.17414	-67.39920	AD10-233b-1(A)	2473	49	30560	620	1171.5	1.6	0.2841	0.002	365	2.7	15100	120	1221.9	1.8	14930	160
Agua Caliente I	AD10-233	-23.17414	-67.39920	AD10-233b-1(B)	4681	94	16600	330	1229.7	3.1	0.3003	0.001	1345	4.2	15573	58	1284.8	3.3	15530	70
Agua Caliente I	AD10-233	-23.17414	-67.39920	AD10-233b-1(C)	4094	82	6530	130	1224.8	1.7	0.296	0.0009	2945	16	15371	48	1279.1	1.8	15350	50
Agua Caliente I	AD10-233	-23.17414	-67.39920	AD10-233b-2(D)	4415	88	13340	280	1265	1.5	0.2996	0.0015	1575	12	15276	81	1320.6	1.6	15240	90

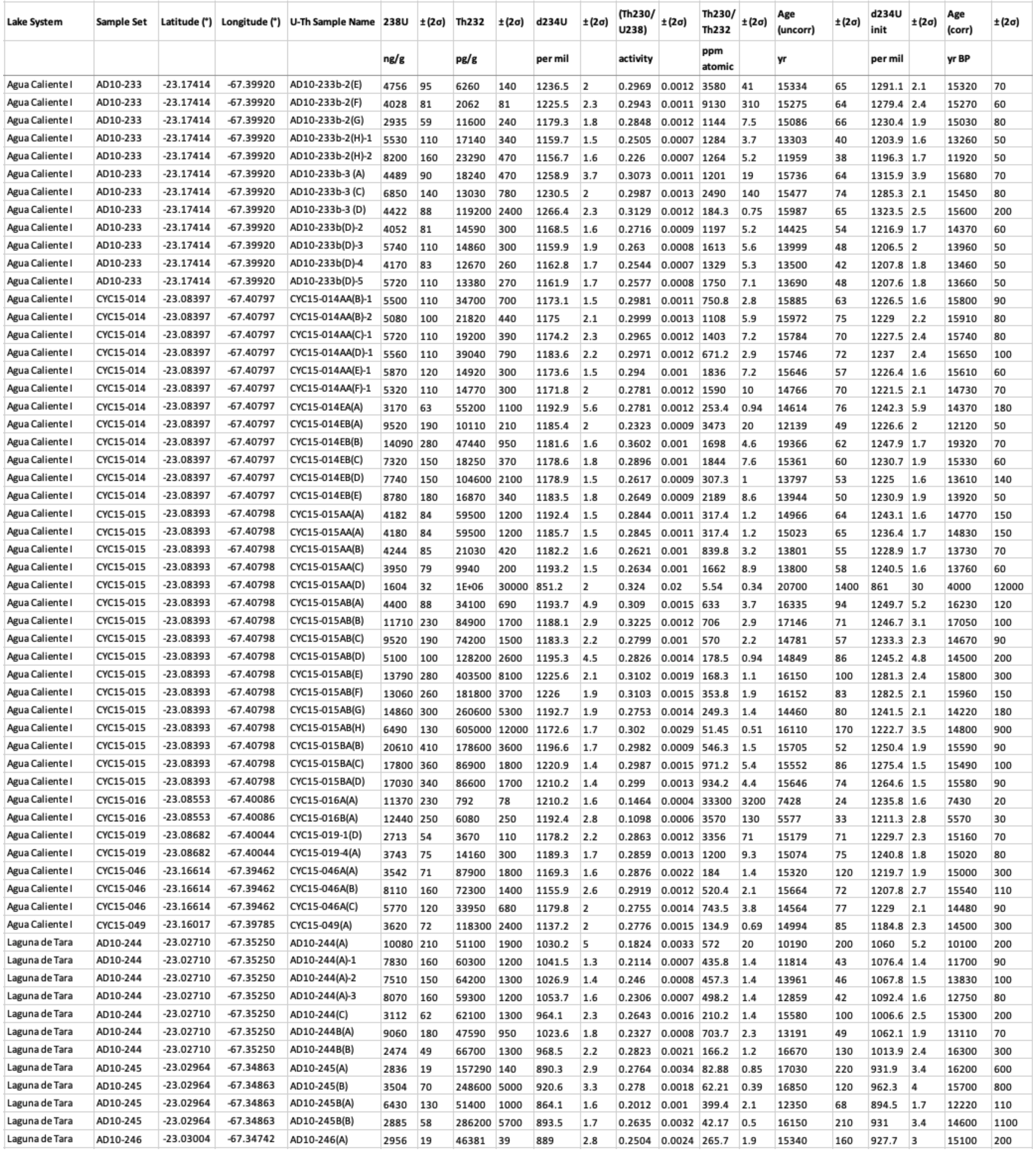

Lake System	Sample Set	Latitude (°)	Longitude (°)	U-Th Sample Name	238U	±(2σ)	Th232	±(2σ)	d234U	±(2σ)	(Th230/ U238)	±(2σ)	Th230/ Th232	±(2σ)	Age (uncorr)	±(2σ)	d234U init	±(2σ)	Age (corr)	±(2σ)
					ng/g		pg/g		per mil		activity		ppm atomic		yr		per mil		yr BP	
Agua Caliente I	AD10-233	-23.17414	-67.39920	AD10-233b-2(E)	4756	95	6260	140	1236.5	2	0.2969	0.0012	3580	41	15334	65	1291.1	2.1	15320	70
Agua Caliente I	AD10-233	-23.17414	-67.39920	AD10-233b-2(F)	4028	81	2062	81	1225.5	2.3	0.2943	0.0011	9130	310	15275	64	1279.4	2.4	15270	60
Agua Caliente I	AD10-233	-23.17414	-67.39920	AD10-233b-2(G)	2935	59	11600	240	1179.3	1.8	0.2848	0.0012	1144	7.5	15086	66	1230.4	1.9	15030	80
Agua Caliente I	AD10-233	-23.17414	-67.39920	AD10-233b-2(H)-1	5530	110	17140	340	1159.7	1.5	0.2505	0.0007	1284	3.7	13303	40	1203.9	1.6	13260	50
Agua Caliente I	AD10-233	-23.17414	-67.39920	AD10-233b-2(H)-2	8200	160	23290	470	1156.7	1.6	0.226	0.0007	1264	5.2	11959	38	1196.3	1.7	11920	50
Agua Caliente I	AD10-233	-23.17414	-67.39920	AD10-233b-3 (A)	4489	90	18240	470	1258.9	3.7	0.3073	0.0011	1201	19	15736	64	1315.9	3.9	15680	70
Agua Caliente I	AD10-233	-23.17414	-67.39920	AD10-233b-3 (C)	6850	140	13030	780	1230.5	2	0.2987	0.0013	2490	140	15477	74	1285.3	2.1	15450	80
Agua Caliente I	AD10-233	-23.17414	-67.39920	AD10-233b-3 (D)	4422	88	119200	2400	1266.4	2.3	0.3129	0.0012	184.3	0.75	15987	65	1323.5	2.5	15600	200
Agua Caliente I	AD10-233	-23.17414	-67.39920	AD10-233b(D)-2	4052	81	14590	300	1168.5	1.6	0.2716	0.0009	1197	5.2	14425	54	1216.9	1.7	14370	60
Agua Caliente I	AD10-233	-23.17414	-67.39920	AD10-233b(D)-3	5740	110	14860	300	1159.9	1.9	0.263	0.0008	1613	5.6	13999	48	1206.5	2	13960	50
Agua Caliente I	AD10-233	-23.17414	-67.39920	AD10-233b(D)-4	4170	83	12670	260	1162.8	1.7	0.2544	0.0007	1329	5.3	13500	42	1207.8	1.8	13460	50
Agua Caliente I	AD10-233	-23.17414	-67.39920	AD10-233b(D)-5	5720	110	13380	270	1161.9	1.7	0.2577	0.0008	1750	7.1	13690	48	1207.6	1.8	13660	50
Agua Caliente I	CYC15-014	-23.08397	-67.40797	CYC15-014AA(B)-1	5500	110	34700	700	1173.1	1.5	0.2981	0.0011	750.8	2.8	15885	63	1226.5	1.6	15800	90
Agua Caliente I	CYC15-014	-23.08397	-67.40797	CYC15-014AA(B)-2	5080	100	21820	440	1175	2.1	0.2999	0.0013	1108	5.9	15972	75	1229	2.2	15910	80
Agua Caliente I	CYC15-014	-23.08397	-67.40797	CYC15-014AA(C)-1	5720	110	19200	390	1174.2	2.3	0.2965	0.0012	1403	7.2	15784	70	1227.5	2.4	15740	80
Agua Caliente I	CYC15-014	-23.08397	-67.40797	CYC15-014AA(D)-1	5560	110	39040	790	1183.6	2.2	0.2971	0.0012	671.2	2.9	15746	72	1237	2.4	15650	100
Agua Caliente I	CYC15-014	-23.08397	-67.40797	CYC15-014AA(E)-1	5870	120	14920	300	1173.6	1.5	0.294	0.001	1836	7.2	15646	57	1226.4	1.6	15610	60
Agua Caliente I	CYC15-014	-23.08397	-67.40797	CYC15-014AA(F)-1	5320	110	14770	300	1171.8	2	0.2781	0.0012	1590	10	14766	70	1221.5	2.1	14730	70
Agua Caliente I	CYC15-014	-23.08397	-67.40797	CYC15-014EA(A)	3170	63	55200	1100	1192.9	5.6	0.2781	0.0012	253.4	0.94	14614	76	1242.3	5.9	14370	180
Agua Caliente I	CYC15-014	-23.08397	-67.40797	CYC15-014EB(A)	9520	190	10110	210	1185.4	2	0.2323	0.0009	3473	20	12139	49	1226.6	2	12120	50
Agua Caliente I	CYC15-014	-23.08397	-67.40797	CYC15-014EB(B)	14090	280	47440	950	1181.6	1.6	0.3602	0.001	1698	4.6	19366	62	1247.9	1.7	19320	70
Agua Caliente I	CYC15-014	-23.08397	-67.40797	CYC15-014EB(C)	7320	150	18250	370	1178.6	1.8	0.2896	0.001	1844	7.6	15361	60	1230.7	1.9	15330	60
Agua Caliente I	CYC15-014	-23.08397	-67.40797	CYC15-014EB(D)	7740	150	104600	2100	1178.9	1.5	0.2617	0.0009	307.3	1	13797	53	1225	1.6	13610	140
Agua Caliente I	CYC15-014	-23.08397	-67.40797	CYC15-014EB(E)	8780	180	16870	340	1183.5	1.8	0.2649	0.0009	2189	8.6	13944	50	1230.9	1.9	13920	50
Agua Caliente I	CYC15-015	-23.08393	-67.40798	CYC15-015AA(A)	4182	84	59500	1200	1192.4	1.5	0.2844	0.0011	317.4	1.2	14966	64	1243.1	1.6	14770	150
Agua Caliente I	CYC15-015	-23.08393	-67.40798	CYC15-015AA(A)	4180	84	59500	1200	1185.7	1.5	0.2845	0.0011	317.4	1.2	15023	65	1236.4	1.7	14830	150
Agua Caliente I	CYC15-015	-23.08393	-67.40798	CYC15-015AA(B)	4244	85	21030	420	1182.2	1.6	0.2621	0.001	839.8	3.2	13801	55	1228.9	1.7	13730	70
Agua Caliente I	CYC15-015	-23.08393	-67.40798	CYC15-015AA(C)	3950	79	9940	200	1193.2	1.5	0.2634	0.001	1662	8.9	13800	58	1240.5	1.6	13760	60
Agua Caliente I	CYC15-015	-23.08393	-67.40798	CYC15-015AA(D)	1604	32	1E+06	30000	851.2	2	0.324	0.02	5.54	0.34	20700	1400	861	30	4000	12000
Agua Caliente I	CYC15-015	-23.08393	-67.40798	CYC15-015AB(A)	4400	88	34100	690	1193.7	4.9	0.309	0.0015	633	3.7	16335	94	1249.7	5.2	16230	120
Agua Caliente I	CYC15-015	-23.08393	-67.40798	CYC15-015AB(B)	11710	230	84900	1700	1188.1	2.9	0.3225	0.0012	706	2.9	17146	71	1246.7	3.1	17050	100
Agua Caliente I	CYC15-015	-23.08393	-67.40798	CYC15-015AB(C)	9520	190	74200	1500	1183.3	2.2	0.2799	0.001	570	2.2	14781	57	1233.3	2.3	14670	90
Agua Caliente I	CYC15-015	-23.08393	-67.40798	CYC15-015AB(D)	5100	100	128200	2600	1195.3	4.5	0.2826	0.0014	178.5	0.94	14849	86	1245.2	4.8	14500	200
Agua Caliente I	CYC15-015	-23.08393	-67.40798	CYC15-015AB(E)	13790	280	403500	8100	1225.6	2.1	0.3102	0.0019	168.3	1.1	16150	100	1281.3	2.4	15800	300
Agua Caliente I	CYC15-015	-23.08393	-67.40798	CYC15-015AB(F)	13060	260	181800	3700	1226	1.9	0.3103	0.0015	353.8	1.9	16152	83	1282.5	2.1	15960	150
Agua Caliente I	CYC15-015	-23.08393	-67.40798	CYC15-015AB(G)	14860	300	260600	5300	1192.7	1.9	0.2753	0.0014	249.3	1.4	14460	80	1241.5	2.1	14220	180
Agua Caliente I	CYC15-015	-23.08393	-67.40798	CYC15-015AB(H)	6490	130	605000	12000	1172.6	1.7	0.302	0.0029	51.45	0.51	16110	170	1222.7	3.5	14800	900
Agua Caliente I	CYC15-015	-23.08393	-67.40798	CYC15-015BA(B)	20610	410	178600	3600	1196.6	1.7	0.2982	0.0009	546.3	1.5	15705	52	1250.4	1.9	15590	90
Agua Caliente I	CYC15-015	-23.08393	-67.40798	CYC15-015BA(C)	17800	360	86900	1800	1220.9	1.4	0.2987	0.0015	971.2	5.4	15552	86	1275.4	1.5	15490	100
Agua Caliente I	CYC15-015	-23.08393	-67.40798	CYC15-015BA(D)	17030	340	86600	1700	1210.2	1.4	0.299	0.0013	934.2	4.4	15646	74	1264.6	1.5	15580	90
Agua Caliente I	CYC15-016	-23.08553	-67.40086	CYC15-016A(A)	11370	230	792	78	1210.2	1.6	0.1464	0.0004	33300	3200	7428	24	1235.8	1.6	7430	20
Agua Caliente I	CYC15-016	-23.08553	-67.40086	CYC15-016B(A)	12440	250	6080	250	1192.4	2.8	0.1098	0.0006	3570	130	5577	33	1211.3	2.8	5570	30
Agua Caliente I	CYC15-019	-23.08682	-67.40044	CYC15-019-1(D)	2713	54	3670	110	1178.2	2.2	0.2863	0.0012	3356	71	15179	71	1229.7	2.3	15160	70
Agua Caliente I	CYC15-019	-23.08682	-67.40044	CYC15-019-4(A)	3743	75	14160	300	1189.3	1.7	0.2859	0.0013	1200	9.3	15074	75	1240.8	1.8	15020	80
Agua Caliente I	CYC15-046	-23.16614	-67.39462	CYC15-046A(A)	3542	71	87900	1800	1169.3	1.6	0.2876	0.0022	184	1.4	15320	120	1219.7	1.9	15000	300
Agua Caliente I	CYC15-046	-23.16614	-67.39462	CYC15-046A(B)	8110	160	72300	1400	1155.9	2.6	0.2919	0.0012	520.4	2.1	15664	72	1207.8	2.7	15540	110
Agua Caliente I	CYC15-046	-23.16614	-67.39462	CYC15-046A(C)	5770	120	33950	680	1179.8	2	0.2755	0.0014	743.5	3.8	14564	77	1229	2.1	14480	90
Agua Caliente I	CYC15-049	-23.16017	-67.39785	CYC15-049(A)	3620	72	118300	2400	1137.2	2	0.2776	0.0015	134.9	0.69	14994	85	1184.8	2.3	14500	300
Laguna de Tara	AD10-244	-23.02710	-67.35250	AD10-244(A)	10080	210	51100	1900	1030.2	5	0.1824	0.0033	572	20	10190	200	1060	5.2	10100	200
Laguna de Tara	AD10-244	-23.02710	-67.35250	AD10-244(A)-1	7830	160	60300	1200	1041.5	1.3	0.2114	0.0007	435.8	1.4	11814	43	1076.4	1.4	11700	90
Laguna de Tara	AD10-244	-23.02710	-67.35250	AD10-244(A)-2	7510	150	64200	1300	1026.9	1.4	0.246	0.0008	457.3	1.4	13961	46	1067.8	1.5	13830	100
Laguna de Tara	AD10-244	-23.02710	-67.35250	AD10-244(A)-3	8070	160	59300	1200	1053.7	1.6	0.2306	0.0007	498.2	1.4	12859	42	1092.4	1.6	12750	80
Laguna de Tara	AD10-244	-23.02710	-67.35250	AD10-244(C)	3112	62	62100	1300	964.1	2.3	0.2643	0.0016	210.2	1.4	15580	100	1006.6	2.5	15300	200
Laguna de Tara	AD10-244	-23.02710	-67.35250	AD10-244B(A)	9060	180	47590	950	1023.6	1.8	0.2327	0.0008	703.7	2.3	13191	49	1062.1	1.9	13110	70
Laguna de Tara	AD10-244	-23.02710	-67.35250	AD10-244B(B)	2474	49	66700	1300	968.5	2.2	0.2823	0.0021	166.2	1.2	16670	130	1013.9	2.4	16300	300
Laguna de Tara	AD10-245	-23.02964	-67.34863	AD10-245(A)	2836	19	157290	140	890.3	2.9	0.2764	0.0034	82.88	0.85	17030	220	931.9	3.4	16200	600
Laguna de Tara	AD10-245	-23.02964	-67.34863	AD10-245(B)	3504	70	248600	5000	920.6	3.3	0.278	0.0018	62.21	0.39	16850	120	962.3	4	15700	800
Laguna de Tara	AD10-245	-23.02964	-67.34863	AD10-245B(A)	6430	130	51400	1000	864.1	1.6	0.2012	0.001	399.4	2.1	12350	68	894.5	1.7	12220	110
Laguna de Tara	AD10-245	-23.02964	-67.34863	AD10-245B(B)	2885	58	286200	5700	893.5	1.7	0.2635	0.0032	42.17	0.5	16150	210	931	3.4	14600	1100
Laguna de Tara	AD10-246	-23.03004	-67.34742	AD10-246(A)	2956	19	46381	39	889	2.8	0.2504	0.0024	265.7	1.9	15340	160	927.7	3	15100	200

Table A.2: U-Th data associated with Chapters 3–5 (continued).

Lake System	Sample Set	Latitude (°)	Longitude (°)	U-Th Sample Name	238U	± (2σ)	Th232	± (2σ)	d234U	± (2σ)	(Th230/ U238)	± (2σ)	Th230/ Th232	± (2σ)	Age (uncorr)	± (2σ)	d234U init	± (2σ)	Age (corr)	± (2σ)
					ng/g		pg/g		per mil		activity		ppm atomic		yr		per mil		yr BP	
Laguna de Tara	AD10-246	-23.03004	-67.34742	AD10-246(B)	2351	47	82800	1700	928.7	7.2	0.2691	0.0015	121.3	0.52	16190	120	970.6	7.6	15600	400
Laguna de Tara	CYC16-045	-23.00291	-67.31172	CYC16-045A(A)	1874	37	116500	2300	943.5	1.7	0.2903	0.0017	74.13	0.43	17420	110	988.4	2.5	16400	700
Laguna de Tara	CYC16-045	-23.00291	-67.31172	CYC16-045A(B)	1758	35	72200	1400	944	1.9	0.2768	0.0016	107.1	0.62	16550	110	987.3	2.3	15900	400
Laguna de Tara	CYC16-045	-23.00291	-67.31172	CYC16-045B(B)	2296	46	179000	3600	964.8	2.1	0.2953	0.0024	60.12	0.49	17530	160	1010.3	3.2	16300	800
Laguna de Tara	CYC16-045	-23.00291	-67.31172	CYC16-045B(C)	5420	110	91300	1800	856.7	1.6	0.1941	0.0008	183	0.76	11941	54	885.4	1.7	11660	190
Laguna de Tara	CYC16-045	-23.00291	-67.31172	CYC16-045B(D)	2037	41	151400	3000	947.7	1.8	0.287	0.0024	61.32	0.51	17160	160	991.5	2.9	16000	800
Laguna de Tara	CYC16-045	-23.00291	-67.31172	CYC16-045B(E)	2015	40	243800	4900	939.2	1.5	0.2951	0.0035	38.72	0.46	17770	230	982.2	3.9	15900	1300
Laguna de Tara	CYC16-045	-23.00291	-67.31172	CYC16-045B(F)	5240	100	103200	2100	854.8	1.6	0.1932	0.001	155.8	0.87	11896	67	883.1	1.7	11600	200
Laguna de Tara	CYC16-045	-23.00291	-67.31172	CYC16-045B(G)	5350	110	352100	7100	857.2	1.6	0.196	0.0021	47.33	0.51	12060	140	884.1	2.5	11000	700
Laguna de Tara	CYC16-045	-23.00291	-67.31172	CYC16-045B(H)	3615	72	263100	5300	850.2	1.7	0.2125	0.0026	46.34	0.57	13180	170	879.4	2.7	12000	800
Laguna de Tara	CYC16-048	-23.00608	-67.33198	CYC16-048B(A)	11450	230	329600	6600	858.9	1.8	0.2064	0.0021	113.9	1.1	12720	140	889.1	2	12300	300
Laguna de Tara	CYC16-048	-23.00608	-67.33198	CYC16-048B(B)	12230	240	362400	7300	858.8	1.6	0.2077	0.0014	111.3	0.75	12808	93	889.1	1.9	12300	300
Laguna de Tara	CYC16-048	-23.00608	-67.33198	CYC16-048B(C)	11340	230	672000	13000	857.1	1.6	0.2128	0.0021	56.98	0.57	13150	140	887.1	2.4	12200	700
Laguna de Tara	CYC16-048	-23.00608	-67.33198	CYC16-048C(A)	10590	210	445600	9000	860.5	1.7	0.2122	0.0015	80.11	0.57	13088	97	891.2	2.2	12400	500
Laguna de Tara	CYC16-048	-23.00608	-67.33198	CYC16-048C(B)	11800	240	415100	8400	855.4	1.6	0.2096	0.0017	94.61	0.78	12950	110	885.8	2	12400	400
Laguna de Tara	CYC16-048	-23.00608	-67.33198	CYC16-048C(C)	12230	240	369200	7400	852.1	2.9	0.2064	0.0014	108.6	0.75	12771	93	882.1	3.1	12300	300
Laguna Miniques	CYC16-023	-23.75992	-67.78862	CYC16-023A(B)	6510	130	9720	200	446.6	1.7	0.1286	0.0005	1367	4.9	10101	40	459.5	1.8	10070	40
Laguna Miniques	CYC16-023	-23.75992	-67.78862	CYC16-023A(C)	19970	400	10540	210	461.2	1.9	0.1425	0.0003	4285	9.9	11132	32	475.9	2	11120	30
Laguna Miniques	CYC16-023	-23.75992	-67.78862	CYC16-023A(D)	16230	320	29300	590	454.9	2.4	0.1288	0.0004	1133	4.1	10063	38	467.9	2.4	10020	50
Laguna Miniques	CYC16-023	-23.75992	-67.78862	CYC16-023A(E)	15320	310	11600	240	462.9	2	0.1486	0.0006	3117	23	11619	50	478.3	2.1	11600	50
Laguna Miniques	CYC16-023	-23.75992	-67.78862	CYC16-023A(F)	9060	180	18010	370	450.5	1.8	0.1463	0.0005	1169	6.3	11529	44	465.4	1.8	11490	50
Laguna Miniques	CYC16-025	-23.75985	-67.78864	CYC16-025AA(A)	4911	98	80600	1600	442.3	1.5	0.1525	0.0006	147.7	0.61	12123	54	457.2	1.6	11800	200
Laguna Miniques	CYC16-025	-23.75985	-67.78864	CYC16-025AA(B)	5440	110	122700	2500	417.1	2.1	0.1304	0.0006	91.8	0.42	10475	55	429	2.2	10000	300
Laguna Miniques	CYC16-025	-23.75985	-67.78864	CYC16-025AA(C)	3804	76	58300	1200	453.5	1.8	0.1537	0.0007	159.3	0.67	12120	58	468.8	1.9	11800	200
Laguna Miniques	CYC16-025	-23.75985	-67.78864	CYC16-025AA(D)	5160	100	11670	230	447	2	0.1454	0.0008	1021	5.8	11490	71	461.7	2.1	11440	80
Laguna Miniques	CYC16-025	-23.75985	-67.78864	CYC16-025AA(E)	5360	110	27730	560	450.4	2	0.1449	0.0006	445.1	1.7	11421	51	465.1	2.1	11310	90
Laguna Miniques	CYC16-025	-23.75985	-67.78864	CYC16-025AA(F)	4947	99	77200	1500	450	2	0.1514	0.0007	154.2	0.7	11963	62	465	2.1	11600	200
Laguna Miniques	CYC16-028	-23.76082	-67.78827	CYC16-028A(A)-1	7320	150	76200	1500	459.7	2	0.0059	0.0002	8.93	0.33	438	16	460	2	220	150
Laguna Miniques	CYC16-028	-23.76082	-67.78827	CYC16-028B(A)-1	8550	170	56100	1100	455.1	1.8	0.0045	0.0002	10.93	0.36	339	11	455.4	1.8	200	90
Laguna Miniques	CYC16-029	-23.76124	-67.78737	CYC16-029AA(A)	3761	75	49020	980	468.7	1.9	0.1271	0.0007	154.8	0.83	9822	58	481.5	2	9550	190
Laguna Miniques	CYC16-029	-23.76124	-67.78737	CYC16-029AA(B)	2726	55	101500	2000	465.1	1.8	0.1506	0.001	64.22	0.43	11762	86	479.8	2	11000	500
Laguna Miniques	CYC16-029	-23.76124	-67.78737	CYC16-029AA(C)	4001	80	10290	220	459.8	2.1	0.1428	0.0015	882	11	11170	130	474.4	2.1	11110	130
Laguna Miniques	CYC16-029	-23.76124	-67.78737	CYC16-029AA(D)	4348	87	12010	250	456.6	2	0.1385	0.0013	796.2	8.7	10840	100	470.7	2	10780	110
Laguna Miniques	CYC16-029	-23.76124	-67.78737	CYC16-029BA(A)	399.7	8	10830	230	495.6	9.4	0.8077	0.0066	473.4	4.4	80400	1200	621	12	79900	1300
Laguna Miniques	CYC16-029	-23.76124	-67.78737	CYC16-029BA(B)	402.1	8	81300	1600	456.2	2.9	0.9176	0.0071	72.03	0.43	101300	1300	600.4	6.3	97000	3000
Laguna Miniques	CYC16-029	-23.76124	-67.78737	CYC16-029BB(A)	359.5	7.2	91500	1800	632.3	3.4	0.2941	0.0051	18.34	0.3	21390	410	662.5	7.2	17000	3000
Laguna Miniques	CYC16-029	-23.76124	-67.78737	CYC16-029CA(B)	2474	49	25340	510	465.3	1.7	0.1406	0.0007	217.9	1.1	10943	59	479.6	1.7	10730	150
Laguna Miniques	CYC16-029	-23.76124	-67.78737	CYC16-029CA(C)	2574	51	21900	440	463.4	1.6	0.1437	0.0006	268.1	1.1	11214	53	478.1	1.7	11040	130
Laguna Miniques	CYC16-029	-23.76124	-67.78737	CYC16-029DA(A)-1	3208	64	108500	2200	465.1	1.8	0.1353	0.0008	63.53	0.38	10513	64	478.1	2	9800	500
Laguna Miniques	CYC16-029	-23.76124	-67.78737	CYC16-029DA(A)-2	3097	62	109100	2200	467.1	6	0.1344	0.0008	60.57	0.35	10427	80	480	6.2	9700	500
Laguna Miniques	CYC16-029	-23.76124	-67.78737	CYC16-029DA(A)-3	3094	62	90000	1800	466.6	1.7	0.134	0.0007	73.14	0.38	10398	58	479.7	1.9	9800	400
Laguna Miniques	CYC16-030	-23.76122	-67.78746	CYC16-030AA(A)	18480	370	9480	210	367	1.5	0.1431	0.0004	4427	39	12000	35	379.7	1.6	11990	40
Laguna Miniques	CYC16-034	-23.76589	-67.78331	CYC16-034AA(A)	7920	160	60400	1200	482.1	1.6	0.0403	0.0003	84	0.69	3004	26	486	1.7	2840	110
Laguna Miniques	CYC16-034	-23.76589	-67.78331	CYC16-034AA(B)	1201	24	49390	990	480.8	2.5	0.2124	0.0012	81.98	0.47	16750	110	502.8	2.8	15900	600
Laguna Miniques	CYC16-034	-23.76589	-67.78331	CYC16-034AA(C)	1245	25	60600	1200	481.5	1.8	0.1848	0.0013	60.24	0.41	14430	110	500.1	2.1	13400	700
Laguna Miniques	CYC16-034	-23.76589	-67.78331	CYC16-034AA(D)	1739	35	93100	1900	495.8	2.1	0.2129	0.0015	63.16	0.45	16610	130	518	2.5	15500	700
Laguna Miniques	CYC16-034	-23.76589	-67.78331	CYC16-034AB(A)	1808	36	87200	1700	485.8	2.1	0.1706	0.0016	56.2	0.52	13210	130	502.9	2.4	12200	700
Laguna Miscanti	CYC16-009	-23.71192	-67.74437	CYC16-009A(A)	5650	110	30700	610	264.1	1.5	0.1641	0.0006	479.6	1.7	15092	63	275.5	1.6	14960	110
Laguna Miscanti	CYC16-009	-23.71192	-67.74437	CYC16-009A(B)	3729	75	34520	700	265.6	2.2	0.1587	0.0009	272.2	1.6	14543	90	276.6	2.3	14320	170
Laguna Miscanti	CYC16-009	-23.71192	-67.74437	CYC16-009A(C)	4189	84	37440	750	264.4	1.9	0.1434	0.0007	254.8	1.3	13074	71	274.2	2	12860	160
Laguna Miscanti	CYC16-009	-23.71192	-67.74437	CYC16-009A(D)	4279	86	152100	3000	282.6	2.5	0.157	0.0011	70.1	0.47	14170	110	293.4	2.6	13300	600
Laguna Miscanti	CYC16-017	-23.71005	-67.76269	CYC16-017-2-A(B)-1	52200	1000	19280	920	331.2	1.5	0.1466	0.0006	6300	270	12661	54	343.2	1.6	12650	50
Laguna Miscanti	CYC16-017	-23.71005	-67.76269	CYC16-017-2-A(C)-1	57400	1100	22330	610	326.8	1.6	0.1143	0.0004	4662	88	9785	35	336	1.7	9780	40
Laguna Miscanti	CYC16-017	-23.71005	-67.76269	CYC16-017-2-A(D)-1	36340	730	13630	500	315.6	1.7	0.1208	0.0004	5110	160	10460	41	325	1.7	10450	40
Laguna Miscanti	CYC16-017	-23.71005	-67.76269	CYC16-017(A)-1	58300	1200	11460	230	335.8	3	0.1314	0.0004	10609	51	11247	45	346.6	3.1	11240	50
Laguna Miscanti	CYC16-017	-23.71005	-67.76269	CYC16-017(A)-2	56500	1100	10900	240	331.5	3.5	0.127	0.0015	10440	150	10880	130	341.8	3.6	10880	130
Laguna Miscanti	CYC16-017	-23.71005	-67.76269	CYC16-017(A)-3	61200	1200	10430	220	330.2	2.2	0.1277	0.0008	11880	110	10960	76	340.5	2.2	10960	80
Laguna Miscanti	CYC16-017	-23.71005	-67.76269	CYC16-017A(B)-1	22700	450	61800	1300	322.7	3.4	0.1119	0.0005	652.4	3.7	9609	51	331.5	3.5	9550	70
Laguna Miscanti	CYC16-017	-23.71005	-67.76269	CYC16-017A(B)-2	23660	470	66600	1400	320.8	2.6	0.1145	0.0005	645.4	4	9852	50	329.8	2.7	9790	70

Table A.3: U-Th data associated with Chapters 3–5 (continued).

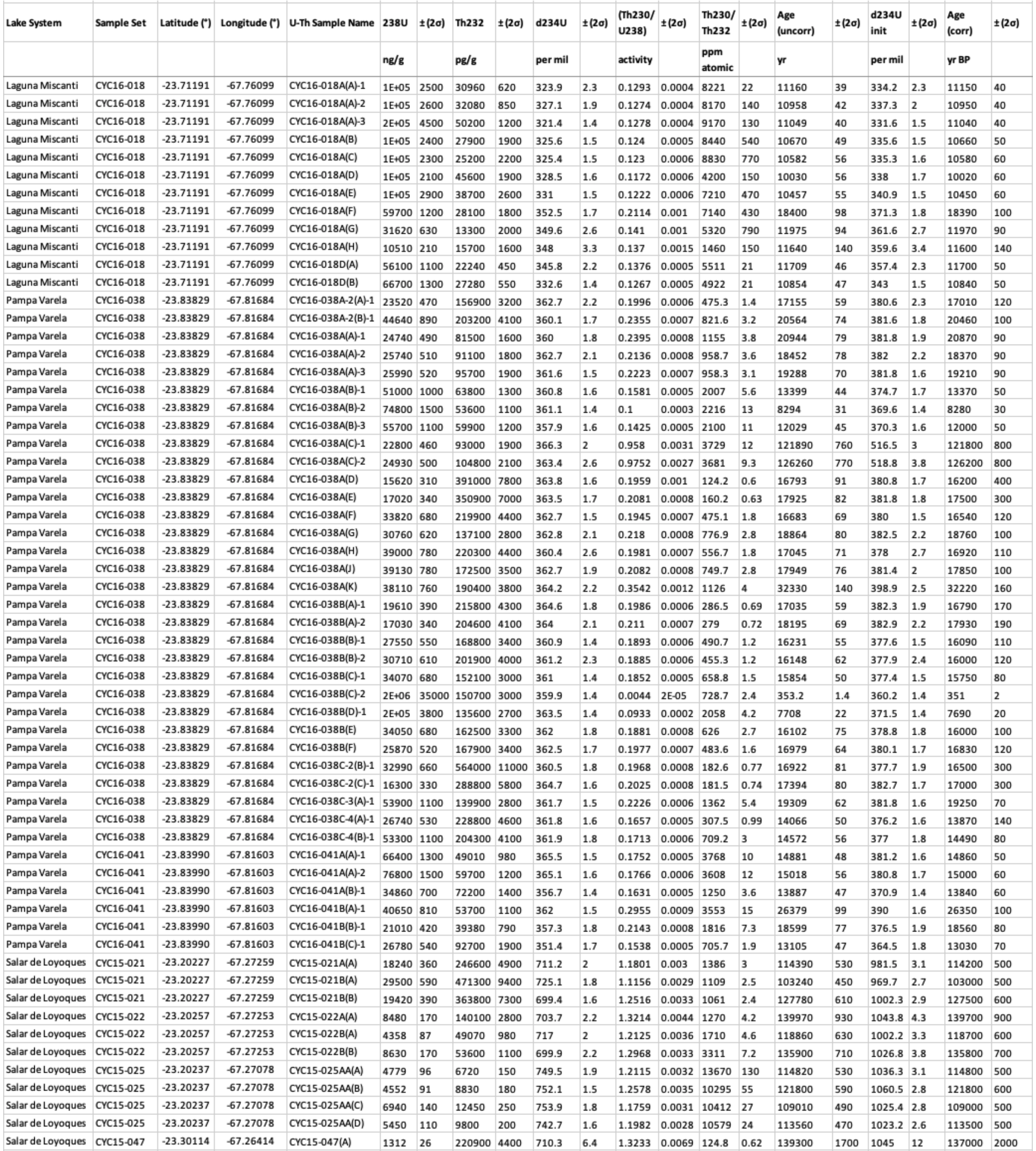

Lake System	Sample Set	Latitude (°)	Longitude (°)	U-Th Sample Name	238U	± (2σ)	Th232	± (2σ)	d234U	± (2σ)	(Th230/ U238)	± (2σ)	Th230/ Th232	± (2σ)	Age (uncorr)	± (2σ)	d234U init	± (2σ)	Age (corr)	± (2σ)
					ng/g		pg/g		per mil		activity		ppm atomic		yr		per mil		yr BP	
Laguna Miscanti	CYC16-018	-23.71191	-67.76099	CYC16-018A(A)-1	1E+05	2500	30960	620	323.9	2.3	0.1293	0.0004	8221	22	11160	39	334.2	2.3	11150	40
Laguna Miscanti	CYC16-018	-23.71191	-67.76099	CYC16-018A(A)-2	1E+05	2600	32080	850	327.1	1.9	0.1274	0.0004	8170	140	10958	42	337.3	2	10950	40
Laguna Miscanti	CYC16-018	-23.71191	-67.76099	CYC16-018A(A)-3	2E+05	4500	50200	1200	321.4	1.4	0.1278	0.0004	9170	130	11049	40	331.6	1.5	11040	40
Laguna Miscanti	CYC16-018	-23.71191	-67.76099	CYC16-018A(B)	1E+05	2400	27900	1900	325.6	1.5	0.124	0.0005	8440	540	10670	49	335.6	1.5	10660	50
Laguna Miscanti	CYC16-018	-23.71191	-67.76099	CYC16-018A(C)	1E+05	2300	25200	2200	325.4	1.5	0.123	0.0006	8830	770	10582	56	335.3	1.6	10580	60
Laguna Miscanti	CYC16-018	-23.71191	-67.76099	CYC16-018A(D)	1E+05	2100	45600	1900	328.5	1.6	0.1172	0.0006	4200	150	10030	56	338	1.7	10020	60
Laguna Miscanti	CYC16-018	-23.71191	-67.76099	CYC16-018A(E)	1E+05	2900	38700	2600	331	1.5	0.1222	0.0006	7210	470	10457	55	340.9	1.5	10450	60
Laguna Miscanti	CYC16-018	-23.71191	-67.76099	CYC16-018A(F)	59700	1200	28100	1800	352.5	1.7	0.2114	0.001	7140	430	18400	98	371.3	1.8	18390	100
Laguna Miscanti	CYC16-018	-23.71191	-67.76099	CYC16-018A(G)	31620	630	13300	2000	349.6	2.6	0.141	0.001	5320	790	11975	94	361.6	2.7	11970	90
Laguna Miscanti	CYC16-018	-23.71191	-67.76099	CYC16-018A(H)	10510	210	15700	1600	348	3.3	0.137	0.0015	1460	150	11640	140	359.6	3.4	11600	140
Laguna Miscanti	CYC16-018	-23.71191	-67.76099	CYC16-018D(A)	56100	1100	22240	450	345.8	2.2	0.1376	0.0005	5511	21	11709	46	357.4	2.3	11700	50
Laguna Miscanti	CYC16-018	-23.71191	-67.76099	CYC16-018D(B)	66700	1300	27280	550	332.6	1.4	0.1267	0.0005	4922	21	10854	47	343	1.5	10840	50
Pampa Varela	CYC16-038	-23.83829	-67.81684	CYC16-038A-2(A)-1	23520	470	156900	3200	362.7	2.2	0.1996	0.0006	475.3	1.4	17155	59	380.6	2.3	17010	120
Pampa Varela	CYC16-038	-23.83829	-67.81684	CYC16-038A-2(B)-1	44640	890	203200	4100	360.1	1.7	0.2355	0.0007	821.6	3.2	20564	74	381.6	1.8	20460	100
Pampa Varela	CYC16-038	-23.83829	-67.81684	CYC16-038A(A)-1	24740	490	81500	1600	360	1.8	0.2395	0.0008	1155	3.8	20944	79	381.8	1.9	20870	90
Pampa Varela	CYC16-038	-23.83829	-67.81684	CYC16-038A(A)-2	25740	510	91100	1800	362.7	2.1	0.2136	0.0008	958.7	3.6	18452	78	382	2.2	18370	90
Pampa Varela	CYC16-038	-23.83829	-67.81684	CYC16-038A(A)-3	25990	520	95700	1900	361.6	1.5	0.2223	0.0007	958.3	3.1	19288	70	381.8	1.6	19210	90
Pampa Varela	CYC16-038	-23.83829	-67.81684	CYC16-038A(B)-1	51000	1000	63800	1300	360.8	1.6	0.1581	0.0005	2007	5.6	13399	44	374.7	1.7	13370	50
Pampa Varela	CYC16-038	-23.83829	-67.81684	CYC16-038A(B)-2	74800	1500	53600	1100	361.1	1.4	0.1	0.0003	2216	13	8294	31	369.6	1.4	8280	30
Pampa Varela	CYC16-038	-23.83829	-67.81684	CYC16-038A(B)-3	55700	1100	59900	1200	357.9	1.6	0.1425	0.0005	2100	11	12029	45	370.3	1.6	12000	50
Pampa Varela	CYC16-038	-23.83829	-67.81684	CYC16-038A(C)-1	22800	460	93000	1900	366.3	2	0.958	0.0031	3729	12	121890	760	516.5	3	121800	800
Pampa Varela	CYC16-038	-23.83829	-67.81684	CYC16-038A(C)-2	24930	500	104800	2100	363.4	2.6	0.9752	0.0027	3681	9.3	126260	770	518.8	3.8	126200	800
Pampa Varela	CYC16-038	-23.83829	-67.81684	CYC16-038A(D)	15620	310	391000	7800	363.8	1.6	0.1959	0.001	124.2	0.6	16793	91	380.8	1.7	16200	400
Pampa Varela	CYC16-038	-23.83829	-67.81684	CYC16-038A(E)	17020	340	350900	7000	363.5	1.7	0.2081	0.0008	160.2	0.63	17925	82	381.8	1.8	17500	300
Pampa Varela	CYC16-038	-23.83829	-67.81684	CYC16-038A(F)	33820	680	219900	4400	362.7	1.5	0.1945	0.0007	475.1	1.8	16683	69	380	1.5	16540	120
Pampa Varela	CYC16-038	-23.83829	-67.81684	CYC16-038A(G)	30760	620	137100	2800	362.8	2.1	0.218	0.0008	776.9	2.8	18864	80	382.5	2.2	18760	100
Pampa Varela	CYC16-038	-23.83829	-67.81684	CYC16-038A(H)	39000	780	220300	4400	360.4	2.6	0.1981	0.0007	556.7	1.8	17045	71	378	2.7	16920	110
Pampa Varela	CYC16-038	-23.83829	-67.81684	CYC16-038A(J)	39130	780	172500	3500	362.7	1.9	0.2082	0.0008	749.7	2.8	17949	76	381.4	2	17850	100
Pampa Varela	CYC16-038	-23.83829	-67.81684	CYC16-038A(K)	38110	760	190400	3800	364.2	2.2	0.3542	0.0012	1126	4	32330	140	398.9	2.5	32220	160
Pampa Varela	CYC16-038	-23.83829	-67.81684	CYC16-038B(A)-1	19610	390	215800	4300	364.6	1.8	0.1986	0.0006	286.5	0.69	17035	59	382.3	1.9	16790	170
Pampa Varela	CYC16-038	-23.83829	-67.81684	CYC16-038B(A)-2	17030	340	204600	4100	364	2.1	0.211	0.0007	279	0.72	18195	69	382.9	2.2	17930	190
Pampa Varela	CYC16-038	-23.83829	-67.81684	CYC16-038B(B)-1	27550	550	168800	3400	360.9	1.4	0.1893	0.0006	490.7	1.2	16231	55	377.6	1.5	16090	110
Pampa Varela	CYC16-038	-23.83829	-67.81684	CYC16-038B(B)-2	30710	610	201900	4000	361.2	2.3	0.1885	0.0006	455.3	1.2	16148	62	377.9	2.4	16000	120
Pampa Varela	CYC16-038	-23.83829	-67.81684	CYC16-038B(C)-1	34070	680	152100	3000	361	1.4	0.1852	0.0005	658.8	1.5	15854	50	377.4	1.5	15750	80
Pampa Varela	CYC16-038	-23.83829	-67.81684	CYC16-038B(C)-2	2E+06	35000	150700	3000	359.9	1.4	0.0044	2E-05	728.7	2.4	353.2	1.4	360.2	1.4	351	2
Pampa Varela	CYC16-038	-23.83829	-67.81684	CYC16-038B(D)-1	2E+05	3800	135600	2700	363.5	1.4	0.0933	0.0002	2058	4.2	7708	22	371.5	1.4	7690	20
Pampa Varela	CYC16-038	-23.83829	-67.81684	CYC16-038B(E)	34050	680	162500	3300	362	1.8	0.1881	0.0008	626	2.7	16102	75	378.8	1.8	16000	100
Pampa Varela	CYC16-038	-23.83829	-67.81684	CYC16-038B(F)	25870	520	167900	3400	362.5	1.7	0.1977	0.0007	483.6	1.6	16979	64	380.1	1.7	16830	120
Pampa Varela	CYC16-038	-23.83829	-67.81684	CYC16-038C-2(B)-1	32990	660	564000	11000	360.5	1.8	0.1968	0.0008	182.6	0.77	16922	81	377.7	1.9	16500	300
Pampa Varela	CYC16-038	-23.83829	-67.81684	CYC16-038C-2(C)-1	16300	330	288800	5800	364.7	1.6	0.2025	0.0008	181.5	0.74	17394	80	382.7	1.7	17000	300
Pampa Varela	CYC16-038	-23.83829	-67.81684	CYC16-038C-3(A)-1	53900	1100	139900	2800	361.7	1.5	0.2226	0.0006	1362	5.4	19309	62	381.8	1.6	19250	70
Pampa Varela	CYC16-038	-23.83829	-67.81684	CYC16-038C-4(A)-1	26740	530	228800	4600	361.8	1.6	0.1657	0.0005	307.5	0.99	14066	50	376.2	1.6	13870	140
Pampa Varela	CYC16-038	-23.83829	-67.81684	CYC16-038C-4(B)-1	53300	1100	204300	4100	361.9	1.8	0.1713	0.0006	709.2	3	14572	56	377	1.8	14490	80
Pampa Varela	CYC16-041	-23.83990	-67.81603	CYC16-041A(A)-1	66400	1300	49010	980	365.5	1.5	0.1752	0.0005	3768	10	14881	48	381.2	1.6	14860	50
Pampa Varela	CYC16-041	-23.83990	-67.81603	CYC16-041A(A)-2	76800	1500	59700	1200	365.1	1.6	0.1766	0.0006	3608	12	15018	56	380.8	1.7	15000	60
Pampa Varela	CYC16-041	-23.83990	-67.81603	CYC16-041A(B)-1	34860	700	72200	1400	356.7	1.4	0.1631	0.0005	1250	3.6	13887	47	370.9	1.4	13840	60
Pampa Varela	CYC16-041	-23.83990	-67.81603	CYC16-041B(A)-1	40650	810	53700	1100	362	1.5	0.2955	0.0009	3553	15	26379	99	390	1.6	26350	100
Pampa Varela	CYC16-041	-23.83990	-67.81603	CYC16-041B(B)-1	21010	420	39380	790	357.3	1.8	0.2143	0.0008	1816	7.3	18599	77	376.5	1.9	18560	80
Pampa Varela	CYC16-041	-23.83990	-67.81603	CYC16-041B(C)-1	26780	540	92700	1900	351.4	1.7	0.1538	0.0005	705.7	1.9	13105	47	364.5	1.8	13030	70
Salar de Loyoques	CYC15-021	-23.20227	-67.27259	CYC15-021A(A)	18240	360	246600	4900	711.2	2	1.1801	0.003	1386	3	114390	530	981.5	3.1	114200	500
Salar de Loyoques	CYC15-021	-23.20227	-67.27259	CYC15-021B(A)	29500	590	471300	9400	725.1	1.8	1.1156	0.0029	1109	2.5	103240	450	969.7	2.7	103000	500
Salar de Loyoques	CYC15-021	-23.20227	-67.27259	CYC15-021B(B)	19420	390	363800	7300	699.4	1.6	1.2516	0.0033	1061	2.4	127780	610	1002.3	2.9	127500	600
Salar de Loyoques	CYC15-022	-23.20257	-67.27253	CYC15-022A(A)	8480	170	140100	2800	703.7	2.2	1.3214	0.0044	1270	4.2	139970	930	1043.8	4.3	139700	900
Salar de Loyoques	CYC15-022	-23.20257	-67.27253	CYC15-022B(A)	4358	87	49070	980	717	2	1.2125	0.0036	1710	4.6	118860	630	1002.2	3.3	118700	600
Salar de Loyoques	CYC15-022	-23.20257	-67.27253	CYC15-022B(B)	8630	170	53600	1100	699.9	2.2	1.2968	0.0033	3311	7.2	135900	710	1026.8	3.8	135800	700
Salar de Loyoques	CYC15-025	-23.20237	-67.27078	CYC15-025AA(A)	4779	96	6720	150	749.5	1.9	1.2115	0.0032	13670	130	114820	530	1036.3	3.1	114800	500
Salar de Loyoques	CYC15-025	-23.20237	-67.27078	CYC15-025AA(B)	4552	91	8830	180	752.1	1.5	1.2578	0.0035	10295	55	121800	590	1060.5	2.8	121800	600
Salar de Loyoques	CYC15-025	-23.20237	-67.27078	CYC15-025AA(C)	6940	140	12450	250	753.9	1.8	1.1759	0.0031	10412	27	109010	490	1025.4	2.8	109000	500
Salar de Loyoques	CYC15-025	-23.20237	-67.27078	CYC15-025AA(D)	5450	110	9800	200	742.7	1.6	1.1982	0.0028	10579	24	113560	470	1023.2	2.6	113500	500
Salar de Loyoques	CYC15-047	-23.30114	-67.26414	CYC15-047(A)	1312	26	220900	4400	710.3	6.4	1.3233	0.0069	124.8	0.62	139300	1700	1045	12	137000	2000

Table A.4: U-Th data associated with Chapters 3–5 (continued).

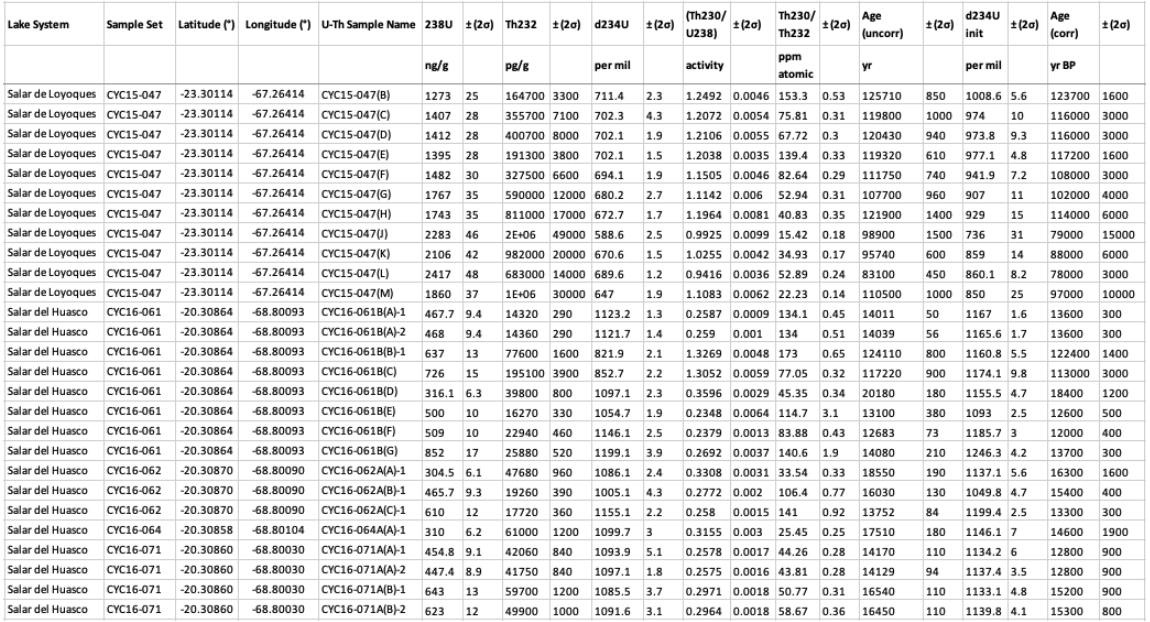

Lake System	Sample Set	Latitude (°)	Longitude (°)	U-Th Sample Name	238U	± (2σ)	Th232	± (2σ)	d234U	± (2σ)	(Th230/ U238)	± (2σ)	Th230/ Th232	± (2σ)	Age (uncorr)	± (2σ)	d234U init	± (2σ)	Age (corr)	± (2σ)
					ng/g		pg/g		per mil		activity		ppm atomic		yr		per mil		yr BP	
Salar de Loyoques	CYC15-047	-23.30114	-67.26414	CYC15-047(B)	1273	25	164700	3300	711.4	2.3	1.2492	0.0046	153.3	0.53	125710	850	1008.6	5.6	123700	1600
Salar de Loyoques	CYC15-047	-23.30114	-67.26414	CYC15-047(C)	1407	28	355700	7100	702.3	4.3	1.2072	0.0054	75.81	0.31	119800	1000	974	10	116000	3000
Salar de Loyoques	CYC15-047	-23.30114	-67.26414	CYC15-047(D)	1412	28	400700	8000	702.1	1.9	1.2106	0.0055	67.72	0.3	120430	940	973.8	9.3	116000	3000
Salar de Loyoques	CYC15-047	-23.30114	-67.26414	CYC15-047(E)	1395	28	191300	3800	702.1	1.5	1.2038	0.0035	139.4	0.33	119320	610	977.1	4.8	117200	1600
Salar de Loyoques	CYC15-047	-23.30114	-67.26414	CYC15-047(F)	1482	30	327500	6600	694.1	1.9	1.1505	0.0046	82.64	0.29	111750	740	941.9	7.2	108000	3000
Salar de Loyoques	CYC15-047	-23.30114	-67.26414	CYC15-047(G)	1767	35	590000	12000	680.2	2.7	1.1142	0.006	52.94	0.31	107700	960	907	11	102000	4000
Salar de Loyoques	CYC15-047	-23.30114	-67.26414	CYC15-047(H)	1743	35	811000	17000	672.7	1.7	1.1964	0.0081	40.83	0.35	121900	1400	929	15	114000	6000
Salar de Loyoques	CYC15-047	-23.30114	-67.26414	CYC15-047(J)	2283	46	2E+06	49000	588.6	2.5	0.9925	0.0099	15.42	0.18	98900	1500	736	31	79000	15000
Salar de Loyoques	CYC15-047	-23.30114	-67.26414	CYC15-047(K)	2106	42	982000	20000	670.6	1.5	1.0255	0.0042	34.93	0.17	95740	600	859	14	88000	6000
Salar de Loyoques	CYC15-047	-23.30114	-67.26414	CYC15-047(L)	2417	48	683000	14000	689.6	1.2	0.9416	0.0036	52.89	0.24	83100	450	860.1	8.2	78000	3000
Salar de Loyoques	CYC15-047	-23.30114	-67.26414	CYC15-047(M)	1860	37	1E+06	30000	647	1.9	1.1083	0.0062	22.23	0.14	110500	1000	850	25	97000	10000
Salar del Huasco	CYC16-061	-20.30864	-68.80093	CYC16-061B(A)-1	467.7	9.4	14320	290	1123.2	1.3	0.2587	0.0009	134.1	0.45	14011	50	1167	1.6	13600	300
Salar del Huasco	CYC16-061	-20.30864	-68.80093	CYC16-061B(A)-2	468	9.4	14360	290	1121.7	1.4	0.259	0.001	134	0.51	14039	56	1165.6	1.7	13600	300
Salar del Huasco	CYC16-061	-20.30864	-68.80093	CYC16-061B(B)-1	637	13	77600	1600	821.9	2.1	1.3269	0.0048	173	0.65	124110	800	1160.8	5.5	122400	1400
Salar del Huasco	CYC16-061	-20.30864	-68.80093	CYC16-061B(C)	726	15	195100	3900	852.7	2.2	1.3052	0.0059	77.05	0.32	117220	900	1174.1	9.8	113000	3000
Salar del Huasco	CYC16-061	-20.30864	-68.80093	CYC16-061B(D)	316.1	6.3	39800	800	1097.1	2.3	0.3596	0.0029	45.35	0.34	20180	180	1155.5	4.7	18400	1200
Salar del Huasco	CYC16-061	-20.30864	-68.80093	CYC16-061B(E)	500	10	16270	330	1054.7	1.9	0.2348	0.0064	114.7	3.1	13100	380	1093	2.5	12600	500
Salar del Huasco	CYC16-061	-20.30864	-68.80093	CYC16-061B(F)	509	10	22940	460	1146.1	2.5	0.2379	0.0013	83.88	0.43	12683	73	1185.7	3	12000	400
Salar del Huasco	CYC16-061	-20.30864	-68.80093	CYC16-061B(G)	852	17	25880	520	1199.1	3.9	0.2692	0.0037	140.6	1.9	14080	210	1246.3	4.2	13700	300
Salar del Huasco	CYC16-062	-20.30870	-68.80090	CYC16-062A(A)-1	304.5	6.1	47680	960	1086.1	2.4	0.3308	0.0031	33.54	0.33	18550	190	1137.1	5.6	16300	1600
Salar del Huasco	CYC16-062	-20.30870	-68.80090	CYC16-062A(B)-1	465.7	9.3	19260	390	1005.1	4.3	0.2772	0.002	106.4	0.77	16030	130	1049.8	4.7	15400	400
Salar del Huasco	CYC16-062	-20.30870	-68.80090	CYC16-062A(C)-1	610	12	17720	360	1155.1	2.2	0.258	0.0015	141	0.92	13752	84	1199.4	2.5	13300	300
Salar del Huasco	CYC16-064	-20.30858	-68.80104	CYC16-064A(A)-1	310	6.2	61000	1200	1099.7	3	0.3155	0.003	25.45	0.25	17510	180	1146.1	7	14600	1900
Salar del Huasco	CYC16-071	-20.30860	-68.80030	CYC16-071A(A)-1	454.8	9.1	42060	840	1093.9	5.1	0.2578	0.0017	44.26	0.28	14170	110	1134.2	6	12800	900
Salar del Huasco	CYC16-071	-20.30860	-68.80030	CYC16-071A(A)-2	447.4	8.9	41750	840	1097.1	1.8	0.2575	0.0016	43.81	0.28	14129	94	1137.4	3.5	12800	900
Salar del Huasco	CYC16-071	-20.30860	-68.80030	CYC16-071A(B)-1	643	13	59700	1200	1085.5	3.7	0.2971	0.0018	50.77	0.31	16540	110	1133.1	4.8	15200	900
Salar del Huasco	CYC16-071	-20.30860	-68.80030	CYC16-071A(B)-2	623	12	49900	1000	1091.6	3.1	0.2964	0.0018	58.67	0.36	16450	110	1139.8	4.1	15300	800

Bibliography

Ainsworth, N.R., Burnett, R.D., Kontrovitz, M., 1990. Ostracod colour change by thermal alteration, offshore Ireland and Western UK. Marine and Petroleum Geology 7, 288–297.

Alam, M.S., Cheng, T., 2014. Uranium release from sediment to groundwater: Influence of water chemistry and insights into release mechanisms. Journal of Contaminant Hydrology 164, 72–87. doi:10.1016/j.jconhyd.2014.06.001.

Allmendinger, R.W., Jordan, T.E., Kay, S.M., Isacks, B.L., 1997. The Evolution of the Altiplano-Puna Plateau of the Central Andes. Annual Review of Earth and Planetary Sciences 25, 139–174. doi:10.1146/annurev.earth.25.1.139.

Ames, L.L., McGarrah, J.E., Walker, B.A., 1983a. Sorption of Trace Constituents from Aqueous Solutions onto Secondary Minerals. II. Radium. Clays and Clay Minerals 31, 321–334.

Ames, L.L., McGarrah, J.E., Walker, B.A., 1983b. Sorption of Uranium and Radium by Biotite, Muscovite, and Phlogopite. Clays and Clay Minerals 31, 343–351.

Ames, L.L., McGarrah, J.E., Walker, B.A., Salter, P.F., 1983c. Uranium and radium sorption on amorphous ferric oxyhydroxide. Chemical Geology 40, 135–148. doi:10.1016/0009-2541(83)90095-5.

Aravena, R., Suzuki, O., Peña, H., Pollastri, A., Fuenzalida, H., Grilli, A., 1999. Isotopic composition and origin of the precipitation in Northern Chile. Applied Geochemistry 14, 411–422. doi:10.1016/S0883-2927(98)00067-5.

Arp, G., 1995. Lacustrine bioherms, spring mounds, and marginal carbonates of the Ries-impact-crater (Miocene, Southern Germany). Facies 33, 35–89. doi:10.1007/BF02537444.

Arp, G., Thiel, V., Reimer, A., Michaelis, W., Reitner, J., 1999. Biofilm exopolymers control microbialite formation at thermal springs discharging into the alkaline Pyramid Lake, Nevada, USA. Sedimentary Geology 126, 159–176. doi:10.1016/S0037-0738(99)00038-X.

Arz, H.W., Pätzold, J., Wefer, G., 1998. Correlated Millennial-Scale Changes in Surface Hydrography and Terrigenous Sediment Yield Inferred from Last-Glacial Marine Deposits off Northeastern Brazil. Quaternary Research 50, 157–166. URL: `http://www.sciencedirect.com/science/article/pii/S0033589498919925`, doi:10.1006/qres.1998.1992.

Avicenna, 1027. The Book of Healing.

Baker, P.A., Seltzer, G.O., Fritz, S.C., Dunbar, R.B., Grove, M.J., Tapia, P.M., Cross, S.L., Rowe, H.D., Broda, J.P., 2001. The history of South American tropical precipitation for the past 25,000 years. Science 291, 640–643. doi:10.1126/science.291.5504.640.

Bakke, J., Lie, Ø., Heegaard, E., Dokken, T., Haug, G.H., Birks, H.H., Dulski, P., Nilsen, T., 2009. Rapid oceanic and atmospheric changes during the Younger Dryas cold period. Nature Geoscience 2, 202–205. URL: `http://www.nature.com/articles/ngeo439`, doi:10.1038/ngeo439.

Balch, D.P., Cohen, A.S., Schnurrenberger, D.W., Haskell, B.J., Valero-Garcés, B.L., Beck, J.W., Cheng, H., Edwards, R.L., 2005. Ecosystem and paleohydrological response to Quaternary climate change in the Bonneville Basin, Utah. Palaeogeography, Palaeoclimatology, Palaeoecology 221, 99–122. doi:10.1016/j.palaeo.2005.01.013.

Balsam, W.L., Deaton, B.C., Damuth, J.E., 1999. Evaluating optical lightness as a proxy for carbonate content in marine sediment cores. Marine Geology 161, 141–153. doi:10.1016/S0025-3227(99)00037-7.

Bar-Matthews, M., Ayalon, A., Gilmour, M., Matthews, A., Hawkesworth, C.J., 2003. Sea-land oxygen isotope relationships from planktonic foraminifera and speleothems in the Eastern Mediterranean region and their implication for paleorainfall during interglacial intervals. Geochimica et Cosmochimica Acta 67, 3181–3199.

Bard, E., Fairbanks, R.G., Hamelin, B., Zindler, A., Chi Track Hoang, 1991. Uranium-234 anomalies in corals older than 150,000 years. Geochimica et Cosmochimica Acta 55, 2385–2390. URL: `https://linkinghub.elsevier.com/retrieve/pii/001670379190115L`, doi:10.1016/0016-7037(91)90115-L.

Bard, E., Rostek, F., Turon, J.L., Gendreau, S., 2000. Hydrological Impact of Heinrich Events in the Subtropical Northeast Atlantic. Science 289, 1321–1324. doi:10.1126/science.289.5483.1321.

Bartlein, P.J., Harrison, S.P., Brewer, S., Connor, S., Davis, B.A.S., Gajewski, K., Guiot, J., Harrison-Prentice, T.I., Henderson, A., Peyron, O., Prentice, I.C., Scholze, M., Seppä, H., Shuman, B., Sugita, S., Thompson, R.S., Viau, A.E., Williams, J., Wu, H., 2011. Pollen-based continental climate reconstructions at 6 and 21 ka: a global synthesis. Climate Dynamics 37, 775–802. URL: `http://link.springer.com/10.1007/s00382-010-0904-1`, doi:10.1007/s00382-010-0904-1.

Bateman, H., 1910. The solution of a system of differential equations occurring in the theory of radio-active transformations. Proc. Cambridge Phil. Soc. 15, 423–427.

Becquerel, H., 1896. On the rays emitted by phosphorescence. Compt. Rend. Hebd. Seances Acad. Sci. 122, 420–421.

Behling, H., W. Arz, H., Pätzold, J., Wefer, G., 2000. Late Quaternary vegetational and climate dynamics in northeastern Brazil, inferences from marine core GeoB 3104-1. Quaternary Science Reviews 19, 981–994. doi:10.1016/S0277-3791(99)00046-3.

Benson, L., 1994. Carbonate deposition, Pyramid Lake subbasin, Nevada: 1. Sequence of formation and elevational distribution of carbonate deposits (Tufas). Palaeogeography, Palaeoclimatology, Palaeoecology 109, 55–87. doi:10.1016/0031-0182(94)90118-X.

Benson, L., Kashgarian, M., Rubin, M., 1995. Carbonate deposition, Pyramid Lake subbasin, Nevada: 2. Lake levels and polar jet stream positions reconstructed from radiocarbon ages and elevations of carbonates (tufas) deposited in the Lahontan basin. Palaeogeography, Palaeoclimatology, Palaeoecology 117, 1–30. doi:10.1016/0031-0182(94)00103-F.

Benson, R.H., 1984. Estimating greater paleodepths with ostracodes, especially in past thermospheric oceans. Palaeogeography, Palaeoclimatology, Palaeoecology 48, 107–141. doi:10.1016/0031-0182(84)90093-2.

Bills, B.G., de Silva, S.L., Currey, D.R., Emenger, R.S., Lillquist, K.D., Donnellan, A., Worden, B., 1994. Hydro-isostatic deflection and tectonic tilting in the central Andes: Initial results of a GPS survey of Lake Minchin shorelines. Geophysical Research Letters 21, 293–296. doi:10.1029/93GL03544.

Bischoff, J.L., aA. Fitzpatrick, J., Rosenbauer, R.J., 1993a. The Solubility and Stabilization of ikaite (CaCO3 6H2O) from 0 ° to 25 °C: Environmental and Paleoclimatic Implications for Thinolite Tufa. doi:10.1086/648194.

Bischoff, J.L., Fitzpatrick, J.a., 1991. U-series dating of impure carbonates: An isochron technique using total-sample dissolution. Geochimica et Cosmochimica Acta 55, 543–554. doi:10.1016/0016-7037(91)90011-S.

Bischoff, J.L., Rosenbauer, R.J., Smith, G.I., 1985. Uranium-Series Dating of Sediments from Searles Lake: Differences Between Continental and Marine Climate Records. Science 227, 1222–1224.

Bischoff, J.L., Stine, S., Rosenbauer, R.J., Fitzpatrick, J.a., Stafford, T.W., 1993b. Ikaite precipitation by mixing of shoreline springs and lake water, Mono Lake, California, USA. Geochimica et Cosmochimica Acta 57, 3855–3865. doi:10.1016/0016-7037(93)90339-X.

Blaauw, M., Christen, J.A., 2011. Flexible paleoclimate age-depth models using an autoregressive gamma process. Bayesian Analysis 6, 457–474. URL: `http://projecteuclid.org/euclid.ba/1339616472`, doi:10.1214/11-BA618.

Blanchard, R.L., Cheng, M.H., Potratz, H.A., 1967. Uranium and Thorium Series Disequilibria in Recent and Fossil Marine Molluscan Shells. Journal of Geophysical Research 72, 4745–4757.

Blard, P.H., Lavé, J., Farley, K.A., Fornari, M., Jiménez, N., Ramirez, V., 2009. Late local glacial maximum in the Central Altiplano triggered by cold and locally-wet conditions during the paleolake Tauca episode (17-15 ka, Heinrich 1). Quaternary Science Reviews 28, 3414–3427. doi:10.1016/j.quascirev.2009.09.025.

Blard, P.H., Sylvestre, F., Tripati, A.K., Claude, C., Causse, C., Coudrain, A., Condom, T., Seidel, J.L., Vimeux, F., Moreau, C., Dumoulin, J.P., Lavé, J., 2011. Lake highstands on the Altiplano (Tropical Andes) contemporaneous with Heinrich 1 and the Younger Dryas: New insights from 14C, U-Th dating and δ18O of carbonates. Quaternary Science Reviews 30, 3973–3989. URL: `http://dx.doi.org/10.1016/j.quascirev.2011.11.001`, doi:10.1016/j.quascirev.2011.11.001.

Bobst, A.L., Lowenstein, T.K., Jordan, T.E., Godfrey, L.V., Ku, T.L., Luo, S., 2001. A 106 ka paleoclimate record from drill core of the Salar de Atacama, northern Chile. Palaeogeography, Palaeoclimatology, Palaeoecology 173, 21–42. URL: `http://linkinghub.elsevier.com/retrieve/pii/S003101820100308X`, doi:10.1016/S0031-0182(01)00308-X.

Bold, H.C., Wyynne, M.J., 1978. Introduction to the algae: Structure and reproduction. Prentice Hall.

Bone, S.E., Dynes, J.J., Cliff, J., Bargar, J.R., 2017. Uranium(IV) adsorption by natural organic matter in anoxic sediments. Proceedings of the National Academy of Sciences 114, 201611918. URL: `http://www.pnas.org/lookup/doi/10.1073/pnas.1611918114`, doi:10.1073/pnas.1611918114.

Bourdon, B., Henderson, G.M., Lundstrom, C.C., Turner, S.P. (Eds.), 2003. Uranium-Series Geochemistry. volume 52. The Mineralogical Society of America.

Braconnot, P., Harrison, S.P., Kageyama, M., Bartlein, P.J., Masson-Delmotte, V., Abe-Ouchi, A., Otto-Bliesner, B., Zhao, Y., 2012. Evaluation of climate models using palaeoclimatic data. Nature Climate Change 2, 417–424. URL: `http://dx.doi.org/10.1038/nclimate1456`, doi:10.1038/nclimate1456.

Braconnot, P., Otto-Bliesner, B., Harrison, S., Joussaume, S., Peterchmitt, J.Y., Abe-Ouchi, A., Crucifix, M., Driesschaert, E., Fichefet, T., Hewitt, C.D., Kageyama, M., Kitoh, A., Laîné, A., Loutre, M.F., Marti, O., Merkel, U., Ramstein, G., Valdes, P., Weber, S.L., Yu, Y., Zhao, Y., 2007. Results of PMIP2 coupled simulations of the Mid-Holocene and Last Glacial Maximum—Part 1: experiments and large-scale features. Climate of the Past 3, 261–277. doi:10.5194/cp-3-261-2007.

Broecker, W.S., 1963. A Preliminary Evoluation of Uranium Series Inequilibrium as a Tool for Absolute Age Measurement on Marine Carbonates. Journal of Geophysical Research 68, 2817–2834.

Broecker, W.S., Orr, P.C., 1958. Radiocarbon chronology of Lake Lahontan and Lake Bonneville. Bulletin of the Geological Society of America 69, 1009–1032. doi:10.1130/0016-7606(1958)69[1009:RCOLLA]2.0.CO;2.

Buchardt, B., Israelson, C., Seaman, P., Stockmann, G., 2001. Ikaite tufa towers in Ikka Fjord, Southwest Greenland: Their formation by mixing of seawater and alkaline spring water. Journal of Sedimentary Research 71, 176–189. doi:10.1306/042800710176.

Buchardt, B., Seaman, P., Stockmann, G., Vous, M., Wilken, U., Duwel, L., Kristiansen, A., Jenner, C., Whiticar, M.J., Kristensen, R.M., Petersen, G.H., Thorbjorn, L., 1997. Submarine columns of ikaite tufa. Nature 390, 129–130. URL: `http://dx.doi.org/10.1038/36474`, doi:10.1038/36474.

Chabaux, F., Bourdon, B., Riotte, J., 2008. Chapter 3 U-Series Geochemistry in Weathering Profiles, River Waters and Lakes, in: Radioactivity in the Environment. volume 13, pp. 49–104. URL: `https://linkinghub.elsevier.com/retrieve/pii/S1569486007000034`, doi:10.1016/S1569-4860(07)00003-4.

Chabaux, F., Riotte, J., Dequincey, O., 2003. U-Th-Ra Fractionation During Weathering and River Transport. Reviews in Mineralogy and Geochemistry 52, 533–576. URL: `https://pubs.geoscienceworld.org/rimg/article/52/1/533-576/87464`, doi:10.2113/0520533.

Chappaz, A., Gobeil, C., Tessier, A., 2010. Controls on uranium distribution in lake sediments. Geochimica et Cosmochimica Acta 74, 203–214. doi:10.1016/j.gca.2009.09.026.

Cheng, H., Adkins, J., Edwards, R., Boyle, E.A., 2000. U-Th dating of deep-sea corals. Geochimica et Cosmochimica Acta 64, 2401–2416. URL: `http://linkinghub.elsevier.com/retrieve/pii/S0016703799004226`, doi:10.1016/S0016-7037(99)00422-6.

Cheng, H., Edwards, R.L., Broecker, W.S., Denton, G.H., Kong, X., Wang, Y., Zhang, R., Wang, X., 2009. Ice age terminations. Science 326, 248–252. doi:10.1126/science.1177840.

Cheng, H., Edwards, R.L., Sinha, A., Spötl, C., Yi, L., Chen, S., Kelly, M., Kathayat, G., Wang, X., Li, X., Kong, X., Wang, Y., Ning, Y., Zhang, H., 2016. The Asian monsoon over the past 640,000 years and ice age terminations. Nature 534, 640–646. URL: `http://www.nature.com/doifinder/10.1038/nature18591`, doi:10.1038/nature18591.

Cheng, H., Lawrence Edwards, R., Shen, C.C., Polyak, V.J., Asmerom, Y., Woodhead, J., Hellstrom, J., Wang, Y., Kong, X., Spötl, C., Wang, X., Calvin Alexander, E., 2013a. Improvements in 230Th dating, 230Th and 234U half-life values, and U-Th isotopic measurements by multi-collector inductively coupled plasma mass spectrometry. Earth and Planetary Science Letters 371-372, 82–91. URL: `http://dx.doi.org/10.1016/j.epsl.2013.04.006`, doi:10.1016/j.epsl.2013.04.006.

Cheng, H., Sinha, A., Cruz, F.W., Wang, X., Edwards, R.L., D'Horta, F.M., Ribas, C.C., Vuille, M., Stott, L.D., Auler, A.S., 2013b. Climate change patterns in Amazonia and biodiversity. Nature Communications 4, 1411. URL: `http://www.ncbi.nlm.nih.gov/pubmed/23361002`, doi:10.1038/ncomms2415.

Chiang, J.C., Lee, S.Y., Putnam, A.E., Wang, X., 2014. South Pacific Split Jet, ITCZ shifts, and atmospheric North–South linkages during abrupt climate changes of the last glacial period. Earth and Planetary Science Letters 406, 233–246. URL: `http://linkinghub.elsevier.com/retrieve/pii/S0012821X14005676`, doi:10.1016/j.epsl.2014.09.012.

Cobbing, E.J., Pitcher, W.S., WIlson, J.J., Baldock, J.W., Taylor, W.P., McCourt, W., Snelling, N.J., 1981. The geology of the Western Cordillera of northern Peru. volume 5. Great Britain Institute of Geological Sciences, Natural Environmental Research Council.

Coe, M.T., Harrison, S.P., 2002. The water balance of northern Africa during the mid-Holocene: an evaluation of the 6 ka BP PMIP simulations. Climate Dynamics 19, 155–166. URL: `http://link.springer.com/10.1007/s00382-001-0219-3`, doi:10.1007/s00382-001-0219-3.

Colman, S., Kaufman, D., Bright, J., Heil, C., King, J., Dean, W., Rosenbaum, J., Forester, R., Bischoff, J., Perkins, M., McGeehin, J., 2006. Age model for a continuous, ca 250-ka Quaternary lacustrine record from Bear Lake, Utah–Idaho. Quaternary Science Reviews 25, 2271–2282. URL: `http://linkinghub.elsevier.com/retrieve/pii/S0277379106001806`, doi:10.1016/j.quascirev.2005.10.015.

Colman, S.M., 1996. Continental Drilling for Paleoclimatic Records: Recommendations from an International Workshop. Technical Report. GeoForschungsZentrum. Potsdam, Germany.

Council, T.C., Bennett, P.C., 1993. Geochemistry of ikaite formation at Mono Lake, California: Implications for the origin of tufa mounds. Geology 21, 971–974. doi:10.1130/0091-7613(1993)021<0971.

Cruz, F.W., Burns, S.J., Jercinovic, M., Karmann, I., Sharp, W.D., Vuille, M., 2007. Evidence of rainfall variations in Southern Brazil from trace element ratios (Mg/Ca and Sr/Ca) in a Late Pleistocene stalagmite. Geochimica et Cosmochimica Acta 71, 2250–2263. URL: `http://linkinghub.elsevier.com/retrieve/pii/S0016703707000804`, doi:10.1016/j.gca.2007.02.005.

Cruz, F.W., Burns, S.J., Karmann, I., Sharp, W.D., Vuille, M., Cardoso, A.O., Ferrari, J.A., Silva Dias, P.L., Viana Jr., O., 2005. Insolation-driven changes in atmospheric circulation over the past 116,000 years in subtropical Brazil. Nature 434, 63–66. doi:10.1038/nature03365.

De Deckker, P., 2002. Ostracod Palaeoecology. The Ostracoda: Applications in Quaternary Research, Geophysical Monograph 131 , 121–134doi:10.1029/131GM06.

Dirección General de Aguas, 1987. Balance hídrico de Chile. URL: `http://sad.dga.cl/ipac20/ipac.jsp?session=1349N4543565L.131053&profile=cirh&uri=link=3100006`

Donohoe, A., Marshall, J., Ferreira, D., McGee, D., 2013. The relationship between ITCZ location and cross-equatorial atmospheric heat transport: From the seasonal cycle to the last glacial maximum. Journal of Climate 26, 3597–3618. doi:10.1175/JCLI-D-12-00467.1.

Dunn, J.R., 1953. The origin of the deposits of tufa in Mono Lake. Journal of Sedimentary Research 23, 18–23. URL: `http://archives.datapages.com/data/sepm/journals/v01-32/data/023/023001/0018.htm`.

Durand, S., Chabaux, F., Rihs, S., Duringer, P., Elsass, P., 2005. U isotope ratios as tracers of groundwater inputs into surface waters: example of the upper rhine hydrosystem. Chemical Geology 220, 1–19.

Dutton, A., Rubin, K., McLean, N., Bowring, J., Bard, E., Edwards, R.L., Henderson, G.M., Reid, M.R., Richards, D.A., Sims, K., Walker, J.D., Yokoyama, Y., 2017. Data reporting standards for publication of U-series data for geochronology and timescale assessment in the earth sciences. Quaternary Geochronology 39, 142–149. URL: `http://dx.doi.org/10.1016/j.quageo.2017.03.001`, doi:10.1016/j.quageo.2017.03.001.

Edwards, R., Gallup, C., Cheng, H., 2003. Uranium-series Dating of Marine and Lacustrine Carbonates. Reviews in Mineralogy and Geochemistry 52, 363–405. URL: `http://rimg.geoscienceworld.org/cgi/doi/10.2113/0520363`, doi:10.2113/0520363.

Edwards, R.L., 1988. High Precition Thorium-230 Ages of Corals and the Timing of Sea Level Fluctuations in the Late Quaternary. Ph.D. thesis. California Insititute of Technology.

Edwards, R.L., Chen, J., Wasserburg, G., 1987. 238U-234U-230Th-232Th systematics and the precise measurement of time over the past 500,000 years. Earth and Planetary Science Letters 81, 175–192. doi:10.1016/0012-821X(87)90154-3.

Falvey, M., Garreaud, R.D., 2005. Moisture variability over the South American Altiplano during the South American low level jet experiment (SALLJEX) observing season. Journal of Geophysical Research: Atmospheres 110, 1–12. doi:10.1029/2005JD006152.

Fleischer, R.L., 1982. Alpha-recoil damage and solution effects in minerals: uranium isotopic disequilibrium and radon release. Geochimica et Cosmochimica Acta 46, 2191–2201. URL: `https://linkinghub.elsevier.com/retrieve/pii/0016703782901946`, doi:10.1016/0016-7037(82)90194-6.

Flusche, M.A., Seltzer, G., Rodbell, D., Siegel, D., Samson, S., 2005. Constraining water sources and hydrologic processes from the isotopic analysis of water and dissolved strontium, Lake Junin, Peru. Journal of Hydrology 312, 1–13. URL: `https://linkinghub.elsevier.com/retrieve/pii/S0022169405000727`, doi:10.1016/j.jhydrol.2005.02.021.

Francke, A., Wagner, B., Just, J., Leicher, N., Gromig, R., Baumgarten, H., Vogel, H., Lacey, J.H., Sadori, L., Wonik, T., Leng, M.J., Zanchetta, G., Sulpizio, R., Giaccio, B., 2016. Sedimentological processes and environmental variability at Lake Ohrid (Macedonia, Albania) between 637 ka and the present. Biogeosciences 13, 1179–1196. doi:10.5194/bg-13-1179-2016.

Frechen, M., Sierralta, M., Oezen, D., Urban, B., 2007. Uranium-series dating of peat from central and Northern Europe, in: Sirocko, F., Claussen, M., Goñi, M.F.S., Litt, T. (Eds.), Developments in Quaternary Science: The Climate of Past Interglacials. Elsevier. volume 7. chapter 8, pp. 83–117. doi:10.1016/S1571-0866(07)80033-9.

Fritz, S.C., Baker, P.a., Lowenstein, T.K., Seltzer, G.O., Rigsby, C.a., Dwyer, G.S., Tapia, P.M., Arnold, K.K., Ku, T.L., Luo, S., 2004. Hydrologic variation during the last 170,000 years in the southern hemisphere tropics of South America. Quaternary Research 61, 95–104. doi:10.1016/j.yqres.2003.08.007.

Fritz, S.C., Baker, P.A., Seltzer, G.O., Ballantyne, A., Tapia, P., Cheng, H., Edwards, R.L., 2007. Quaternary glaciation and hydrologic variation in the South American tropics as reconstructed from the Lake Titicaca drilling project. Quaternary Research 68, 410–420. doi:10.1016/j.yqres.2007.07.008.

Fuenzalida, H., Rutllant, J., 1987. Origen del vapor de agua que precipita sobre el Altiplano de Chile.

Gallup, C.D., Edwards, R.L., Johnson, R.G., 1994. The timing of high sea levels over the past 200,000 years. Science 263, 796–800.

Gandu, A.W., Silva Dias, P.L., 1998. Impact of tropical heat sources on the South American tropospheric upper circulation and subsidence. Journal of Geophysical Research 103, 6001. doi:10.1029/97JD03114.

Garreaud, R., Vuille, M., Clement, A.C., 2003. The climate of the Altiplano: Observed current conditions and mechanisms of past changes. Palaeogeography, Palaeoclimatology, Palaeoecology 194, 5–22. doi:10.1016/S0031-0182(03)00269-4.

Garreaud, R.D., 1999. Multiscale Analysis of the Summertime Precipitation over the Central Andes. Monthly Weather Review 127, 901–921. doi:10.1175/1520-0493(1999)127<0901:MAOTSP>2.0.CO;2.

Garreaud, R.D., Aceituno, P., 2001. Interannual Rainfall Variability over the South American Altiplano. Journal of Climate 14, 2779–2789. URL: `http://journals.ametsoc.org/doi/abs/10.1175/1520-0442(2001)014%3C2779:IRVOTS%3E2.0.CO;2`, doi:10.1175/1520-0442(2001)014<2779:IRVOTS>2.0.CO;2.

Garreaud, R.D., Vuille, M., Compagnucci, R., Marengo, J., 2009. Present-day South American climate. Palaeogeography, Palaeoclimatology, Palaeoecology 281, 180–195. URL: `http://dx.doi.org/10.1016/j.palaeo.2007.10.032`, doi:10.1016/j.palaeo.2007.10.032.

Garreaud, R.D., Wallace, J.M., 1997. The Diurnal March of Convective Cloudiness over the Americas. Monthly Weather Review 125, 3157–3171. doi:10.1175/1520-0493(1997)125<3157:TDMOCC>2.0.CO;2.

Gayo, E.M., Latorre, C., Jordan, T.E., Nester, P.L., Estay, S.A., Ojeda, K.F., Santoro, C.M., 2012. Late Quaternary hydrological and ecological changes in the hyperarid core of the northern Atacama Desert (~21 °S). Earth-Science Reviews 113, 120–140. URL: `http://dx.doi.org/10.1016/j.earscirev.2012.04.003`, doi:10.1016/j.earscirev.2012.04.003.

Geyh, M.A., Mu, H., 2005. Numerical 230Th/U dating and a palynological review of the Holsteinian/Hoxnian Interglacial. Quaternary Science Reviews 24, 1861–1872. doi:10.1016/j.quascirev.2005.01.007.

Gierlowski-Kordesch, E.H., 2010. Lacustrine carbonates. Developments in Sedimentology: Carbonates in Continental Settings: Facies, Environments and Processes 61, 2–70.

Giosan, L., Flood, R.D., Aller, R.C., 2002. Paleoceanographic significance of sediment color on western North Atlantic drifts: I. Origin of color. Marine Geology 189, 25–41. URL: `https://linkinghub.elsevier.com/retrieve/pii/S0025322702003225` `https://linkinghub.elsevier.com/retrieve/pii/S0025322702003213`, doi:10.1016/S0025-3227(02)00321-3.

Golubic, S., 1973. Relationship between blue-green algae and carbonate deposits. The Biology of Blue-Gren Algae, Botanical Monograph 9 , 434–472.

Grimm, A.M., 2011. Interannual climate variability in South America: Impacts on seasonal precipitation, extreme events, and possible effects of climate change. Stochastic Environmental Research and Risk Assessment 25, 537–554. doi:10.1007/s00477-010-0420-1.

Groot, M.H.M., Bogotá, R.G., Lourens, L.J., Hooghiemstra, H., Vriend, M., Berrio, J.C., Tuenter, E., Van Der Plicht, J., Van Geel, B., Ziegler, M., Weber, S.L., Betancourt, A., Contreras, L., Gaviria, S., Giraldo, C., González, N., Jansen, J.H.F., Konert, M., Ortega, D., Rangel, O., Sarmiento, G., Vandenberghe, J., Van Der Hammen, T., Van Der Linden, M., Westerhoff, W., 2011. Ultra-high resolution pollen record from the northern Andes reveals rapid shifts in montane climates within the last two glacial cycles. Climate of the Past 7, 299–316. doi:10.5194/cp-7-299-2011.

Grosjean, M., Geyh, M.A., Messerli, B., Schotterer, U., 1995. Late-glacial and early Holocene lake sediments, ground-water formation and climate in the Atacama Altiplano 22-24 °S. Journal of Paleolimnology 14, 241–252. doi:10.1007/BF00682426.

Grosjean, M., van Leeuwen, J.F.N., van der Knaap, W.O., Geyh, M.A., Ammann, B., Tanner, W., Messerli, B., Núñez, L.A., Valero-Garcés, B.L., Veit, H., 2001. A 22,000 C-14 year BP sediment and pollen record of climate change from Laguna Miscanti (23 °S), northern Chile. Global and Planetary Change 28, 35–51. doi:10.1016/S0921-8181(00)00063-1.

Grzymko, T.J., Marcantonio, F., McKee, B.A., Mike Stewart, C., 2007. Temporal variability of uranium concentrations and 234U/238U activity ratios in the Mississippi river and its tributaries. Chemical Geology 243, 344–356. URL: `https://linkinghub.elsevier.com/retrieve/pii/S0009254107002434`, doi:10.1016/j.chemgeo.2007.05.024.

Haase-Schramm, A., Goldstein, S.L., Stein, M., 2004. U-Th dating of Lake Lisan (late Pleistocene dead sea) aragonite and implications for glacial east Mediterranean climate change. Geochimica et Cosmochimica Acta 68, 985–1005. URL: `http://linkinghub.elsevier.com/retrieve/pii/S0016703703005647`, doi:10.1016/j.gca.2003.07.016.

Halbach, P., Von Borstel, D., Gundermann, K.d., 1980. The uptake of uranium by organic substances in a peat bog environment on a granitic bedrock. Chemical Geology 29, 117–138.

Hamelin, B., Bard, E., Zindler, A., Fairbanks, R.G., 1991. 234U/238U mass spectrometry of corals: How accurate is the UTh age of the last interglacial period? Earth and Planetary Science Letters 106, 169–180. URL: `https://linkinghub.elsevier.com/retrieve/pii/0012821X9190070X`, doi:10.1016/0012-821X(91)90070-X.

Hansen, B.C.S., Wright, H.E., Bradbury, J.P., 1984. Pollen studies in the Junín area, central Peruvian Andes. Geological Society of America Bulletin 95, 1454. URL: `https://pubs.geoscienceworld.org/gsabulletin/article/95/12/1454-1465/186834`, doi:10.1130/0016-7606(1984)95<1454:PSITJA>2.0.CO;2.

Hatfield, R., Woods, A., Lehmann, S., Weidhaas, N., Chen, C., Kück, J., Pierdominici, S., Stoner, J., Abbott, M., Rodbell, D., 2019. Stratigraphic correlation and splice generation for sediments recovered from a large-lake drilling project: an example from lake junín, peru. Journal of Paleolimnology , 1–18doi:10.1007/s10933-019-00098-w.

Helmke, J.P., Schulz, M., Bauch, H.A., 2002. Sediment-Color Record from the Northeast Atlantic Reveals Patterns of Millennial-Scale Climate Variability during the Past 500,000 Years. Quaternary Research 57, 49–57. URL: `https://www.cambridge.org/core/product/identifier/S0033589400010565/type/journal_article`, doi:10.1006/qres.2001.2289.

Henderson, G.M., 2002. Seawater (234U/238U) during the last 800 thousand years. Earth and Planetary Science Letters 199, 97–110. URL: `https://linkinghub.elsevier.com/retrieve/pii/S0012821X02005563`, doi:10.1016/S0012-821X(02)00556-3.

Henderson, G.M., Anderson, R.F., 2003. The U-series Toolbox for Paleoceanography. Reviews in Mineralogy and Geochemistry 52, 493–531. URL: `https://pubs.geoscienceworld.org/rimg/article/52/1/493-531/87463`, doi:10.2113/0520493.

Henderson, G.M., Robinson, L.F., Cox, K., Thomas, A.L., 2006. Recognition of non-Milankovitch sea-level highstands at 185 and 343 thousand years ago from

U-Th dating of Bahamas sediment. Quaternary Science Reviews 25, 3346–3358. URL: `https://linkinghub.elsevier.com/retrieve/pii/S0277379106001363`, doi:10.1016/j.quascirev.2006.03.003.

Holmes, A., 1911. The association of lead with uranium in rock-minerals, and its application to the measurement of geological time. Proceedings of the Royal Society of London. Series A, Containing Papers of a Mathematical and Physical Character 85, 248–256.

Holmes, J., 1998. Chapter 10: The palaeoenvironmental significance of iron and manganese in non-marine ostracod shells: a preliminary analysis, in: Holmes, J., Lynch, K. (Eds.), The Kingston Papers: a geographical perspective on the environment, economy, and society. Kingston University School of Geography. chapter Holmes, pp. 198–212.

Holmes, J.A., Chivas, A.R., 2002. Ostracod shell chemistry - overview. Geophysical Monograph Series 131, 185–204. doi:10.1029/131GM10.

Houze, R.A., 1997. Stratiform Precipitation in Regions of Convection: A Meteorological Paradox? Bulletin of the American Meteorological Society 78, 2179–2196. doi:10.1175/1520-0477(1997)078<2179:SPIROC>2.0.CO;2.

Hudson, A.M., Quade, J., 2013. Long-term east-west asymmetry in monsoon rainfall on the Tibetan Plateau. Geology 41, 351–354. doi:10.1130/G33837.1.

IAEA/WMO, 2015. Global Network of Isotopes in Precipitation. Technical Report. URL: `http://www.iaea.org/water`.

Inden, R.F., Coalson, E.B., Field, C., 1996. Phosphoria Formation (Permian) Cycles in the Bighorn Basin, Wyoming, with Emphasis on the Ervay Member, in: Longman, M.W., Sonnenfield, M.D. (Eds.), Paleozoic Systems of the Rocky Mountain Region. Society for Sedimentary Geology, pp. 379–404.

Isaks, B.L., 1988. Uplift of the Central Andean Plateau and bending of the Bolivian orocline. Journal of Geophysical Research 93, 3211–3231. doi:10.1029/JB093iB04p03211.

Israelson, C., Björck, S., Hawkesworth, C.J., Possnert, G., 1997. Direct U-Th dating of organic- and carbonate-rich lake sediments from southern Scandinavia. Earth and Planetary Science Letters 153, 251–263. doi:10.1016/S0012-821X(97)00184-2.

Ivanovich, M., Harmon, R., 1992. Uranium-series Disequilibrium: Applications to Earth, Marine, and Environmental Sciences. Oxford University Press, New York.

Jaffey, A.H., Flynn, K.F., Glendenin, L.E., Bentley, W.C., Essling, A.M., 1971. Precision measurement of half-lives and specific activities of U235 and U238. Physical Review C 4, 1889–1906. doi:10.1103/PhysRevC.4.1889.

James, N.P., Bourque, P.A., 1992. Reefs and mounds. Facies Models: Response to Sea Level Change , 323–347.

James, N.P., Choquette, P.W., 1984. Diagenesis 9. Limestones-the meteoric diagenetic environment. Geoscience Canada 11, 161–194. URL: `http://journals.hil.unb.ca/index.php/GC/article/viewArticle/3395`.

Jansen, J.H.F., Woensdregt, G.F., Kooistra, M.J., Van Der Gaast, S.J., 1987. Ikaite pseudomorphs in the Zaire deep-sea fan: an intermediate between calcite and porous calcite. Geology 15, 245–248. doi:10.1130/0091-7613(1987)15<245:IPITZD>2.0.CO.

Ji, J., Shen, J., Balsam, W.L., Chen, J., Liu, L., Liu, X., 2005. Asian monsoon oscillations in the northeastern Qinghai–Tibet Plateau since the late glacial as interpreted from visible reflectance of Qinghai Lake sediments. Earth and Planetary Science Letters 233, 61–70. URL: `https://linkinghub.elsevier.com/retrieve/pii/S0012821X05001275`, doi:10.1016/j.epsl.2005.02.025.

Jones, C., Carvalho, L.M.V., Liebmann, B., 2012. Forecast Skill of the South American Monsoon System. Journal of Climate 25, 1883–1889. URL: `http://journals.ametsoc.org/doi/abs/10.1175/JCLI-D-11-00586.1`, doi:10.1175/JCLI-D-11-00586.1.

Joussaume, S., Taylor, K.E., Braconnot, P., Mitchell, J.F.B., Kutzbach, J.E., Harrison, S.P., Prentice, I.C., Broccoli, A.J., Abe-Ouchi, A., Bartlein, P.J., Bonfils, C., Dong, B., Guiot, J., Herterich, K., Hewitt, C.D., Jolly, D., Kim, J.W., Kislov, A., Kitoh, A., Loutre, M.F., Masson, V., McAvaney, B., McFarlane, N., de Noblet, N., Peltier, W.R., Peterschmitt, J.Y., Pollard, D., Rind, D., Royer, J.F., Schlesinger, M.E., Syktus, J., Thompson, S., Valdes, P., Vettoretti, G., Webb, R.S., Wyputta, U., 1999. Monsoon changes for 6000 years ago: Results of 18 simulations from the Paleoclimate Modeling Intercomparison Project (PMIP). Geophysical Research Letters 26, 859–862. doi:10.1029/1999GL900126.

Kanner, L.C., Burns, S.J., Cheng, H., Edwards, R.L., 2012. High-Latitude Forcing of the South American Summer Monsoon During the Last Glacial. Science 335, 570–573. doi:10.1126/science.1213397.

Karanovic, I., 2012. Recent freshwater ostracods of the world: Crustacea, Ostracoda, Podocopida. Springer Science & Business Media.

Kaufman, A., Broecker, W., 1965. Comparison of Th230 and C14 Ages for Carbonate Materials from Lakes Lahontan and Bonneville. Journal of Geophysical Research 70, 4039–4054.

Kaufman, A., Broecker, W.S., Ku, T.L., Thurber, D.L., 1971. The status of U-series methods of mollusk dating. Geochimica et Cosmochimica Acta 35, 1155–1183. doi:10.1016/0016-7037(71)90031-7.

Kaufman, A., Yechieli, Y., Gardosh, M., 1992. Reevaluation of the Lake-Sediment Chronology in the Dead-Sea Basin, Israel, Based on New Th-230/U Dates. Quaternary Research 38, 292–304.

Kay, S.M., Coira, B.L., 2009. Shallowing and steepening subduction zones, continental lithospheric loss, magmatism, and crustal flow under the Central Andean Altiplano-Puna Plateau, in: Kay, S.M., Ramos, V.A., Dickinson, W.R. (Eds.), Backbone of the Americas: Shallow Subduction, Plateau Uplift, and Ridge and Terrane Collision: Geological Society of America Memoir. The Geological Society of America. volume 204, pp. 229–259. doi:10.1130/2009.1204(11).

Kelly, S.D., Newville, M.G., Cheng, L., Kemner, K.M., Sutton, S.R., Fenter, P., Sturchio, N.C., Spötl, C., 2003. Uranyl Incorporation in Natural Calcite. Environmental Science & Technology 37, 1284–1287. URL: `https://pubs.acs.org/doi/10.1021/es025962f`, doi:10.1021/es025962f.

Kelly, S.D., Rasbury, E.T., Chattopadhyay, S., Kropf, A.J., Kemner, K.M., 2006. Evidence of a Stable Uranyl Site in Ancient Organic-Rich Calcite. Environmental Science & Technology 40, 2262–2268. URL: `https://pubs.acs.org/doi/10.1021/es051970v`, doi:10.1021/es051970v.

Kigoshi, K., 1971. Alpha-Recoil Thorium-234: Dissolution into Water and the Uranium-234/Uranium-238 Disequilibrium in Nature. Science 173, 47–48. URL: `http://www.sciencemag.org/cgi/doi/10.1126/science.173.3991.47`, doi:10.1126/science.173.3991.47.

Kiro, Y., Goldstein, S., Kushnir, Y., Stein, M., Lazar, B., 2018. Droughts and tropical-induced rainfall in the east mediterranean during warm periods, in: Goldschmidt Abstracts.

Kliem, P., Enters, D., Hahn, A., Ohlendorf, C., Lisé-Pronovost, A., St-Onge, G., Wastegård, S., Zolitschka, B., the Pasado Science Team, 2013. Lithology, radiocarbon chronology and sedimentological interpretation of the lacustrine record from Laguna Potrok Aike, southern Patagonia. Quaternary Science Reviews 71, 54–69. doi:10.1016/j.quascirev.2012.07.019.

Knutti, R., Sedláček, J., 2013. Robustness and uncertainties in the new CMIP5 climate model projections. Nature Climate Change 3, 1–5. URL: `http://dx.doi.org/10.1038/nclimate1716`, doi:10.1038/nclimate1716.

Kohfeld, K.E., Harrison, S.P., 2000. How well can we simulate past climates? Evaluating the models using global paleoenvironmental datasets (Kohfield and Harrison 2000). Quaternary Science Reviews 19, 321–346.

König, I., Haeckel, M., Drodt, M., Suess, E., Trautwein, A.X., 1999. Reactive Fe(II) layers in deep-sea sediments. Geochimica et Cosmochimica Acta 63, 1517–1526. URL: `https://linkinghub.elsevier.com/retrieve/pii/S0016703799001040`, doi:10.1016/S0016-7037(99)00104-0.

König, I., Lougear, A., Bruns, P., Grützner, J., Trautwein, A., Dullo, W.C., 2000. Iron oxidation in sediment cores (Site 1062) during six months of storage in the Ocean Drilling Program archive. Proceedings of the Ocean Drilling Program, Scientific Results. volume 172. pp. 1–11.

Kronfeld, J., 1974. Uranium deposition and Th-234 alpha-recoil: An explanation for extreme U-234/U-238 fractionation within the Trinity aquifer. Earth and Planetary Science Letters 21, 327–330. URL: `https://linkinghub.elsevier.com/retrieve/pii/0012821X74901691`, doi:10.1016/0012-821X(74)90169-1.

Kronfeld, J., Godfrey-Smith, D., Johannessen, D., Zentilli, M., 2004. Uranium series isotopes in the avon valley, nova scotia. Journal of Environmental Radioactivity 73, 335–352.

Kronfeld, J., Vogel, J.C., 1991. Uranium isotopes in surface waters from southern Africa. Earth and Planetary Science Letters 105, 191–195. doi:10.1016/0012-821X(91)90130-A.

Ku, T.L., Knauss, K.G., Mathieu, G.G., 1977. Uranium in open ocean: concentration and isotopic composition. Deep Sea Research 24, 1005 – 1017. URL: `http://www.sciencedirect.com/science/article/pii/0146629177905719`, doi:https://doi.org/10.1016/0146-6291(77)90571-9.

Ku, T.L., Liang, Z.C., 1984. The Dating of Impure Carbonates with Decay-Series Isotopes. Nuclear Instruments and Methods in Physics Research 223, 563–571. doi:10.1360/zd-2013-43-6-1064.

Ku, T.L., Luo, S., Lowenstein, T.K., Li, J., Spencer, R.J., 1998. U-Series Chronology of Lacustrine Deposits in Death Valley, California. Quaternary Research 50, 261–275.

Kutterolf, S., Schindlbeck, J.C., Anselmetti, F.S., Ariztegui, D., Brenner, M., Curtis, J., Schmid, D., Hodell, D., Mueller, A., Pérez, W., Schwalb, A., Frische, M., Wang, K.L., 2016. A 400-ka tephrochronological framework for Central America from Lake Petén Itzá (Guatemala) sediments. Quaternary Science Reviews 150, 200–220. doi:10.1016/j.quascirev.2016.08.023.

Lambert, F., Delmonte, B., Petit, J., Bigler, M., Kaufmann, P., Hutterli, M., Stocker, T., Ruth, U., Steffensen, J., Maggi, V., 2008. Dust-climate couplings over the past 800,000 years from the EPICA Dome C ice core. Nature 452, 616–619. doi:10.1038/nature06763.

Lamy, F., Klump, J., Hebbeln, D., Wefer, G., 2000. Late Quaternary rapid climate change in northern Chile. Terra Nova 12, 8–13. URL: `http://doi.wiley.com/10.1046/j.1365-3121.2000.00265.x%5Cnpapers2://publication/doi/10.` doi:10.1046/j.1365-3121.2000.00265.x.

Langmuir, D., 1978. Uranium solution-mineral equilibria at low temperatures with applications to sedimentary ore deposits. Geochimica et Cosmochimica Acta 42, 547–569.

Langmuir, D., Herman, J.S., 1980. The mobility of thorium in natural waters at low temperatures. Geochimica et Cosmochimica Acta 44, 1753–1766. URL: `papers2://publication/uuid/5E9E5D34-242B-4117-8B39-BF4464A10B4B`.

Larsen, D., 1994. Origin and paleoenvironmental significance of calcite pseudomorphs after ikaite in the Oligocene Creede Formation, Colorado. Journal of Sedimentary Research A64, 593–603.

Laskar, J., Robutel, P., Joutel, F., Gastineau, M., Correia, A.C.M., Levrard, B., 2004. A long-term numerical solution for the insolation quantities of the Earth. Astronomy and Astrophysics 428, 261–285. doi:10.1051/0004-6361:20041335.

Latorre, C., Betancourt, J.L., Arroyo, M.T.K., 2006. Late Quaternary vegetation and climate history of a perennial river canyon in the Río Salado basin (22 °S) of Northern Chile. Quaternary Research 65, 450–466. doi:10.1016/j.yqres.2006.02.002.

Lenhart, J.J., Cabaniss, S.E., MacCarthy, P., Honeyman, B.D., 2000. Uranium (VI) complexation with citric, humic and fulvic acids. Radiochimica Acta 88, 345–353.

Lenters, J.D., Cook, K.H., 1997. On the Origin of the Bolivian High and Related Circulation Features of the South American Climate. Journal of the Atmospheric Sciences 54, 656–678. doi:10.1175/1520-0469(1997)054<0656:OTOOTB>2.0.CO;2.

Li, J., Lowenstein, T.K., Brown, C.B., Ku, T.L., Luo, S., 1996. A 100 ka record of water tables and paleoclimates from salt cores, Death Valley, California. Palaeogeography, Palaeoclimatology, Palaeoecology 123, 179–203.

Lin, J.C., Broecker, W.S., Hemming, S.R., Hajdas, I., Anderson, R.F., Smith, G.I., Kelley, M., Bonani, G., 1998. A Reassessment of U-Th and 14C Ages for Late-Glacial High-Frequency Hydrological Events at Searles Lake, California. Quaternary Research 49, 11–23. URL: `http://www.sciencedirect.com/science/article/pii/S0033589497919499`, doi:10.1006/qres.1997.1949.

Lisiecki, L.E., Raymo, M.E., 2005. A Pliocene-Pleistocene stack of 57 globally distributed benthic δ18O records. Paleoceanography 20. URL: `http://doi.wiley.com/10.1029/2004PA001071`, doi:10.1029/2004PA001071.

Longman, M.W., 1980. Carbonate Diagenetic Textures from Nearsurface Diagenetic Environments. American Association of Petroleum Geologists Bulletin 64, 461–487.

Lowell, T.V., Heusser, C.J., Andersen, B.G., Moreno, P.I., Hauser, A., Heusser, L.E., Schlüchter, C., Marchant, D.R., Denton, G.H., 1995. Interhemispheric Correlation of Late Pleistocene Glacial Events. Science 269, 1541–1549.

Lowenstein, T.K., Hein, M.C., Bobst, A.L., Jordan, T.E., Ku, T.L., Luo, S., 2003. An assessment of stratigraphic completeness in climate-sensitive closed-basin lake sediments: Salar de Atacama, Chile. Journal of Sedimentary Petrology 73, 91–104.

Ludwig, K.R., 2003. Mathematical-Statistical Treatment of Data and Errors for 230Th/U Geochronology. Reviews in Mineralogy and Geochemistry 52, 631–656. doi:10.2113/0520631.

Ludwig, K.R., 2012. User's Manual for Isoplot Version 3.75–4.15: A Geochronological Toolkit for Microsoft Excel. Technical Report 5. Berkeley Geochronological Center Special Publication.

Ludwig, K.R., Paces, J.B., 2002. Uranium-series dating of pedogenic silica and carbonate, Crater Flat, Nevada. Geochimica et Cosmochimica Acta 66, 487–506. doi:10.1016/S0016-7037(01)00786-4.

Luo, S., Ku, T.L., 1991. U-series isochron dating: A generalized method employing total-sample dissolution. Geochimica et Cosmochimica Acta 55, 555–564. doi:10.1016/0016-7037(91)90012-T.

Lyle, M., 1983. The brown-green color transition in marine sediments: A marker of the Fe(III)-Fe(II) redox boundary. Limnol. Oceanogr. 28, 1026–1033.

Ma, Z., Wang, Z., Liu, J., Yuan, B., Xiao, J., Zhang, G., 2004. U-series chronology of sediments associated with Lake Quaternary fluctuations, Balikun Lake, northwestern China. Quaternary International 121, 89–98.

Mackay, A.W., Bezrukova, E.V., Boyle, J.F., Holmes, J.A., Panizzo, V.N., Piotrowska, N., Shchetnikov, A., Shilland, E.M., Tarasov, P., White, D., 2013. Multiproxy evidence for abrupt climate change impacts on terrestrial and freshwater ecosystems in the Ol'khon region of Lake Baikal, central Asia. Quaternary International 290-291, 46–56. URL: `http://dx.doi.org/10.1016/j.quaint.2012.09.031` `https://linkinghub.elsevier.com/retrieve/pii/S1040618212032041`, doi:10.1016/j.quaint.2012.09.031.

Magaritz, M., Aravena, R., Peña, H., Suzuki, O., Grilli, A., 1989. Water chemistry and isotope study of streams and springs in northern Chile. Journal of Hydrology 108, 323–341. doi:10.1016/0022-1694(89)90292-8.

Magrin, G.O., Marengo, J.A., Boulanger, J.P., Buckeridge, M.S., Castellanos, E., Poveda, G., Scarano, F.R., Vicuña, S., 2014. Central and South America, in: Barros, V.R., Field, C.B., Dokken, D.J., Mastrandrea, M.D., Mach, K.J., Bilir, T.E., Chatterjee, M., Ebi, K.L., Estrada, Y.O., Genova, R.C., Girma, B., Kissel, E.S., Levy, A.N., MacCracken, S., Mastrandrea, P.R., White, L.L. (Eds.), Climate Change 2014: Impacts, Adaptation, and Vulnerability. Part B: Regional Aspects: Contribution of Working Group II to the Fifth Assessment Report of the Intergovernmental Panel on Climate Change. Cambridge University Press, Cambridge, United Kingdom. volume 2, pp. 1499–1566.

Marengo, J., 2004. Interdecadal and long term rainfall variability in the Amazon basin. Theoretical and Applied Climatology 78, 79–96.

Marengo, J.A., Liebmann, B., Grimm, A.M., Misra, V., Silva Dias, P.L., Cavalcanti, I.F.A., Carvalho, L.M.V., Berbery, E.H., Ambrizzi, T., Vera, C.S., Saulo, A.C., Nogues-Paegle, J., Zipser, E., Seth, A., Alves, L.M., 2012. Recent developments on the South American monsoon system. International Journal of Climatology 32, 1–21. doi:10.1002/joc.2254.

McGee, D., Donohoe, A., Marshall, J., Ferreira, D., 2014. Changes in ITCZ location and cross-equatorial heat transport at the Last Glacial Maximum, Heinrich Stadial 1, and the mid-Holocene. Earth and Planetary Science Letters 390, 69–79. URL: `http://dx.doi.org/10.1016/j.epsl.2013.12.043`, doi:10.1016/j.epsl.2013.12.043.

McGee, D., Quade, J., Edwards, R.L., Broecker, W.S., Cheng, H., Reiners, P.W., Evenson, N., 2012. Lacustrine cave carbonates: Novel archives of paleohydrologic change in the Bonneville Basin (Utah, USA). Earth and Planetary Science Letters 351-352, 182–194. URL: `http://linkinghub.elsevier.com/retrieve/pii/S0012821X1200386X`, doi:10.1016/j.epsl.2012.07.019.

McIntyre, G., Brooks, C., Compston, W., Turek, A., 1966. The statistical assessment of Rb-Sr isochrons. Journal of Geophysical Research 71, 5459–5468.

McLaren, S.J., Rowe, P.J., 1996. The reliability of uranium-series mollusc dates from the western Mediterranean basin. Quaternary Science Reviews 15, 709–717. doi:10.1016/0277-3791(96)00032-7.

Messerli, B., Grosjean, M., Vuille, M., 1997. Water Availability, Protected Areas, and Natural Resources in the Andean Desert Altiplano. Mountain Research and Development 17, 229–238.

Metcalfe, S., Say, A., Black, S., McCulloch, R., O'Hara, S., 2002. Wet conditions during the last glaciation in the Chihuahuan Desert, Alta Babicora Basin, Mexico. Quaternary Research 57, 91–101. doi:10.1006/qres.2001.2292.

Mix, A.C., Harris, S.E., Janecek, T.R., 1995. Estimating lithology from nonintrusive reflectance spectra: Leg 138. Proceedings of the Ocean Drilling Program, Scientific Results 138.

Morales, M.S., Carilla, J., Grau, H.R., Villalba, R., 2015. Multi-century lake area changes in the Andean high-elevation ecosystems of the Southern Altiplano. Climate of the Past Discussions 11, 1821–1855. URL: `http://www.clim-past-discuss.net/11/1821/2015/`, doi:10.5194/cpd-11-1821-2015.

Mosblech, N.A.S., Bush, M.B., Gosling, W.D., Hodell, D., Thomas, L., van Calsteren, P., Correa-Metrio, A., Valencia, B.G., Curtis, J., van Woesik, R., 2012. North Atlantic forcing of Amazonian precipitation during the last ice age. Nature Geoscience 5, 817–820. URL: `http://oro.open.ac.uk/34485/`, doi:10.1038/ngeo1588.

Müller, G., 1971. 'Gravitational' cement: An indicator for the vadose zone of the subaerial diagenetic environment, in: Bricker, O.P. (Ed.), Carbonate Cements. Johns Hopkins Press, Baltimore, MD, pp. 301–302.

Murphy, R.J., Lenhart, J.J., Honeyman, B.D., 1999. The sorption of thorium (IV) and uranium (VI) to hematite in the presence of natural organic matter. Colloids and Surfaces A: Physicochemical and Engineering Aspects 157, 47–62. URL: `http://linkinghub.elsevier.com/retrieve/pii/S0927775799001156`, doi:10.1016/S0927-7757(99)00115-6.

Nagao, S., Nakashima, S., 1992. The factors controlling vertical color variations of North Atlantic Madeira Abyssal Plain sediments. Marine Geology 109, 83–94. URL: `https://linkinghub.elsevier.com/retrieve/pii/0025322792902224`, doi:10.1016/0025-3227(92)90222-4.

Nester, P.L., Gayó, E., Latorre, C., Jordan, T.E., Blanco, N., 2007. Perennial stream discharge in the hyperarid Atacama Desert of northern Chile during the latest Pleistocene. Proceedings of the National Academy of Sciences of the United States of America 104, 19724–19729. doi:10.1073/pnas.0705373104.

Nishizawa, T., Tanaka, M., 1983. The Annual Change in the Tropospheric Circulation and the Rainfall in South America. Archives for Meteorology, Geophysics, and Bioclimatology B, 107–116.

Nogués-Paegle, J., Mechoso, C.R., Fu, R., Berbery, E.H., Chao, W.C., Chen, T.C., Cook, K., Diaz, A.F., Enfield, D., Ferreira, R., Grimm, A.M., Kousky, V.E., Liebmann, B., Marengo, J.A., Mo, K., Neelin, J.D., Paegle, J., Robertson, A.W., Seth, A., Vera, C.S., Zhou, J., 2002. Progress in Pan American CLIVAR Research: Understanding the South American Monsoon. Meteorologica 27, 1–30. doi:cptec.inpe.br/walmeida/2004/05.13.14.45.34-0.

Nowaczyk, N.R., Haltia, E.M., Ulbricht, D., Wennrich, V., Sauerbrey, M.A., Rosén, P., Vogel, H., Francke, A., Meyer-Jacob, C., Andreev, A.A., Lozhkin, A.V., 2013. Chronology of Lake El'gygytgyn sediments – A combined magnetostratigraphic, palaeoclimatic and orbital tuning study based on multi-parameter analyses. Climate of the Past 9, 2413–2432. doi:10.5194/cp-9-2413-2013.

Oehlerich, M., Mayr, C., Griesshaber, E., Lücke, A., Oeckler, O.M., Ohlendorf, C., Schmahl, W.W., Zolitschka, B., 2013. Ikaite precipitation in a lacustrine environment - implications for palaeoclimatic studies using carbonates from Laguna Potrok Aike (Patagonia, Argentina). Quaternary Science Reviews 71, 46–53. URL: `http://dx.doi.org/10.1016/j.quascirev.2012.05.024`, doi:10.1016/j.quascirev.2012.05.024.

Oviatt, C.G., McCoy, W.D., Nash, W.P., 1994. Sequence stratigraphy of lacustrine deposits: a Quaternary example from the Bonneville basin, Utah. Geological Society of America Bulletin 106, 133–144. URL: `http://gsabulletin.gsapubs.org/content/106/1/133.short`, doi:10.1130/0016-7606(1994)106<0133.

Palacios-Fest, M.R., Alin, S.R., Cohen, A.S., Tanner, B., Heuser, H., 2005. Paleolimnological investigations of anthropogenic environmental change in Lake Tanganyika: IV. Lacustrine paleoecology. Journal of Paleolimnology 34, 51–71. doi:10.1007/s10933-005-2397-1.

Peng, T.H., Goddard, J.G., Broecker, W.S., 1978. A Direct Comparison of 14C and 230Th Ages at Searles Lake, California. Quaternary Research 9, 319–329.

Pérez, L., Lorenschat, J., Bugja, R., Brenner, M., Scharf, B., Schwalb, A., 2010. Distribution, diversity and ecology of modern freshwater ostracodes (Crustacea), and hydrochemical characteristics of Lago Petén Itzá, Guatemala. Journal of Limnology 69, 146–159.

Perez-Sanz, A., Li, G., González-Sampériz, P., Harrison, S.P., 2014. Evaluation of modern and mid-Holocene seasonal precipitation of the Mediterranean and northern Africa in the CMIP5 simulations. Climate of the Past 10, 551–568. URL: `http://www.clim-past.net/10/551/2014/`, doi:10.5194/cp-10-551-2014.

Peterson, L.C., Haug, G.H., 2006. Variability in the mean latitude of the Atlantic Intertropical Convergence Zone as recorded by riverine input of sediments to the Cariaco

Basin (Venezuela). Palaeogeography, Palaeoclimatology, Palaeoecology 234, 97–113. doi:10.1016/j.palaeo.2005.10.021.

Peterson, L.C., Haug, G.H., Hughen, K.A., Röhl, U., 2000. Rapid changes in the hydrologic cycle of the tropical Atlantic during the last glacial. Science 290, 1947–1951. doi:10.1126/science.290.5498.1947.

Petit, J., Jouzel, J., Raynaud, D., Barkov, N., Barnola, J.M., Basile, I., Bender, M., Chappellaz, J., Davis, M., Delaygue, G., Delmotte, M., Kotlyakov, V., Legrand, M., Lipenkov, V., Lorius, C., Pépin, L., Ritz, C., Saltzman, E., Stievenard, M., 1999. Climate and atmospheric history of the past 420,000 years from the Vostok ice core, Antarctica. Nature 399, 429–436. doi:10.1038/20859.

Phillips, F.M., Zreda, M.G., Ku, T.L., Luo, S., Huang, Q., Elmore, D., Kubik, P.W., Sharma, P., 1993. 230Th/234U and 36Cl dating of evaporite deposits from the western Qaidam Basin, China: Implications for glacial-period dust export from Central Asia. Geological Society of America Bulletin 105, 1606–1616.

Pigati, J.S., Springer, K.B., Honke, J.S., 2019. Desert wetlands record hydrologic variability within the Younger Dryas chronozone, Mojave Desert, USA. Quaternary Research 91, 51–62. URL: `https://www.cambridge.org/core/product/identifier/S0033589418000145/type/journal_article`, doi:10.1017/qua.2018.14.

Placzek, C., Patchett, P.J., Quade, J., Wagner, J.D.M., 2006a. Strategies for successful U-Th dating of paleolake carbonates: An example from the Bolivian Altiplano. Geochemistry, Geophysics, Geosystems 7, Q05024. doi:10.1029/2005GC001157.

Placzek, C., Quade, J., Betancourt, J.L., Jonathan, P., Rech, J.A., Latorre, C., Matmon, A., Holmgren, C., English, N.B., Patchett, P.J., 2009. Climate in the Dry Central Andes Over Geologic, Millenial, and Interannual Timescales. Annals of the Missouri Botanical Garden 96, 386–397. doi:10.3417/2008019.

Placzek, C., Quade, J., Patchett, P.J., 2006b. Geochronology and stratigraphy of late Pleistocene lake cycles on the southern Bolivian Altiplano: Implications for causes of tropical climate change. Bulletin of the Geological Society of America 118, 515–532. doi:10.1130/B25770.1.

Placzek, C.J., Quade, J., Patchett, P.J., 2013. A 130 ka reconstruction of rainfall on the Bolivian Altiplano. Earth and Planetary Science Letters 363, 97–108. doi:10.1016/j.epsl.2012.12.017.

Plater, A.J., Ivanovich, M., Dugdale, R.E., 1992. Uranium series disequilibrium in river sediments and waters: the significance of anomalous activity ratios. Applied Geochemistry 7, 101–110. doi:10.1016/0883-2927(92)90029-3.

Porcelli, D., Andersson, P., Wasserburg, G., Ingri, J., Baskaran, M., 1997. The importance of colloids and mires for the transport of uranium isotopes through the Kalix River watershed and Baltic Sea. Geochimica et Cosmochimica Acta 61, 4095–4113. URL: `http://linkinghub.elsevier.com/retrieve/pii/S0016703797002354`, doi:10.1016/S0016-7037(97)00235-4.

Powell, R., Hergt, J., Woodhead, J., 2002. Improving isochron calculations with robust statistics and the bootstrap. Chemical Geology 185, 191–204. URL: `http://linkinghub.elsevier.com/retrieve/pii/S000925410100403X`, doi:10.1016/S0009-2541(01)00403-X.

Prokopenko, A.A., Hinnov, L.A., Williams, D.F., Kuzmin, M.I., 2006. Orbital forcing of continental climate during the Pleistocene: a complete astronomically tuned climatic record from Lake Baikal, SE Siberia. Quaternary Science Reviews 25, 3431–3457. doi:10.1016/j.quascirev.2006.10.002.

Przybylowicz, W., Schwarcz, H.P., Latham, A.G., 1991. Dirty calcites 2. Uranium-series dating of artificial calcite-detritus mixtures. Chemical Geology: Isotope Geoscience Section 86, 161–178. doi:10.1016/0168-9622(91)90060-A.

Qin, B., Harrison, S.P., Kutzbach, J.E., 1998. Evaluation of modelled regional water balance using lake status data: A comparison of 6 ka simulations with the NCAR CCM. Quaternary Science Reviews 17, 535–548. doi:10.1016/S0277-3791(98)00011-0.

Quade, J., Dettinger, M.P., Carrapa, B., DeCelles, P., Murray, K.E., Huntington, K.A., Cartwright, A., Canavan, R.R., Gehrels, G., Clementz, M., 2015. The growth of the central Andes, 22 S–26 S. Geodynamics of a Cordilleran Orogenic System: The Central Andes of Argentina and Northern Chile: Geological Society of America Memoir 212.

Quade, J., Rech, J.A., Betancourt, J.L., Latorre, C., Quade, B., Rylander, K.A., Fisher, T., 2008. Paleowetlands and regional climate change in the central Atacama Desert, northern Chile. Quaternary Research 69, 343–360. doi:10.1016/j.yqres.2008.01.003.

Reeder, R.J., Nugent, M., Lamble, G.M., Tait, C.D., Morris, D.E., 2000. Uranyl Incorporation into Calcite and Aragonite: XAFS and Luminescence Studies. Environmental Science & Technology 34, 638–644. URL: `https://pubs.acs.org/doi/10.1021/es990981j`, doi:10.1021/es990981j.

Reeder, R.J., Nugent, M., Tait, C.D., Morris, D.E., Heald, S.M., Beck, K.M., Hess, W.P., Lanzirotti, A., 2001. Coprecipitation of Uranium(VI) with Calcite: XAFS, micro-XAS, and luminescence characterization. Geochimica et Cosmochimica Acta 65, 3491–3503. URL: `http://linkinghub.elsevier.com/retrieve/pii/S0016703701006470`, doi:10.1016/S0016-7037(01)00647-0.

Riding, R., 1979. Origin and diagenesis of lacustrine algal bioherms at the margin of the Ries crater, Upper Miocene, southern Germany. Sedimentology 26, 645–680. URL: `http://dx.doi.org/10.1111/j.1365-3091.1979.tb00936.x`, doi:10.1111/j.1365-3091.1979.tb00936.x.

Rissmann, C., Leybourne, M., Benn, C., Christenson, B., 2015. The origin of solutes within the groundwaters of a high Andean aquifer. Chemical Geology 396, 164–181. URL: `http://linkinghub.elsevier.com/retrieve/pii/S0009254114005877`, doi:10.1016/j.chemgeo.2014.11.029.

Roberts, H.M., Bryant, C.L., Huws, D.G., Lamb, H.F., 2018. Generating long chronologies for lacustrine sediments using luminescence dating: a 250,000 year record from Lake Tana, Ethiopia. Quaternary Science Reviews 202, 66–77. URL: `https://doi.org/10.1016/j.quascirev.2018.10.037`, doi:10.1016/j.quascirev.2018.10.037.

Robinson, L.F., Adkins, J.F., Fernandez, D.P., Burnett, D.S., Wang, S.L., Gagnon, A.C., Krakauer, N., 2006. Primary U distribution in scleractinian corals and its implications for U series dating. Geochemistry, Geophysics, Geosystems 7. doi:10.1029/2005GC001138.

Robinson, L.F., Henderson, G.M., Hall, L., Matthews, I., 2004. Climatic Control of Riverine and Seawater Uranium-Isotope Ratios. Science 305, 851–854. URL: `http://www.sciencemag.org/cgi/doi/10.1126/science.1099673`, doi:10.1126/science.1099673.

Robinson, L.F., Henderson, G.M., Slowey, N.C., 2002. U-Th dating of marine isotope stage 7 in Bahamas slope sediments. Earth and Planetary Science Letters 196, 175–187. doi:10.1016/S0012-821X(01)00610-0.

Rodbell, D.T., Abbott, M.B., the 2011 ICDP Lake Junin Working Group, 2012. Workshop on drilling of Lake Junin, Peru: Potential for development of a continuous tropical climate record. Scientific Drilling 3, 58–60. doi:10.2204/iodp.sd.13.10.2011.

Roehrig, R., Bouniol, D., Guichard, F., Hourdin, F., Redelsperger, J.L., 2013. The Present and Future of the West African Monsoon: A Process-Oriented Assessment of CMIP5 Simulations along the AMMA Transect. Journal of Climate 26, 6471–6505. URL: `http://journals.ametsoc.org/doi/abs/10.1175/JCLI-D-12-00505.1`, doi:10.1175/JCLI-D-12-00505.1.

Rouchy, J.M., Servant, M., Fournier, M., Causse, C., 1996. Extensive carbonate algal bioherms in upper Pleistocene saline lakes of the central Altiplano of Bolivia. Sedimentology 43, 973–993. doi:10.1111/j.1365-3091.1996.tb01514.x.

Rowe, P.J., Richards, D.A., Atkinson, T.C., Bottrell, S.H., Cliff, R.A., 1997. Geochemistry and radiometric dating of a Middle Pleistocene peat. Geochimica et Cosmochimica Acta 61, 4201–4211. doi:10.1016/S0016-7037(97)00213-5.

Rowell, D.P., 2012. Sources of uncertainty in future changes in local precipitation. Climate Dynamics 39, 1929–1950. URL: `http://link.springer.com/10.1007/s00382-011-1210-2`, doi:10.1007/s00382-011-1210-2.

Rudnick, R., Gao, S., 2003. Composition of the Continental Crust, in: Treatise on Geochemistry. Elsevier. volume 3, pp. 1–64. doi:10.1016/B0-08-043751-6/03016-4.

Rutllant, J., Ulriksen, P., 1979. Boundary-layer dynamics of the extremely arid northern part of Chile: The Antofagasta Field Experiment. Boundary Layer Meteorology 17, 41–55.

Sarin, M., Krishnaswami, S., Moore, W., et al., 1990. Chemistry of uranium, thorium, and radium isotopes in the ganga-brahmaputra river system: Weathering processes and fluxes to the bay of bengal. Geochimica et Cosmochimica Acta 54, 1387–1396.

Saulo, A.C., Nicolini, M., Chou, S.C., 2000. Model characterization of the South American low-level flow during the 1997–1998 spring–summer season. Climate Dynamics 16, 867–881.

Schmeide, K., Pompe, S., Bubner, M., Heise, K.H., Bernhard, G., Nitsche, H., 2000. Uranium(VI) sorption onto phyllite and selected minerals in the presence of humic acid. Radiochimica Acta 88, 723–728. URL: `http://www.degruyter.com/view/j/ract.2000.88.issue-9-11/ract.2000.88.9-11.723/ract.200` doi:10.1524/ract.2000.88.9-11.723.

Schnurrenberger, D., Russell, J., Kelts, K., 2003. Classification of lacustrine sediments based on sedimentary components. Journal of Paleolimnology 29, 141–154.

Schoelle, P.A., Ulmer-Schoelle, D.S., 2003. Syngenetic/Eogenetic Marine Diagenesis, in: Lorenz, J.C. (Ed.), AAPG Memoir 77: A Color Guide to the Petrography of Carbonate Rocks: Grains, textures, porosity, diagenesis. The American Association of Petroleum Geologists, Tulsa, Oklahoma. chapter Chapter 23, p. 328.

Schoene, B., Condon, D.J., Morgan, L., McLean, N., 2013. Precision and Accuracy in Geochronology. Elements 9, 19–24. doi:10.2113/gselements.9.1.19.

Schwalb, A., Locke, S.M., Dean, W.E., 1995. Ostracode δ^{18}O and δ^{13}C evidence of Holocene environmental changes in the sediments of two Minnesota lakes. Journal of Paleolimnology 14, 281–296. doi:10.1007/BF00682429.

Schwarcz, H.P., Latham, A.G., 1989. Dirty calcites 1. Uranium-series dating of contaminated calcite using leachates alone. Chemical Geology: Isotope Geoscience Section 80, 35–43. doi:10.1016/0168-9622(89)90046-8.

Selleck, B.W., Carr, P.F., Jones, B.G., 2007. A Review and Synthesis of Glendonites (Pseudomorphs after Ikaite) with New Data: Assessing Applicability as Recorders of Ancient Coldwater Conditions. Journal of Sedimentary Research 77, 980–991. doi:10.2110/jsr.2007.087.

Seltzer, G., Rodbell, D., Burns, S., 2000. Isotopic evidence for late Quaternary climatic change in tropical South America. Geology 28, 35. URL: `https://pubs.geoscienceworld.org/geology/article/28/1/35-38/187921`, doi:10.1130/0091-7613(2000)28<35:IEFLQC>2.0.CO;2.

Seluchi, M.E., Saulo, A.C., Nicolini, M., Satyamurty, P., 2003. The Northwestern Argentinean Low: A Study of Two Typical Events. Monthly Weather Review 131, 2361–2378. doi:10.1175/1520-0493(2003)131<2361:TNALAS>2.0.CO;2.

Shakun, J.D., Clark, P.U., He, F., Marcott, S.A., Mix, A.C., Liu, Z., Otto-Bliesner, B., Schmittner, A., Bard, E., 2012. Global warming preceded by increasing carbon dioxide concentrations during the last deglaciation. Nature 484, 49–54. doi:10.1038/nature10915.

Shanahan, T.M., Peck, J.A., McKay, N., Heil, C.W., King, J., Forman, S.L., Hoffmann, D.L., Richards, D.A., Overpeck, J.T., Scholz, C., 2013. Age models for long lacustrine sediment records using multiple dating approaches – An example from Lake Bosumtwi, Ghana. Quaternary Geochronology 15, 47–60. URL: `http://dx.doi.org/10.1016/j.quageo.2012.12.001` `https://linkinghub.elsevier.com/retrieve/pii/S1871101412001872`, doi:10.1016/j.quageo.2012.12.001.

Shearman, D.J., McGugan, A., Stein, C., Smith, A.J., 1989. Ikaite, CaCO3 6H2O, precursor of the thinolites in the Quaternary tufas and tufa mounds of the Lahontan and Mono Lake Basins, western United States. Geological Society of America Bulletin 101, 913–917. doi:10.1130/0016-7606(1989)101<0913.

Shearman, D.J., Smith, A.J., 1985. Ikaite, the parent mineral of jarrowite-type pseudomorphs. Proceedings of the Geologists' Association 96, 305–314. URL: `http://www.scopus.com/inward/record.url?eid=2-s2.0-0022214193&partnerID=tZOtx3y1`, doi:10.1016/S0016-7878(85)80019-5.

Shen, C.C., Lawrence Edwards, R., Cheng, H., Dorale, J.A., Thomas, R.B., Bradley Moran, S., Weinstein, S.E., Edmonds, H.N., 2002. Uranium and thorium isotopic and concentration measurements by magnetic sector inductively coupled plasma mass spectrometry. Chemical Geology 185, 165–178. doi:10.1016/S0009-2541(01)00404-1.

Shen, C.C., Wu, C.C., Cheng, H., Edwards, R.L., Hsieh, Y.T., Gallet, S., Chang, C.C., Li, T.Y., Lam, D.D., Kano, A., Hori, M., Spötl, C., 2012. High-precision and high-resolution carbonate 230Th dating by MC-ICP-MS with SEM protocols. Geochimica et Cosmochimica Acta 99, 71 – 86. URL: `http://www.sciencedirect.com/science/article/pii/S0016703712005248`, doi:https://doi.org/10.1016/j.gca.2012.09.018.

Shepherd, T.G., 2014. Atmospheric circulation as a source of uncertainty in climate change projections. Nature Geoscience 7, 703–708. URL: `http://www.nature.com/doifinder/10.1038/ngeo2253`, doi:10.1038/ngeo2253.

Silva, V.B.S., Kousky, V.E., 2012. The South American Monsoon System: Climatology and Variability, in: Wang, S.Y., Gillies, R.R. (Eds.), Modern Climatology. InTech, pp. 123–152. URL: `http://www.intechopen.com/books/modern-climatology/the-south-american-monsoon-system-c`

Skrivanek, A., Li, J., Dutton, A., 2018. Relative sea-level change during the Last Interglacial as recorded in Bahamian fossil reefs. Quaternary Science Reviews 200, 160–177. URL: `https://linkinghub.elsevier.com/retrieve/pii/S0277379118304384`, doi:10.1016/j.quascirev.2018.09.033.

Smith, A.J., Delorme, L.D., 2010. Ostracoda. Ecology and Classification of North American Freshwater Invertebrates , 725–771doi:10.1016/B978-0-12-374855-3.00019-4.

Smith, J.A., Finkel, R.C., Farber, D.L., Rodbell, D.T., Seltzer, G.O., 2005a. Moraine preservation and boulder erosion in the tropical Andes: Interpreting old surface exposure ages in glaciated valleys. Journal of Quaternary Science 20, 735–758. doi:10.1002/jqs.981.

Smith, J.A., Rodbell, D.T., 2010. Cross-cutting moraines reveal evidence for north atlantic influence on glaciers in the tropical Andes. Journal of Quaternary Science 25, 243–248. doi:10.1002/jqs.1393.

Smith, J.A., Seltzer, G.O., Farber, D.L., Rodbell, D.T., Finkel, R.C., 2005b. Early local last glacial maximum in the tropical Andes. Science 308, 678–681. doi:10.1126/science.1107075.

Smith, W., 1816. Strata identified by organized fossils: containing prints on colored paper of the most characteristic specimens in each stratum.

Stein, M., Goldstein, S.L., 2006. U-Th and radiocarbon chronologies of late Quaternary lacustrine records of the Dead Sea basin: Methods and applications, in: Enzel, Y., Agnon, A., Stein, M. (Eds.), New frontiers in Dead Sea paleoenvironmental research: Geological Society of America Special Paper 401. Geological Society of America. volume 401, pp. 141–154. URL:

`https://pubs.geoscienceworld.org/books/book/558/chapter/3802608/`, doi:10.1130/2006.2401(09).

Steno, N., 1669. De Solido Intra Solidum Naturaliter Contento Dissertationis Prodromus. Ph.D. thesis.

Steponaitis, E., Andrews, A., McGee, D., Quade, J., Hsieh, Y.T., Broecker, W.S., Shuman, B.N., Burns, S.J., Cheng, H., 2015. Mid-Holocene drying of the U.S. Great Basin recorded in Nevada speleothems. Quaternary Science Reviews , 1–12URL: `http://linkinghub.elsevier.com/retrieve/pii/S0277379115001535`, doi:10.1016/j.quascirev.2015.04.011.

Stirling, C., Lee, D.C., Christensen, J., Halliday, A., 2000. High-precision in situ 238U–234U–230Th isotopic analysis using laser ablation multiple-collector ICPMS. Geochimica et Cosmochimica Acta 64, 3737–3750. URL: `https://linkinghub.elsevier.com/retrieve/pii/S0016703700004579`, doi:10.1016/S0016-7037(00)00457-9.

Stockhecke, M., Kwiecien, O., Vigliotti, L., Anselmetti, F.S., Beer, J., Çağatay, M.N., Channell, J.E., Kipfer, R., Lachner, J., Litt, T., Pickarski, N., Sturm, M., 2014. Chronostratigraphy of the 600,000 year old continental record of Lake Van (Turkey). Quaternary Science Reviews 104, 8–17. doi:10.1016/j.quascirev.2014.04.008.

Stríkis, N.M., Chiessi, C.M., Cruz, F.W., Vuille, M., Cheng, H., Barreto, E.A.S., Mollenhauer, G., Kasten, S., Karmann, I., Edwards, R.L., Bernal, J.P., Sales, R., 2015. Timing and structure of Mega-SACZ events during Heinrich Stadial 1. Geophysical Research Letters 42, 1–8. doi:10.1002/2015GL064048.Received.

Suess, E., Balzer, W., Hesse, K.F., Müller, P.J., Ungerer, C.A., Wefer, G., 1982. Calcium Carbonate Hexahydrate from Organic-Rich Sediments of the Antarctic Shelf: Precursors of Glendonites. Science 216, 1128–1131. URL: `http://www.sciencemag.org/cgi/doi/10.1126/science.216.4550.1128`, doi:10.1126/science.216.4550.1128.

Swainson, I.P., Hammond, R.P., 2001. Ikaite, CaCO3 · 6H2O: Cold comfort for glendonites as paleothermometers. American Mineralogist 86, 1530–1533.

Sylvestre, F., Servant, M., Servant-Vildary, S., Causse, C., Fournier, M., Ybert, J.P., 1999. Lake-Level Chronology on the Southern Bolivian Altiplano (18 °–23 °S) During Late-Glacial Time and the Early Holocene. Quaternary Research 51, 54–66. URL: `isi:000078140200005` `https://www.cambridge.org/core/product/identifier/S0033589400033937/type/journal_article`, doi:10.1006/qres.1998.2017.

Thornalley, D.J.R., Bauch, H.A., Gebbie, G., Guo, W., Ziegler, M., Bernasconi, S.M., Barker, S., Skinner, L.C., Yu, J., 2015. A warm and poorly ventilated deep Arctic Mediterranean during the last glacial period. Science 349, 706–710.

Thurber, D.L., 1962. Anomalous U^{234}/U^{238} in nature. Journal of Geophysical Research 67, 4518–4520.

Tomlinson, C.W., 1916. The origin of red beds: a study of the conditions of origin of the Permo-Carboniferous and Triassic red beds of the western United States. The Journal of Geology 24, 153–179.

Torfstein, A., Goldstein, S.L., Kushnir, Y., Enzel, Y., Haug, G., Stein, M., 2015. Dead Sea drawdown and monsoonal impacts in the Levant during the last interglacial. Earth and Planetary Science Letters 412, 235–244. URL: `http://dx.doi.org/10.1016/j.epsl.2014.12.013`, doi:10.1016/j.epsl.2014.12.013.

Trachsel, M., Telford, R.J., 2017. All age-depth models are wrong, but are getting better. The Holocene 27, 860–869. URL: `http://journals.sagepub.com/doi/10.1177/0959683616675939`, doi:10.1177/0959683616675939.

Valero-Garcés, B., Grosjean, M., Schwalb, A., Geyh, M., Messerli, B., Kelts, K., 1996. Limnogeology of Laguna Miscanti: evidence for mid to late Holocene moisture changes in the Atacama Altiplano (Northern Chile). Journal of Paleolimnology 16, 1–21. doi:10.1007/BF00173268.

Valero-Garcés, B.L., Grosjean, M., Kelts, K., Schreier, H., Messerli, B., 1999. Holocene lacustrine deposition in the Atacama Altiplano: Facies models, climate and tectonic forcing. Palaeogeography, Palaeoclimatology, Palaeoecology 151, 101–125. doi:10.1016/S0031-0182(99)00018-8.

Van Der Wijk, A., El-Daoushy, F., Arends, A.R., Mook, W.G., 1986. Dating peat with U/Th disequilibrium: Some geochemical considerations. Chemical Geology: Isotope Geoscience Section 59, 283–292. doi:10.1016/0168-9622(86)90077-1.

Vera, C., Higgins, W., Amador, J., Ambrizzi, T., Garreaud, R., Gochis, D., Gutzler, D., Lettenmaier, D., Marengo, J., Mechoso, C.R., Nogues-Paegle, J., Silva Dias, P.L., Zhang, C., 2006. Toward a unified view of the American monsoon systems. Journal of Climate 19, 4977–5000. doi:10.1175/JCLI3896.1.

Vermeesch, P., 2018. IsoplotR: A free and open toolbox for geochronology. Geoscience Frontiers 9, 1479–1493. doi:10.1016/j.gsf.2018.04.001.

Vicuña, S., McPhee, J., Garreaud, R.D., 2012. Agriculture vulnerability to climate change in a snowmelt driven basin in semiarid Chile. J. Water Resour. Plann. Manage. 138, 431–441. doi:10.1061/(ASCE)WR.1943-5452.0000202.

Vuille, M., 1999. Atmospheric circulation over the Bolivian Altiplano during dry and wet periods and extreme phases of the Southern Oscillation. International Journal of Climatology 19, 1579–1600. doi:10.1002/(SICI)1097-0088(19991130)19:14<1579::AID-JOC441>3.0.CO;2-N.

Vuille, M., Baumgartner, M.F., 1993. Hydrologic Investigations in the North Chilean Altiplano Using Landsat - MSS and - TM data. Geocarto International 3, 35–45. doi:10.1080/10106049309354418.

Vuille, M., Bradley, R.S., Keimig, F., 2000. Interannual climate variability in the Central Andes and its relation to tropical Pacific and Atlantic forcing. Journal of Geophysical Research 105, 12447. doi:10.1029/2000JD900134.

Vuille, M., Keimig, F., 2004. Interannual variability of summertime convective cloudiness and precipitation in the central Andes derived from ISCCP-B3 data. Journal of Climate 17, 3334–3348. doi:10.1175/1520-0442(2004)017<3334:IVOSCC>2.0.CO;2.

Wade, B.L., 2014. Chasing South America's monsoon. Science 346, 1042–1043.

Wang, J., Fang, X., Appel, E., Zhang, W., 2013. Magnetostratigraphic and radiometric constraints on salt formation in the Qaidam Basin, NE Tibetan Plateau. Quaternary Science Reviews 78, 53–64. URL: `http://dx.doi.org/10.1016/j.quascirev.2013.07.017`, doi:10.1016/j.quascirev.2013.07.017.

Wang, X., Auler, A.S., Edwards, R.L., Cheng, H., Cristalli, P.S., Smart, P.L., Richards, D.a., Shen, C.C., 2004. Wet periods in northeastern Brazil over the past 210 kyr linked to distant climate anomalies. Nature 432, 740–743. doi:10.1038/nature03067.

Wang, X., Auler, A.S., Edwards, R.L., Cheng, H., Ito, E., Solheid, M., 2006. Interhemispheric anti-phasing of rainfall during the last glacial period. Quaternary Science Reviews 25, 3391–3403. doi:10.1016/j.quascirev.2006.02.009.

Wang, X., Auler, A.S., Edwards, R.L., Cheng, H., Ito, E., Wang, Y., Kong, X., Solheid, M., 2007. Millennial-scale precipitation changes in southern Brazil over the past 90,000 years. Geophysical Research Letters 34, 1–5. doi:10.1029/2007GL031149.

Wang, Y.J., Cheng, H., Edwards, R.L., An, Z.S., Wu, J.Y., Shen, C.C., Dorale, J.A., 2001. A high-resolution absolute-dated late Pleistocene Monsoon record from Hulu Cave, China. Science 294, 2345–2348. doi:10.1126/science.1064618.

Wendt, I., Carl, C., 1991. The statistical distribution of the mean squared weighted deviation. Chemical Geology: Isotope Geoscience section 86, 275–285. URL: `https://linkinghub.elsevier.com/retrieve/pii/016896229190010T`, doi:10.1016/0168-9622(91)90010-T.

Winograd, I.J., Coplen, T.B., Landwehr, J.M., Riggs, A.C., Ludwig, K.R., Szabo, B.J., Kolesar, P.T., Revesz, K.M., 1992. Continuous 500,000-Year Climate Record From Vein Calcite in Devils-Hole, Nevada. Science 258, 255–260.

Wood, R.D., Imahori, W., 1959. Geographical Distribution of Characeae. Bulletin of the Torrey Botanical Club 86, 172–183.

Woods, A., Rodbell, D., Abbott, M., Hatfield, R.G., Chen, C.Y., Lehmann, S., McGee, D., Weidhaas, N., Tapia, P.M., Valero-Garcés, B.L., Bush, M., Stoner, J.S., 2019. Abrupt arctic warming repeatedly led to prolonged drought and glacial retreat in the tropical andes during the last glacial cycle. EarthArXiv doi:10.31223/osf.io/7hd3a.

Wright, H.E., 1983. Late-Pleistocene Glaciation and Climate around the Junín Plain, Central Peruvian Highlands. Geografiska Annaler. Series A, Physical Geography 65, 35–43. URL: `http://www.jstor.org/stable/520719`.

Wrozyna, C., Frenzel, P., Daut, G., Mäusbacher, R., Zhu, L., Schwalb, A., 2012. Holocene Lake-Level Changes of Lake Nam Co, Tibetan Plateau, Deduced from Ostracod Assemblages and δ^{18}O and δ^{13}C Signatures of Their Valves. Developments in Quaternary Science 17, 281–295. doi:10.1016/B978-0-444-53636-5.00016-0.

Xuan, C., Channell, J.E., Hodell, D.A., 2016. Quaternary magnetic and oxygen isotope stratigraphy in diatom-rich sediments of the southern Gardar Drift (IODP Site U1304, North Atlantic). Quaternary Science Reviews 142, 74–89.

Yliruokanen, I., 1980. The occurence of uranium in some finnish peat bogs. Kemia-Kemi 7, 213–217.

York, D., 1968. Least squares fitting of a straight line with correlated errors. Earth and Planetary Science Letters 5, 320–324. URL: `http://www.sciencedirect.com/science/article/pii/S0012821X68800597`, doi:https://doi.org/10.1016/S0012-821X(68)80059-7.

Yu, G., Harrison, S.P., Xue, B., 2001. Lake status records from China: Data Base Documentation. MPI-BGC Technical Report 4, 240.

Zhou, J., Lau, K.M., 1998. Does a monsoon climate exist over South America? Journal of Climate 11, 1020–1040. doi:10.1175/1520-0442(1998)011<1020:DAMCEO>2.0.CO;2.

Ziegler, L., Constable, C., Johnson, C., Tauxe, L., 2011. PADM2M: a penalized maximum likelihood model of the 0–2 Ma palaeomagnetic axial dipole moment. Geophysical Journal International 184, 1069–1089.